

MODELING AND CONTROL OF MEMS MICROMIRROR ARRAYS WITH
NONLINEARITIES AND PARAMETRIC UNCERTAINTIES

By

JESSICA RAE BRONSON

A DISSERTATION PRESENTED TO THE GRADUATE SCHOOL
OF THE UNIVERSITY OF FLORIDA IN PARTIAL FULFILLMENT
OF THE REQUIREMENTS FOR THE DEGREE OF
DOCTOR OF PHILOSOPHY

UNIVERSITY OF FLORIDA

2007

© 2007 Jessica Rae Bronson

To my parents

ACKNOWLEDGMENTS

I thank first of all, my supervisory committee chair, Gloria Wiens, for the opportunities to attend the University of Florida and to conduct this work. She is also responsible for providing me with the exceptional experience of working closely with Sandia National Laboratories through the summer internship program. I also thank James Allen for his guidance as my mentor at Sandia National Laboratories and for shaping the scope of this work. I thank all my committee members, Louis Cattafesta, Norman Fitz-Coy, and Toshikazu Nishida for their time and consideration.

Additionally I thank my family, especially my parents, for their loving support in all of my endeavors. I also thank my many friends and classmates in the Space, Automation, and Manufacturing Mechanisms (SAMM) Laboratory and in the Department of Mechanical and Aerospace Engineering for their friendship and camaraderie. In particular, I thank Adam Watkins for the many roles he plays as friend, colleague, mentor and partner.

TABLE OF CONTENTS

	<u>Page</u>
ACKNOWLEDGMENTS	4
LIST OF TABLES	8
LIST OF FIGURES	9
ABSTRACT	17
 CHAPTER	
1 INTRODUCTION	19
1.1 Motivation	19
1.2 Research Objectives	20
2 LITERATURE REVIEW	23
2.1 Microelectromechanical Systems	23
2.2 Micromirrors and Applications	24
2.3 Electrostatic Actuation and Instability	28
2.3.1 Modeling, Pull-in and Hysteresis	28
2.3.2 Design Techniques to Eliminate Pull-in	31
2.3.3 Capacitive and Charge Control Techniques to Eliminate Pull-in	32
2.3.4 Closed-loop Voltage Control to Eliminate Pull-in	33
2.4 Feedback Control Techniques Applied to MEMS	34
2.4.1 Linear Control	35
2.4.2 Adaptive and Robust Control	37
2.4.3 Nonlinear Control	39
2.5 Sensing Methods for Feedback	41
2.6 Summary Remarks	43
3 MICROMIRROR MODELING AND STATIC PERFORMANCE	45
3.1 Description of the SUMMiT V Microfabrication Process	45
3.2 Micromirror Actuator Description	47
3.3 Electrostatic Actuation and Instability	50
3.3.1 Parallel Plate Electrostatics	50
3.3.2 Parallel Plate Torsion Actuator	56
3.4 Model for Vertical Comb Drive Actuator	60
3.4.1 Mechanical Model	61
3.4.2 Electrostatic Model	63
3.4.3 Electromechanical Model	66
3.4.4 Linear Approximation	70
3.4.5 Bifurcation Analysis	73
3.5 Chapter Summary	78

4	UNCERTAINTY ANALYSIS AND EXPERIMENTAL CHARACTERIZATION	81
4.1	Parametric Uncertainty and Sensitivity Analysis.....	81
4.1.1	Effects of Individual Parameter Variations.....	84
4.1.2	Monte Carlo Simulations	91
4.2	Experimental Characterization.....	100
4.2.1	Equipment Description	100
4.2.2	Static Results for Single Micromirrors	103
4.2.3	Static Results for Micromirror Arrays	105
4.3	Chapter Summary.....	111
5	DYNAMIC MODEL AND HYSTERESIS STUDY	113
5.1	Dynamic Model and Resonant Frequency Determination.....	113
5.1.1	Modal Analysis	114
5.1.2	Dynamic Characterization.....	119
5.2	Open-Loop Step Response.....	122
5.2.1	Effects of Parametric Uncertainty on Step Response	123
5.2.2	Effects of Pull-in and Hysteresis on Open-Loop Response.....	123
5.2.3	Continuous Characterization of Micromirror Arrays.....	126
5.3	Hysteresis Case Study: Progressive-Linkage.....	128
5.3.1	Progressive-Linkage Design	128
5.3.2	Open-Loop Response Using a Progressive-Linkage	135
5.3.3	Parametric Sensitivity of the Progressive-Linkage	135
5.3.4	Progressive-Linkage Prototype	139
5.5	Chapter Summary.....	144
6	CONTROL DESIGN AND SIMULATION	146
6.1	PID Control.....	147
6.1.1	PID Control Theory	147
6.1.2	PID Results	148
6.1.3	PID Controller Response to Hysteresis.....	149
6.2	LQR Control	154
6.2.1	LQR Control Theory	154
6.2.2	State Estimation	159
6.2.3	LQR Results.....	160
6.2.4	LQR Controller Response to Hysteresis	163
6.3	Modeling the Micromirror Array.....	164
6.3.1	Modeling the Array of Mirrors	165
6.3.2	Sensor Types	167
6.4	Modeling the Sensor Response.....	170
6.4.1	PSD Response.....	174
6.4.2	CCD Response.....	179
6.4.3	Summary of Sensor Analysis.....	181
6.5	Chapter Summary.....	181

7	CONCLUSIONS AND FUTURE WORK.....	183
APPENDIX		
A	MODEL GEOMETRY.....	188
B	MONTE CARLO SIMULATION INPUTS.....	189
C	LASER DOPPLER VIBROMETER RESULTS.....	200
	LIST OF REFERENCES.....	208
	BIOGRAPHICAL SKETCH.....	218

LIST OF TABLES

<u>Table</u>	<u>page</u>
2-1 Summary of feedback control papers discussed in the literature review.....	36
3-1 Mean and standard deviation of fabrication variations for layer thickness in the SUMMiT V surface micromachining process.	47
3-2 Mean and standard deviation of fabrication variations of line widths in SUMMiT V.	47
3-3 Values output from finite element analysis of mechanical spring stiffness.....	63
3-4 Comparison of polynomial fit for approximation of capacitance function.....	66
3-5 Comparison of polynomial fit for approximation of capacitance function.....	66
3-6 List of parameters used for this analysis.....	78
4-1 Mean and standard deviation of fabrication variations for layer thickness in the SUMMiT V surface micromachining process.	82
4-2 Mean and standard deviation of fabrication variations of line widths in SUMMiT V.	82
4-3 Spring stiffness values for changing dimensional and material parameters.	85
4-4 Results from the Monte Carlo simulations for the capacitance values in terms of mean, standard deviation, and the percent change from nominal.....	97
4-5 Mean and standard deviation for pull-in angle and voltage from sets of mirrors on all three arrays tested.	108
5-1 Modal analysis results for first 10 modes and their natural frequencies, and the participation factors and ratios for each direction.....	118
5-2 The first three natural frequencies determined from the LDV experiment.	122
5-3 Link length dimensions used for progressive-linkage design.....	134
5-4 Joint dimensions used for progressive-linkage design.....	134
5-5 Uncertainties in the joint dimensions for a proposed progressive-linkage design.....	138

LIST OF FIGURES

<u>Figure</u>	<u>page</u>
2-1 The SEM images of MEMS devices created using SUMMiT V microfabrication process.....	25
2-2 Images of micromirror arrays developed in industry.....	26
2-3 Adaptive optics (AO) mirror used for wavefront correction.....	27
2-4 Use of an AO MEMS programmable diffraction grating for spectroscopy.....	27
3-1 Drawing of the SUMMiT V structural and sacrificial layers	46
3-2 Area with nominal dimensions L and w with the dashed line indicating the actual area due to error in the line width.....	47
3-3 Images of the micromirror array	48
3-4 Illustration of mirrors operating as an optical diffraction grating.....	48
3-5 Micrograph of an array of mirrors and schematic of mirror with hidden vertical comb drive.....	49
3-6 Solid model of micromirror showing polysilicon layer names from SUMMiT V.....	49
3-7 Schematic of a parallel plate electrostatic actuator modeled as a mass-spring-damper system.....	51
3-8 Static equilibrium relationship for the parallel plate electrostatic actuator.....	54
3-9 Electrostatic force for different voltages and mechanical force showing pull-in for the electrostatic parallel plate actuator.....	54
3-10 Pull-in function for the parallel-plate electrostatic actuator.....	55
3-11 Static equilibrium relationships for the parallel plate actuator using different spring constants.....	56
3-12 Schematic of a torsion electrostatic actuator.....	57
3-13 Static equilibrium relationships for the torsion actuator.....	59
3-14 Pull-in function for the torsion actuator.....	60
3-15 Drawing of the mechanical spring that supports the micromirrors and provides the restoring force.....	61

3-16	Image of the mechanical spring that supports the micromirror indicating boundary conditions and location for applying displacement loads for finite element analysis.	62
3-17	Image from ANSYS of the deformed spring and the outline of the undeformed shape after displacements are applied.....	63
3-18	Solid model geometry of the unit cell used in the electrostatic FEA simulation.....	65
3-19	Capacitance calculation as a function of rotation angle, θ , calculated using 3D FEA and varying orders of polynomial curve fit approximations.....	66
3-20	Plot of the Pull-in function $PI(\theta)$ for the micromirror with the vertical comb drive actuator showing that pull-in occurs at 16.5 degrees.....	67
3-21	Electrostatic and Mechanical torque as a function of rotation angle, θ , and voltage for different voltage values.	68
3-22	Torque as a function of rotation angle, θ , and voltage for different values of mechanical spring constant.	69
3-23	Plot of static equilibrium behavior, showing pull-in and hysteresis, predicted from the model.....	69
3-24	Static equilibrium relationships for the nonlinear plant model, and the linear plant approximation.	70
3-25	Static equilibrium relationships for the nonlinear plant model, and the small signal model linearized about an operating point (θ_0, V_0)	72
3-26	Illustration of piecewise linearization about multiple operating points.....	73
3-27	Plot showing the roots of the function $F(x_1)$ occur where the function crosses zero.....	76
3-28	Bifurcation diagram for a MEMS torsion mirror with electrostatic vertical comb drive actuator.	79
3-29	Bifurcation diagram showing the effects of different spring constants.	79
4-1	Fabrication tolerances can changes the thicknesses of the layers, resulting in changes in the final geometry dimensions.....	82
4-2	Fabrication tolerances can change the dimensions of a fabricated geometry, affecting the final shape, volume, and mass.	83
4-3	Nominal dimensions used to calculate the volume of the moving mass.	83
4-4	Capacitance functions for the electrostatic model with parametric changes in the layer thickness of the structural polysilicon.....	88

4-5	Capacitance functions for the electrostatic model with parametric changes in the layer thickness of the Dimple3 backfill and the sacrificial oxide.....	88
4-6	Capacitance functions for the electrostatic model with parametric changes in the linewidth error of the structural polysilicon layers.....	89
4-7	Static displacement relationships for the micromirror model with parametric changes in the layer thickness of the structural polysilicon.....	89
4-8	Static displacement relationships for the micromirror model with parametric changes in the layer thickness of the Dimple3 backfill and the sacrificial oxide.....	90
4-9	Static displacement relationships for the micromirror model with parametric changes in the linewidth error of the structural polysilicon layers.....	90
4-10	Sensitivity of voltage with respect to changes in line width for each value of θ	92
4-11	Sensitivity of voltage with respect to changes in layer thickness for each value of θ	92
4-12	Gaussian distribution with a mean of 0 and standard deviation of 1.....	94
4-13	Histogram for mechanical stiffness when accounting for variations in thickness of MMPoly1 and Young's modulus.....	95
4-14	Histogram for mechanical stiffness taking into account variations in thickness of MMPoly1, Young's modulus, and linewidth of MMPoly1.....	95
4-15	Results from the capacitance simulation for 250 random variable sets that show the effects of parametric uncertainty on the electrostatic model.....	96
4-16	Static displacement results of 250 Monte Carlo simulations with random Gaussian distributed dimensional variations.....	98
4-17	Histogram of values from the Monte Carlo simulations for the layer thickness of Sacox3.....	99
4-18	Static displacement curves from the Monte Carlo simulations that indicate the effect of large variations in the Sacox3 layer thickness.....	99
4-19	Diagram of an optical profiler measurement system.....	101
4-20	Six mirrors from the micromirror array measured with the optical profiler system.....	102
4-21	Data records from the SureVision display that show the cross-section profile of the tilt angle measurements.....	103
4-22	Micrograph image of a single micromirror.....	104

4-23	Experimental static results taken from individual micromirrors that are not in an array.	104
4-24	Approximate locations of data collection on all three arrays.	106
4-25	Experimental results from array 1, area A.	106
4-26	Experimental results from array 2, areas D and E.	107
4-27	Experimental results from array 3, areas A and D.	107
4-28	Nominal model with experimental data.	109
4-29	Model-predicted results from 100 simulations with parameters determined by random Gaussian variations, shown with experimental data.	109
5-1	Open-loop nonlinear plant response to a step input of 7 degrees for different damping ratios.	114
5-2	Solid model created for modal analysis.	118
5-3	Time series data of the micromirror response to an acoustic impulse taken with a laser doppler vibrometer.	120
5-4	Results from the LDV experiment showing resonant peaks.	121
5-5	Open-loop response to a step input of 7 degrees for the nonlinear plant dynamics and variations in spring stiffness, k_m	124
5-6	Open-loop nonlinear plant response to a step input of 7 degrees for 50 random parameter variations.	124
5-7	Open-loop responses to a sinusoidal input showing hysteresis.	126
5-8	Open-loop responses to a step command showing overshoot that result in pull-in.	126
5-9	Results from dynamic study showing pull-in and hysteresis.	127
5-10	Results showing the hysteretic behavior of the micromirrors.	128
5-11	Diagram of four-bar mechanism for progressive linkage analysis.	130
5-12	Cantilever beam with cross-section $w \times t$, and length L	131
5-13	Free body diagrams for each member of the linkage.	132
5-14	Progressive-linkage behavior for different values of r_o in μm	132

5-15	Progressive linkage output for r_o equal to 9 μm along with the electrostatic torque curves and the linear restoring torque.....	133
5-16	Static θ - V relationship for micromirror with a progressive-linkage.....	134
5-17	Bifurcation diagram for micromirror using a progressive-linkage to avoid pull-in behavior.....	136
5-18	Bifurcation diagram for the micromirrors using a progressive-linkage to avoid pull-in behavior for different values of mechanical stiffness.....	136
5-19	Open-loop responses to a sinusoidal input for the device using a progressive-linkage...	137
5-20	Open-loop response to a step input for device using a progressive-linkage.....	137
5-21	Results of parametric analysis for individual errors in joint fabrication of the progressive-linkage.....	140
5-22	Fifty Monte Carlo simulation results for varying the joint fabrication parameters for the progressive-linkage design.....	140
5-23	Schematic drawing of the prototype progressive linkage spring.....	141
5-24	Micrograph of the prototype micromirror with a progressive linkage spring.....	141
5-25	Experimental data collected for the prototype of the micromirror with the progressive-linkage.....	143
5-26	Results from FEA of the prototype progressive-linkage design for linear and nonlinear deflection analysis shows the prototype progressive-linkage fails to produce the desired stiffness profile.....	143
6-1	Basic block diagram with unity feedback.....	146
6-2	Block diagram with PID controller.....	148
6-3	Step responses for PID controller.....	150
6-4	Closed-loop PID response to different step inputs when the spring constant is varied by $\pm 10\%$	150
6-5	Closed-loop PID response to a step input of 7 degrees for 50 random sets of parametric variations.....	151
6-6	Closed-loop PID response to a commanded position in the unstable region.....	153
6-7	Closed-loop step responses for PID controller for a system using a progressive-linkage.....	153

6-8	General block diagram for LQR controller problem	154
6-9	Block diagram of LQR control with an internal model for tracking a step command. ...	158
6-10	Block diagram of LQR controller using a state-estimator for a plant without an integrator.....	159
6-11	Step responses for LQR controller.....	161
6-12	Closed-loop LQR response to a step input of 7 degrees for 50 random parameter variations.....	162
6-13	Closed-loop step responses for LQR controller for a system using a progressive-linkage.....	164
6-14	Schematic of modeling an array of mirrors as a SIMO system.....	165
6-15	Schematic drawing of an array of 5 mirrors.....	166
6-16	Illustration of the measured center of gravity (CG) on a 1-D PSD when there are errors in the spacing and linearity of the micromirrors.....	168
6-17	Illustration of the measured center of gravity (CG) on a 2-D PSD when there are errors in the spacing and linearity of the micromirrors.....	168
6-18	Illustration of the measured errors of the reflected light from two micromirror arrays onto a CCD.....	169
6-19	Schematic of the beam steering experiment with only one micromirror.....	171
6-20	Geometry used to determine the angle of incidence and reflection.....	172
6-21	Calculating the reflected ray of light.....	173
6-22	The intersection of the line from B0 to R and the plane C occurs at point P.....	174
6-23	Schematic of 5 micromirrors in an array reflecting light onto a PSD sensor	175
6-24	Calibration of the PSD for ideal case of five micromirrors.....	176
6-25	Open-loop results to a step response for an array of 5 micromirrors with model uncertainty.....	176
6-26	Open-loop response for system with one broken mirror and 4 ideal mirrors, measured by a PSD	177
6-27	Incorporating feedback control into array model.....	177
6-28	Controlled PID step response using PSD sensor	178

6-29	Controlled LQR step response using PSD sensor.....	178
6-30	Closed-loop response for system with one broken mirror and 4 ideal mirrors, for a PID controller and a PSD sensor.	179
6-31	Schematic of 5 micromirrors in an array reflecting light onto a CCD sensor where each separate location of the light can be measured.	180
6-32.	Closed-loop response for system with one broken mirror and 4 ideal mirrors, for a PID controller and a CCD sensor.....	180
A-1	Geometry dimensions in μm for creating electrostatic model.	188
B-1	Histogram of values for the thickness of layer MMPoly0.....	189
B-2	Histogram of values for the thickness of layer MMPoly1.....	190
B-3	Histogram of values for the thickness of layer MMPoly2.....	190
B-4	Histogram of values for the thickness of layer MMPoly3.....	191
B-5	Histogram of values for the thickness of layer MMPoly4.....	191
B-6	Histogram of values for the thickness of Dimple3 backfill.	192
B-7	Histogram of values for the thickness of layer Sacox1.....	192
B-8	Histogram of values for the thickness of layer Sacox2.....	193
B-9	Histogram of values for the thickness of layer Sacox3.....	193
B-10	Histogram of values for the thickness of layer Sacox4.....	194
B-11	Histogram of values for the linewidth variation of layer MMPoly2.	194
B-12	Histogram of values for the linewidth variation of layer MMPoly3.	195
B-13	Histogram of values for the linewidth variation of layer MMPoly4.	195
B-14	Histogram of the mass values calculated from the parametric variation data.	196
B-15	Histogram of values from the Monte Carlo simulations for the linewidth error of MMPoly2.....	196
B-16	Static displacement curves from the Monte Carlo simulations that indicate the effect of large variations in the linewidth error of MMPoly2.....	197
B-17	Histogram of values from the Monte Carlo simulations for the layer thickness of MMPoly1.....	197

B-18	Static displacement curves from the Monte Carlo simulations that indicate the effect of large variations in the thickness of MMPoly1.....	198
B-19	Histogram of values from the Monte Carlo simulations for the layer thickness of Sacox4.....	198
B-20	Static displacement curves from the Monte Carlo simulations that indicate the effect of large variations in the thickness of Sacox4.	199
C-1	Magnitude results of FFT for device 1, trial 1.....	200
C-2	Magnitude results of FFT for device 1, trial 2.....	200
C-3	Magnitude results of FFT for device 1, trial 3.....	201
C-4	Magnitude results of FFT for device 1, trial 4.....	201
C-5	Magnitude results of FFT for device 1, trial 5.....	202
C-6	Magnitude results of FFT for device 2, trial 1.....	202
C-7	Magnitude results of FFT for device 2, trial 2.....	203
C-8	Magnitude results of FFT for device 2, trial 3.....	203
C-9	Magnitude results of FFT for device 2, trial 4.....	204
C-10	Magnitude results of FFT for device 2, trial 5.....	204
C-11	Magnitude results of FFT for device 3, trial 1.....	205
C-12	Magnitude results of FFT for device 3, trial 2.....	205
C-13	Magnitude results of FFT for device 3, trial 3.....	206
C-14	Magnitude results of FFT for device 3, trial 4.....	206
C-15	Magnitude results of FFT for device 3, trial 5.....	207

Abstract of Dissertation Presented to the Graduate School
of the University of Florida in Partial Fulfillment of the
Requirements for the Degree of Doctor of Philosophy

MODELING AND CONTROL OF MEMS MICROMIRROR ARRAYS WITH
NONLINEARITIES AND PARAMETRIC UNCERTAINTIES

By

Jessica Rae Bronson

December 2007

Chair: Gloria J. Wiens
Major: Mechanical Engineering

Micromirror arrays have resulted in some of the most successful and versatile microelectromechanical system (MEMS) devices for applications including optical switches, scanning and imaging, and adaptive optics. Many of these devices consist of large arrays of micromirrors, and it is desirable to ensure accurate positioning capabilities for each mirror in the array despite the presence of nonlinearities or parametric uncertainties from the fabrication process. This research develops analytical models in the electrostatic and mechanical domains to study the effect of fabrication tolerances and uncertainties, electrostatic pull-in, and hysteresis on the performance of micromirror arrays, and presents solutions to improve device performance.

To achieve these goals, extensive modeling of the electrostatic micromirror arrays is presented. As with many MEMS devices that operate in multiple physical domains, the modeling considers both electrical and mechanical characteristics. The electrical model consists of determining the electrostatic torque produced when an actuation voltage is applied. The mechanical model considers the opposing torque provided by the supporting torsion spring. These models are also used to evaluate the sensitivity of the micromirrors to parametric uncertainties from the fabrication process by considering the effect of each fabrication tolerance individually and also their combined effects using Monte Carlo simulations. Additional

characterization of the system dynamics is presented through modal analysis in which the results for the full 6 degree-of-freedom (DOF) device are compared to the 1 DOF model assumptions. The devices are characterized by measuring the micromirror rotation as a function of the actuation voltage using an optical profiler to determine static performance, as well as measuring the electrostatic pull-in and hysteresis behavior. The measurements, taken for multiple mirrors across three different arrays, validate the results from analytical models, and demonstrate the need to compensate for differences in performance.

Results from the modeling and characterization are used to develop passive and active control techniques to ensure accurate position tracking across an array of devices in the presence of model uncertainties. A passive design method is presented called a progressive-linkage that is intended to eliminate the occurrence of electrostatic pull-in and hysteresis. Also, classical and optimal feedback control techniques are utilized to further delineate the impact of the parametric uncertainties on the system performance. As these mirrors are arranged in an array, the performance of individual mirrors is examined, and then this control is extended to the problem of controlling an array. This array control problem is explored by considering different types of feedback error metrics and the sensors that may be used to provide the feedback signal for this system.

The impact of the work presented in this dissertation is an increased understanding of the complexities of designing and operating arrays of electrostatic micromirrors for high-precision applications. The modeling methods developed may be extended in future work to include design optimization to decrease the effects of parametric uncertainty on the micromirror performance, as well as developing systems that can easily incorporate feedback mechanisms for implementation of the closed-loop control algorithms.

CHAPTER 1 INTRODUCTION

1.1 Motivation

Micromirror arrays have resulted in some of the most successful and versatile microelectromechanical system (MEMS) devices for applications including optical switches for telecommunications, scanning and imaging for projection displays, diffraction gratings for spectroscopy, and adaptive optics for wave front correction. Many of these devices consist of large arrays of micromirrors. As such, it is desirable to ensure accurate positioning capabilities for each mirror in the array despite the presence of outside disturbances or variations from the fabrication process. The errors due to the fabrication process can be attributed in part to small deviations in dimensional or material properties. It is the effects of these errors that can have significant impact on the performance of the final product. As such, it is important to evaluate the sensitivity of the micromirror design to determine the potential limitations on the device performance.

The diminutive scale of MEMS devices makes electrostatic actuation a popular and effective means of driving micromirrors. One limiting factor to most electrostatic actuators is the electrostatic pull-in instability that occurs when the electrostatic force overcomes the mechanical restoring force. When pull-in occurs, the device can no longer maintain an equilibrium position and will move to its fully actuated position, limiting the full scanning range available. Another phenomenon associated with this instability is that once the mirror has pulled-in, the voltage required to maintain the fully actuated position is lower than the pull-in voltage. The mirror will not return from this position until the actuating voltage has been reduced below a certain threshold. In order to understand these phenomena, theoretical models may be developed for the electrostatic and mechanical domains. These models can then be

utilized to evaluate the effects of fabrication errors and determine the performance limitations of the micromirrors. These issues can be mitigated through the successful application of design methods as well as through feedback control.

Currently, state-of-the-art micromirror arrays rely on open-loop actuation that may limit the device to on/off digital operation or require extensive calibration for analog performance [1], [2]. Many of today's emerging technologies, however, require true analog positioning capabilities. Therefore, in order to guarantee precision and accuracy of the mirror position for analog operation, closed-loop feedback control techniques are considered essential. Feedback control has long been used in many macro-scale systems, yet limited work has been done to apply these techniques to MEMS systems. An additional need arises in the use of very large arrays of micromirror devices. While control of one mirror may be a straightforward task, it becomes much more difficult to extend that control to a very large system. The micromirror arrays in this research are constrained such that the micromirrors are not individually controllable, creating a unique control application to a single-input/multiple-output system (SIMO). This also gives rise to the question of obtaining an appropriate feedback signal for a system of arrays. The types of sensing used to gather the feedback information as well as how this information is used are critical issues.

1.2 Research Objectives

The objective of this research is to develop analytical models to study the effect of fabrication tolerances and uncertainties, electrostatic pull-in and hysteresis on the performance of micromirror arrays that are used in adaptive optics applications requiring precise and accurate positioning. The modeling techniques allow for analysis of the system in both the electrostatic and the mechanical domains using a combination of analytical models and finite element analysis (FEA). These theoretical results are compared to experimental characterization data.

The models are also used to determine the potential effects of parametric uncertainties in the fabrication process, and to estimate the sensitivity of the micromirror design to these uncertainties. This information is valuable in determining the possible limits on performance that can be achieved through only open-loop actuation methods. These models also characterize the effects of electrostatic instability and the resulting hysteresis. The modeling is extended from the initial quasi-static approximation to include the dynamic behavior of the system. After thorough analysis and characterization of the system behavior, several solutions are presented to improve the performance and positioning accuracy of the micromirror devices. These solutions, including passive and active controls, are developed to ensure that the device performance will be robust in the presence of system nonlinearities and parametric uncertainties. A passive design solution, called a progressive-linkage, is presented that will eliminate the effects of electrostatic pull-in and hysteresis, thus extending the stable range of motion for the micromirrors. The theoretical design approach is presented along with discussion and analysis regarding the sensitivity of the linkage to fabrication errors, as well as an initial prototype attempt. Active control solutions, including classical and optimal control design, are presented as an investigation of feedback control methodologies for use on micromirrors that can be used to achieve high precision positioning. The sources of nonlinearities and parametric uncertainties previously identified and quantified during the modeling and characterization of the devices now forms an error basis for examining the robust performance of the control algorithms.

In Chapter 2, an overview of previous work from the literature on micromirror arrays, their applications, and control of MEMS devices is presented for identifying the underlying issues impeding further development and implementation. This led to the motivation of the work presented in the remaining chapters of this dissertation including analytical modeling and the

study of effects of fabrication tolerances and uncertainties, dynamic performance and passive control. Chapter 3 provides the static modeling for the micromirrors and Chapter 4 analyzes the sensitivity of the devices with respect to fabrication tolerances, comparing the model results to experimental characterization data. Chapter 5 discusses the dynamic system, including characterizing the resonant modes and studying the effect of electrostatic hysteresis. The progressive-linkage design is presented as a solution to the problems caused by electrostatic pull-in. Upon identifying the model uncertainties and behavioral characteristics of these micromirrors, an investigation of closed-loop control methods is conducted in Chapter 6 to further delineate the impact of the parametric uncertainties on system performance. The controllers are compared and evaluated in simulation to determine their effectiveness for position control in the presence of model uncertainties for a single mirror and a spectrum of uncertainties across the array. In order to evaluate the array performance, the method of sensing the position of the micromirrors is critical, and several sensor types are considered. Finally, the conclusions of this study are given in Chapter 7, along with directions for future work.

CHAPTER 2 LITERATURE REVIEW

In this chapter, a review of the literature concerning applications of micromirrors, modeling of electrostatic devices, and the design of feedback controllers for MEMS devices and related adaptive optics systems is presented. This review is intended to provide an overview of the current state of research on electrostatic micromirrors and the control of MEMS devices so as to identify underlying issues impeding further development and implementation. A brief introduction to MEMS and microfabrication methods is presented, followed by a discussion of applications for micromirror technology. Electrostatic actuation is used widely for MEMS devices, and it is the actuation method used by the micromirror arrays presented in this dissertation; therefore a discussion of electrostatic actuation and the pull-in instability is given, including modeling methods and the different methods that are dedicated to addressing pull-in. Control applications to MEMS is a relatively new area of research, therefore a thorough discussion is included of control methods that have been applied to a variety of MEMS devices with many different methods of actuation in addition to electrostatic. The chapter closes with remarks summarizing the findings of this review and outlining the specific areas of research that are currently lacking, and that will be addressed in the remainder of this document.

2.1 Microelectromechanical Systems

Microelectromechanical Systems (MEMS) refer to mechanical and electrical structures used to create sensors and actuators with feature sizes ranging from 1 μm to 1 mm. MEMS have found successful applications in many markets, most notably nozzles for inkjet printing, accelerometers for automotive airbags, blood pressure sensors for health care, optical switches and arrays for communications and projection displays. This remarkable technology is continuing to expand and promises to bring revolutionary capabilities to nearly every industry.

MEMS are batch fabricated, typically making them inexpensive, using a microfabrication process such as bulk or surface micromachining [3]. This technology is founded on fabrication techniques first used for integrated circuits (IC) and utilizes the same lithographic patterning techniques. Bulk micromachining techniques rely on selective etching to remove material from the whole to form structures with wells and trenches [4]. Surface micromachining is considered an additive technique that creates mechanisms by layering a structural layer, such as polysilicon, with a sacrificial layer, such as silicon dioxide (oxide) [5]. Through a repeated series of lithography, etching and deposition, freestanding structures are created.

As with any manufacturing or machining process, fabrication tolerances can give rise to parametric uncertainties causing the dimensions of fabricated device to vary slightly from the intended design. For microfabrication this is due to small over or under etching of layers as well as variations in material properties, and misalignment between layers [7]-[12]. All these variations can occur across the wafer as well as from batch to batch. Chapter 3 provides further analysis on the influence of fabrication variations on device performance.

The process utilized to create the devices discussed in this research is Sandia's Ultra-planar, Multi-level MEMS Technology (SUMMiT V), developed by Sandia National Laboratories that utilizes five structural layers of polysilicon [6]. The specifics of the fabrication process are discussed further in Chapter 3. Examples of structures that can be created using this process seen in Figure 2-1 show scanning electron micrographs (SEMs) of a mechanical gear hub and a cross-section of a pin-joint that allows rotation. These are excellent examples of the complex structures created from layering simple, 2-D geometry.

2.2 Micromirrors and Applications

Micromirrors are one of the most widely used and commercially viable applications for MEMS technology. The small size of these devices makes them ideal for optical switching and

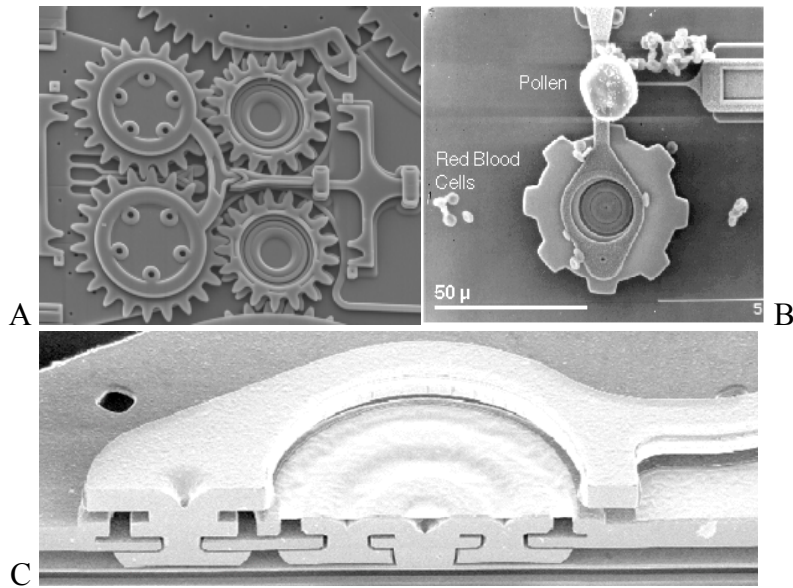


Figure 2-1. The SEM images of MEMS devices created using SUMMiT V microfabrication process. A) Micromachined gears. B) Micromachined gears. C) A cross-section view of a pin-joint that allows for gear rotation. (Courtesy of Sandia National Laboratories, SUMMiT Technologies, www.mems.sandia.gov).

scanning operations at very high speeds. Both single mirrors and large arrays are used for optical switches for communications [13]-[19], scanning and imaging for projection displays [2], [20], diffraction gratings for optical spectroscopy [21]-[25], and beam steering for adaptive optics [26]-[32] and free-space communication [33], [34].

An example of micromirrors that have been commercially successful is the Texas Instruments' Digital Micromirror Device™ (DMD) that uses millions of torsional electrostatic micromirrors to manipulate light. Applications for the DMD include projection displays, televisions, laser printers, image processing, light modulation, and optical switching [2], [20]. The success of many of these applications relies on purely digital functioning that is not suitable for more advanced applications that require analog operation, such as adaptive optics (AO). Sandia National Laboratories developed electrostatic micromirror arrays to be used as instrumentation for adaptive optics in space applications [35]. Images of Texas Instruments' DMD and the Sandia micromirrors are shown in Figure 2-2.

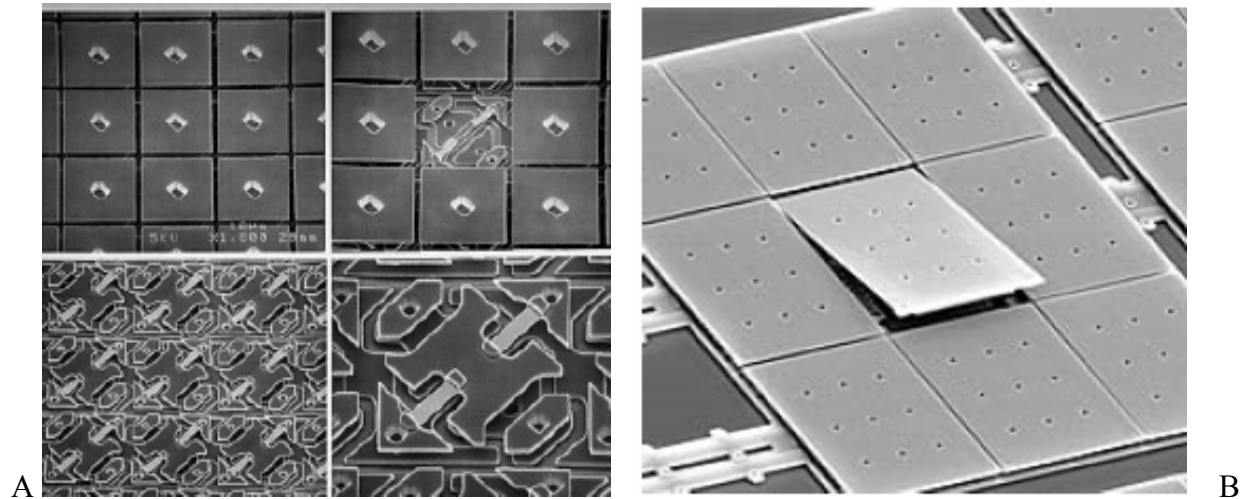


Figure 2-2. Images of micromirror arrays developed in industry. A) Texas Instruments' Digital Micromirror Device (DMD) and B) Sandia National Laboratories' AO micromirror array. (Courtesy of Texas Instruments, www.ti.com, and Sandia National Laboratories, SUMMiT Technologies, www.mems.sandia.gov).

Adaptive optics (AO) refers to optical components such as mirrors or lenses that are able to change shape or orientation in order to manipulate a light source. Adaptive arrays of large mirrors (on the order of meters in diameter) have long been used in astronomy to correct for atmospheric distortions in images from space [36]. This same concept can be achieved with MEMS micromirror arrays for use in wavefront corrections and spectroscopy. Figure 2-3 shows a general schematic of how wavefront correction is achieved using adaptive optics. A distorted wavefront is reflected onto an adaptive optics device which is deformed accordingly to eliminate the distortions in the original wavefront. The newly corrected wavefront is split and sent to a detector (e.g. camera) and to a sensor that measures the wavefront and sends this signal to a control system that directs the motions of the deformable mirror. These kinds of systems traditionally rely on expensive wavefront sensors to sense the wavefront and direct the mirror's actions. However there are many new applications that are utilizing MEMS micromirrors and lenslet arrays to replace the traditional wavefront sensors. Horenstein et al. demonstrate wavefront correction using the Texas Instruments' DMD [30]. Another example of

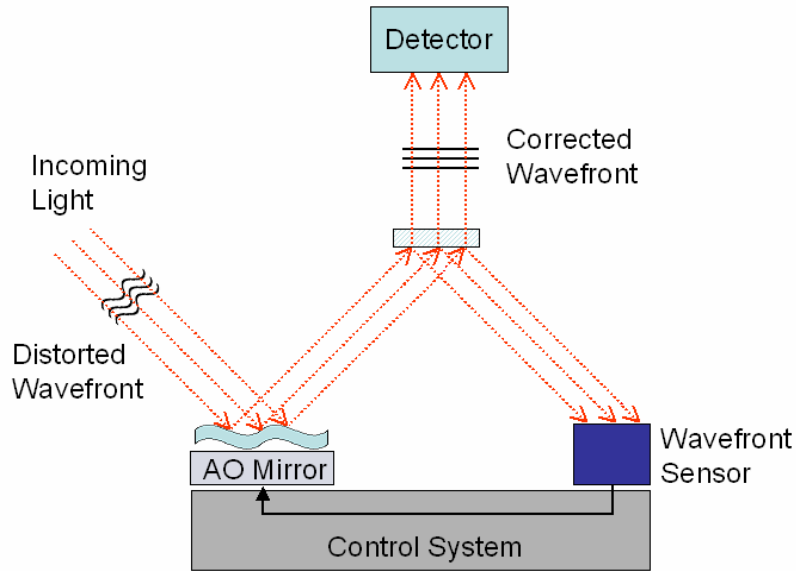


Figure 2-3. Adaptive optics (AO) mirror used for wavefront correction.

micromirrors used for AO include Boston Micromachine's Deformable Mirrors (DM), which have been used for image correction in telescopes, microscopes, and Optical Coherence Tomography (OCT) [29], [31], [32]. AO micromirrors are also being used for imaging of the human retina [37], [38].

Another variation of AO uses arrays of micromirrors to create programmable diffraction gratings for use in spectroscopy [21]-[25]. As shown in Figure 2-4, light sent through a sample, such as a chemical, gas, or material, is diffracted into its spectrum by a fixed grating. This is

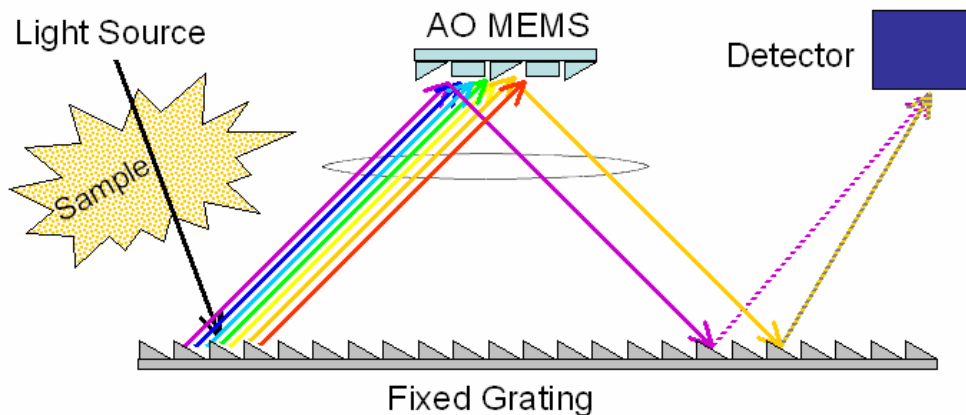


Figure 2-4. Use of an AO MEMS programmable diffraction grating for spectroscopy.

then sent to the MEMS diffraction grating that is set to filter light in specific regions of the spectrum. The filtered light is sent back to the fixed grating and then collected by a detector. The light measured in the detector can be used to determine the material composition of the sample.

2.3 Electrostatic Actuation and Instability

The examples of micromirrors presented in Section 2.2 all use electrostatic actuation, which is popular in MEMS as it is easy to implement using the silicon-based semiconductor structural materials available in most MEMS fabrication processes. The theory of operation for electrostatic actuation is presented in detail in Chapter 3, and is discussed here more generally to give an understanding of the current modeling methods and the challenges with this type of actuation, including nonlinear behavior and electrostatic instability.

2.3.1 Modeling, Pull-in and Hysteresis

The theory of electrostatic actuation relies on established relationships regarding the energy generated in an electric field when a charge differential is applied to two bodies, such as in a capacitor [3]. The energy in this electric field creates an attractive force between the two plates, and this is the principle exploited for electrostatic actuation. The equations used to describe the electrostatic forces are derived from the energy in the electric field between the charged electrodes, and often assumptions are made in calculating the capacitance using analytical expressions that neglect the fringe field effects. It is typical in MEMS devices, such as parallel plate actuators or torsion micromirrors, for one set of the charged electrodes to be stationary, and the other electrode to be supported by a flexible suspension or spring that allows it to move. The spring suspension counteracts the attractive electrostatic force with an opposing mechanical force that can constrain the degrees of freedom of the moving plate and ensure that the two electrodes do not come into contact.

Many electrostatic actuators exhibit the well-documented phenomenon of electrostatic pull-in. The electrostatic force is nonlinear as it is inversely proportional to the square of the electrode gap. Pull-in, sometimes called snap-down, occurs when the electrostatic force generated by the actuator exceeds the mechanical restoring force of the structure. The result is that the device reaches an unstable position and subsequently is pulled down to the substrate at its maximum displacement. The electrostatic instability has been studied extensively and the pull-in characteristics can be modeled fairly accurately [3], [14], [39]-[52], [106]. Pull-in for a parallel-plate actuator occurs at one-third of the separation gap, which greatly limits the actuator stroke.

Another phenomenon associated with pull-in instability is that once the mirror has pulled-in, the voltage required to maintain the pull-in position is lower than the pull-in voltage. The mirror will not return from this position until the actuating voltage has been reduced below the holding-voltage. The result of this holding effect is hysteresis. Electrostatic hysteresis behaves differently from hysteresis that is common in piezoelectric or thermal actuators where continuous motion is possible in both directions. Electrostatic systems experience a dead-band after pull-in in which no actuation is even possible until the applied voltage drops below the holding threshold. The effects of pull-in and hysteresis are a challenge in achieving stable, controllable actuation over the maximum range of motion of an electrostatic micromirror.

The behavior of electrostatic actuators has been modeled throughout the literature using analytical expressions for cases of simple electrode geometry, such as parallel plate actuation [3], [24], [41]-[43], [49], [64], [106]. When the electrode geometry becomes more complex, such as the case when the actuators use vertical comb drives, finite element analysis (FEA) can be used to numerically calculate the properties of the electric field. Hah, et al. use a 2D Maxwell solver

and then integrate the results over the length of the mirror to predict the 3D electric field [14], [46]. This method can be advantageous for computational efficiency, as a 2D FEA simulation will likely take less time than a 3D model. There can be benefits to using a 3D FEA solution, which is the modeling method that is employed in this dissertation. A full 3D electrostatic model can allow easily for evaluation of the effects of complex electrode shapes, such as shapes that do not have a constant cross-section along the length of the device. These non-constant cross-sections could be designed on purpose to study the effects of changing electrode shape, or can be the result of processing. Etching procedures in both bulk and surface micromachining can inherently result in sloping sidewalls or uneven surfaces [3]-[5]. Therefore, 3D analysis may be more computationally intensive, but it also allows for the study of more sophisticated geometries. Regardless of the modeling method used, it is possible to describe the static behavior of the actuators and the position and voltage at which pull-in and the release will occur. Electrostatic instability is also an example of bifurcation behavior, and once an equation of motion is determined for the device, the pull-in can be examined from stability theory [106]. Bifurcation analysis is demonstrated in Chapter 3 of this dissertation.

The modeling performed for electrostatic devices typically assumes that they are operated below the resonant frequencies of the device. The pull-in phenomena is affected by resonance and it has been shown that parallel plate actuators driven at their resonant frequency have a greater range of motion compared to the one-third gap limitation for frequencies below resonance [40]. Additional model assumptions that are commonly made are that the device operates only in its intended degrees of freedom as prescribed by the operating conditions and the mechanical suspension design. In cases with multiple degrees of freedom, such as 2DOF

mirrors, positioners, or gyroscopes that have coupling between the DOF, it is crucial to take this into account during the model development [10], [11].

Many of the first generation of micromirror devices, such as Texas Instruments' DMD, use pull-in as an advantage that allows for open-loop, on/off binary actuation at reduced voltages [2], [53]. While the actual pull-in voltage of the device may vary slightly from mirror to mirror due to variations in dimension and material properties, reliable open-loop operation can still be guaranteed by ensuring that the actuation voltage is sufficiently high enough to capture the pull-in effects for all the mirrors despite these variations. The hysteresis phenomena can also be beneficially exploited, since once a mirror is pulled-in it can be held there at a reduced voltage, which decreases power consumption. While the electrostatic instability can be advantageous for digital applications, it is an obstacle for the application of micromirrors with continuous, analog actuation capabilities.

The issue of electrostatic pull-in has been thoroughly documented and there has been a considerable amount of research conducted to find ways to avoid pull-in for electrostatic micromirrors in order to move beyond binary positioning capabilities and achieve full, analog positioning for applications such as scanning and adaptive optics. Attempted solutions to this problem have included design techniques to alter the electrostatic or mechanical forces of the device, capacitive and charge control techniques, and closed-loop feedback control. A review of these methods is given in the following sections.

2.3.2 Design Techniques to Eliminate Pull-in

There are multiple design methods researchers have employed to address the problem of electrostatic pull-in to achieve an extended range of travel for electrostatic actuators. Some have employed geometrical design changes to achieve increased stability. These methods have included tailoring the electrode geometry [54] or applying insulating layers of dielectric material

[55]. Changes in the electrode geometry are especially effective for torsional microactuators as they do not have a constant electrostatic force generated over the surface of the actuator as it tilts. Changes to device geometry are sometime limited by other design or fabrication constraints.

The use of nonlinear flexures has also been used to ensure that, as the electrostatic force increases, the mechanical restoring force of the devices also increases to compensate. Burns and Bright developed nonlinear flexures that utilize a series of linear flexural elements that are designed to engage the device at predetermined deflections [56]. This effectively creates a piecewise linear stiffness profile. A similar concept of creating nonlinear stiffness has been explored by Bronson et al. in [57], [58] and will be discussed further in Section 5.3. The leveraged-bending approach introduced by Hung and Senturia [24] uses the stress-stiffening of a fixed-fixed beam to generate the nonlinear mechanical force needed to achieve controllable positioning over the entire range of motion of a polychrometer programmable diffraction grating [21]-[23]. The cost of using these techniques is a higher actuation voltage needed to achieve large, stable deflections.

2.3.3 Capacitive and Charge Control Techniques to Eliminate Pull-in

The issue of controlling the electrostatic instability has been addressed by using capacitive and charge control methods. Seeger and Crary [59] proposed a simple method that incorporates a capacitor in series with the actuator to provide stabilizing negative feedback. This passively controls the voltage across the actuator electrodes as the gap width changes. They showed theoretically that this method can be used to stabilize across the entire gap. The tradeoff is that higher voltages are required to stabilize the actuator using this method. This concept is extended by Seeger and Boser using a switched-capacitor circuit to control charge across the actuator and reduces the actuation voltage requirements [60]. Seeger and Crary neglected to take into account nonlinear deformation of the elastic members of the actuator. Once these nonlinear deformation

terms are considered however, the method is found to only partially stabilize the system [61], [62]. Other issues such as residual charge and parasitic capacitance addressed by Chan and Dutton [61], [63] were shown to limit the actuator travel to less than full range. Chan and Dutton also introduced a folded capacitor design that could be fabricated in the surface micromachining MUMPS process as part of the device itself and showed that this series capacitor method can be used to increase the stable range of electrostatic torsion actuators up to 60% of the initial gap with the cost of using higher actuation voltages.

Other work has used similar charge control strategies that have resulted in reduced voltage penalties and extended travel [64]-[66]. Current leakage has been shown to create drift of steady-state positions and this can be overcome using discharge methods that resemble sigma-delta operations, but the results can lead to ‘ringing’, or chatter about the steady-state position [66]. A related method uses an inductor and capacitor in series and has been shown to increase the stable range of travel at lower voltages, but this technique cannot be easily implemented with MEMS technology due to a lack of inductors available in integrated circuits that meet the high inductance requirements [67]. These methods show that charge control schemes can be utilized to extend the range of travel and in some cases even improve the transient response as well [64]. In order to overcome the limitations imposed by parasitics, leakage, and residual charge more involved methods must be employed using charging/discharging cycles, controlling clock frequencies and complex circuit implementations.

2.3.4 Closed-loop Voltage Control to Eliminate Pull-in

There are cases where a closed-loop control technique has been used for attenuating and stabilizing electrostatic instability. Voltage control methods have been explored to achieve stabilization beyond the pull-in point [68], [69]. Chu, and Pister discuss the effect of introducing a voltage control law into a system of electrostatically actuated parallel-plates and shows

theoretical stability at small gap distances [68]. Chen, et al., introduced a method for extending the travel range of a torsional actuator by implementing voltage control to achieve desired electrostatic torque profiles that can by-pass the pull-in point. This method was successful up to approximately 80% of the initial gap [69].

2.4 Feedback Control Techniques Applied to MEMS

The previous discussion highlights several of the problems with current electrostatic devices that have impeded the development of highly accurate and precise analog micromirror arrays. These problems, including the limitations imposed by electrostatic instability as well as the variable behaviors that result from fabrication uncertainties, have been addressed using closed-loop control methods. Feedback control can help to increase the stable region of operation for electrostatically actuated devices, provide accurate and precise positioning that is robust with respect to variations in device fabrication, and also reject outside disturbances such as vibrations and other noise sources. As seen in recent literature and summarized in Table 2-1, controllers have been successful at both extending travel range of electrostatic actuators and for improving tracking, disturbance rejection, transient response, system bandwidth and stability, and reducing steady-state errors. Within the work that has been done to design and implement feedback control systems on MEMS devices, a wide array of techniques and methods have been employed, including linear-time-invariant (LTI) techniques such as proportional-integrator-derivative (PID), robust, adaptive, and nonlinear control design. Some researchers address both achieving actuation in the unstable range of motion and improved transient performance [15], [70]-[74]. The control techniques presented in this review of the literature are not limited to electrostatic micromirrors, but include a variety of devices and actuation methods to illustrate the range of methods that have been employed for control of MEMS devices.

The controls literature reveals the many methods have been suggested as improvements to facing the problems outlined above. Linear methods in some cases are insufficient, and more advanced techniques have not been implemented due to the complexities required. An extended review is given here of these controller methods and their applications for the benefit of the reader. However, the work in this dissertation focuses mostly on modeling the behavior and examining the effects of nonlinearity and uncertainties and the impact these have on control implementation.

2.4.1 Linear Control

While all real systems will have nonlinearities, it is common engineering practice to treat them as linear whenever possible. These assumptions and approximations, when acceptable, greatly simplify analytical models as well as allow for the use of a wide range of linear control methods. The use of classical, linear controller design such as PID, lead-lag, and state-variable is adequate for these systems for which the systems operate in a small range of motion avoiding nonlinear behavior [75]-[77], or in which the nonlinearities are small enough to be neglected [78]-[80].

In the case of systems with large nonlinearities, such as those from electrostatics, it can be a challenge to apply linear control design and ensure that a controller designed for the linear system will be able to operate on the actual nonlinear plant. Despite the considerable nonlinearities associated with electrostatic actuation, linearization of the plant model is often done to allow for the use of linear-time-invariant (LTI) control methods. The nonlinear effects of electrostatic actuation are perhaps most evident for parallel-plate actuator systems. Lu and Fedder used a linearized plant model for a parallel-plate type actuator and designed a LTI controller for both extended range of travel and position control [71]. The LTI controller was designed and simulated on the linearized plant model and showed theoretically that very large

Table 2-1. Summary of feedback control papers discussed in the literature review.

Ref.	Author	Control Type	Control Objective	System Type	Experimental/ Feedback Type
[68]	[Chu, Pister, 1994]	Nonlinear	Increase Stability	Parallel-Plate Electrostatic	No
[84]	[Lyshevski, 2001]	Nonlinear	Stability, Position Tracking	Electromagnetic MEMS Motor	No
[72]	[Piyabongkarn, et al., 2005]	Nonlinear	Position Tracking	Electrostatic Lateral Comb Drive Parallel-Plate	Yes, Capacitive
[85]	[Zhu, et al., 2006]	Nonlinear	Position Control	Electrostatic Parallel-Plate	No
[74]	[Miathripala, et al., 2003]	Nonlinear	Stability	Electrostatic	No
[73]	[Sane, 2006]	Nonlinear	Increase Stability, Position Tracking	Parallel-Plate Electrostatic	No
[77]	[Horsley, et al., 1999]	Classical (PD, Phase- lead)	Position Control Position Control, Dynamic Response (Settling Time), Disturbance Rejection	Parallel-Plate Electrostatic	Yes, Capacitive, Laser Doppler Vib. (LDV)
[78]	[Pannu, et al., 2000]	Classical (PID)	Disturbance Rejection	Magnetic Micromirror Electrostatic Lateral Comb Drive	Yes, Position Sensing Detector (PSD)
[75]	[Cheung, et al., 1996]	State-Feedback	Position Control	Electrostatic Lateral Comb Drive	Yes, Capacitive
[70], [71]	[Lu, Fedder, 2002, 2004]	Classical (P)	Increase Stability, Position Tracking	Parallel-Plate Electrostatic	Yes, Capacitive
[15]	[Chu, et al., 2005]	State-Feedback	Increase Stability, Position Tracking	Electrostatic Torsion Micromirror (2DOF)	Yes, Current Meas. and PSD
[79], [80]	[Messenger, et al., 2004, 2006]	Classical (P, PI, Lead- Lag)	Position Control	Thermal actuator	Yes, Piezoresistive
[82]	[Hernandez, et al., 1999]	Robust (Mu-Synthesis)	Position Tracking	Dual-Stage Disk Drive Piezoelectric Torsion Mirror (2DOF, not MEMS)	Yes, unspecified
[27]	[Kim, et al., 2004]	Adaptive control, Robust (H-Infinity)	Disturbance Rejection (Wavefront Correction)	Electromagnetic MEMS Torsion Mirror (2DOF)	Yes, PSD
[26]	[Arancibia, et al., 2004]	Adaptive Control	Disturbance Rejection (Wavefront Correction)	Electromagnetic MEMS Torsion Mirror (2DOF)	Yes, PSD
[76]	[Liao, et al., 2005]	Adaptive Control	Position Control	Electrostatic Torsion Micromirror	Yes, Capacitive, LDV
[10], [11]	[Park, Horowitz, 2001, 2003]	Adaptive Control	Disturbance Rejection	MEMS Gyroscope	No
[83]	[Liaw, et al., 2006]	Sliding Mode Control (SMC)	Position Tracking	Piezoelectric Actuators (PEA) (not MEMS)	Yes, unspecified
[33], [34]	[Gorman, et al., 2003, 2005]	SMC	Position Tracking	PEA (not MEMS) Dual-Stage Disk Drive	No
[86]	[Lee, et al., 2000]	SMC	Position Tracking	Electromagnetic MEMS Torsion Mirror (2DOF)	No
[81]	[Yazdi, et al., 2003]	SMC	Increase Stability	Electromagnetic MEMS Torsion Mirror (2DOF)	Yes, PSD
[87]	[Chiou, et al., 2002]	Fuzzy Logic	Dynamic response (reduce rise time)	Electromagnetic MEMS Torsion Mirror	No

stable deflections could be achieved for this linearized plant. The LTI controller did not account for the higher order nonlinear effects of the actuator, initial conditions or external disturbances, and when the controller was implemented on the nonlinear plant, the maximum achievable stable travel range was insufficient to reach the stated goal for stable range of motion. The LTI controller was unable to satisfy both the stability conditions and disturbance rejection for large deflections of the actuator, meaning that it could not attain the large deflections predicted for the given controller design [71]. This illustrates the importance of considering robust operation of the controller, especially when using a linearized plant model for a highly nonlinear system. Linearized control is limited by the true nonlinearities of the system including the effects of unmodeled dynamics, parameter uncertainties, disturbances, and stability, and it is most appropriate for cases in which these effects are small. It is crucial to have an understanding of the system behavior and its nonlinearities prior to the implementation of such control methods.

2.4.2 Adaptive and Robust Control

In utilizing closed-loop feedback control techniques for MEMS devices, robustness becomes a commonly desired quality [26], [27], [70]-[72], [76], [81], [82]. Robustness is important in MEMS control systems as there can be many uncertainties introduced through variations in the device parameters, including geometry and material properties that arise from the fabrication process, as well as nonlinearities in the dynamics and disturbances from noise or other external influences. There are many ways to compensate for these uncertainties and develop robustly stable systems.

An advantage of adaptive control over other methods, like PID, is that the controller can compensate for uncertainties from fabrication, reject disturbance, and achieve desired tracking objectives by continuously updating the controller parameters according to the actual system performance [76]. When applying adaptive control it is very important to have an accurate

system model. The actual system output is compared to the estimated output predicted by the model and this error is used to determine the controller gains during each step. If the predictive plant model does not reflect the actual system behavior well, then large errors can lead to poor performance and sometimes cause the system to go unstable [26], [27]. Calculating the controller gains at each step in real-time can be difficult to implement, requires computationally intensive algorithms and cannot be done compactly in an analog circuit.

Adaptive methods have been employed to account for parametric uncertainties within the plant that arise from variations from the fabrication process. For actuators with performance that is highly sensitive to fabrication variations, adaptive techniques may also be used for parameter estimation. In the case of [72], the actuator dynamics of lateral electrostatic comb drives are sensitive to fabrication errors arising from the alignment tolerances of bulk-micromachining. Adaptive control has also been applied to MEMS gyroscopes, which are known to suffer from parametric variations from the fabrication process that degrade the performance [10], [11]. References [26], [27] demonstrate the use of adaptive control techniques for rejecting disturbances that occur in adaptive optics applications when there is turbulence in the atmosphere that affects the optical wave front. Kim et al. examined the control of piezoelectric mirrors. These mirrors are not MEMS devices, however the control methods and application to adaptive optics still warrants discussion. This work showed that using a combination of linear time invariant (LTI) H-infinity control and adaptive control resulted in good disturbance rejection of band-limited noise and the H-infinity controller improved performance by eliminating steady-state drift and reducing noise [26].

There are few examples of robust control design methods such as H-infinity and mu-synthesis that have been applied to MEMS systems. In addition to the use of H-infinity control

demonstrated by Kim, et al. for a non-MEMS micromirror system [26], mu-synthesis controller design was applied to a dual-stage actuator system for track-following in a hard-disk drive [82]. The controller design was successful in simulations, but no experimental work has been done so far. The application of mu-synthesis to design robust controllers has not been specifically applied to a strictly MEMS device. Difficulties in implementing these types of controllers arise if the order of the controller is very high, in which case model order reduction can be used. In summary, adaptive and robust control techniques appear promising at solving the issues of controlling MEMS devices that are fabricated with parametric uncertainties, but only if the system has very accurate models, and the sources of the uncertainties are clearly identified within the model. In addition, these methods have largely only been evaluated in simulation thus far because of implementation issues including high order controllers, lack of adequate sensing methods, and difficulty in realizing the control in hardware.

2.4.3 Nonlinear Control

The instability problem posed by parallel-plate electrostatic systems has been a fertile area for applications of nonlinear control techniques that incorporate Lyapunov stability analysis [68], [72]-[74], [76], [85]. A general overview of Lyapunov stability analysis and how it applies to nonlinear controller design or MEMS is given by [84]. It is clear that this method is mathematically intensive and that proving global asymptotic stability of the Lyapunov function is not a trivial matter. In the case of Maithrapala, et al., the researchers use a nonlinear state feedback controller with a nonlinear observer to stabilize an electrostatic parallel plate actuator in its unstable range and to improve the performance by reducing overshoot and decreasing settling time [74]. The resulting control law is determined to have good performance at 80% of the electrode gap in simulation; however it is only locally asymptotically stable. Several researchers have developed controllers to extend the range of stability for parallel-plate

electrostatics, and have achieved excellent results based on numerical simulations [73], [85]. However, like other advanced control techniques discussed here, the resulting control laws are not be easily amenable to implementation in analog circuitry and thus the results have not been tested experimentally.

Additional control techniques that have been used include sliding mode control (SMC), which can also be robust to plant variations, have good disturbance rejection and compact implementation schemes. SMC is a digital, nonlinear control method generally good for systems with nonlinearities and parametric uncertainties and tends to produce low order controllers. Lee et al. used a discrete-time SMC for a dual-stage actuator for hard-disk drives to track a desired trajectory so as to avoid unwanted excitation of any resonant modes [86]. SMC was also applied to the problem of electrostatic pull-in instability of two-axis torsion micromirrors [81]. SMC operates through switching pulses that can result in chattering of the actuated device about the steady state value, although attempts have been made to reduce this effect [83].

Although electrostatic systems are known to have hysteresis, there is little work examining its effects on system performance and control. Piezoelectric actuators have significant hysteresis in both traditional piezoelectric stack actuators and newer MEMS devices that utilize piezoelectric materials. Liaw, et al. examines a traditional piezoelectric stack actuator, which is in itself not a MEMS device but is used for micro and nano-scale manipulation [83]. A robust sliding mode controller is developed that takes into account bounded parametric uncertainties and hysteresis. The controller was implemented in an experimental system and found to have good trajectory tracking with minimal tracking error and hysteretic behavior. Thermal actuators also have hysteretic behavior, and Gorman et al. designed a robust controller for a thermally actuated, microfabricated nanopositioner that uses a multi-loop control scheme based on SMC

[33]. This robust motion controller is shown in simulation to be able to track trajectories and reject disturbances to the system given *a priori* knowledge of the model uncertainty.

Chiou et al. [87] examine the use of fuzzy control for a micromirror that is actuated using an array of electrodes that allow for a large number of positions using programmed digital operation. The fuzzy controller showed improvement in the transient response over the open-loop system in simulation, but issues concerning feedback signal and controller implementation are not addressed.

In summary, nonlinear control techniques have been shown to be effective at addressing the control of MEMS devices in theory, but like with adaptive and robust control, experimental validation is thus far missing. It is clear from examining these various control methods that as the techniques become more complex to account for robust performance and system nonlinearities, the implementation issues also become more complicated. While many of the papers in the literature discuss robustness of the control system, very few go into great depth of defining the system uncertainties and determining the acceptable margins for the uncertainty. Therefore it is not always clear if meaningful robustness is achieved for the system. Detailed exploration of the uncertainties and the nonlinear behaviors is needed to further understand these issues.

2.5 Sensing Methods for Feedback

In order to implement closed-loop control, a feedback signal is required. Optical beam steering methods are considered in the scope of this research; however it is important to note other sensing methods that may be used. There are multiple sensing mechanisms that have been employed to produce feedback of position and rate for MEMS actuators. These include optical, capacitive, and piezoresistive methods. One optical method that has been shown to produce a good feedback signal is one in which the micromirrors steer a laser beam to a target

photosensitive diode (PSD) to track the position of the mirror [15], [26], [27], [78] , [81]. Like many optical methods, beam steering does not always offer the benefit of reducing the size of physical implementation that can be achieved with capacitive or piezoresistive methods. Size may be reduced in some cases by utilizing vertical cavity surface emitting lasers (VCSELs) as the laser source, as was done in [13]. Other optical methods include using an atomic force microscope (AFM) or laser Doppler vibrometer (LDV) [77]. Both of these methods have been used and require special equipment that is only practical to use in a laboratory setup.

Capacitive sensing can be done by measuring changes in capacitance as the electrostatic device moves. This method can produce very good signals, but does require additional circuitry to use the signal [71], [72], [75]-[77], [96]. Depending on the complexity and fabrication process abilities, this circuitry is able to be incorporated directly onto the chip as an analog signal processor [71]. In some cases, estimators and observers must be employed to estimate and extract the states of the system (position, velocity) from the sensor data. A Kalman filter, which uses an observer and compares the actual response to the observer response, was used by Cheung, et al. to estimate position and velocity based on the change in capacitance [75].

Piezoresistive sensing has already successfully been used in pressure sensors, shear sensors [88]-[91] and acoustic sensor applications [92], [93]. It is relatively easy to implement in silicon surface-micromachining processes by utilizing a Wheatstone bridge and does not require CMOS to obtain a signal. The piezoresistive properties of silicon and polysilicon make it suitable for feedback applications. Although polysilicon has a lower piezoresistive effect than single crystal silicon, it has been used successfully as a sensing mechanism. Piezoresistive sensing created within the SUMMiT fabrication process is demonstrated in [91] and [94]. Messenger, et al. has successfully demonstrated the use of surface micromachined polysilicon to sense displacement

of a linear thermal actuator and then use that information to perform PID position control [79], [80]. Drawbacks to piezoresistive sensing include a large area needed for the resistor elements and drift due to temperature and time.

Noise is the limiting factor for any type of sensor. Microsensors are susceptible to Brownian motion noise, $1/f$ noise, and thermal noise. Piezoresistive sensors have been shown in the past to be most affected by $1/f$ noise [95]. Many researchers have experienced the limits of a high signal-to-noise ratio and it can limit the bandwidth of the system [79], [80]. In some cases the noisy sensor output can be filtered to achieve better response characteristics.

2.6 Summary Remarks

The results of this literature review reveal that there is still work that remains to be completed toward the development of robust micromirror devices. The issue of electrostatic pull-in and hysteresis has been addressed by making design modifications to the electrostatic devices as well as with feedback control methods including LTI control, nonlinear control, and sliding mode control. The literature has demonstrated cases in which electrostatic pull-in has been successfully mitigated, but not entirely eliminated. A disadvantage to methods that incorporate nonlinear mechanical springs into the system is that they require higher actuation voltages. In this dissertation, electrostatic pull-in is addressed by introducing a novel design technique called the progressive-linkage to create a nonlinear restoring force. This progressive-linkage has the advantage of having a continuous spring force over other designs that use discontinuous, piece-wise defined stiffness profiles. While this approach still has the disadvantage of higher actuation voltages, the benefits gained via this continuous passive control approach of the nonlinearities in the system reduce the need for the complex control approaches identified in the above literature review. This passive control approach should minimize the degree of hysteresis resulting from the pull-in phenomenon, an issue that has largely been

unaddressed. This is an issue in which feedback control methods can also be applied to help reduce the recovery time for hysteresis that occurs after pull-in. Bifurcation theory is used in this dissertation as another method for capturing these nonlinear behaviors in the dynamic modeling.

It is also evident that there has been considerable study regarding parallel-plate electrostatic actuators for which analytical relationships are known and are well defined from physics. There has been less work done to model more intricate electrostatic configurations such as those of vertical comb drives. Hah, et al. use 2D electrostatic models to determine the electrostatic performance of vertical comb-drive actuated micromirrors [14]. While this approach is intended to be more computationally efficient, it can limit the types and range of electrode geometries that can be easily analyzed. In this dissertation, 3D FEA modeling is used to determine the electrostatic characteristics of the micromirrors, and the FEA need only be done one time for a given dimensional configuration, thus the computational costs remain low. In addition, this work presents a detailed modeling approach to study the effects of fabrication uncertainties along with characterization data for multiple devices that demonstrate variations in actuator response.

Different control methods including PID, and LQR, are applied to the micromirror arrays in this dissertation to compare the performance of each method and to further delineate the impact of the parametric uncertainties on system performance. While a variety of controller design methods have been utilized for MEMS devices, very few have considered optimal control applications to electrostatic micromirrors. This dissertation also addresses a unique issue of how to control an array of micromirrors that are not individually controllable. The micromirror arrays examined here have single-input/multiple-output (SIMO) characteristics, providing an interesting challenge to determining the appropriate sensors and error metrics to apply to feedback.

CHAPTER 3 MICROMIRROR MODELING AND STATIC PERFORMANCE

This chapter presents the micromirror array devices chosen for in depth study and experimental validation. These devices are arrays of electrostatic micromirrors developed by Sandia National Laboratories (SNL) for application to adaptive optics diffraction gratings like those discussed in Section 2.2. A description of the SUMMiT V surface micromachining process shows how these devices are made and gives some insight into sources of parametric uncertainties that arise through the fabrication process. The static performance, described in terms of the relationship of the actuation voltage applied and the resulting rotation angle of the micromirror, is examined by developing models for the mechanical and electrostatic behaviors. Electrostatic instability can also be predicted in terms of the pull-in angle, voltage, and hysteresis. The static performance model is developed and presented here along with analysis of the nonlinear behaviors of electrostatic instability and hysteresis.

3.1 Description of the SUMMiT V Microfabrication Process

The micromirror array is fabricated in the SUMMiT V surface micromachining process at SNL. Figure 3-1 shows a diagram of the fabrication process from the SUMMiT V design manual in which the five alternating polysilicon structural layers (mmpoly) and four silicon dioxide sacrificial layers (sacox) are labeled along with their nominal thickness values [6]. (For further information on surface micromachining fabrication, see [5].)

As with all manufacturing processes, there are machining tolerances in surface micromachining that affect the final dimensions of the finished product. These tolerances can result in slight deviations of the dimensions from the intended nominal values. Material properties, such as Young's modulus and Poisson's ratio, are also variable and dependent on film thickness and processing methods [12], [97]. The result can be that the fabricated devices will

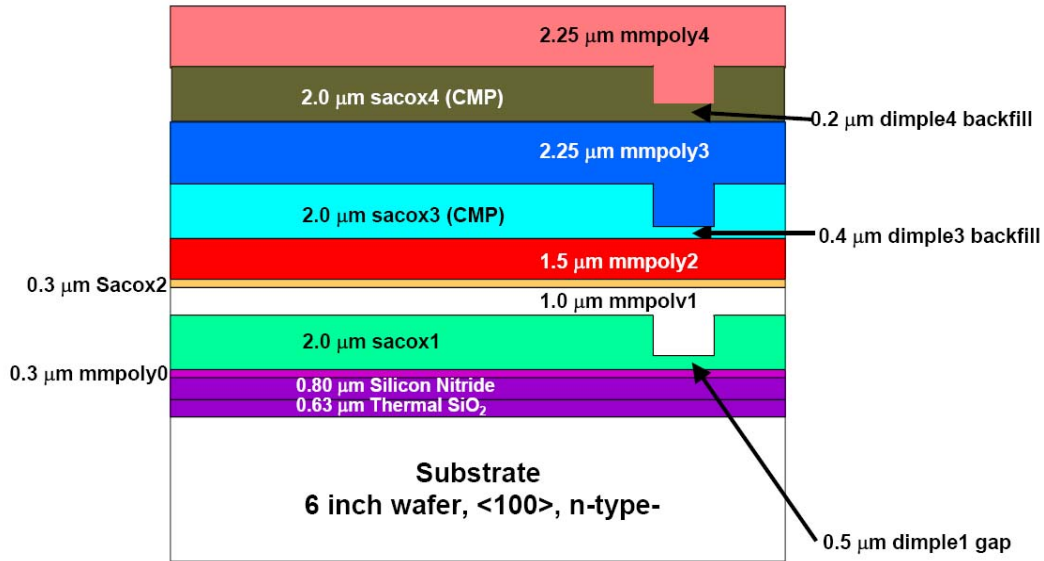


Figure 3-1. Drawing of the SUMMiT V structural and sacrificial layers. (Courtesy of Sandia National Laboratories, SUMMiT Technologies, www.mems.sandia.gov)

not behave as predicted, or that devices of the same design can behave differently from one another. Dimensional variations can affect spring constants, resonant frequencies, and electrical characteristics [7]-[9], [98]. Information on fabrication tolerances for the SUMMiT process is available in the design manual [6], and those values relevant to this discussion are listed in Tables 3-1 and 3-2. This information was gathered through diagnostic process testing as described in [98]. Table 3-1 gives the mean and standard deviations of the thicknesses of the layers of polysilicon and silicon dioxide. Table 3-2 gives values for variations in the dimensions of the line widths of the device design. Figure 3-2 illustrates the effect of line width variation, showing that for a desired area of dimension L by w , the actual fabricated area may be slightly less, indicated by the dashed lines. Note that negative values indicate an inward bias resulting in the actual size being smaller than drawn. The variability of the Young's modulus, E , is not listed in the SUMMiT design manual, however information published in the literature has found it to be 164.3 GPa with a standard deviation of ± 3.2 GPa, which indicates a variation of $\pm 2\%$ [97].

This information is useful for considering the effects of parametric uncertainties from the fabrication process on the device performance. This subject will be considered more fully in Chapter 4.

Table 3-1. Mean and standard deviation of fabrication variations for layer thickness in the SUMMiT V surface micromachining process.

Layer	Mean (μm)	Std. Dev. (μm)
MMPOLY0	0.29	0.002
SACOX1	2.04	0.021
MMPOLY1	1.02	0.0023
SACOX2	0.3	0.0044
MMPOLY2	1.53	0.0034
SACOX3	1.84	0.54
DIMPLE3 Backfill	0.4	0.0053
MMPOLY3	2.36	0.0099
SACOX4	1.75	0.0045
MMPOLY4	2.29	0.0063

Table 3-2. Mean and standard deviation of fabrication variations of line widths in SUMMiT V.

Layer	Mean (μm)	Std. Dev. (μm)
MMPOLY2	-0.08	0.03
MMPOLY3	-0.07	0.05
MMPOLY4	-0.24	0.05

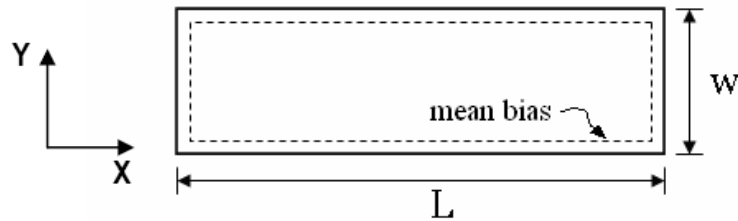


Figure 3-2. Area with nominal dimensions L and w with the dashed line indicating the actual area due to error in the line width.

3.2 Micromirror Actuator Description

The micromirror arrays are shown packaged in a standard 24-pin dual in-line package (DIP) in Figure 3-3. A magnified view of the surface of the array is also shown. The device contains six groupings of micromirror arrays, and the particular grouping that is studied here is indicated by a box drawn around it. This array contains 416 micromirrors arranged in 32 rows

and 13 columns. Each individual mirror is $20 \times 156 \mu\text{m}^2$. These arrays were originally designed at SNL to create a programmable diffraction grating for use in making spectral measurements.

Figure 3-4 illustrates the operation of the arrays as a diffraction grating in which the light source striking normal to the surface of the mirrors when they are flat is reflected back on the same path. When several mirrors are tilted, some light is reflected off at an angle. The result of this is that the light is selectively diffracted.

The micromirrors are one-degree of freedom, actuated electrostatically and are shown schematically in Figure 3-5. The electrostatic micromirror arrays have a ground plane and a

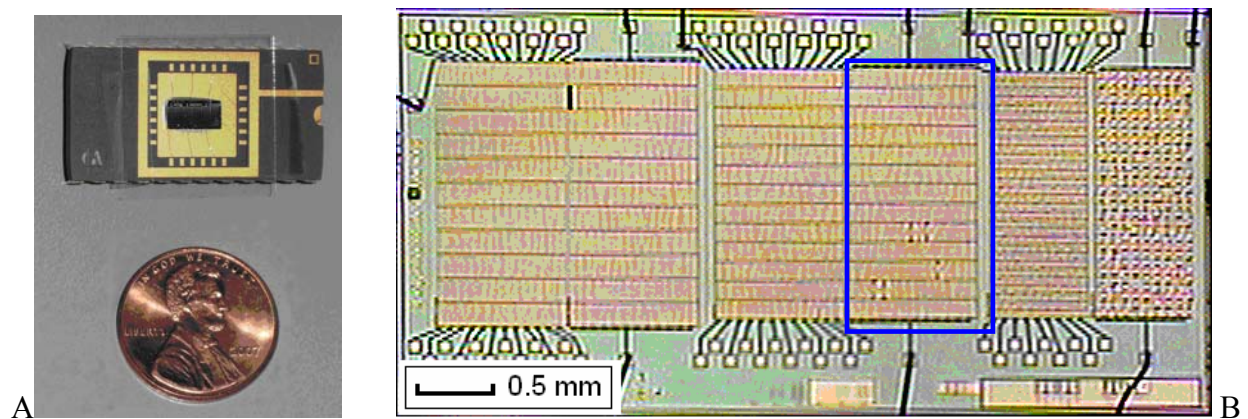


Figure 3-3. Images of the micromirror array. A) Packaged device. B) Micrograph of the surface of the array.

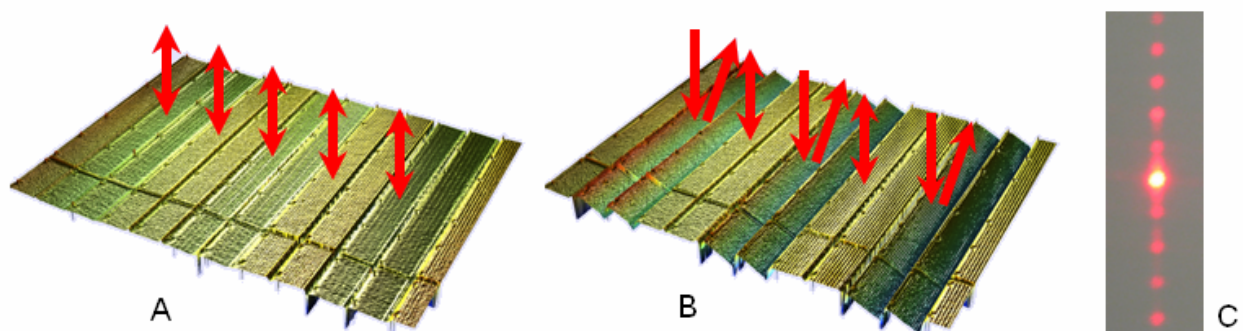


Figure 3-4. Illustration of mirrors operating as an optical diffraction grating. A) When the mirrors are not actuated (i.e. flat), the incident light is reflected straight back. B) For mirrors that are actuated (i.e. tilted), the incident light is reflected off at an angle. C) This results in a diffraction pattern of the light.

series of vertically offset comb fingers, all contained underneath a flat mirror surface. Having the vertical comb drive beneath the mirror rather than just a parallel-plate capacitor attenuates the electrostatic field and increases the stable range of motion of the device. This also allows for large arrays with high fill factors, making them a good choice for analog scanning devices. A

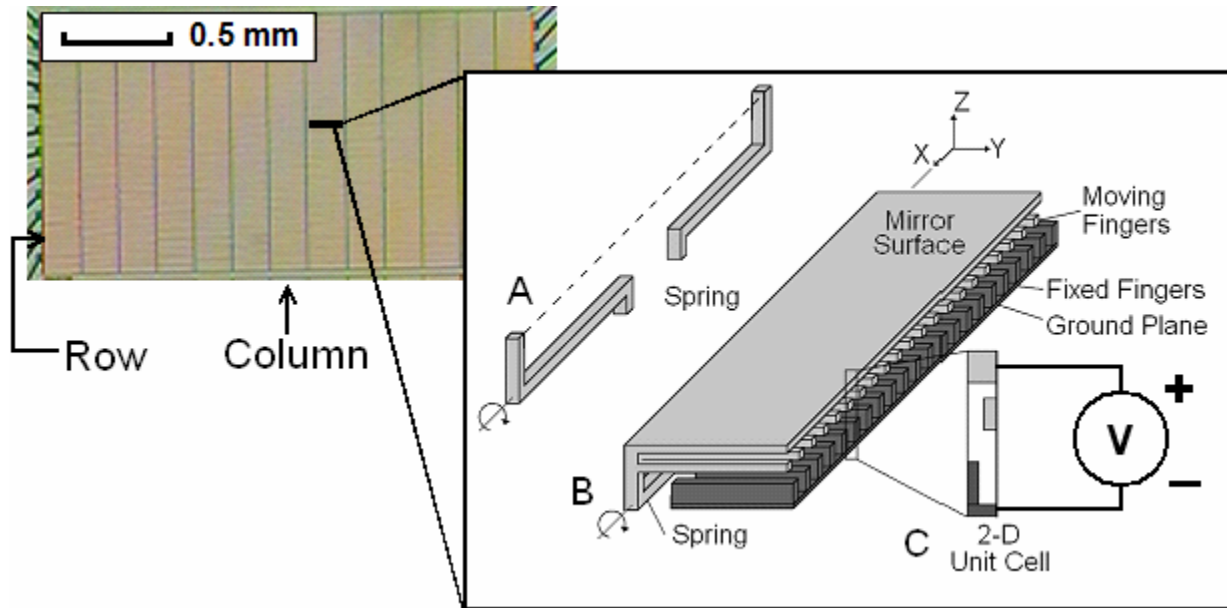


Figure 3-5. Micrograph of an array of mirrors and schematic of mirror with hidden vertical comb drive. A) The torsion spring. B) The full device. C) A 2-D cross-section view of a unit cell (figure not to scale).

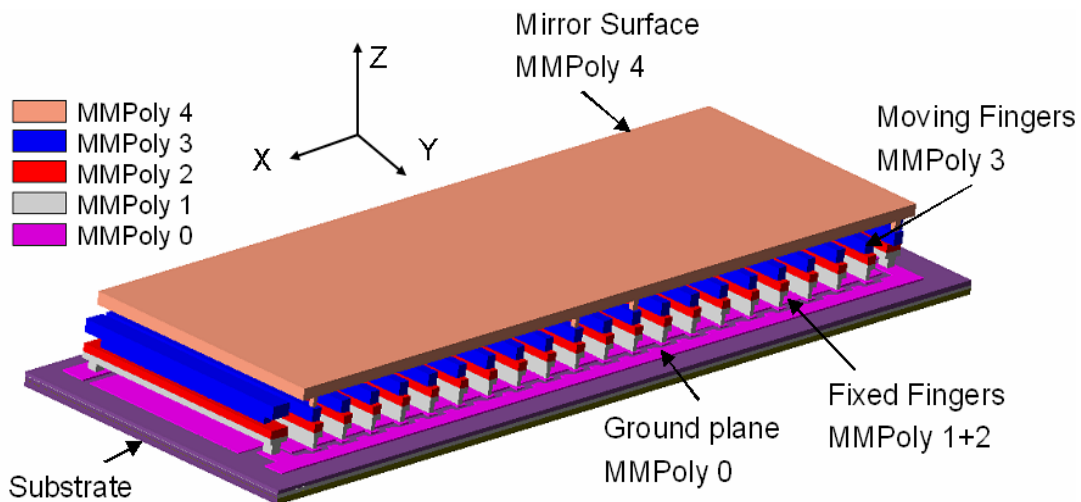


Figure 3-6. Solid model of micromirror showing polysilicon layer names from SUMMiT V.

voltage potential is applied across the fixed fingers and the moving fingers of the device creating an electrostatic force. This force causes the mirror to rotate about an axis supported by the hidden spring suspension, shown separately in Figure 3-5(a). Not shown in the drawing is a design constraint that restricts the motion of the fixed-end of the mirror plate from moving a large distance in the Z-direction. While some motion may occur, the assumption is made that this device acts in one degree-of-freedom by rotating about the x-axis. Figure 3-6 shows a 3D model identifying the fabrication layers used to create the micromirrors.

3.3 Electrostatic Actuation and Instability

Many electrostatic actuators exhibit the well-documented phenomenon of electrostatic pull-in. The electrostatic force is nonlinear, as it is inversely proportional to the square of the electrode gap. Pull-in, sometimes called snap-down, occurs when the electrostatic force generated by the actuator exceeds the mechanical restoring force of the structure. The result is that the device reaches an unstable position and subsequently is pulled down to the substrate at its maximum displacement. Another phenomenon associated with pull-in instability is that once the mirror has pulled-in, the voltage required to maintain the pull-in position is lower than the pull-in voltage. The mirror will not return from this position until the actuating voltage has been reduced below the holding-voltage. The result of this holding effect is hysteresis.

This section will examine the modeling of the electrostatic-mechanical system and the instability phenomena. The case of parallel plate electrostatics is examined and used to derive general relationships for modeling the system. This is extended to a torsion electrostatic actuator to illustrate the complications that arise from adding complexity to the system geometry.

3.3.1 Parallel Plate Electrostatics

Consider a parallel plate capacitor, such as shown in Figure 3-7, in which the top plate is supported by a spring, with spring constant k_m , and the bottom plate is fixed. Damping in the

system is represented by the damping coefficient, b . The plates are separated by a distance of x_0 , and have an overlapping area of A .

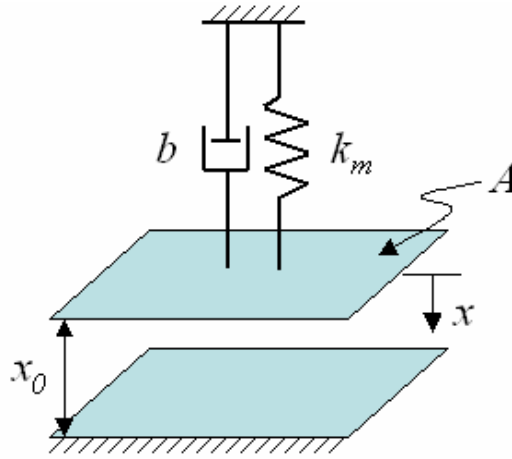


Figure 3-7. Schematic of a parallel plate electrostatic actuator modeled as a mass-spring-damper system.

The equation of motion for this mass-spring-damper system is derived by the balance of the forces on the system from Newton's second law

$$\sum F = m\ddot{x} \quad (3-1)$$

where m is the mass of the moving plate. When the top plate is displaced in the positive x -direction, shown in Figure 3-7, the motion is opposed by the force from the mechanical spring, which is assumed to be linear, and follows Hooke's law. The mechanical spring constant is k_m .

$$F_m = -k_m x \quad (3-2)$$

The damping force is assumed to be linearly proportional to the velocity by a factor of b , the damping coefficient.

$$F_b = -b\dot{x} \quad (3-3)$$

When a voltage potential is applied across the two plates, an electrostatic force is generated that attracts the top plate to the bottom. The electrostatic force for a system operating in air is derived from the energy, U , of an electric field, E , integrated over a volume, v .

$$U = \frac{\epsilon_0}{2} \int_v |E|^2 dv \quad (3-4)$$

where ϵ_0 is the permittivity of free space, 8.854×10^{-12} F/m. The electric field is given by

$$E = \frac{Q}{\epsilon_0 A} \quad (3-5)$$

where Q is the electric charge. The charge, Q , can be written as

$$Q = CV \quad (3-6)$$

where C is the capacitance, and V is the voltage. The capacitance between two parallel plate actuators is given in terms of the overlapping area of the plates, A , and the distance between the two plates.

$$C(x) = \frac{\epsilon_0 A}{(x_0 - x)} \quad (3-7)$$

Equation 3-4 can be rewritten as

$$U = \frac{1}{2} CV^2 = \frac{\epsilon_0 V^2 A}{2(x_0 - x)} \quad (3-8)$$

The electrostatic force is thus written as

$$F_e = -\frac{\partial U}{\partial(x_0 - x)} = -\frac{1}{2} \frac{\partial C}{\partial(x_0 - x)} V^2 = \frac{1}{2} \frac{\epsilon_0 AV^2}{(x_0 - x)^2} \quad (3-9)$$

The force balance for the system yields the equation of motion.

$$F_e = m\ddot{x} + b\dot{x} + k_m x \quad (3-10)$$

The static equilibrium for the system reduces to only the electrostatic force, and the mechanical force.

$$-\frac{1}{2} \frac{\partial C}{\partial(x_0 - x)} V^2 = \frac{1}{2} \frac{\epsilon_0 AV^2}{(x_0 - x)^2} = k_m x \quad (3-11)$$

Equation 3-11 can be interpreted to show the relationship between the voltage and the displacement, as plotted in Figure 3-8 for system of parallel plates with the area, A , equal to $100 \times 100 \mu\text{m}^2$, an initial gap, x_0 , equal to $10 \mu\text{m}$, and a mechanical spring constant of k_m equal to $1 \text{ N}/\mu\text{m}$. From this, it is clear that there is a maximum voltage for the system, and that there can be multiple solutions for the same applied voltage. This behavior is the result of the electrostatic pull-in instability. It turns out that the solutions in the lower portion of Figure 3-8 are stable solutions and the solutions in the upper portion are unstable. The maximum voltage value corresponds to the actuation voltage at which pull-in occurs, and the maximum stable position for parallel plate actuator occurs at one-third the gap between the electrodes.

To further explore the pull-in phenomena, the static relationship in Equation 3-11 can be examined graphically, by plotting the electrostatic force and the mechanical force separately in Figure 3-9. The electrostatic force is a function of both the displacement and the voltage. Static equilibrium occurs where the electrostatic force lines and the mechanical force line cross each other. As was shown in Figure 3-8, there are instances where the mechanical and electrostatic lines intersect at more than one point. Because of the nonlinear behavior of the electrostatic force, there is a point at which the electrostatic torque exceeds the ability of the mechanical spring and equilibrium can no longer be maintained. This is referred to as electrostatic pull-in. At the pull-in point, both the electrostatic and mechanical torques are equal in magnitude and slope and thus only have one point of intersection between these forces on the graph [14], [46]. Stable static solutions occur before the pull-in point, while unstable solutions occur after. This slope equality is written by taking the first derivative with respect to the displacement of Equation 3-11.

$$-\frac{1}{2} \frac{\partial^2 C}{\partial (x_0 - x)^2} V^2 = k_m \quad (3-12)$$

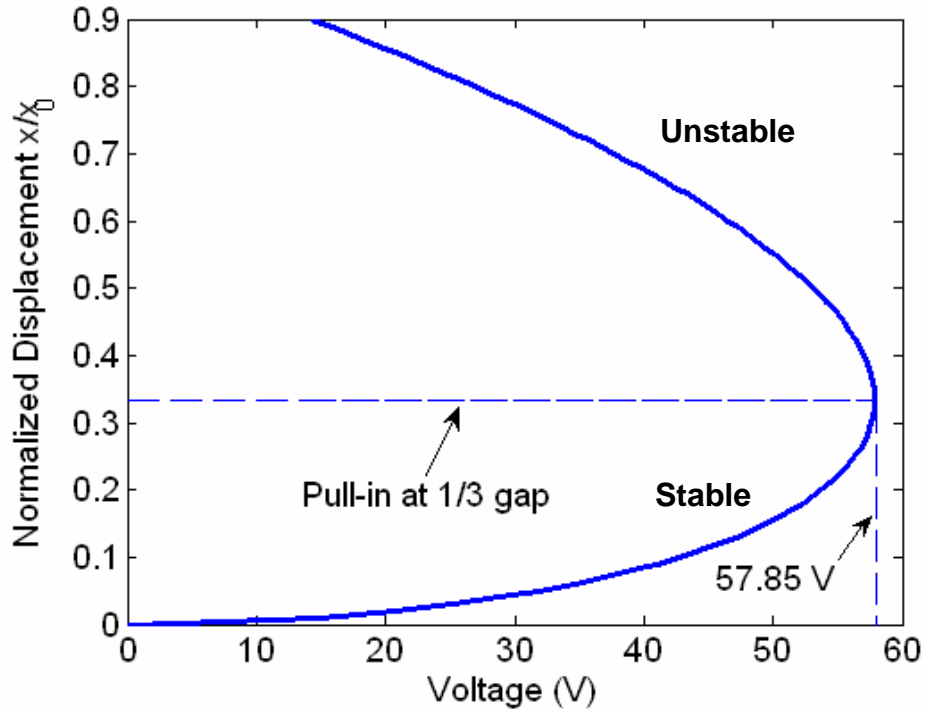


Figure 3-8. Static equilibrium relationship for the parallel plate electrostatic actuator.

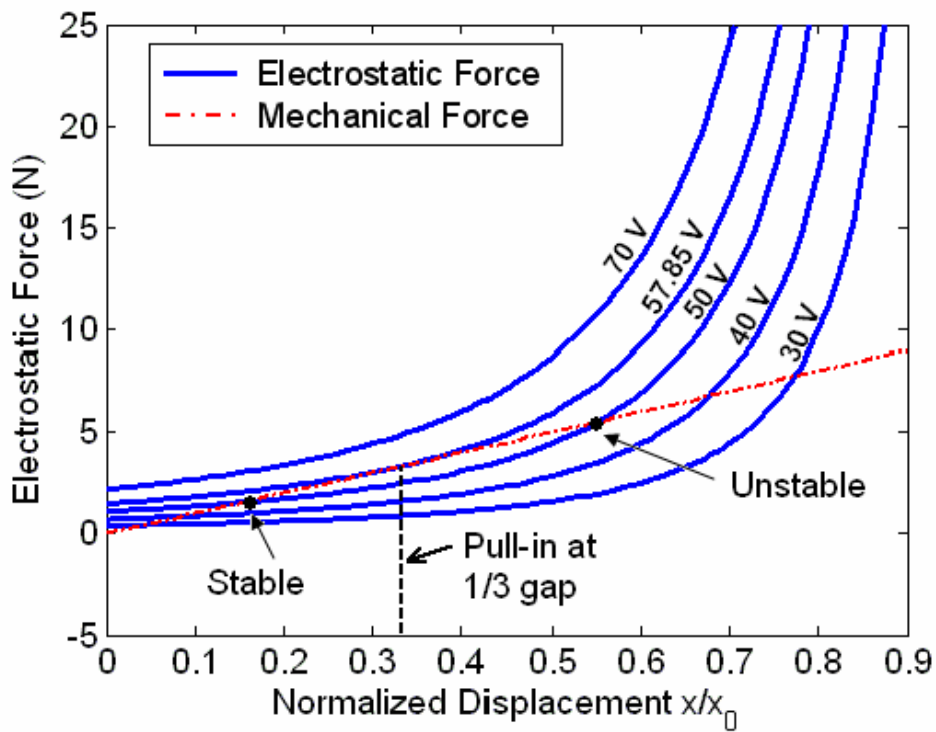


Figure 3-9. Electrostatic force for different voltages and mechanical force showing pull-in for the electrostatic parallel plate actuator.

Substituting Equation 3-12 into 3-11 and evaluating at the pull-in position results in the following relationship that is only a function of the capacitance and the pull-in position, x_{PI} .

$$\left(\frac{\partial C}{\partial(x_0 - x)} \right)_{x=x_{PI}} - x_{PI} \left(\frac{\partial^2 C}{\partial(x_0 - x)^2} \right)_{x=x_{PI}} = 0 \quad (3-13)$$

Assuming that the restoring springs are linearly deformed in the range of actuation, the pull-in angle is independent of the spring stiffness, and depends only on the angle of rotation. A pull-in function, $PI(x)$, is defined to determine the pull-in angle, which occurs when $PI(x)$ is equal to zero.

$$PI(x_0 - x) = \left(\frac{\partial C}{\partial(x_0 - x)} \right) - (x_0 - x) \left(\frac{\partial^2 C}{\partial(x_0 - x)^2} \right) \quad (3-14)$$

In turn, once the pull-in angle is determined, the pull-in voltage can be calculated by the following expression,

$$V_{PI} = \sqrt{\frac{2k_m x_{PI}}{\left(-\frac{\partial C}{\partial(x_0 - x)} \right)_{x_0 - x = x_{PI}}} } \quad (3-15)$$

The pull-in function for the parallel plate electrostatic actuators is shown in Figure 3-10,

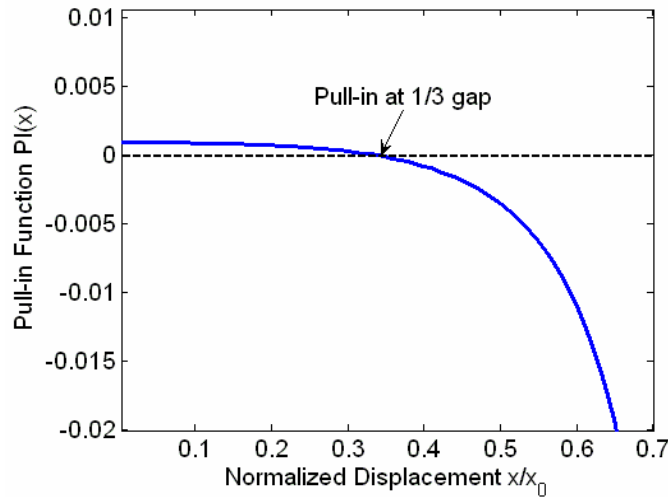


Figure 3-10. Pull-in function for the parallel-plate electrostatic actuator.

and verifies that pull-in does occur at 1/3 the gap between the plates. The pull-in voltage is calculated from Equation 3-15 to be equal to 57.85 V.

To further investigate the effects of changing the spring constant on the pull-in, the static equilibrium relationships are plotted for different values of the mechanical spring constant in Figure 3-11. This shows that even for a different spring constant, the pull-in displacement location remains at 1/3 the gap, while the pull-in voltage changes.

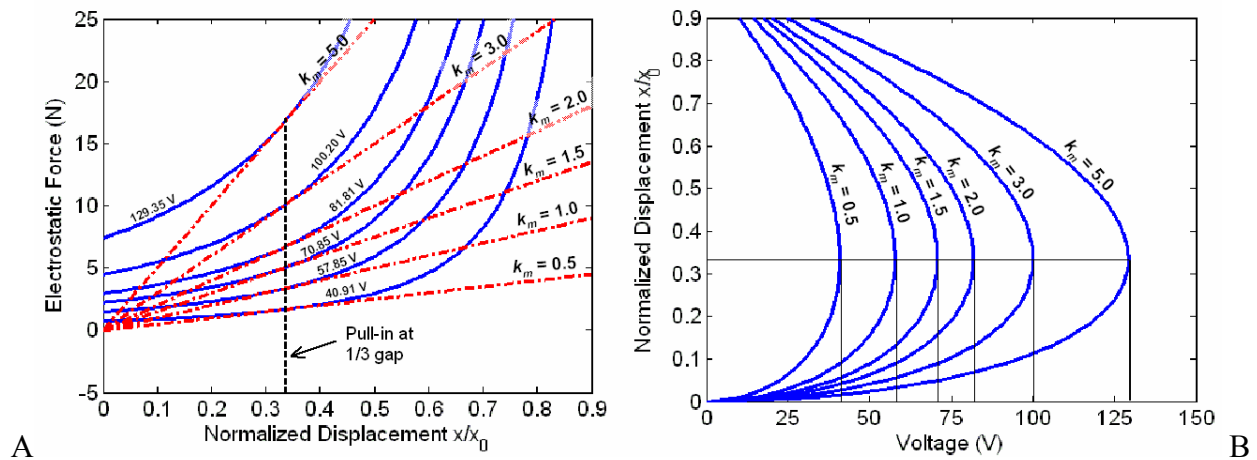


Figure 3-11. Static equilibrium relationships for the parallel plate actuator using different spring constants. A) The electrostatic and mechanical forces. B) The static displacement-voltage relationships.

3.3.2 Parallel Plate Torsion Actuator

Consider the case of an electrostatic parallel plate actuator that is supported by torsion springs, such as shown in Figure 3-12. This actuator rotates about the axis of the torsion springs, and the displacement may be described in terms of the angle of that rotation, θ .

The general relationships for electrostatic actuation that were derived in Section 3.3.1 may also be derived for this type of torsion actuator in terms of torques instead of forces. The sum of the torques for the system describes the equation of motion for the system. The micromirror can be considered as a one-degree-of-freedom mass-spring damper system of the form

$$J\ddot{\theta} + b\dot{\theta} + k_m\theta = T_e(\theta, V) \quad (3-16)$$

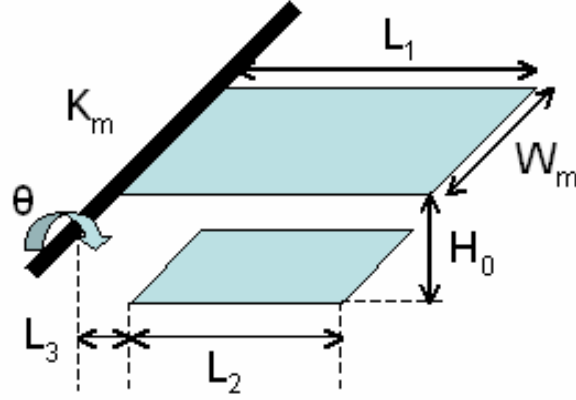


Figure 3-12. Schematic of a torsion electrostatic actuator.

where J is the mass moment of inertia, b is the damping coefficient, k_m is the mechanical spring constant, and T_e is the electrostatic torque, which is represented by the following,

$$T_e = \frac{1}{2} \frac{\partial C}{\partial \theta} V^2 \quad (3-17)$$

where C is the capacitance, θ is the angle of rotation about the X-axis, and V is the voltage potential. The mechanical system is governed by the stiffness of the support structure of the mirrors. It is assumed that the spring suspension provides a linear mechanical restoring torque, T_m , to the system that can be represented as,

$$T_m = k_m \theta \quad (3-18)$$

where k_m is the rotational spring constant. Static equilibrium occurs in the device when the electrostatic torque is equal to the mechanical restoring torque. Therefore, the static device behavior, which is the relationship of the actuation voltage, V , to the rotation angle, θ , is determined by equating Equations 3-17 and 3-18.

$$\frac{1}{2} \left(\frac{\partial C}{\partial \theta} \right) V^2 = k_m \theta \quad (3-19)$$

As was previously shown for parallel-plate electrostatics, there is a point at which the electrostatic torque exceeds the ability of the mechanical spring and equilibrium can no longer be

maintained. This is referred to as electrostatic pull-in. At the pull-in point, both the electrostatic and mechanical torques are equal in magnitude and slope [14], [46]. As was shown previously for the parallel-plate actuator, electrostatic pull-in can be considered as the mechanical and electrostatic torques being equal, as in Equation 3-19, and their first derivatives being equal.

$$\frac{1}{2} \left(\frac{\partial^2 C}{\partial \theta^2} \right) V^2 = k_m \quad (3-20)$$

Combining Equations 3-19 and 3-20 and evaluating at the pull-in angle results in the following relationship that is only a function of the capacitance and the pull-in angle, θ_{PI} .

$$\left(\frac{\partial C}{\partial \theta} \right)_{\theta=\theta_{PI}} - \theta_{PI} \left(\frac{\partial^2 C}{\partial \theta^2} \right)_{\theta=\theta_{PI}} = 0 \quad (3-21)$$

Assuming that the restoring springs are linearly deformed in the range of actuation, the pull-in angle is independent of the spring stiffness, and depends only on the angle of rotation. A pull-in function, $PI(\theta)$, is defined to determine the pull-in angle, which occurs when $PI(\theta)$ is equal to zero.

$$PI(\theta) = \left(\frac{\partial C}{\partial \theta} \right) - \theta \left(\frac{\partial^2 C}{\partial \theta^2} \right) \quad (3-22)$$

In turn, once the pull-in angle is determined, the pull-in voltage can be calculated by the following expression,

$$V_{PI} = \sqrt{\frac{2k_m \theta_{PI}}{\left(\frac{\partial C}{\partial \theta} \right)_{\theta=\theta_{PI}}}} \quad (3-23)$$

Thus far, the only difference between modeling the torsion actuator and the parallel plate actuator is that the parallel plate actuator has linear displacement, while the torsional has rotational motion. Therefore, the equations for each system are very similar. The difference in

evaluating the torsion actuator becomes apparent however when the capacitance for the system is calculated. Unlike the parallel-plate actuator, the torsion actuator does not have a constant gap between the top and bottom electrodes when it moves. Considering the system drawn in Figure 3-12, the capacitance for a torsion actuator in terms of the angle of rotation about its axis is given as

$$C(\theta) = \frac{\epsilon_0 W_m}{\theta} \left\{ \ln \left(1 - \beta \xi \frac{\theta}{\theta_{\max}} \right) - \ln \left(1 - \xi \frac{\theta}{\theta_{\max}} \right) \right\} \quad (3-24)$$

where β is L_3/L_2 , ξ is L_2/L_1 and θ_{\max} is H_0/L_1 [46]. From Equation 3-24 it is possible to calculate the performance for a torsion actuator. The pull-in function for this system is

$$PI(\theta) = \frac{\epsilon_0 W_m}{\theta^2} \left[\frac{3 \frac{\xi \theta}{\theta_{\max}} - 4 \left(\frac{\xi \theta}{\theta_{\max}} \right)^2}{\left(1 - \frac{\xi \theta}{\theta_{\max}} \right)^2} - \frac{3 \frac{\beta \xi \theta}{\theta_{\max}} - 4 \left(\frac{\beta \xi \theta}{\theta_{\max}} \right)^2}{\left(1 - \frac{\beta \xi \theta}{\theta_{\max}} \right)^2} + 3 \ln \left(\frac{1 - \frac{\xi \theta}{\theta_{\max}}}{1 - \frac{\beta \xi \theta}{\theta_{\max}}} \right) \right] \quad (3-25)$$

As an example, consider a system with the following geometric variables: $k_m = 1 \text{ N-}\mu\text{m}$, $\theta_{\max} = 10^\circ$, $W_m = 100 \mu\text{m}$, $\beta = 0.5$, $\xi = 0.5$. The static equilibrium for this system can be evaluated by examining the electrostatic and mechanical torques, as shown in Figure 3-13. The

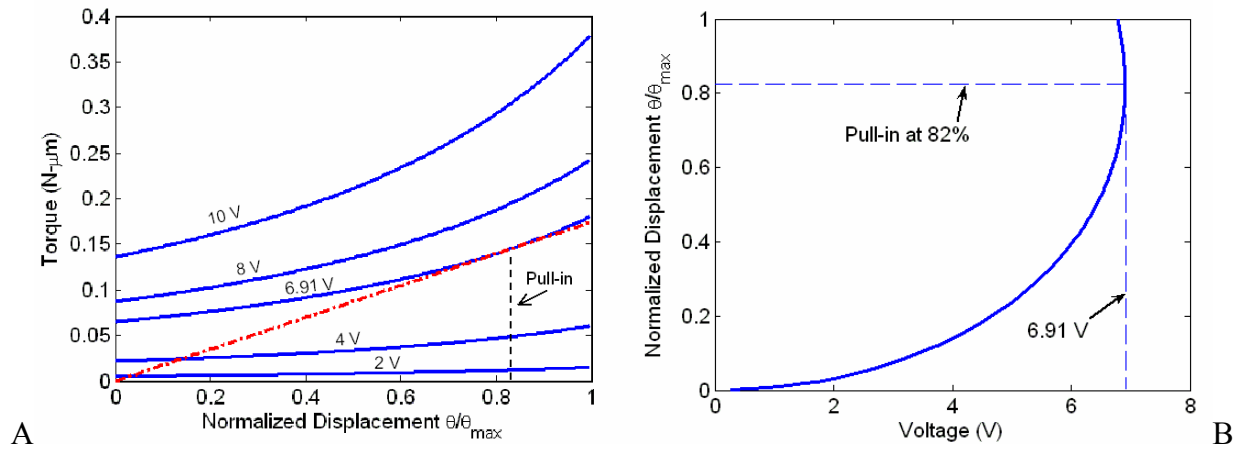


Figure 3-13. Static equilibrium relationships for the torsion actuator. A) The electrostatic and mechanical torques. B) The static rotation-voltage relationship.

displacement as a function of the voltage is also shown in Figure 3-13. The pull-in function from Equation 3-25 is plotted in Figure 3-14. From these figures, it is found that the pull-in for this system occurs at 82% of maximum rotation angle for the system. For the given spring constant, the pull-in voltage is 6.91 V. As with the parallel plate actuator, the pull-in angle will remain the same despite the mechanical spring constant, but the pull-in voltage will change. The pull-in angle can change, however, if the system geometry is changed. This is different from the parallel-plate actuator, which always pulls in at 1/3 the gap.

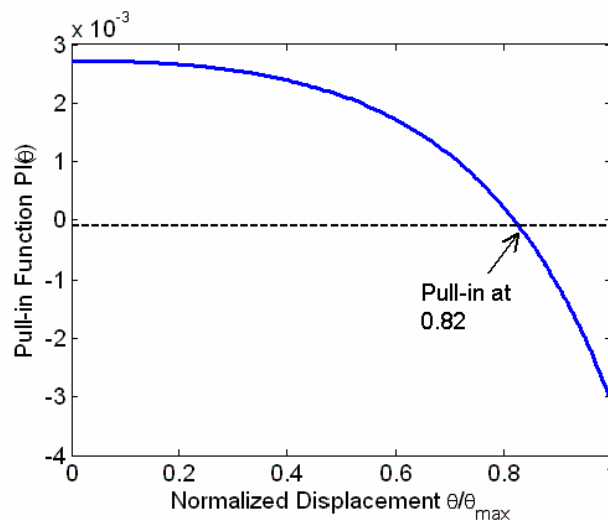


Figure 3-14. Pull-in function for the torsion actuator.

3.4 Model for Vertical Comb Drive Actuator

From the previous section it becomes clear that analytically describing the performance of an electrostatic actuator becomes more difficult as the geometry of the electrodes becomes more complex. In fact, it is very difficult to describe the capacitance for the micromirror devices that operate via vertical comb drive actuators. Thus it becomes necessary to employ FEA to assist in developing the system model. The device operates in both the mechanical and the electrical domains. Therefore, the model is developed for the mechanical and the electrostatic functions separately. The following analysis presents the model first in the mechanical domain and then

the electrostatic. The two models are then combined to determine theoretically the static behavior of the mirrors, including pull-in and hysteresis.

3.4.1 Mechanical Model

The mechanical spring is shown in Figure 3-15 with the fabrication layers labeled. The spring has two anchor points that connect to the ground layer (MMPoly0) and thin beams in the MMPoly1 layer to provide the restoring force. The layer MMPoly3, which is used to create the moving comb fingers, has a dimple cut in the center of the spring mechanism that, when actuated, comes into contact with the anchor (MMPoly2) and allows the mirror surface to pivot about this point. An alternative depiction is shown in Figure 3-16 in which the spring is considered as thin beams that are fixed to the substrate in two places. The length and cross-sectional area of the MMPoly1 beams is given in Figure 3-16 to be $33\ \mu\text{m}$ and $1 \times 1\ \mu\text{m}^2$, respectively. The value for Young's modulus is 164.3 GPa, and Poisson's ratio is 0.22. To determine the stiffness of this mechanical spring, a simple model is created in ANSYS Finite Element Analysis (FEA) program using Beam189 elements, which are capable of nonlinear large deflection analysis [99]. The boundary conditions constrain all motion in six-degrees-of-freedom at the two anchor points.

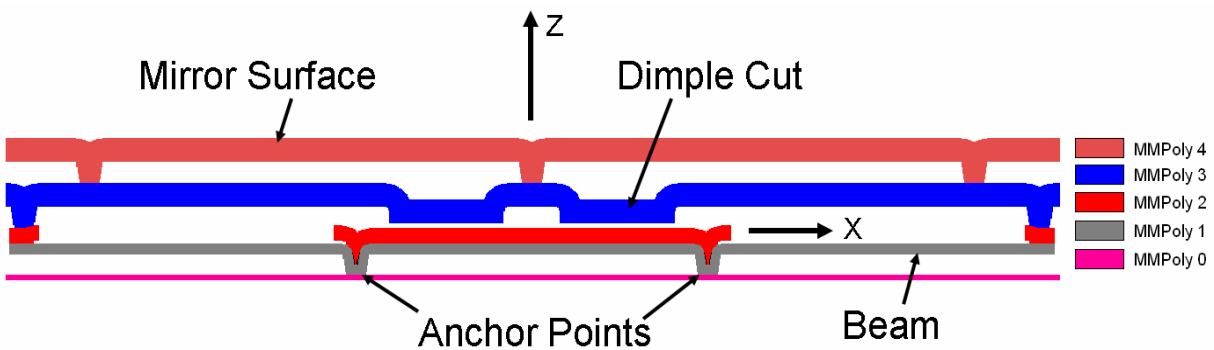


Figure 3-15. Drawing of the mechanical spring that supports the micromirrors and provides the restoring force.

Displacement loads are applied in all six-degrees-of-freedom at the point indicated in Figure 3-16 that corresponds to the pivot point created by the MMPoly3 dimple. The FEA determines the forces and stresses in the beam elements after the displacement loads are applied. The deformed shape of the structure is shown in Figure 3-17. Assuming Hooke's law for the force applied to a linear spring, the spring stiffness in all six degrees-of-freedom can be calculated. The linear spring assumption is verified by performing nonlinear FEA over the entire range of motion of the spring displacement from zero to nineteen degrees. The results are listed in Table 3-3, retaining 4 significant figures. The stiffness in X, Y, and Z refer to the stiffness of the spring in each respective axis direction, and q_X , q_Y , and q_Z refer to the rotational stiffness about the axes X, Y, and Z, respectively. It is clear that the spring is not very stiff in the Y and Z directions. The torsional stiffness about the X axis, q_X , is lower than those about the Y or Z axes, meaning that the mirror is able to rotate about the X axis, while it is resistant to off-axis rotations about the Y or Z. It is the value of q_X equal to 612.4 pN-m/rad that is used for k_m in Equation 3-17.

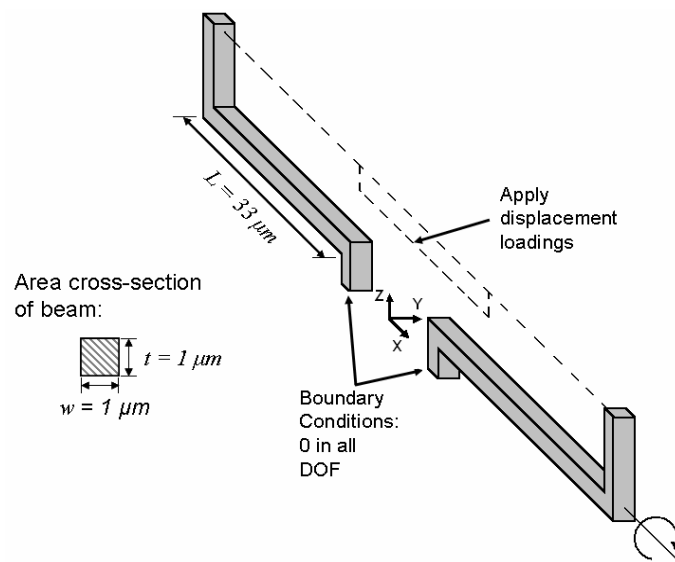


Figure 3-16. Image of the mechanical spring that supports the micromirror indicating boundary conditions and location for applying displacement loads for finite element analysis.

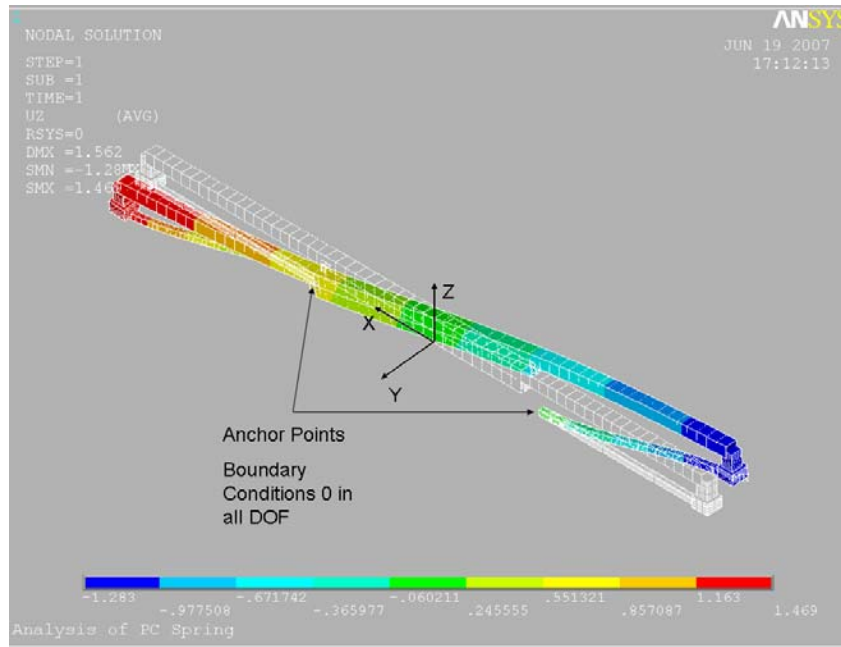


Figure 3-17. Image from ANSYS of the deformed spring and the outline of the undeformed shape after displacements are applied. The displacement is amplified by a scale factor of 4.

Table 3-3. Values output from finite element analysis of mechanical spring stiffness.

Parameter	Value
X stiffness	744.7 pN/m
Z stiffness	7.946 pN/m
Y stiffness	1.266 pN/m
qX stiffness	612.4 pN-m/rad
qZ stiffness	11360 pN-m/rad
qY stiffness	16310 pN-m/rad

3.4.2 Electrostatic Model

In order to compute the electrostatic torque values in Equation 3-16, it is necessary to find an expression for the capacitance as a function of the rotation angle. For parallel-plate electrostatics, this can be done quite easily as an analytical expression is known. Because of the more complex electrode geometry created by the inclusion of the vertical comb drive, the capacitance of the device cannot be as easily derived. To determine the charge created by the electrostatic field, 3-D FEA is used to calculate the capacitance as a function of θ .

The symmetry of the device design makes it convenient to model only a small section of the device, termed the unit cell. A cross-section of a unit cell made up of one-half of one moving comb finger and one half the associated fixed comb finger and portions of the ground plane and mirror surface is shown in Figure 3-5(c). The model of the geometry in Figure 3-18 is created in ANSYS. The nominal dimensions used to create this model are given in Appendix A. For an electrostatic analysis, the volume of the surrounding fluid, in this case ambient air, is created around the device geometry, and it is this air volume that is meshed and analyzed to determine the electrostatic field generated as the mirror and moving finger rotate about an axis parallel to the X-axis in the figure. An arbitrary voltage differential, V , is applied as shown in the drawing. The only relevant material properties needed in this analysis are the permittivity of free space, ϵ_0 , which is 8.854×10^{-12} F/m, and the relative permittivity of the dielectric medium, ϵ , which in this case for air, is equal to 1. The analysis calculates the total charge of the electric field, W , and then calculates the capacitance for a given θ position as

$$C = 2 \frac{W}{V^2} \quad (3-25)$$

Using numerical values generated in the electrostatic FEA model, Equation 3-24 is applied to calculate the capacitance at discrete points as the geometry of the mirror surface and moving comb finger rotate through a range of motion from 0 to 19 degrees. A polynomial least-squares fit of these capacitance values is used to find an analytical expression for the capacitance. The capacitance as a function of θ is approximated with an n^{th} order polynomial curve fit.

$$C(\theta) = N(P_1\theta^n + P_2\theta^{n-1} + \dots + P_n\theta + P_{n+1}) \quad (3-26)$$

where the coefficients of the polynomial are P_i , ($i = 1, 2, \dots, n, n+1$), and N is the total number of unit cells. The results of this analysis are plotted in Figure 3-19 along with a comparison of first, second, third, and fourth order polynomial curve fit approximations of the data. The coefficients

for these curve fit approximations are listed in Table 3-4. Table 3-5 compares the quality of the different order polynomial approximations compared to the FEA data points. One metric to evaluate the fit quality for a curve fit is the norm of the residuals, $normr$. The smaller the value of $normr$ is, the better the approximation. Another standard metric is the sum of the square of the residuals, r^2 , which is calculated from $normr$ by

$$r^2 = 1 - \frac{normr^2}{(n-1)s^2} \quad (3-27)$$

where n is the number of data points (FEA data), and s is the standard deviation of the curve fit approximation from the data. A value of r^2 equal to one indicates a perfect fit. It is clear that a higher order polynomial does a slightly better job of capturing the nature of the capacitance data. However, the first order linear curve fit can still be sufficient for analysis in the stable range of motion. It will not be as accurate at predicting the pull-in behavior. The advantage of using the first order fit is that its derivative which is used in Equation 3-16 is a constant, thus simplifying the plant model to a linear approximation in V^2 . In order to capture the nonlinear behaviors of pull-in and hysteresis, the fourth order polynomial curve fit approximation is used in Section 3.4.4. The effects of different linear approximations in the model are discussed further in Chapter 5.

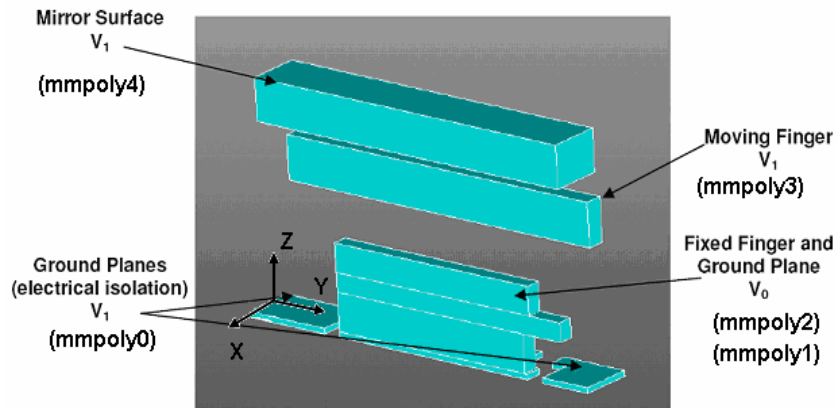


Figure 3-18. Solid model geometry of the unit cell used in the electrostatic FEA simulation.

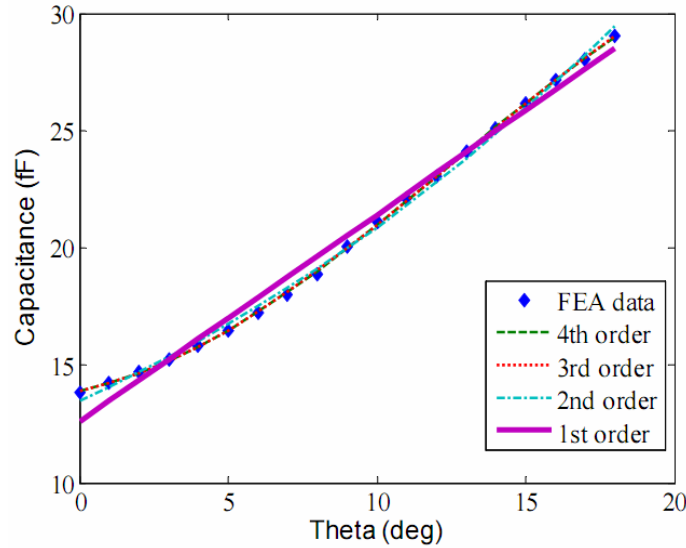


Figure 3-19. Capacitance calculation as a function of rotation angle, θ , calculated using 3D FEA and varying orders of polynomial curve fit approximations.

Table 3-4. Comparison of polynomial fit for approximation of capacitance function

Order	P1	P2	P3	P4	P5
4	0.023120	-0.013678	0.004164	0.000109	0.000106
3	0.000848	0.001280	0.000299	0.000103	--
2	0.001680	0.000250	0.000104	--	--
1	0.000777	0.000078	--	--	--

Table 3-5. Comparison of polynomial fit for approximation of capacitance function

Order	normr	s	n	r^2
4	1.1192E-05	0.000185	18	0.999785
3	1.1463E-05	0.000185	18	0.999775
2	3.6691E-05	0.000185	18	0.997691
1	8.608E-05	0.0001854	18	0.987166

3.4.3 Electromechanical Model

Taking both the mechanical and electrostatic models into account, the static behavior of the system can now be predicted using Equations 3-16 to 3-20. Equations 3-18 to 3-20 calculate the electrostatic pull-in characteristics of the device. A plot of the pull-in function is shown in Figure 3-20 where pull-in occurs when the function equals zero at 16.5 degrees. Using this value in Equation 3-20, the pull-in voltage is 71.06 V.

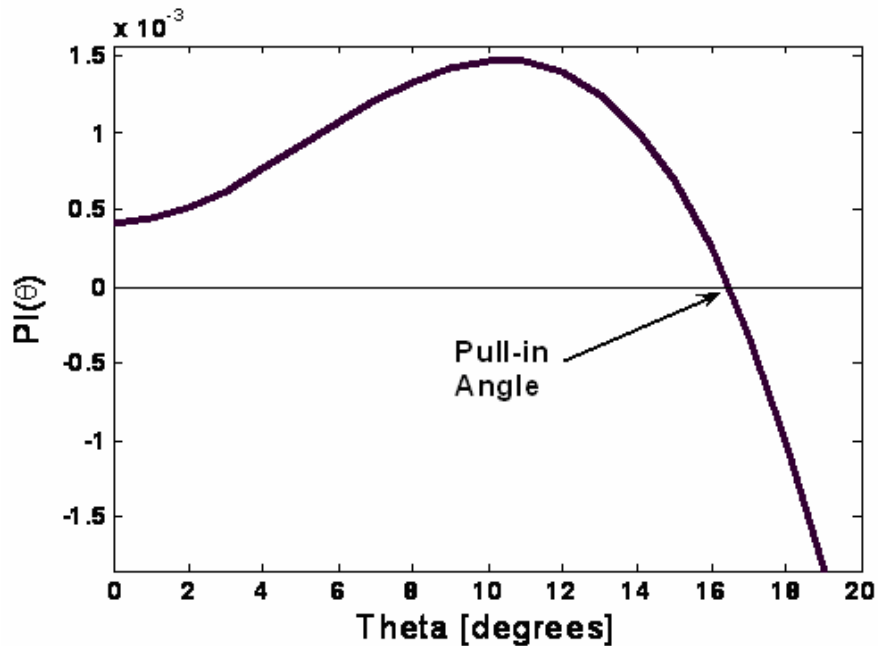


Figure 3-20. Plot of the Pull-in function $PI(\theta)$ for the micromirror with the vertical comb drive actuator showing that pull-in occurs at 16.5 degrees.

The static equilibrium behavior can also be evaluated from Equations 3-16, and 3-17, respectively. When the mechanical and electrostatic torques are equal to each other, the system is in static equilibrium. This can be shown graphically by plotting these values. Figure 3-21 shows the electrostatic torque as a function of rotation angle for different values of voltage ranging from 10 volts to 80 volts. The straight line on the plot corresponds to the mechanical restoring torque of the spring from Equation 3-17. At every point where the mechanical torque and the electrostatic torque lines cross, they are in equilibrium indicating a stable position. There is a point at which this line runs tangent to the electrostatic torque, and this indicates the electrostatic pull-in point, which corresponds to the calculated values of 16.5°, and 71.06 volts. The electrostatic torque curve at the pull-in voltage, V_{PI} , is also indicated in Figure 3-21. The pull-in angle for a linear spring is determined completely by the electrostatic torque. For a different value of the mechanical spring constant, k_m , the slope of the mechanical torque line

would be different, but it would still run tangent to the electrostatic torque at the same pull-in angle. Only the value of the pull-in voltage would be affected. This is shown in Figure 3-22. The pull-in instability is known to cause hysteresis in the device behavior, and this too can be predicted using this modeling approach. After the device has pulled-in, it is possible to reduce the voltage below the pull-in voltage without releasing the device. This is referred to the holding voltage. Once the voltage has been reduced below this holding voltage threshold, the device will release from its pulled-in position, but it will return to a position different from the pull-in position. From this electromechanical analysis, it is determined that the holding voltage is 68.89 V. The static behavior of the device is shown in Figure 3-23, including the pull-in point and the hysteresis loop. This type of curve will be referred to as a θ - V profile, and represents the static calibration for the device.

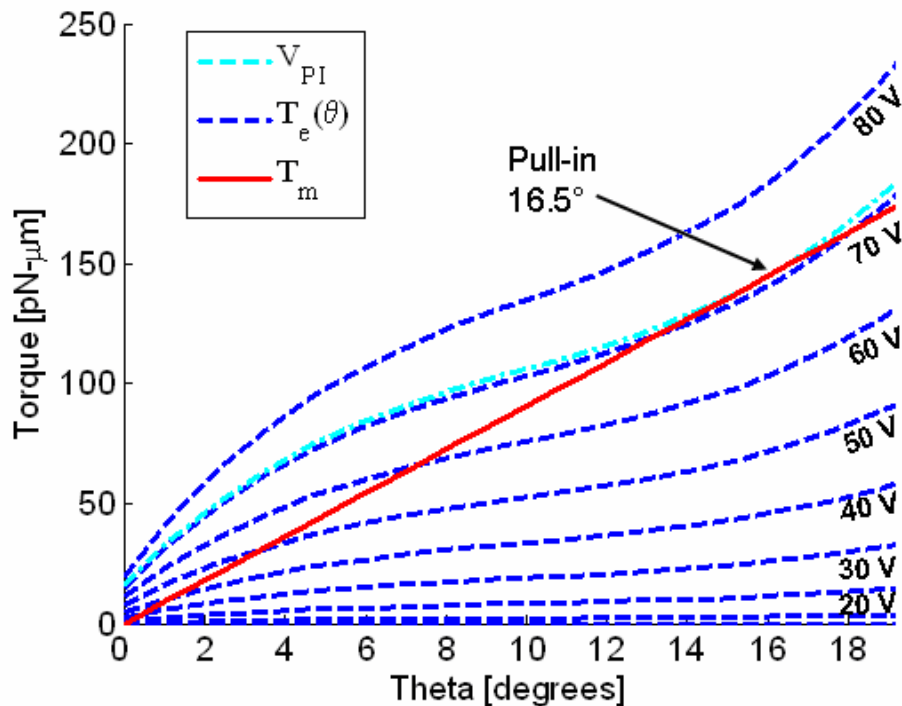


Figure 3-21. Electrostatic and Mechanical torque as a function of rotation angle, theta, and voltage for different voltage values.

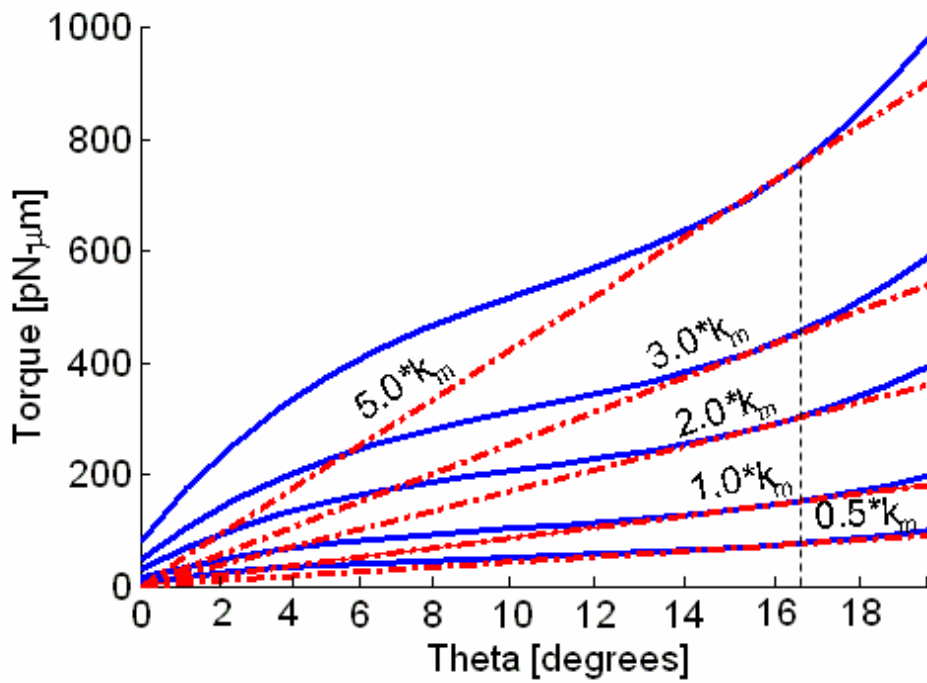


Figure 3-22. Torque as a function of rotation angle, theta, and voltage for different values of mechanical spring constant.

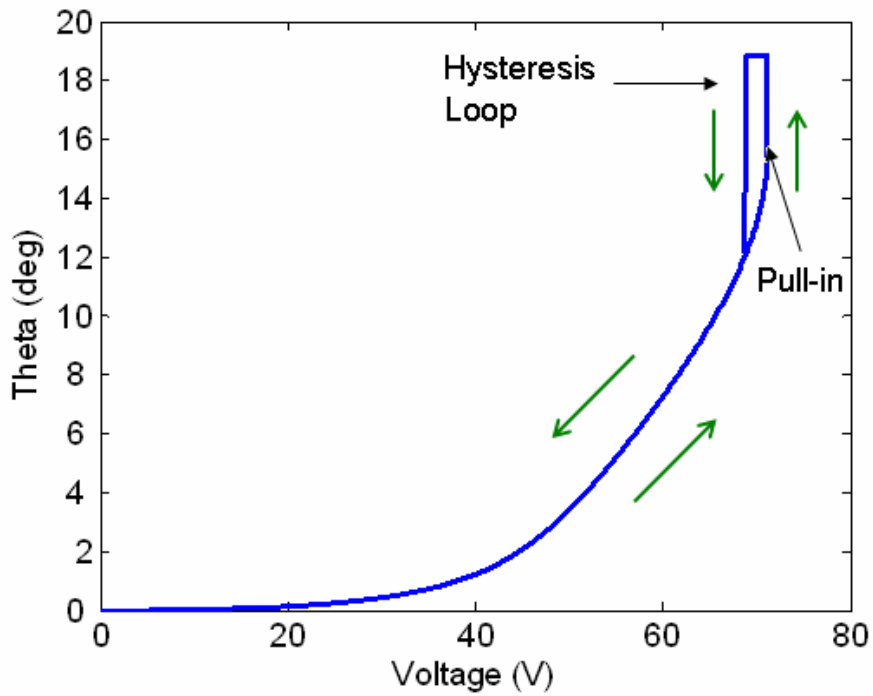


Figure 3-23. Plot of static equilibrium behavior, showing pull-in and hysteresis, predicted from the model.

3.4.4 Linear Approximation

Recall from the discussion in Section 3.4.2 of the electrostatic model development that the capacitance function is approximated using a polynomial curve fit, and that different orders of polynomial can be used. For this system, the nonlinear behavior of the electrostatic instability is best captured using a higher order polynomial; however a first order function is still able to approximate the system performance. Using a first order approximation makes the derivative term of the capacitance a constant value, which greatly simplifies the dynamics and allows the system to be modeled as linear. The effects of using a higher order curve fit versus the first order are more apparent by looking at the static equilibrium relationship between the applied voltage, V , and the rotation angle, θ . This is shown in Figure 3-24 for the fourth order fit, called the nonlinear model, and the first order fit, called the linear capacitance approximation model. It is clear that by using the lower order model approximation there is a difference between the

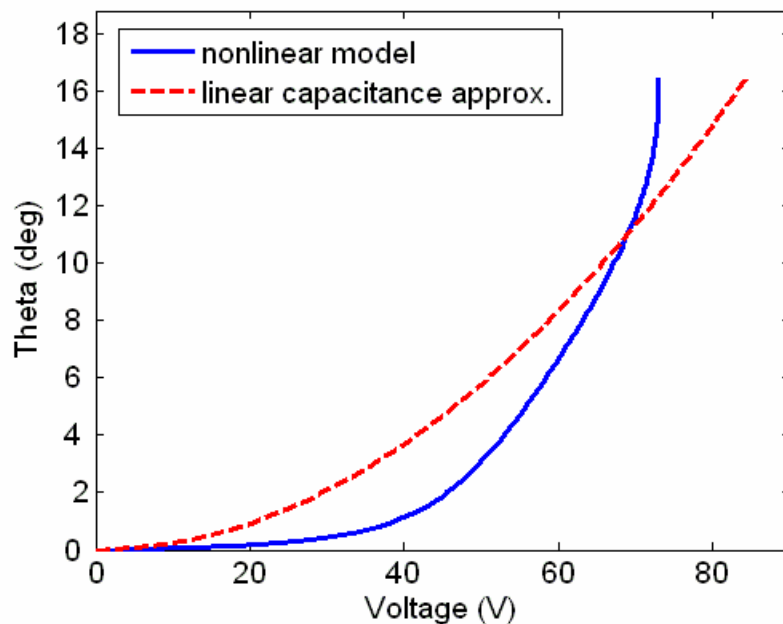


Figure 3-24. Static equilibrium relationships for the nonlinear plant model, and the linear plant approximation.

predicted static performances. To establish the effects of model uncertainty on micromirror arrays, the linear model is used as a basis for designing controllers in Chapter 5. The linear model is suitable to the design of the controller, but the resulting control law must still be able to perform well on the nonlinear system.

For a system in which the capacitance cannot be adequately modeled as linear, such as the case of parallel plate electrostatics, a higher order approximation is required. In this case, it is possible to linearize the second order dynamic model in Equation 3-16 about an operating point (θ_0, V_0) using the Taylor series expansion (TSE) [36]. This can be considered as the small signal model approximation about $\delta\theta$ and δV . Doing so yields the following linear system model,

$$J\delta\ddot{\theta} + b\delta\dot{\theta} + k_m\delta\theta = k_e\delta\theta + C\delta V \quad (3-28)$$

The linearization in Equation 3-28 includes a term that is dependent only on the rotation angle that can be considered the electrostatic spring force, k_e [20].

$$k_e = \frac{1}{2} \left(\frac{d^2C}{d\theta^2} \Big|_{\theta=\theta_0} \right) V_0^2 \quad (3-29)$$

The nonlinear torque approximation is reduced to a constant.

$$C_T = V_0 \frac{dC}{d\theta} \Big|_{\theta_0} \quad (3-30)$$

When linearizing a function about an operating point, it is desirable that the linear model will provide an adequate estimate of the nonlinear function within a small range about that operating point. For systems that are operating over a large range or have very nonlinear characteristics, this linearization may not provide a satisfactory estimate of the nonlinear function. To illustrate the effect of the small signal linearization, Figure 3-25 shows the static equilibrium relationship between rotation angle and actuation voltage for the nonlinear system

model and for the small signal model linearized about the operating point (7 degrees, 54 volts). The inset shows the small signal response for $\delta\theta$, δV .

It is clear in Figure 3-25 that this linear estimate of the nonlinear system does not capture all of the static performance characteristics over the entire range of operation, but is adequate enough for a portion of the range from 5 to 14 degrees. In order to cover the full range of actuation, a piecewise linearization can be done at different operating points. This piecewise linearization approach would represent the system response as shown in Figure 3-26.

The linearized models discussed above are important when considering control design techniques that require a linear transfer function or state-space model for the design process. Of the two linearization methods discussed, the first method of using a linear capacitance approximation is used throughout this dissertation whenever the linear system model is required. This method was chosen for its ease of use.

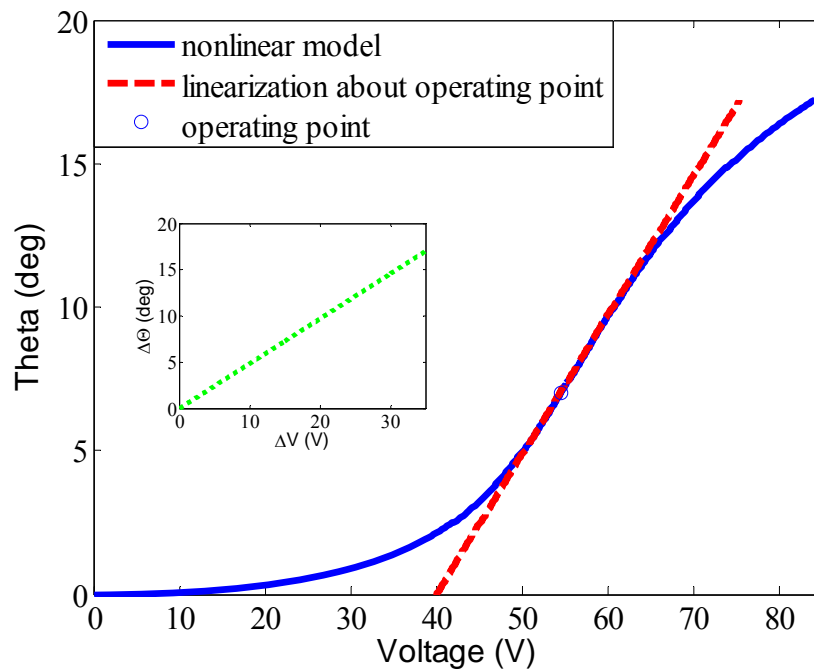


Figure 3-25. Static equilibrium relationships for the nonlinear plant model, and the small signal model linearized about an operating point (θ_0 , V_0).

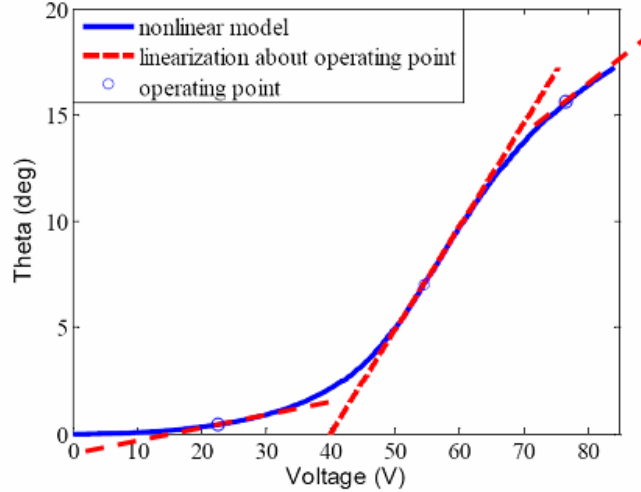


Figure 3-26. Illustration of piecewise linearization about multiple operating points.

3.4.5 Bifurcation Analysis

Electrostatic instability is an example of bifurcation, and the stability of the system can be examined by looking at the dynamics of the actuator and finding the fixed-point solutions [106], [107]. One advantage of evaluating the bifurcation behavior of the device is that unlike the methods used in Equations 3-14 and 3-15, the mechanical spring constant is not required to be linear. This analysis will be used again in Chapter 5 to determine the effects of a nonlinear spring constant on the electrostatic pull-in. Here, the spring constant is still assumed to be linear, and the results may be compared to those obtained using Equations 3-14 and 3-15.

The state space model for the system is

$$\begin{aligned}
 x_1 &= \theta \\
 x_2 &= \dot{\theta} \\
 \begin{bmatrix} \dot{x}_1 \\ \dot{x}_2 \end{bmatrix} &= \begin{bmatrix} x_2 \\ \frac{1}{J} T_e(x_1) - \frac{b}{J} x_2 - \frac{k_m}{J} x_1 \end{bmatrix}
 \end{aligned} \tag{3-31}$$

Recall that T_e is a function of the capacitance expression from Equation 3-26. In order to capture the nonlinear effects of the system, a fourth-order curve fit approximation is used. The fixed points occur at $x_2 = 0$ and

$$T_e(x_1) - k_m x_1 = 0 \quad (3-32)$$

This can be expressed in full as

$$\frac{1}{2}N(4P_1x_1^3 + 3P_2x_1^2 + 2P_3x_1 + P_4)V^2 - k_mx_1 = 0 \quad (3-33)$$

Equation 3-33 is a cubic polynomial equation for which finding the roots has been the subject of considerable study [110]. One solution is to write the polynomial as

$$Ax_1^3 + Bx_1^2 + Cx_1 + D = A(x_1 - \theta_{e1})(x_1 - \theta_{e2})(x_1 - \theta_{e3}) = 0 \quad (3-34)$$

where θ_{e1} , θ_{e2} and θ_{e3} are the three roots, and the coefficients A , B , C and D are

$$A = 2NV^2P_1 \quad (3-35)$$

$$B = \frac{3}{2}NV^2P_2 \quad (3-36)$$

$$C = NV^2P_3 - k_m \quad (3-37)$$

$$D = \frac{1}{2}NV^2P_4 \quad (3-38)$$

Further, define

$$q = \frac{9ABC - 27A^2D - 2B^3}{54A^3} \quad (3-39)$$

$$u = \sqrt{\left(\frac{3AC - B^2}{9A^2}\right)^3 + q^2} \quad (3-40)$$

$$s = \sqrt[3]{q + u} \quad (3-41)$$

$$t = \sqrt[3]{q - u} \quad (3-42)$$

The roots of Equation 3-34 are

$$\theta_{e1} = s + t - \frac{B}{3A} \quad (3-43)$$

$$\theta_{e2} = -\frac{1}{2}(s+t) - \frac{B}{3A} + \frac{\sqrt{3}}{2}(s-t)i \quad (3-44)$$

$$\theta_{e3} = -\frac{1}{2}(s+t) - \frac{B}{3A} - \frac{\sqrt{3}}{2}(s-t)i \quad (3-45)$$

The roots of Equation 3-33 can be found to determine the static voltage-displacement relationship, as was done previously in Section 3.4.3. Solving this equation gives the fixed points as functions of the control parameter V . The roots of this expression can be examined graphically by defining a function $F(x_1)$ as

$$F(x_1) = T_e - T_m = \frac{1}{2}V^2 \frac{\partial C}{\partial x_1} - k_m x_1 \quad (3-46)$$

In Figure 3-27, $F(x_1)$ is plotted for varying values of voltage, V . The roots of $F(x_1)$ correspond to the zero crossings on the figure. Notice that there are three roots for each line of constant voltage, and this corresponds to $F(x_1)$ being a third order polynomial. The roots that occur to the left of zero degrees theta are solutions that are non-physical solutions and are thus ignored. The solutions of function $F(x_1)$ that occur for positive values of theta can have either two roots, one root, or zero roots. For a sufficiently small voltage, there are two roots. In this case the electrostatic force is low enough that the linear spring force can balance it, creating a stationary state. As the voltage is increased, the electrostatic force increases, eventually overwhelming the linear spring force and all the steady-state solutions disappear. This is another description of the pull-in instability caused by the disappearance of all physically possible steady-state solutions [106].

Now that the steady state solutions of the system can be determined, it is the stability of those solutions that must be determined. A Jacobian matrix is found by taking the Taylor series expansion of Equation 3-31 and retaining only the first order terms [107].

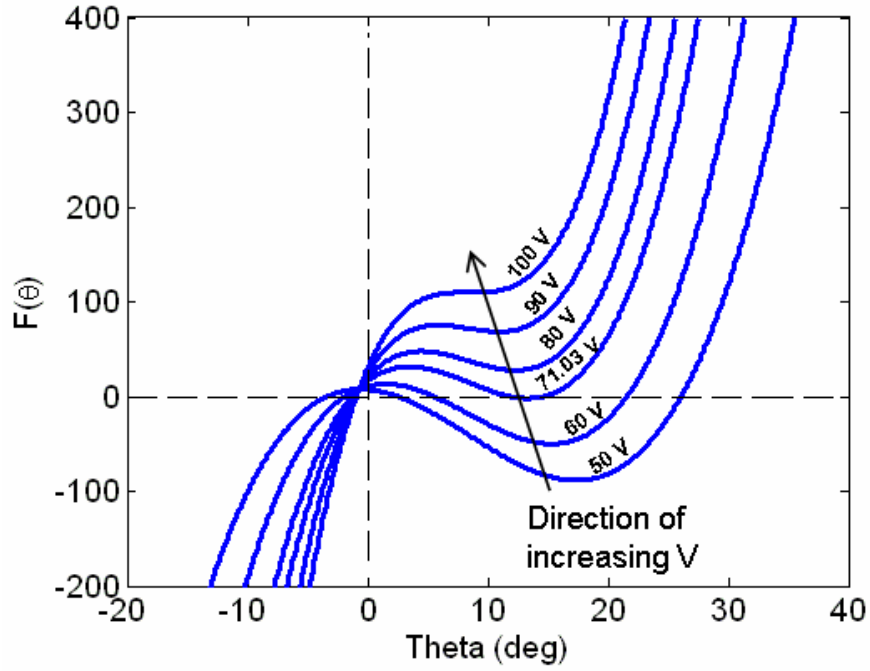


Figure 3-27. Plot showing the roots of the function $F(x_1)$ occur where the function crosses zero.

$$Df(\bar{x}) = \begin{bmatrix} 0 & 1 \\ \left(\frac{1}{J} \frac{\partial T_e(x_1)}{\partial x_1} - \frac{k_m}{J} \right) & -\frac{b}{J} \end{bmatrix} \quad (3-47)$$

where

$$\frac{\partial T_e(x_1)}{\partial x_1} = \frac{1}{2} N(12P_1x_1^2 + 6P_2x_1 + 2P_3)V^2 \quad (3-48)$$

The Jacobian defined in Equation 3-47 relates the perturbation of the states from equilibrium as

$$\begin{Bmatrix} \Delta \dot{x}_1 \\ \Delta \dot{x}_2 \end{Bmatrix} = \left[Df(\bar{x}) \Big|_{\bar{x} = \begin{Bmatrix} \theta_{e1} \\ 0 \end{Bmatrix}} \right] \begin{Bmatrix} \Delta x_1 \\ \Delta x_2 \end{Bmatrix} \quad (3-49)$$

The stability is determined by evaluating the matrix in Equation 3-47 at the fixed points and determining the eigenvalues. The fixed point solution is stable when the real part of the eigenvalues is less than zero. The eigenvalues, λ_j for $j = 1, 2$, are calculated for each fixed point solution (i.e., roots θ_{e1} , θ_{e2} and θ_{e3}). This is expressed as

$$\lambda_j = \frac{1}{2} \frac{b}{J} \pm \frac{1}{2} \sqrt{\left(\frac{b}{J}\right)^2 + 4 \left(\frac{1}{J} \frac{\partial T_e(\theta_{ei})}{\partial x_1} - \frac{k_m}{J}\right)}$$

$$j = 1, 2$$

$$i = 1, 2, 3$$
(3-50)

Substituting Equation 3-48 into 3-50 gives the expression for the eigenvalue problem in terms of the expression for the capacitance.

$$\lambda_j = \frac{1}{2} \frac{b}{J} \pm \frac{1}{2} \sqrt{\left(\frac{b}{J}\right)^2 + 4 \left(\frac{1}{2J} N(12P_1\theta_{ei}^2 + 6P_2\theta_{ei} + 2P_3)V^2 - \frac{k_m}{J}\right)}$$

$$j = 1, 2$$

$$i = 1, 2, 3$$
(3-51)

To evaluate the eigenvalues and their stability, an expression for the damping in the system must be defined. In a MEMS system such as this, the dominant source of damping comes from the squeeze-film effect, in which air that is compressed between very small spaces begins to act as a viscous fluid [3]. Squeeze-film damping is dependent on the device geometry, and expressions are known for parallel plate actuators and for torsion plate actuators. As was the case with the electrostatic model development, the complex geometry of the vertical comb drive micromirrors makes determining the squeeze-film damping coefficient analytically difficult. For the purpose of this discussion, an approximation is made to consider the squeeze-film damping term for a torsional plate developed by Pan, et al [100].

$$b = K_{rot} \frac{\eta L w^5}{g^3}$$
(3-52)

where L is the length of the plate, w the width, g is the gap between the plates, and η is the absolute viscosity of the fluid. The term K_{rot} is

$$K_{rot} = \frac{48}{\pi^6 \left[\left(\frac{w}{L}\right)^2 + 4\right]}$$
(3-53)

. Table 3-6 lists the values of additional parameters for this analysis. This estimate for squeeze-film damping is used here for simplicity.

The resulting bifurcation diagram in Figure 3-28 shows a saddle node bifurcation at 16.5 degrees and 71.06 V. This is in agreement with the pull-in results from Section 3.4.3. Figure 3-29 shows the bifurcation diagram for different values of the mechanical spring constant, k_m , to illustrate how changing the spring constant for a linear spring only affects the pull-in voltage.

Table 3-6. List of parameters used for this analysis.

Parameter	Value	
ρ , density of polysilicon	2331	kg/m ³
η , absolute viscosity of air	1.73e-5	N-s/m ²
L , length of mirror	20	μm
w , width of mirror	100	μm
g , gap between plates	11.25	μm
N , number of unit cells	54	

3.5 Chapter Summary

The electrostatic modeling in this chapter reveals the performance characteristics of a micromirror based on the nominal design parameters of the device. The model is developed by considering the mechanical spring element and the electrostatic actuation forces separately. Doing so allows for greater understanding of the role of each energy domain in determining the performance of the electromechanical device. It can also be useful in the design stages of an electrostatic micromirror to see the effects of changing the design to have a different spring stiffness or electrode shape. The electrostatic instability phenomenon is described in analytic terms that can be used to predict the pull-in angle, pull-in voltage, and the hysteresis behaviors of the device. The electrostatic behaviors are also examined through bifurcation analysis.

It is discussed in the description of the fabrication process in Section 3.1 that there are certain errors that occur in the geometry and the material properties during fabrication.

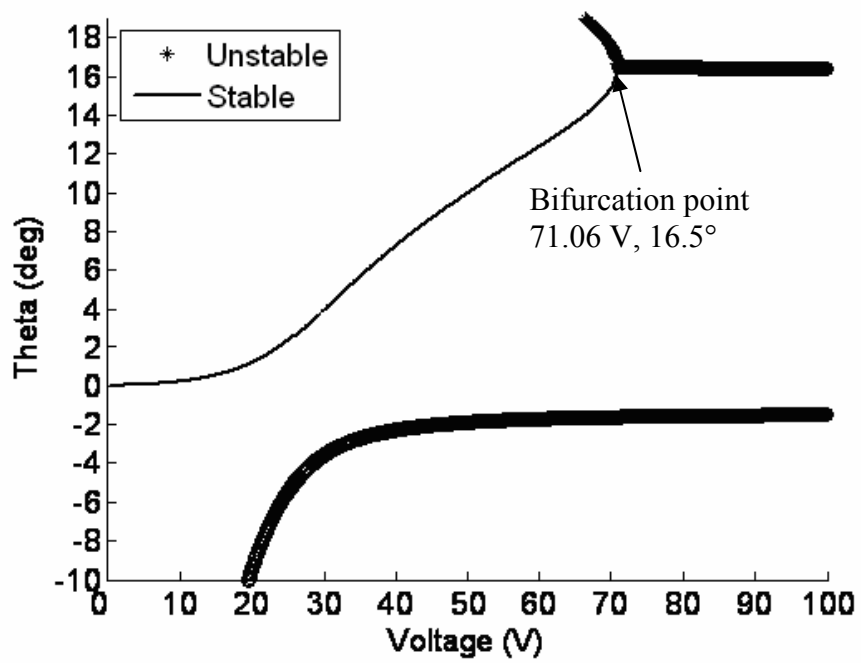


Figure 3-28. Bifurcation diagram for a MEMS torsion mirror with electrostatic vertical comb drive actuator.

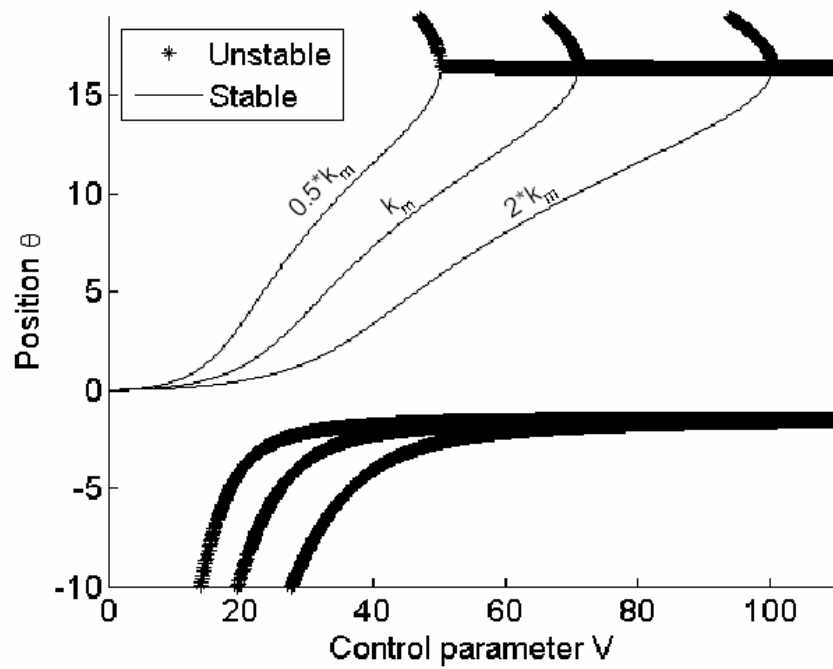


Figure 3-29. Bifurcation diagram showing the effects of different spring constants.

Information on these errors is available in the process design manual, and gives a MEMS designer a reasonable expectation of the precision available from the micromachining process. The next chapter will use the modeling methods developed here to examine the effects of parametric uncertainties that come from the fabrication process, and what these errors in dimensions and material properties can do to the performance of a microdevice.

CHAPTER 4 UNCERTAINTY ANALYSIS AND EXPERIMENTAL CHARACTERIZATION

Chapter 3 presented the description of the micromirrors and demonstrated the modeling methods used to predict the static behavior of the devices. While one may assume that the micromirrors were fabricated exactly to the nominal design specifications for dimension and material properties, it is well established that surface micromachining processes have machining tolerances that result in small parametric errors in the finished devices. The effects of these fabrication variations in dimension and material property are examined utilizing the modeling methods put forth in Chapter 3 for the electrostatic micromirrors. The effects of varying a single parameter at a time are examined first to determine the sensitivity of the design to a given parametric uncertainty. Then, combinations of uncertainties are evaluated using Monte Carlo simulations. The results obtained from the models in Chapters 3 and 4 are then compared to experimental characterization data that was obtained using an optical profiler.

4.1 Parametric Uncertainty and Sensitivity Analysis

Recall from the discussion in Section 3.1, that fabrication tolerances for surface micromachining processes can result in final dimensions that differ from the intended design. The SUMMiT V design manual gives values of dimensional tolerances in layer thickness and linewidth error, shown first in Tables 3-1 and 3-2 respectively, and reprinted in this chapter for convenience as Tables 4-1 and 4-2. These show that dimensions can vary by as much as eight percent in layer thickness, and as much as twenty-nine percent for width dimensions on a feature size of 2 microns [6]. The result can be that the fabricated devices will not behave as predicted, or that devices of the same design can behave differently from one another. Dimensional variations can affect spring constants, resonant frequencies, and electrical characteristics.

Table 4-1. Mean and standard deviation of fabrication variations for layer thickness in the SUMMiT V surface micromachining process.

Layer	Mean (μm)	Std. Dev. (μm)
MMPOLY0	0.29	0.002
SACOX1	2.04	0.021
MMPOLY1	1.02	0.0023
SACOX2	0.3	0.0044
MMPOLY2	1.53	0.0034
SACOX3	1.84	0.54
DIMPLE3 Backfill	0.4	0.0053
MMPOLY3	2.36	0.0099
SACOX4	1.75	0.0045
MMPOLY4	2.29	0.0063

Table 4-2. Mean and standard deviation of fabrication variations of line widths in SUMMiT V.

Layer	Mean (μm)	Std. Dev. (μm)
MMPOLY2	-0.08	0.03
MMPOLY3	-0.07	0.05
MMPOLY4	-0.24	0.05

Changes in layer thickness result in differences in the vertical spacing of the final device dimensions, as shown in Figure 4-1. The thickness of the structural polysilicon layers have an obvious impact on the final device dimensions, however the thickness of the sacrificial oxide layers plays an important role in determining the intermediate spacing of the structural layers. The linewidth variations of the polysilicon layers also contribute to the final fabricated dimensions of a given geometry being different from the nominal, designed values. Figure 4-2 shows that changes in any of the dimensions can result in a final geometry that is different from the nominal design, which affects the size, shape, volume, and mass of the device.

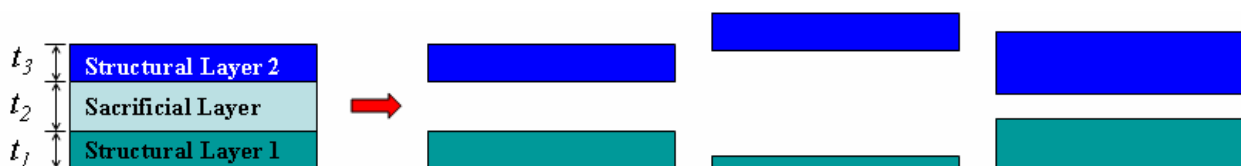


Figure 4-1. Fabrication tolerances can changes the thicknesses of the layers, resulting in changes in the final geometry dimensions.

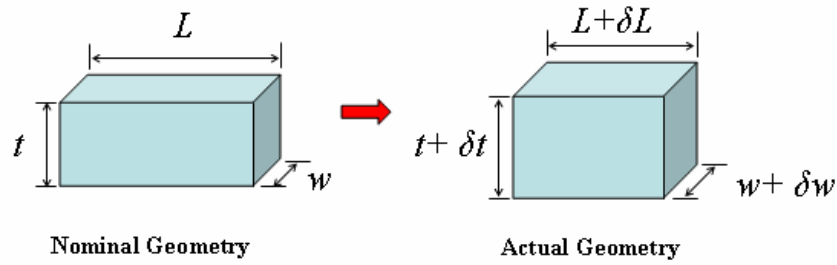


Figure 4-2. Fabrication tolerances can change the dimensions of a fabricated geometry, affecting the final shape, volume, and mass.

The mass for the micromirror array devices can be estimated from the volume of the moving components, which are the mirror surface and the moving comb fingers. The nominal dimensions for these components are shown in Figure 4-3. Once the fabrication tolerances are considered, it becomes clear that the mass of these parts will be affected by the changes in the geometry. Calculating the volume and multiplying by the density of polysilicon (2331 kg/m^3), the nominal mass of these components is $2.34 \times 10^{-11} \text{ kg}$.

The mechanical spring constant is affected by changes to the geometry of the spring and variations in the Young's Modulus. The electrostatic model is also affected by these changes. The following sections will examine the effects of the dimensional tolerances on the performance of the devices using the modeling methods developed in Chapter 3. First, the

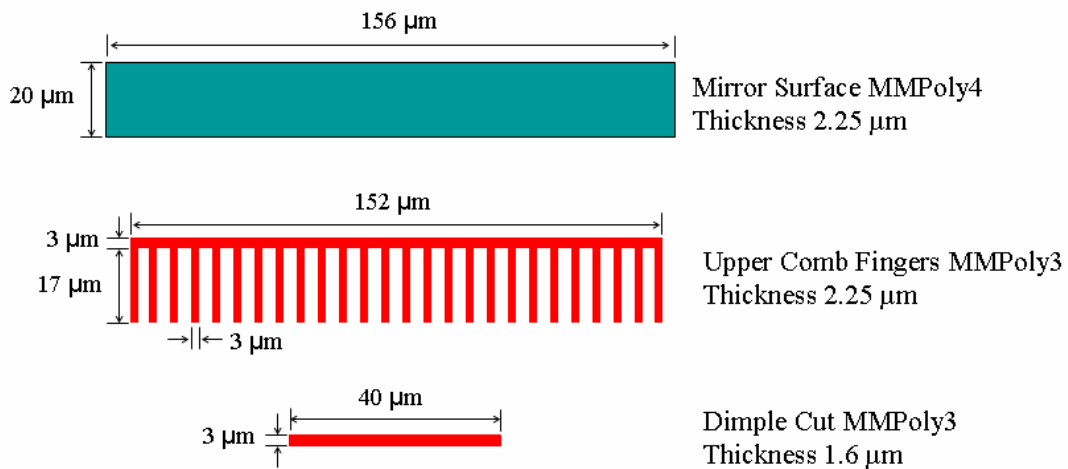


Figure 4-3. Nominal dimensions used to calculate the volume of the moving mass.

contributions of each individual parameter variation are considered to try to identify the effect of any given parameter on the final device performance. Through sensitivity analysis, it can be determined which key parameters have the most effect on the final device performance. Because these variations can occur in any combination with each other, there are an exceedingly large number of possibilities. Therefore, in order to understand the effects of these fabrication variations on the device performance, Monte Carlo simulations are done to give an idea of the combined effects of multiple parameter variations.

4.1.1 Effects of Individual Parameter Variations

To understand the effects of a single parameter variation on the system, the device performance is determined using the modeling methods developed in Chapter 3 as only one parameter is allowed to change at a time. There are fourteen parameter variations to be considered, and they include ten variations in layer thickness listed in Table 4-1, three linewidth variations listed in Table 4-2, and one material property variation for the Young's modulus of polysilicon. A change in a single parameter can cause both the mechanical spring constant and the electrostatic capacitance to change from the nominal model. First, the effects on the mechanical model are examined, followed by the electrostatic.

The mechanical model described in Section 3.4.1 is a spring in which the stiffness is determined by the dimensions of the beam members, as well as the material properties of Young's modulus and Poisson's ratio. Recall that the main structural element of the spring is a set of two thin beams constructed in the MMPoly1 layer, which was shown in Figure 3-7. The length of this beam and the cross-sectional area are the most critical dimensions for determination of the beam stiffness. Therefore, the dimension variation in the thickness of the MMPoly1 layer is considered, as well as uncertainty in the Young's modulus as calculated by Jensen et al. to be $164.3 \text{ GPa} \pm 3.2 \text{ GPa}$ [97]. Poisson's ratio is still assumed to be a constant at

0.22 as there is no available data to suggest that it varies. Table 4-3 shows the effects of changing the MMPoly1 thickness as well as the Young's modulus on the value of the spring constant.

While there is no data given in the SUMMiT V design manual [6] regarding line width variations for MMPoly1, it is possible that this variation does occur. The layers MMPoly1 and MMPoly2 are most often used together to create one thicker, laminate layer of polysilicon, therefore, diagnostic data is only collected for MMPoly1/2 laminate [98]. As an additional study, analysis is done here for cases in which line width variations for MMPoly1 are considered to be equal to those of MMPoly2, as $80 \text{ nm} \pm 30 \text{ nm}$. This analysis is also included in the results of Table 4-3.

The first entry in Table 4-3 is the nominal model value, and each subsequent value of the mechanical spring constant, k_m , is compared to this value in terms of the percent change. When only the thickness of layer MMPoly1 and the Young's modulus are considered, the spring constant is found to vary between -1.95% to 5.66% from the nominal spring constant. By

Table 4-3. Spring stiffness values for changing dimensional and material parameters.

Layer Thickness MMPoly1 μm	Young's Modulus, E GPa	Change in Linewidth MMPoly1 μm	Spring Stiffness, K_m pN-m	% change from nominal
1.0000	164.30	0.00	612.35	0.00
1.0200	164.30	0.00	634.72	3.65
1.0223	164.30	0.00	637.33	4.08
1.0177	164.30	0.00	632.12	3.23
1.0000	167.50	0.00	624.28	1.95
1.0000	161.10	0.00	600.43	-1.95
1.0200	167.50	0.00	647.03	5.66
1.0200	161.10	0.00	622.36	1.63
1.0200	164.30	0.08	730.98	19.37
1.0200	164.30	-0.08	546.91	-10.69
1.0000	164.30	0.08	706.55	15.38
1.0000	164.30	-0.08	526.56	-14.01

considering the effects of variations in the linewidth of MMPoly1, the resulting spring constants are found to vary significantly from -14.01% to 19.37% from the nominal value. From this it is clear that including the effects of linewidth variation can have a significant effect on the spring constant. As stated previously, there is no available recorded data to indicate that linewidth variations do occur in MMPoly1. However, it is reasonable to assume linewidth variations do exist for MMPoly1 as these variations are present in all other layers. For the remaining analysis in this section, linewidth variations in MMPoly1 will be omitted from consideration and are only included here to demonstrate that these errors can have a very large impact on structural stiffness.

In the case of the mechanical spring constant, there are only a few parametric variations to consider. As the capacitance for the device is dependent upon the geometric spacing of the device components, the electrostatic model will be affected much more by any changes in layer thickness or in linewidth. To see the effects of the individual parameters, electrostatic analysis was done for each of the thirteen structural parameters in which each parameter was allowed in turn to be increased by a value of its standard deviation as listed in Tables 4-1 and 4-2.

The results are shown in terms of the capacitance in Figures 4-4, 4-5, and 4-6. Figure 4-4 shows the capacitance function for changes in the thickness of the polysilicon structural layers, MMPoly0, MMPoly1, MMPoly2, MMPoly3, and MMPoly4. The nominal capacitance function is shown for a comparison using the nominal dimensions of the device. It is evident that making changes individually to these parameters has little effect on the electrostatic model for the device. Figure 4-5 shows the capacitance function for changes in the thickness of the Dimple3 backfill, and the sacrificial oxide layers Sacox1, Sacox2, Sacox3, and Sacox4. In the case of Sacox3, it is clear that this parameter alone plays a significant role in determining the

electrostatic characteristics of the micromirror. Sacox3 is the sacrificial layer that determines the spacing between the fixed comb fingers in layer MMPoly2, and the moving comb fingers in layer MMPoly3. Figure 4-6 shows the capacitance functions calculated for changing the area dimensions of the device in the linewidths of layers MMPoly2, MMPoly3, and MMPoly4. The capacitance curve does deviate some from the nominal model for these parametric variations, particularly in MMPoly2.

This analysis is extended to see the combined electromechanical effect of the parametric variations in terms of the static displacement curves. Figure 4-7, 4-8, and 4-9 show these results. Figure 4-7 shows the θ - V curves for the micromirrors when the structural polysilicon layers are each varied. The results here are similar to the results for the capacitance function in Figure 4-4, in that changes in these parameters do not appear to have a significant affect on the device performance. It is worth noting however that the layer thickness of MMPoly1 does have a slight effect on the altering the systems static behavior and this is because the layer MMPoly1 plays a significant role in determining the mechanical spring stiffness. Figure 4-8 demonstrates the sensitivity of the micromirror to variations in the thickness of Sacox3, similar to that seen in the capacitance function of Figure 4-5. Likewise, Figure 4-9 shows small deviations in the static displacement curves when the linewidths of the polysilicon layers are changed. It is clear that some parameters have a larger effect on the final static performance of the device, most prominently is Sacox3. Parametric sensitivity analysis is another way to examine how sensitive the modeled system is to variations in a given parameter. Sensitivity, S , can be defined as the percent change in the output of the system divided by the percent change in the parameter of interest, a . In this case, the output of the system can be considered as the voltage required to achieve a desired position, θ . That is,

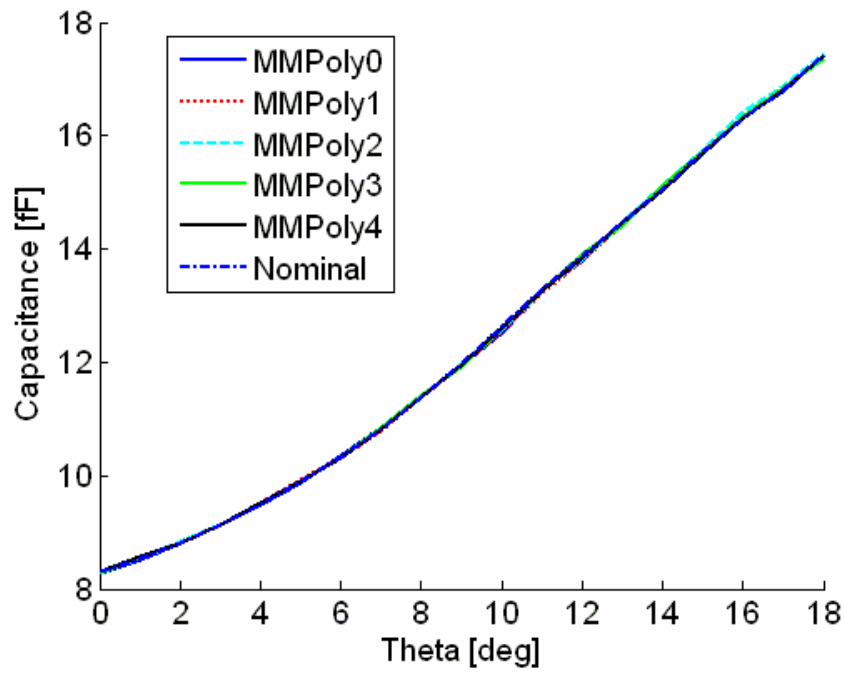


Figure 4-4. Capacitance functions for the electrostatic model with parametric changes in the layer thickness of the structural polysilicon.

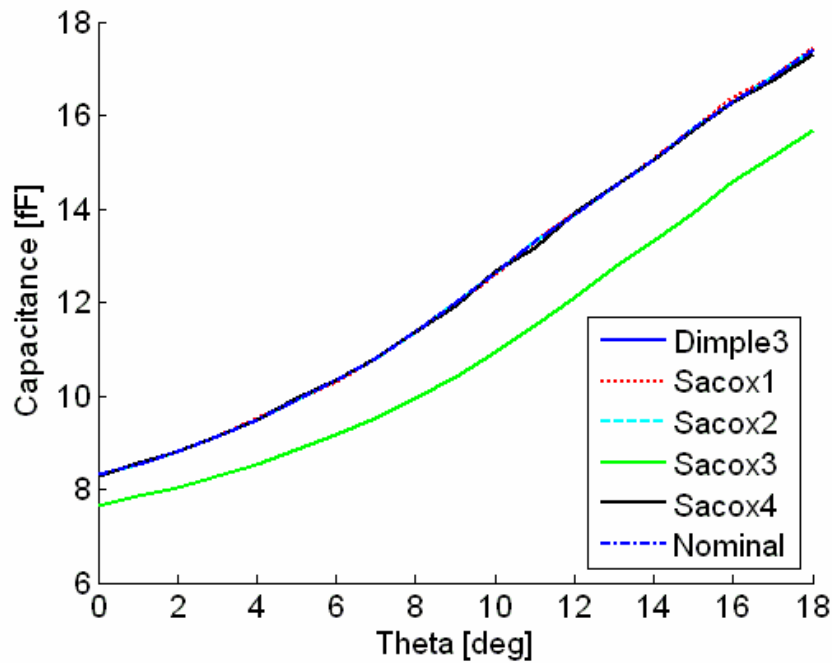


Figure 4-5. Capacitance functions for the electrostatic model with parametric changes in the layer thickness of the Dimple3 backfill and the sacrificial oxide.

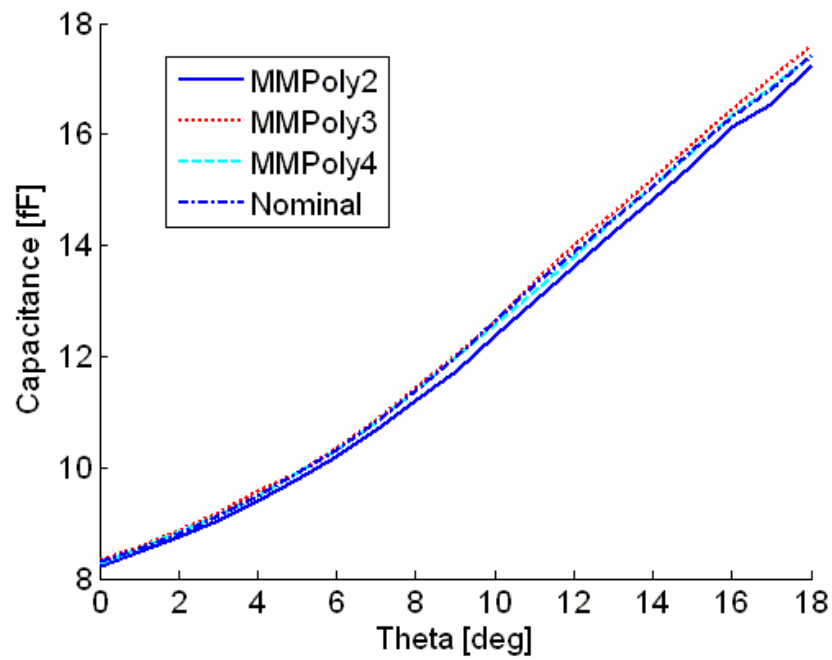


Figure 4-6. Capacitance functions for the electrostatic model with parametric changes in the linewidth error of the structural polysilicon layers.

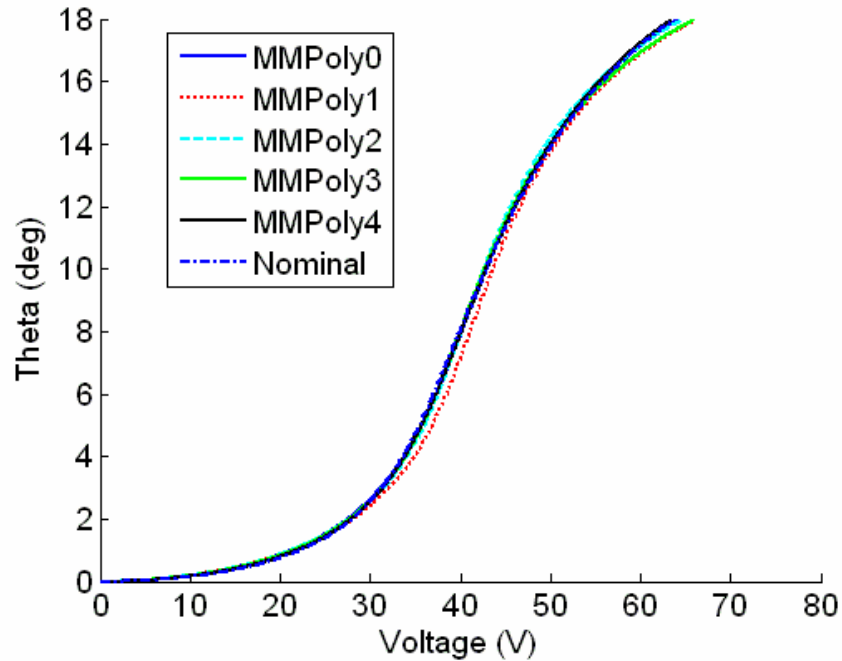


Figure 4-7. Static displacement relationships for the micromirror model with parametric changes in the layer thickness of the structural polysilicon.

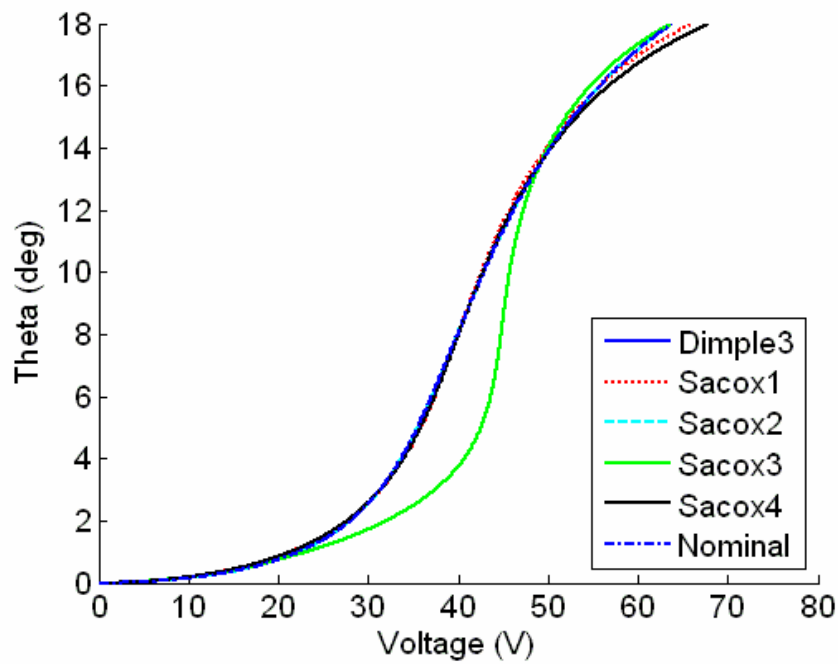


Figure 4-8. Static displacement relationships for the micromirror model with parametric changes in the layer thickness of the Dimple3 backfill and the sacrificial oxide.

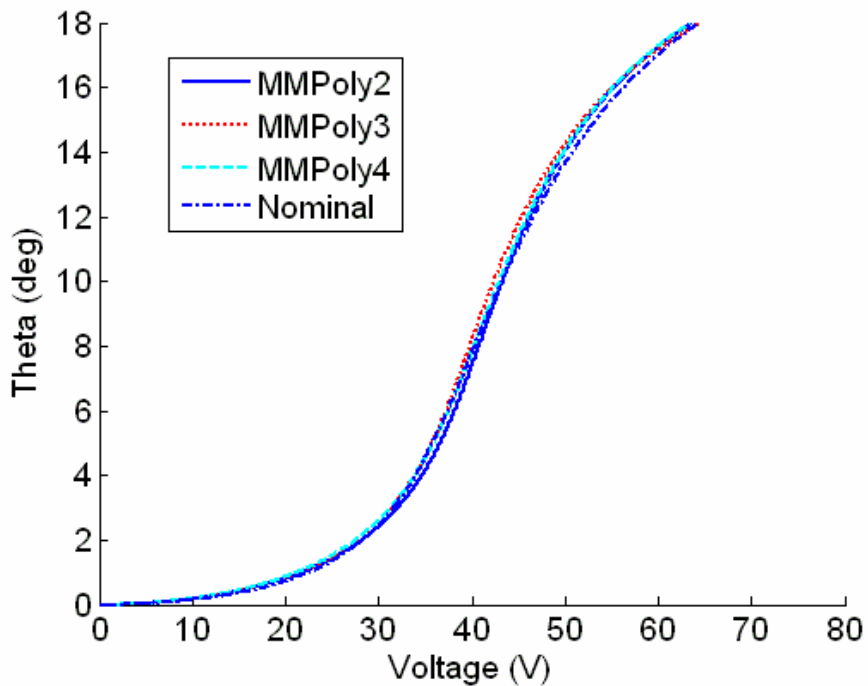


Figure 4-9. Static displacement relationships for the micromirror model with parametric changes in the linewidth error of the structural polysilicon layers.

$$S = \frac{\left| \frac{\Delta V(\theta)}{V_{nom}(\theta)} \right|}{\left| \frac{\Delta a}{a_0} \right|} = \frac{\left| \frac{V_a(\theta)}{V_{nom}(\theta)} - 1 \right|}{\left| \frac{a}{a_0} - 1 \right|} \quad (4-1)$$

where S is the sensitivity with respect to parameter a , $V_a(\theta)$ is the voltage required to achieve a position of θ for a model with a variation in parameter a , a_0 is the nominal value of the parameter, and $V_{nom}(\theta)$ is the voltage required to achieve a position of θ for the nominal model.

Figure 4-10 displays the sensitivity of the system to changes in line widths. The same analysis for variations in layer thickness is given in Figure 4-11. The four parameters with the highest sensitivities are the thicknesses of layers MMPoly1, Sacox1, Sacox3, and Sacox4. Variations in the parameters Dimple3 backfill and Sacox2 have the lowest sensitivities; nearly zero for the entire range of motion. This analysis reveals which geometric parameters in the device design are expected to be the most sensitive to the changes in dimensions from fabrication tolerances. This kind of analysis can also be very useful during the design stage of a new device as it can be used in conjunction with optimal design methods to reduce the effects of parametric uncertainty on the operation of the completed device. However examination of the individual parametric effects will only reveal a partial understanding of the effects of the fabrication tolerances on device performance, and it is therefore beneficial to consider the effects on the system when multiple fabrication errors are present. This is done in the following section using Monte Carlo simulations.

4.1.2 Monte Carlo Simulations

As in the previous section, there are fourteen different parameters of interest in this analysis, and performing the model analysis for every possible combination of parametric variation would be a very large and time-consuming task. Each of these parameters is assumed to vary within a Gaussian distribution defined by the mean and standard deviation information

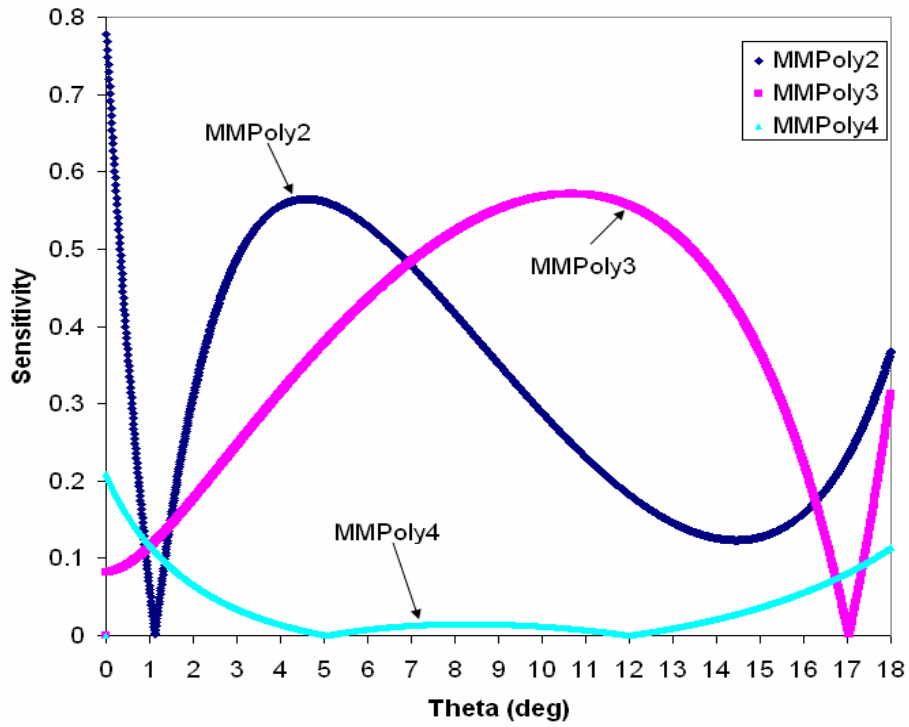


Figure 4-10. Sensitivity of voltage with respect to changes in line width for each value of θ .

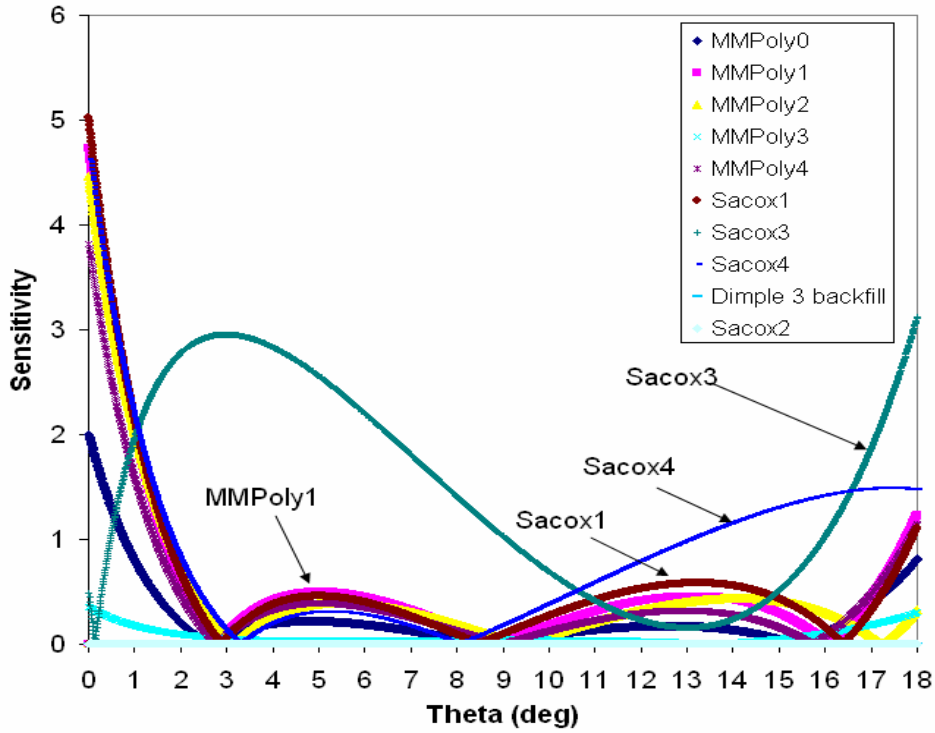


Figure 4-11. Sensitivity of voltage with respect to changes in layer thickness for each value of θ .

from the fabrication data in Tables 4-1 and 4-2, and from the studies on material properties in [97]. Monte Carlo simulations provide an effective method for examining the effects of these parametric uncertainties by randomly choosing values from the Gaussian distribution and running a large number of model simulations. In the analysis here, 250 simulations are done. From these 250 sets of randomly generated Gaussian parameters, the effects of the fabrication tolerances on the system performance can be determined. The histograms for each parametric variable are shown in Appendix B to show the distribution of each variable generated in the simulations. The histogram of the resulting mass that is calculated for each of the 250 sets of variables is also shown in Appendix B.

It is possible that the fabrication tolerances could have some systematic correlations, such as all of the polysilicon layers for a given fabrication run having thicker layers at the same time. As there is no data to support this idea however, it can only be assumed that each parameter is allowed to vary independently from the others. A Gaussian, or normal, distribution is given by the following expression [109]

$$G_{X,\sigma}(x) = \frac{1}{\sigma\sqrt{2\pi}} e^{-(x-X)^2/2\sigma^2} \quad (4-2)$$

where X is the mean value of the data set, σ is the standard deviation, and x is the data being measured. The Gaussian distribution for a set of data with a mean of zero and a standard deviation of one is plotted in Figure 4-12. This figure also illustrates that 95% of the values of x fall between -1.96 and 1.96, which is considered the 95% confidence interval for this distribution. This is also very close to falling between -2σ and 2σ , which constitutes 95.45%.

Using the randomly generated variables, it is possible to analyze the impact of these fabrication variations on the mechanical spring constant. First, this is done for the case in which only the layer thickness of MMPoly1 and the Young's modulus are allowed to vary. The

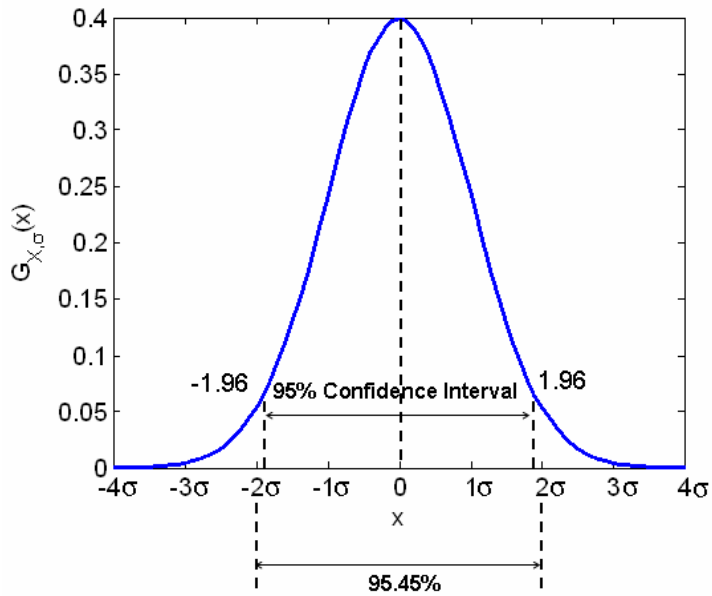


Figure 4-12. Gaussian distribution with a mean of 0 and standard deviation of 1.

resulting spring constants, k_m , had a mean of 634.21 pN-m and a standard deviation of ± 12.17 pN-m. Using twice the standard deviation ($\pm 2\sigma$) to represent the 95% confidence interval (CI) for the mechanical stiffness values, one can say that there is a 95% chance that the mechanical stiffness will fall between the values of 609.87 pN-m and 658.55 pN-m. This corresponds to a variation in the mechanical spring stiffness of $\pm 3.84\%$ from the mean.

It was shown previously in Table 4-3 that if the linewidth of MMPoly1 is allowed to vary by the same level of uncertainty as the MMPoly2 linewidth, there is a significant impact on the spring constant. Repeating that analysis here for the 250 Monte Carlo simulations but this time mechanical spring constant results for each analysis respectively. The effect of the MMPoly1 linewidth variation is included here to once again show the large effect this variable has on the mechanical spring stiffness, however the MMPoly1 linewidth variation will not be considered in the remaining analyses.

The Monte Carlo simulations are conducted on the electrostatic model as well, using the same set of 250 randomly generated variables that are used in the mechanical spring constant

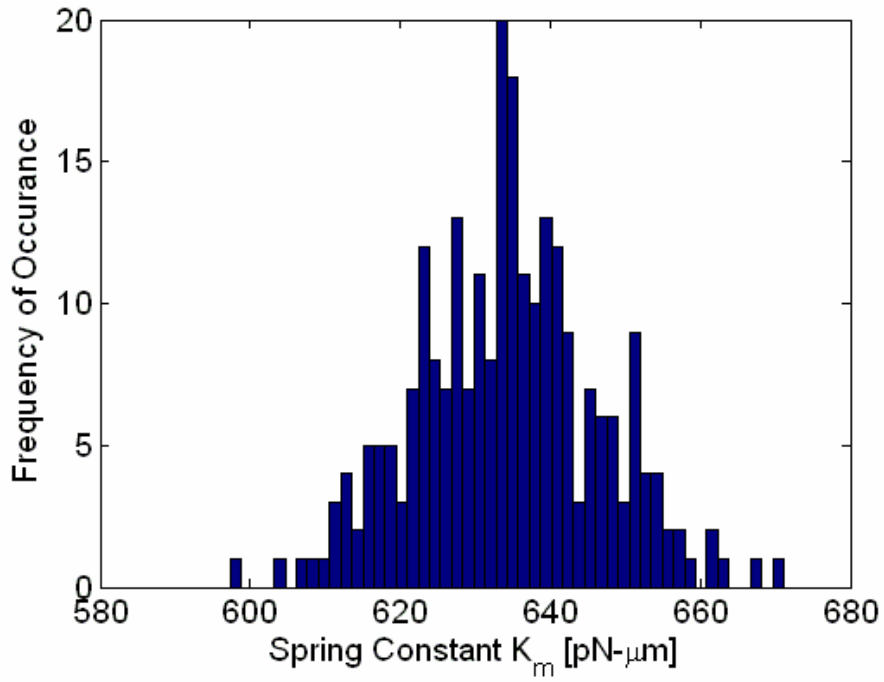


Figure 4-13. Histogram for mechanical stiffness when accounting for variations in thickness of MMPoly1 and Young's modulus.

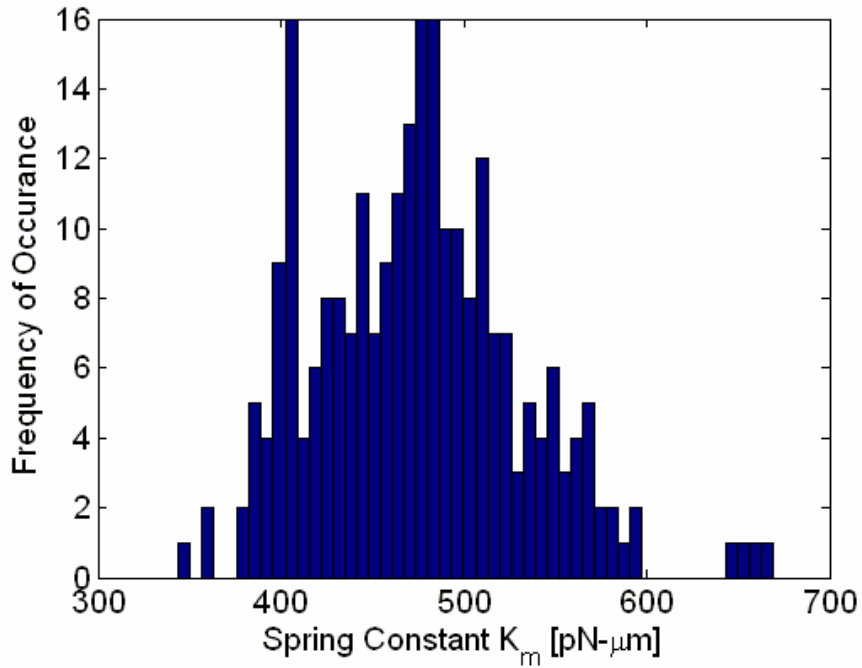


Figure 4-14. Histogram for mechanical stiffness taking into account variations in thickness of MMPoly1, Young's modulus, and linewidth of MMPoly1.

analysis. These variables are kept consistent throughout this analysis to ensure the results will be accurate when the electrostatic and mechanical simulation results are combined. As was seen in the above analyses, the structural polysilicon layers affect the device dimensions, and the sacrificial oxide layers affect the spacing of the geometry in the Z-direction. The capacitance function is affected by both these changes in dimensions. Material properties do not play a role in the electrostatic analysis. Figure 4-15 shows the results of the calculated capacitance functions for 250 simulations using randomly chosen sets of variables. In order to classify the capacitance simulation results in terms of the mean and standard deviation, it is necessary to look at the capacitance values calculated at each value of theta and determine the mean and standard deviation at each point. This is done in Table 4-4, and the 95% confidence interval values for capacitance vary from $\pm 18.47\%$ at zero degrees of rotation and $\pm 27.83\%$ at eight degrees of rotation.

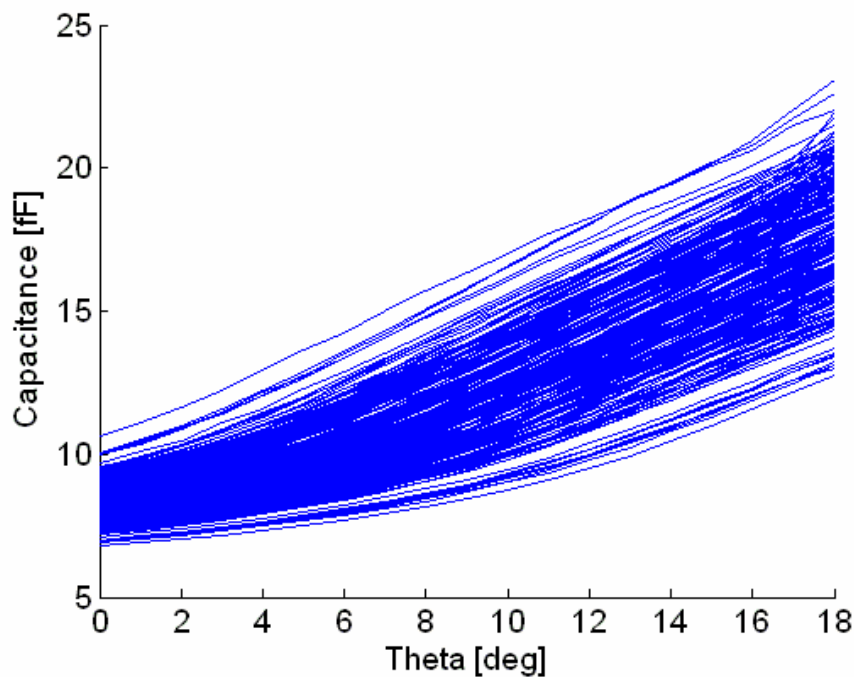


Figure 4-15. Results from the capacitance simulation for 250 random variable sets that show the effects of parametric uncertainty on the electrostatic model.

Table 4-4. Results from the Monte Carlo simulations for the capacitance values in terms of mean, standard deviation, and the percent change from nominal.

Theta (deg)	Mean Capacitance (fF)	St. Dev. (fF)	± % change (95% CI)
0	0.0005	4.73E-05	18.47
1	0.0285	0.0028	19.65
2	0.0295	0.0031	20.81
3	0.0306	0.0034	22.16
4	0.0318	0.0037	23.58
5	0.0331	0.0041	24.88
6	0.0346	0.0045	26.06
7	0.0363	0.0049	26.92
8	0.0381	0.0052	27.59
9	0.0399	0.0056	27.81
10	0.0419	0.0058	27.83
11	0.0440	0.0061	27.61
12	0.0461	0.0063	27.11
13	0.0483	0.0065	27.10
14	0.0504	0.0065	25.88
15	0.0526	0.0066	25.26
16	0.0547	0.0068	24.72
17	0.0570	0.0072	25.31
18	0.0592	0.0078	26.30

Taking the results of the mechanical and electrostatic analyses together gives a picture of the overall effect that parametric fabrication errors can have on the system performance in terms of the θ - V profile. Figure 4-16 shows the results of doing this for the 250 simulations using the randomly chosen variables. Given the large number of possible combinations of dimensions that affect both the mechanical and electrostatic models, using 250 samples may not be enough to give a complete statistical representation of all the numerous possible combinations; however it is sufficient to show trends in the model predicted results. These results are compared to experimental characterization data in Section 4.2.

It is evident from these results that the parametric uncertainty that arises from the fabrication process alone can have a significant performance effect on the static displacement behavior of the micromirrors. Because the variable sets used in these simulations are randomly generated, it is difficult to obtain a sense for the role that each individual parameter, or even combinations of parameters have on the overall performance of the micromirrors. Recall from

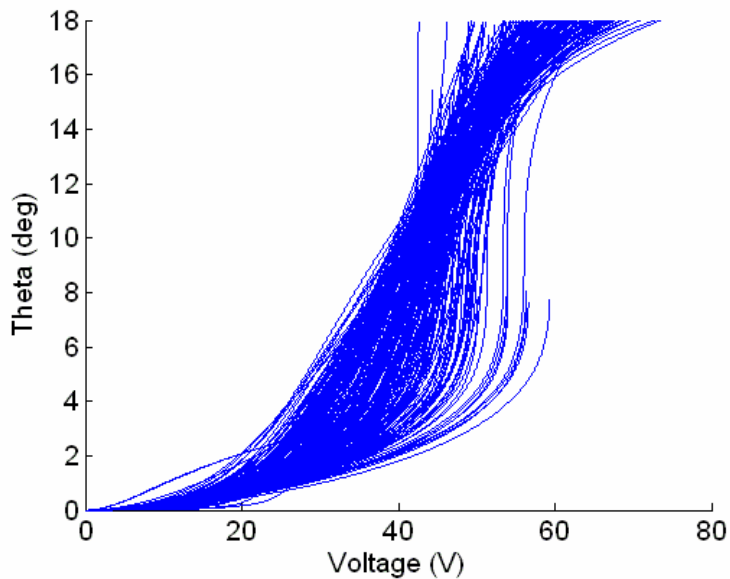


Figure 4-16. Static displacement results of 250 Monte Carlo simulations with random Gaussian distributed dimensional variations.

the sensitivity analysis in Section 3.5.1 that some variables had a significantly larger effect on the system performance, most notable the layer thickness of Sacox3. To understand the impact this particular variable had in the results from the Monte Carlo simulations, it is possible to try to isolate the contribution from Sacox3 by first considering only the results that occur for large deviation in Sacox3 thickness. Figure 4-17 shows the histogram of the Sacox3 values used in the Monte Carlo simulations. The values in blue correspond to those that lie within the 95% confidence interval. The values in red represent the other 5% of values that fall at the extreme ends of the distribution. Figure 4-18 shows the simulation results for the θ - V profiles that are colored to correspond to the values of Sacox3 thickness. The lines in blue are the results that correspond to Sacox3 values within the 95% confidence interval, while the lines in red are the results from the parametric variations that lie outside this interval. This gives a clear indication that for extreme differences in the Sacox3 thickness, the resulting θ - V profile will also have the most extreme behavior. This analysis was done for additional variables to try to determine a

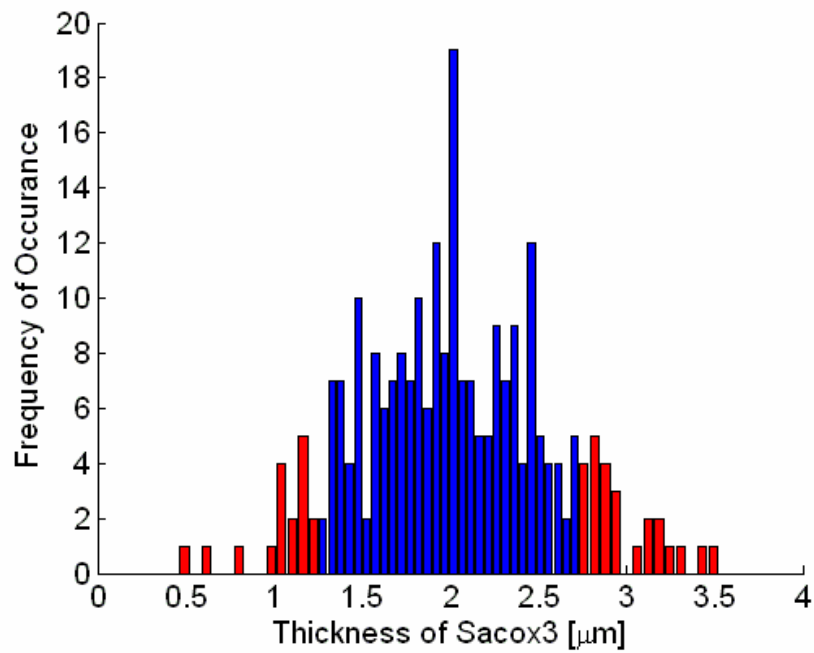


Figure 4-17. Histogram of values from the Monte Carlo simulations for the layer thickness of Sacox3. Values in blue lie within the 95% confidence interval, and values in red lie without.

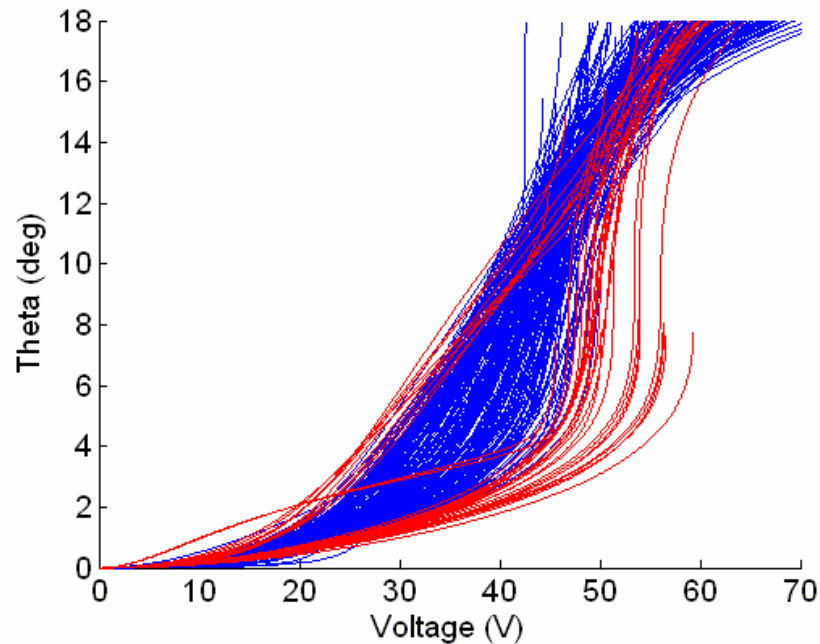


Figure 4-18. Static displacement curves from the Monte Carlo simulations that indicate the effect of large variations in the Sacox3 layer thickness. Curves in blue have Sacox3 values that lie within the 95% confidence interval, and lines in red have Sacox3 values that lie in the remaining 5% of the distribution.

pattern of contributions; however the results for the other parameters did not show any detectable correlations to the performance. This same analysis for the variables of linewidth in MMPoly2, thickness of MMPoly1, and thickness of Sacox4 are included in Appendix B. Changes in each of these variables show a cluster of profiles in the middle region of the randomly generated θ - V profiles, which is the opposite of the impact of changes to Sacox3.

4.2 Experimental Characterization

This section presents experimental characterization and validation of the models developed in the preceding sections. Static characterization measurements for the micromirror device were taken using a WYKO NT1100 Optical Profiler to determine the θ - V profiles for the mirrors [101]. This measurement tool is able to make measurements of out-of-plane deflections as the micromirrors are given different actuation signals. This information can be used to determine how variable the θ - V profiles are for mirrors within the arrays, and from one array to another. Measurements were taken with the system in static mode, in which the voltage is applied at different values, returning to zero voltage between each deflection measurement. Static measurement results are provided for the arrays of micromirrors described, as well as for a set of single micromirrors that are not part of an array. These results are compared to the model predictions, validating the results of the model in determining the static performance, and pull-in behavior. The experimental results taken from different micromirrors across three different arrays demonstrate significant differences in behavior among them. This further illustrates the presence of parameter variations within a given array as well as between arrays of the same device design.

4.2.1 Equipment Description

The WYKO NT1100 optical profiling system uses interferometric measurements to determine the out-of-plane measurements of a surface. The working principle of the instrument

is shown in Figure 4-19. Light travels from the light source and is divided by a beam splitter. One beam is sent to the reference mirror of the Mirau interferometer, and the other beam is directed onto the measurement sample. The reflections of the two beams are recombined into one beam, and because they have traveled different distances in their respective paths, they are no longer in phase. Thus, the newly recombined beams form interference fringes which are recorded by an optical detector array. The digital information from the detector is processed to determine the surface measurement of the sample.

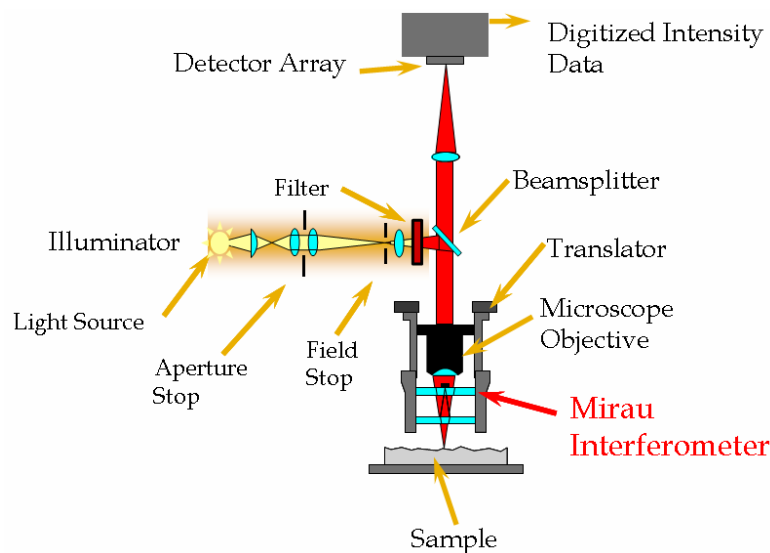


Figure 4-19. Diagram of an optical profiler measurement system.

The optical profiling system is able to take measurements in static mode, in which the MEMS device is not in motion when the measurement is taken, as well as in dynamic mode, capturing the motion of the device under excitation. The surface measurements are recorded into a database, specified by the user, and an example of a surface measurement taken for the micromirror arrays is shown as a 3D image in Figure 4-20. This image shows six mirrors from the array, four of which are tilted by an applied actuation voltage of 60 V. The two mirrors in the center are left without any actuation, and this arrangement proves useful as these mirrors can become a zero reference from which the other measurements are taken. While the data for the

tilted mirrors is recorded into a database, it is also possible to review each individual measurement that has been taken. This is helpful to ensure that the data is recorded accurately, and gives insight into how the angular tilt measurement of the mirrors is determined. The data can be reviewed using WYKO SureVision software, which accompanies the optical profiling system. This program allows the user to examine 3D images, such as that in Figure 4-20, as well as look at cross-sections of the data. Figure 4-21 shows a cross section of the micromirror data

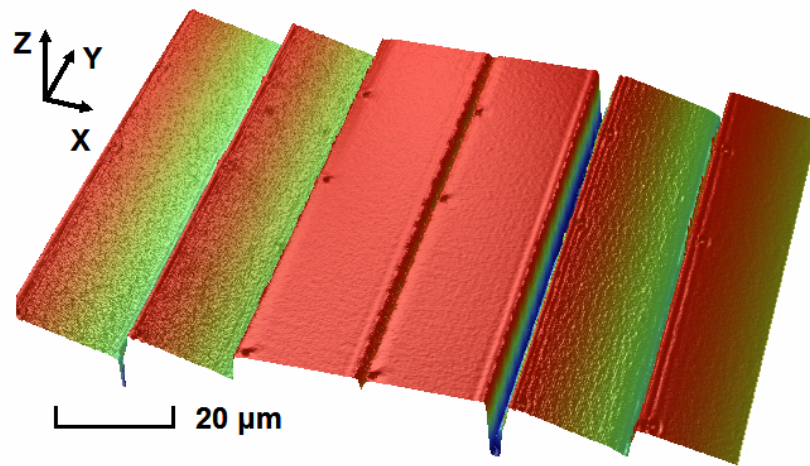


Figure 4-20. Six mirrors from the micromirror array measured with the optical profiler system. In which the four tilted mirrors appear as diagonal lines. The tilt angle measurement is determined from the displacement measurements in the vertical, out-of-plane, Z-direction, and the horizontal, in-plane X-direction. Thus, the angle of tilt is found from the tangent relationship of the X and Z measurements. Any measurement errors in X or Z will result in an error in the angle measurement as well. This error will be discussed in more detail in the following sections. Figure 4-21 also shows an example of a measurement in which the profiling system failed to properly record the data. This illustrates the difficulties encountered in obtaining these measurements, as the micromirrors are actuated to very large angular displacements that are more difficult for the system to record. A poorly constructed data record such as the one shown

in Figure 4-21 is too sparse to be relied upon for a measurement and should be discarded.

Unfortunately, these incomplete and sometimes erroneous records are sometimes recorded into the database files. For this reason, each of the data records has been individually examined and verified to ensure the most accurate of measurement results.

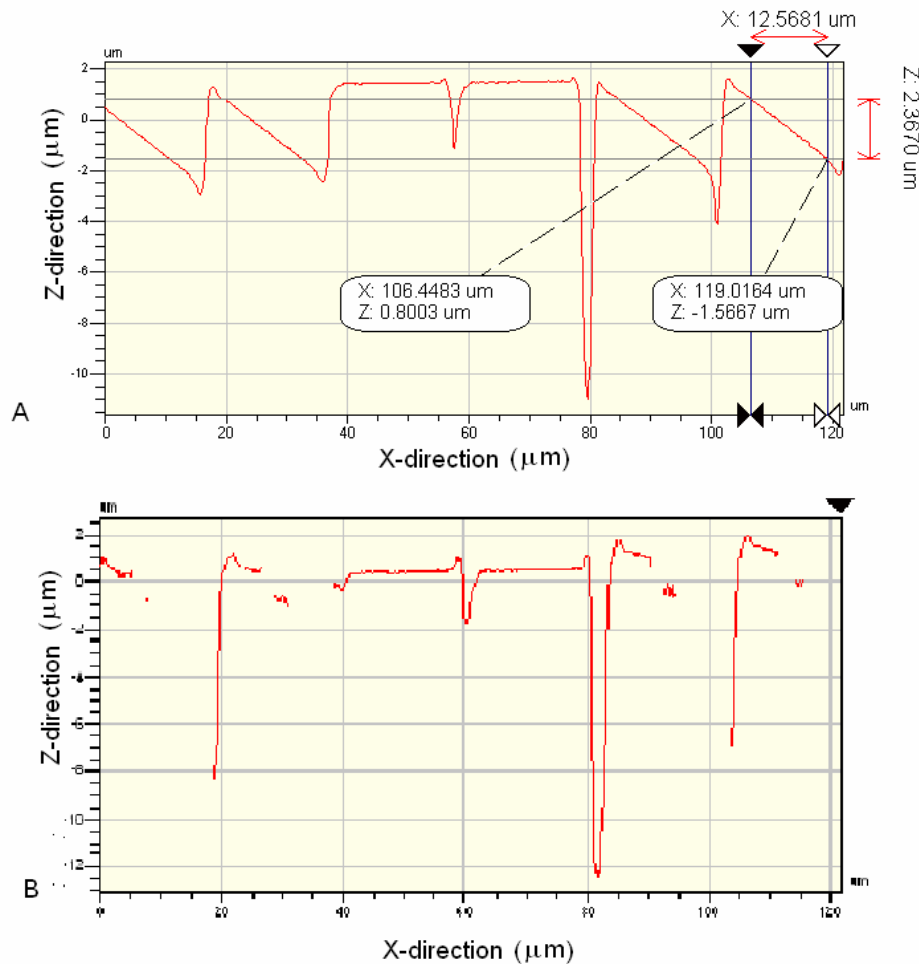


Figure 4-21. Data records from the SureVision display that show the cross-section profile of the tilt angle measurements. A) An example that clearly shows the cross-sectional measurements. B) An example of a poorly recorded data file that cannot be used.

4.2.2 Static Results for Single Micromirrors

To validate the single micromirror models, a set of single micromirrors were fabricated and analyzed. These mirrors, shown in a micrograph in Figure 4-22, were characterized in the static mode of testing, in which voltages are reset to zero for each measurement, using a WYKO

NT1100 optical profiler at Sandia National Laboratories. In Figure 4-22, the square bond pad on the left is $100 \times 100 \mu\text{m}^2$ and the micromirror on the right has dimensions $156 \times 20 \mu\text{m}^2$. The results from these single mirrors are shown in Figure 4-23. It is clear that the pull-in point for this set of experimental data is similar to the data collected on the arrays, and the pull-in angle, 13.87° , is at the lower range of the pull-in angles for the arrays of mirrors. The pull-in voltage is 71.5 V, similar to the values for the micromirror arrays and very close to the predicted value. At the time this data was recorded, the calibration and resolution of the machine were not recorded; therefore it is not possible to discuss the specific errors that are associated with this data. However, the standard operation of the WYKO NT1100 is supposed to be on the order of nanometers.

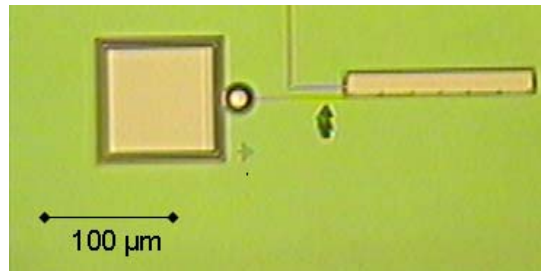


Figure 4-22. Micrograph image of a single micromirror.

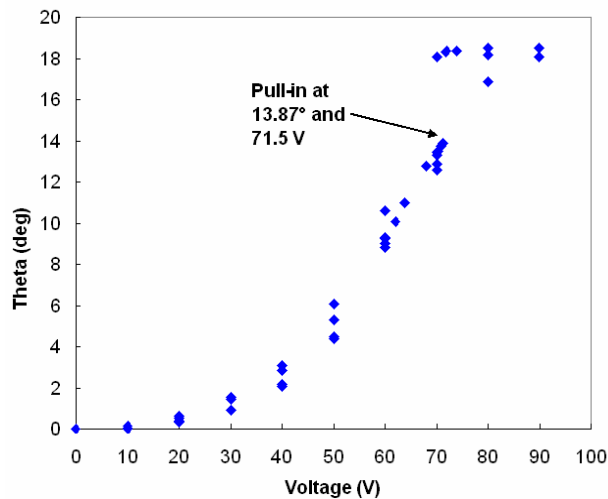


Figure 4-23. Experimental static results taken from individual micromirrors that are not in an array.

4.2.3 Static Results for Micromirror Arrays

Experimental data on the performance of the micromirror arrays was acquired using a WYKO NT1100 Optical Profiler located at the Veeco company offices in Chads Ford, PA. This machine was calibrated to a National Institute of Standards and Technology (NIST) traceable standard to be accurate to one-half of one percent (0.5%) of an 82 nm step. This corresponds to height measurements accurate to 0.410 nm. As the tilt angle measurements are determined from the inverse tangent of the Z over the X measurement, shown above in Figure 4-21, this amount of error in the Z-direction corresponds to an error in the tilt angle measurement of $\pm 0.0235^\circ$. This amount of error is too small to even demonstrate on the plots of the data as error bars. While the measurement equipment is believed to operate true to its calibration standards, there is evidence from researchers in [112] that this optical profiling system may be subject to larger errors. Measurements of the θ - V profile for micromirrors taken from different sections across the array for three different micromirror arrays were taken. These results were obtained using the static mode of measurement in which the voltage signal is reset to zero between each measurement. The approximate locations of data collection for all three arrays are shown in Figure 4-24 and these locations are labeled. These areas were chosen to try to gain an understanding of any changes in the performance across the array.

Shown in Figures 4-25, 4-26, and 4-27, data from 5 different areas (consisting of four mirrors actuated and two mirrors for reference) on the arrays from among the 3 arrays reveals that there is considerable variation in the behaviors of the individual mirrors. Each array consisted of 416 mirrors arranged in 32 rows and 13 columns. Data was collected from different areas in the arrays in order to examine how the micro performance varies in different locations within the array. Table 4-5 gives a summary of the pull-in angle and voltages for the data. The

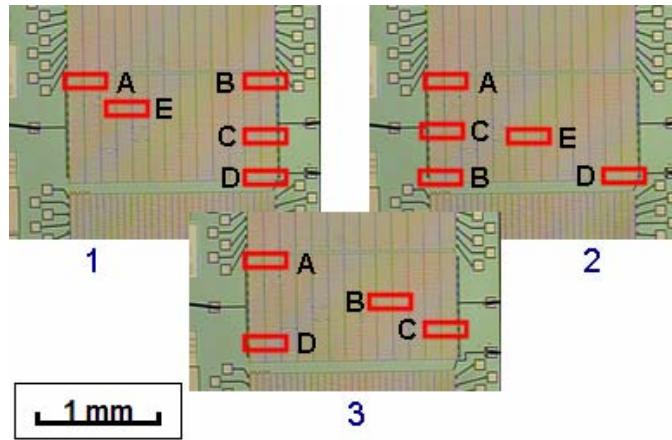


Figure 4-24. Approximate locations of data collection on all three arrays.

average pull-in angles for arrays 1, 2, and 3 are 14.27° , 13.54° , and 15.89° , respectively. While these values do not agree exactly with the predicted pull-in value of 16.5° from the analytical model, the lowest value is within 20 percent. Also, the values listed in Table 4-6 are averaged values over multiple data sets. From Figures 4-25 through 4-27, it is evident that in many cases the mirrors did experience pull-in very close to the predicted angle of 16.5° . The pull-in voltages

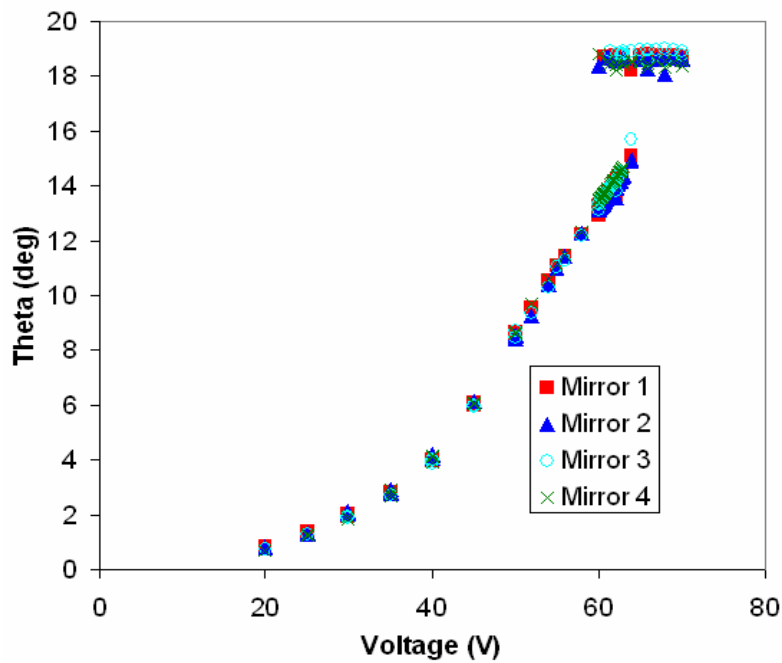


Figure 4-25. Experimental results from array 1, area A.

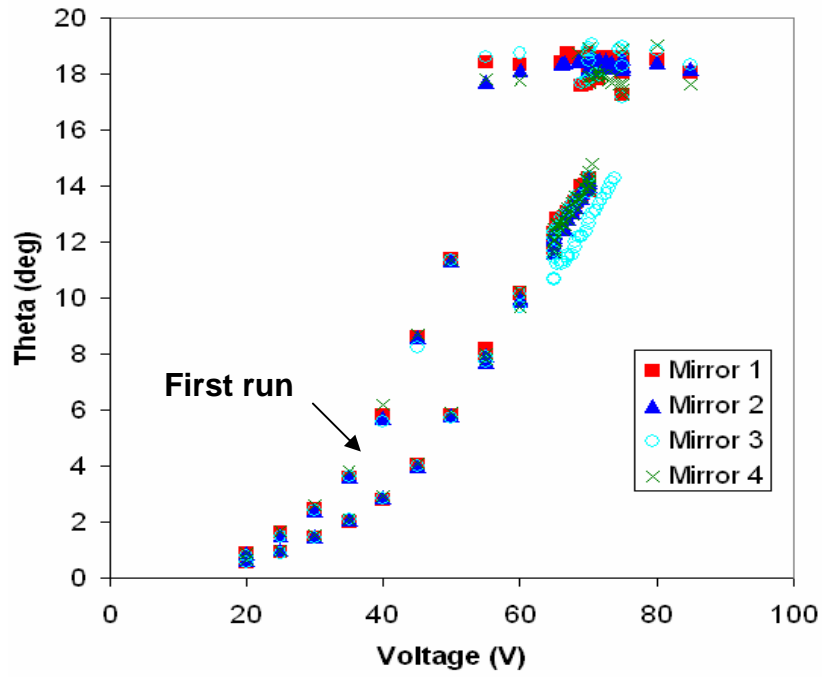


Figure 4-26. Experimental results from array 2, areas D and E.

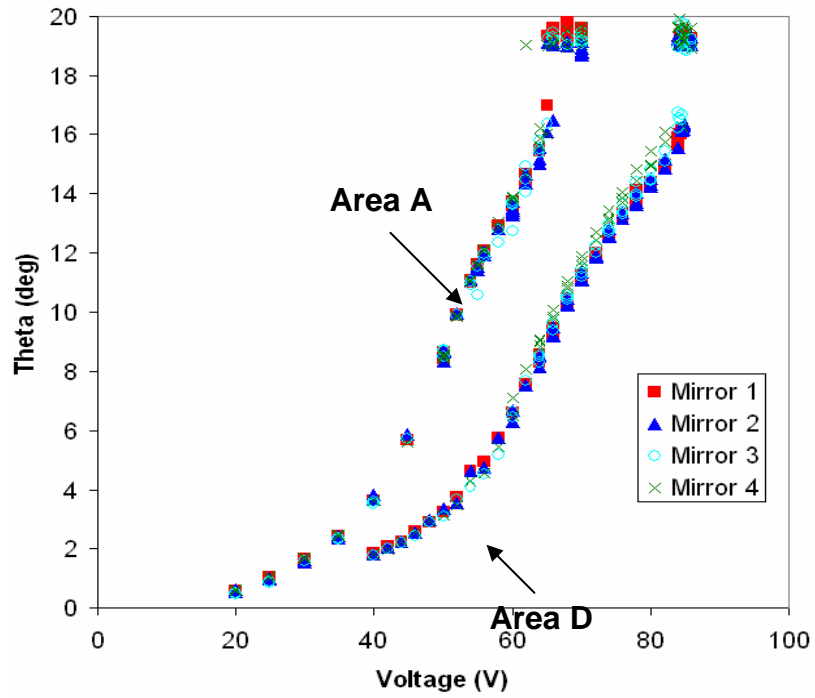


Figure 4-27. Experimental results from array 3, areas A and D.

Table 4-5. Mean and standard deviation for pull-in angle and voltage from sets of mirrors on all three arrays tested.

Array #	Area	θ_{PI} (Deg)		V_{PI} (V)	
		Mean	St. Dev.	Mean	St. Dev.
1	D	14.27	0.85	62.27	1.75
2	E	13.93	0.62	68.81	2.57
2	D	13.15	0.88	67.17	2.31
3	A	15.89	0.53	64.4	0.62
3	D	15.88	0.49	83.53	1.17

for arrays 1, 2, and 3 are 62.27 V, 67.99 V, and 73.96 V, respectively. It should be noted that for array 3, there is a large difference in the pull-in voltage observed at two different locations on the array. Compared to the predicted pull-in voltage of 71 V, these values are within 12 percent.

Measurements on the mirrors in these experiments were often conducted such that tests were performed repeatedly on the same set of micromirrors before changing the location of data collection, or switching to a different array. It was observed during the experiments that after a device had sat idle without actuation voltage applied, the devices behaved differently when actuated for the first time, as opposed to subsequent measurements taken on the same mirrors directly afterward. The likely reason for this is a charging effect that occurs after the first actuation of the device after it has sat idle for some time. Figure 4-26 shows this occurred for array 2 when multiple sets of data were taken.

Figure 4-28 shows the data from all three devices together along with the model predicted behavior of the device using the nominal model geometry of the micromirror design presented in Section 3.4.3. The nominal geometry refers to the dimensions of the micromirror based on the original design, not considering any fabrication-induced variations. It is clear that the nominal model falls close to the middle of the widely scattered experimental results. Section 4.1.2 presented the results of the electromechanical model for 250 randomly varied sets of dimensional and material parameters. These modeled variations are compared to the experimental data in

Figure 4-29, and it is evident that the experimental values fall mostly within the bounds of the modeled variation results.

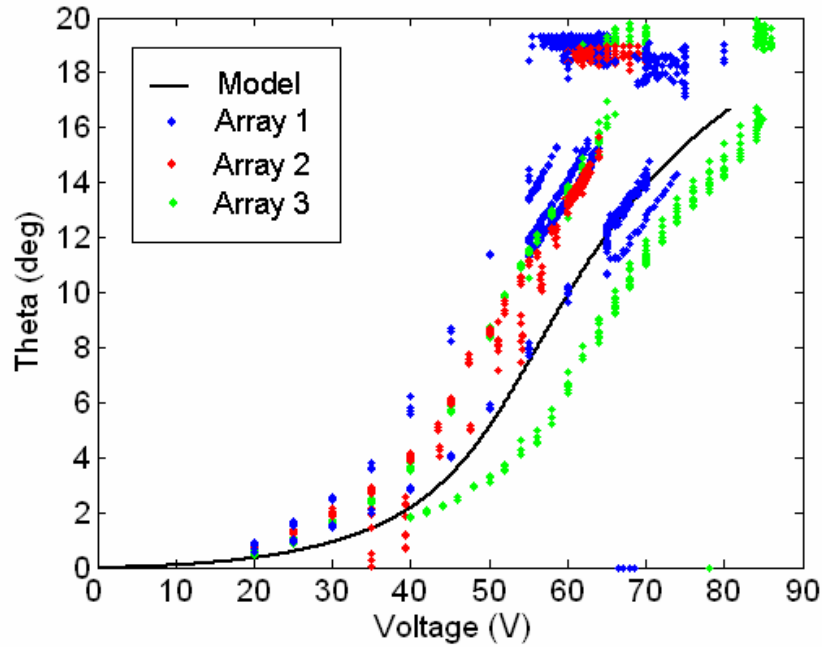


Figure 4-28. Nominal model with experimental data.

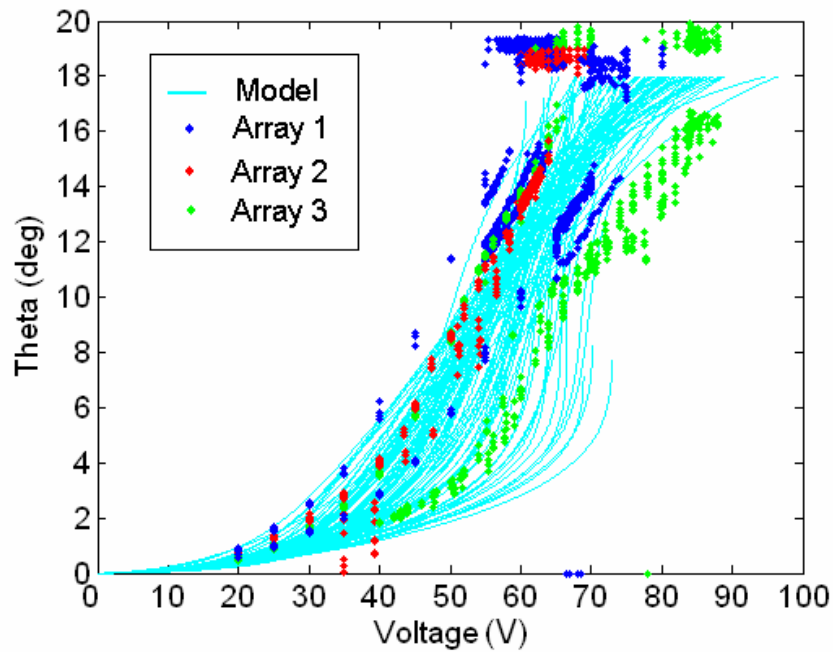


Figure 4-29. Model-predicted results from 100 simulations with parameters determined by random Gaussian variations, shown with experimental data.

The model results were calculated based on known fabrication tolerances, but this alone does not entirely explain the variations in the device performances. Fabrication variations are known to occur across the wafer as well as from one process batch to the next, but it is not definitively known if large variations occur locally such that they can have significant effect on the micromirrors within each array. The experimental data presented above showed variations between results for different areas in array 3. This indicates the presence of fabrication variations across the array. However within each area on the array, the group of mirrors exhibited relatively small differences in their results until their individual pull-in voltages. In addition, the differences in the pull-in voltage could indicate that the mechanical stiffness used to calculate the modeled value is different from the actual stiffness values of the micromirrors. While it is not completely known the causes of these differences in performance, it is apparent from the data that considerable performance variation can occur.

The effects of fabrication variation on the performance are best illustrated by the case of Sacox3, which was shown in Figure 4-8 to have a significant effect on the θ -V profile, causing it to deviate outward to the right of the other curves. This same behavior is seen again in the Monte Carlo simulation results of Figure 4-18 in which those cases with large variations of Sacox3 outside the 95 percent confidence interval. Upon comparison of the of the Monte Carlo simulation results and the experimental results in Figure 4-29, it is seen that the experimental results do not exhibit behavior that is consistent with that of very large Sacox3 variations. This suggests that in the fabrication of these particular micromirror arrays, a large variation of the Sacox3 layer thickness did not occur. Plots included in Appendix B study the effects of large variations in the linewidth of MMPoly2, and the layer thickness of MMPoly1 and Sacox4. These plots did not indicate a clear connection between the Monte Carlo simulation results and

the effects of these three fabrication errors; therefore it is not possible to make a conclusion from the experimental results as to the presence or magnitude of fabrication errors in these three variables. To do so properly would require diagnostic data regarding the exact layer thicknesses and linewidth errors collected for a given array of micromirrors, and this data is not available here.

4.3 Chapter Summary

This chapter continues the electromechanical device modeling for the micromirrors that was developed first in Chapter 3, and expands the analysis to include the effects of fabrication tolerances on the performance of the micromirrors. By looking at the individual contributions of particular parameters, it is evident that the layer thickness of Saco3 has the largest effect on the static displacement behavior for the micromirrors. The other parameters appear through sensitivity analysis to also play less distinct roles when considered individually, but when multiple parametric uncertainties are considered, the overall effect of the fabrication variations is evident. Monte Carlo simulations are conducted to examine the effects of parametric uncertainties, and this reveals the full extent to which the precision of the micromachining process can dictate performance.

The micromirror modeling is then compared to static experimental characterization data that was collected using an optical profiler that is capable of making non-contact displacement measurements. The results are reported for some individual micromirrors tested at Sandia National Labs, and then additional results are given for the micromirror arrays tested on a separate measurement system at Veeco, Inc. From these measurements, the static equilibrium behaviors of the micromirrors is determined, as well as the pull-in angle, and pull-in voltage. Taking measurements at different location on three different micromirror arrays begins to show that there can be considerable variation in the performance. When these experimental results are

compared to the uncertainty modeling results, it reinforces the notion that this variation can be the result of microfabrication errors. While the manufacturers of the optical profiling system do claim a very high level of accuracy for measurements made using their equipment, recent studies of the machine conducted by Mattson show that the measurements can be susceptible to larger errors [112]. It is not known if the measurements taken for the micromirror devices are in fact showing larger deviations in the data due to this kind of measurement error. This type of study would be valuable for future work.

CHAPTER 5
DYNAMIC MODEL AND HYSTERESIS STUDY

Previous results only considered the static performance of the micromirrors after they have reached a steady-state value. Here, the dynamics of the system are taken into consideration in order to examine the effects of natural frequency and damping on the time response of the system. Modal analysis and dynamic characterization are performed to determine the natural frequencies of the micromirror and the mode shapes. It becomes clear that parametric uncertainty in the micromirrors also affects the dynamic performance of these mirrors. Most notably, the effects of the uncertainty on the behavior of the electrostatic instability may be seen. In addition to modeling the pull-in and hysteresis behaviors of the open-loop system, a case study is presented for a progressive-linkage that can be applied to alter the stiffness of the system to avoid these undesirable behaviors.

5.1 Dynamic Model and Resonant Frequency Determination

It is convenient to rewrite the model dynamics in Equation 3-16 in terms of natural frequency, ω_n , and the damping ratio, ζ .

$$\omega_n = \sqrt{\frac{k_m}{J}} \quad (5-1)$$

$$\zeta = \frac{b}{2\sqrt{k_m J}} \quad (5-2)$$

Written in state-space form, the system is described as follows,

$$\begin{aligned} x_1 &= \theta \\ x_2 &= \dot{\theta} \end{aligned} \quad (5-3)$$

$$\begin{Bmatrix} \dot{x}_1 \\ \dot{x}_2 \end{Bmatrix} = \begin{bmatrix} 0 & 1 \\ -\omega_n & -2\zeta\omega_n \end{bmatrix} \begin{Bmatrix} x_1 \\ x_2 \end{Bmatrix} + \begin{Bmatrix} 0 \\ \frac{1}{2J} \frac{dC}{dx_1} V^2 \end{Bmatrix}$$

From the linearized dynamic model discussed in Section 3.4.4 using a first order polynomial approximation for the capacitance function, the derivative of the capacitance is a constant.

Therefore, the natural frequency of the lumped-parameter model determined from Equation 5-1 is found to be approximately 188 kHz.

As stated previously in Section 3.4.5, the squeeze-film damping coefficient is difficult to predict analytically for this model, and based on values from similar devices in [71], the damping ratio is assumed to be approximately 0.3. The damping ratio has a significant effect on the open-loop performance of the system, as seen in Figure 5-1 for damping ratios ranging from 0.1 to 1.

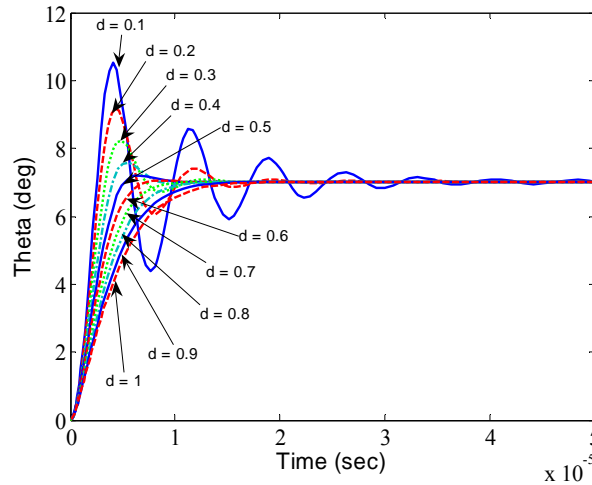


Figure 5-1. Open-loop nonlinear plant response to a step input of 7 degrees for different damping ratios.

5.1.1 Modal Analysis

In addition to using the lumped parameter model to estimate the natural frequency of the micromirror devices, modal analysis is done to determine the natural frequencies and the mode shapes. The analysis is performed for an undamped system, and the equation of motion expressed in matrix notation is

$$[M]\{\ddot{u}\} + [K]\{u\} = \{0\} \quad (5-4)$$

where M and K are the mass and stiffness matrices, respectively, and u is the displacement vector. Free harmonic vibrations of the structure are of the form

$$\{u\} = \{\phi\}_i \cos \omega_i t \quad (5-5)$$

where $\{\phi\}_i$ is the eigenvector representing the i^{th} natural frequency, ω_i is the i^{th} natural frequency (rad/s), and t is time. Substituting Equation 5-5 into 5-4 yields

$$\left(-\omega_i^2 [M] + [K]\right)\{\phi\}_i = \{0\} \quad (5-6)$$

Ignoring the trivial solution to Equation 5-6, which is $\{\phi\}_i = \{0\}$, then the following expression must be true.

$$\left|[K] - \omega_i^2 [M]\right| = 0 \quad (5-7)$$

Equations 5-6 and 5-7 form the eigenvalue problem, and the solutions are the natural frequencies, ω_i , and the eigenvectors $\{\phi\}_i$.

The participation factor is related to the eigenvector, and it identifies the amount each mode contributes to the total response in a particular direction [113]. A small participation factor means that an excitation in that direction will not excite the mode in that direction. A large participation factor indicates that the mode can be excited by motion in that direction. The participation factor can be used to determine the direction of motion in each mode that dominates the response. As defined in reference [99], the participation factor for the i^{th} mode, γ_i , is given by

$$\gamma_i = \{\phi\}_i^T [M] \{D\} \quad (5-8)$$

The vector D describes the excitation direction and is of the form

$$\{D\} = [T] \{e\} \quad (5-9)$$

where $\{e\}$ are the six possible unit vectors. $\{D\}$ is further described in terms of the individual excitations, D_i^a , for DOF j in direction a . The directions of excitation, a , can be either X, Y, Z, or rotations about these axes, ROTX, ROTY, ROTZ.

$$\{D\} = [D_1^a D_2^a D_3^a \dots]^T \quad (5-10)$$

The matrix $[T]$ is

$$[T] = \begin{bmatrix} 1 & 0 & 0 & 0 & (Z - Z_0) & -(Y - Y_0) \\ 0 & 1 & 0 & -(Z - Z_0) & 0 & (X - X_0) \\ 0 & 0 & 1 & (Y - Y_0) & -(X - X_0) & 0 \\ 0 & 0 & 0 & 1 & 0 & 0 \\ 0 & 0 & 0 & 0 & 1 & 0 \\ 0 & 0 & 0 & 0 & 0 & 1 \end{bmatrix} \quad (5-11)$$

in which X, Y, and Z represent the global Cartesian coordinates, and X_0 , Y_0 , and Z_0 are the global Cartesian coordinates of a point about which the rotation are done.

Modal analysis is performed for the micromirrors using the ANSYS finite element analysis software. The solid model of the structure is shown in Figure 5-2 and consists of the mechanical spring, the mirror surface and the moving comb fingers. The fixed comb finger electrodes may be ignored as they are not part of the moving structure. The structure is anchored to ground in all degrees-of-freedom at the base of the mechanical springs. This solid model is meshed with solid92 elements which have 3DOF at each node. The modal analysis is performed using the Block Lanczos method which is appropriate for large symmetric eigenvalue problems [99]. The results from the analysis give the first ten natural frequencies, as well as modal participation factors, listed in Table 5-1. The ratio of each participation factor to the largest participation factor value for a given direction is also listed in Table 5-1, in which a ratio of one indicates the mode that contributes the most to the response in that direction.

The mass calculated from the modal analysis is 2.44×10^{-11} kg. The mass result that was reported in Chapter 4 based on the volume of the moving geometry was 2.34×10^{-11} kg, which matches the ANSYS calculated result within 4 percent. The difference in these values arises from the inclusion of additional components in the ANSYS model that are not included in the volume calculation done in previously. These additional components include the mechanical spring and its supports.

The results of this analysis indicate that the first mode of vibration for the micromirror structure occurs at 84.74 kHz. This is considerably lower than the value of 188 kHz calculated in Section 5.1 where it was assumed that the micromirror acts only in one degree-of-freedom, rotating about the X-axis (ROTX). It is likewise assumed that the first natural frequency will occur in this rotational direction and be given by Equation 5-1. The results from the modal analysis for the first mode at 84.74 kHz do in fact show that the dominant direction of the response at this frequency is in the ROTX direction. This is determined by comparing the values of the participation factors for each direction for this mode and it validates the one-degree-of-freedom assumption for the model in Equation 5-3. The largest participation factor is $6.5E-05$ for the ROTX direction, and this is an order of magnitude larger than the next largest participation factor which occurs in the Z-direction. While it is verified that the primary motion for the first resonant frequency occurs in the ROTX direction, the modal analysis results reveal that the resonant motion is more complex than one degree-of-freedom motion and in fact, the first resonant frequency excites motion in both the X-axis (ROTX) and the Z-direction. The motion that occurs in the Z-direction will affect the compliance of the system, which will result in a different natural frequency than that predicted using Equation 5-1, which assumes one degree-of-freedom motion about the X-axis only. The spring stiffness results presented in Table

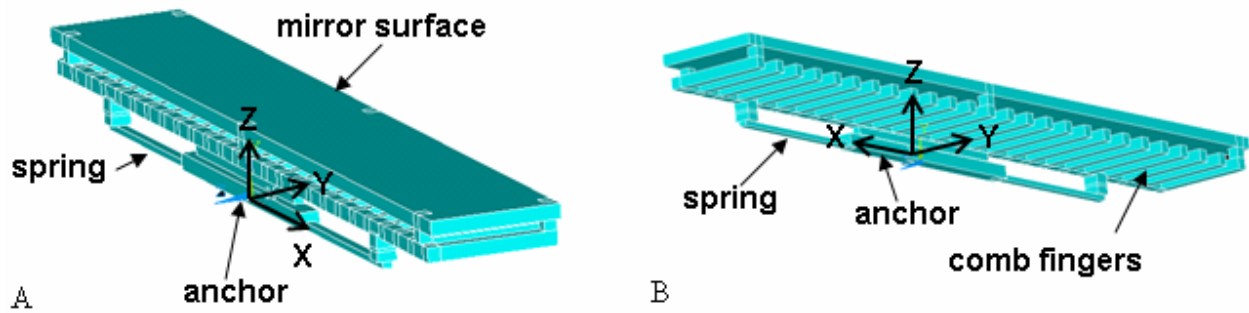


Figure 5-2. Solid model created for modal analysis. A) View of the top and back. B) View of the bottom showing the comb fingers.

Table 5-1. Modal analysis results for first 10 modes and their natural frequencies, and the participation factors and ratios for each direction.

Mode	Freq. (Hz)	X-Direction		Y-Direction		Z-Direction	
		Participation Factor	Ratio	Participation Factor	Ratio	Participation Factor	Ratio
1	84736.51	2.1183E-10	0.000087	2.7197E-06	0.758918	3.5955E-06	1.000000
2	120372.52	9.5920E-07	0.394546	8.8566E-10	0.000247	-4.3162E-09	0.001200
3	162970.10	-1.3215E-07	0.054358	3.5837E-06	1.000000	-3.0841E-06	0.857751
4	164493.10	8.3800E-07	0.344691	5.5914E-07	0.156023	-4.8219E-07	0.134109
5	391530.45	8.0827E-10	0.000332	1.7035E-06	0.475336	9.7970E-08	0.252526
6	1208580.00	4.6105E-08	0.018964	-2.2081E-08	0.006161	7.5056E-08	0.020875
7	1310412.38	-2.4312E-06	1.000000	-3.6331E-09	0.001014	2.7242E-09	0.000758
8	1610211.37	3.1366E-07	0.129016	5.4173E-08	0.015116	-3.3755E-09	0.000939
9	1696417.45	3.0772E-07	0.126574	2.2398E-08	0.006250	1.1384E-08	0.003166
10	1853628.28	-2.9854E-07	0.127970	1.9532E-07	0.054501	-1.2589E-08	0.003501

Mode	Freq. (Hz)	ROTX-Direction		ROTY-Direction		ROTZ-Direction	
		Participation Factor	Ratio	Participation Factor	Ratio	Participation Factor	Ratio
1	84736.51	6.4831E-05	1.000000	-8.7467E-08	0.000395	4.3414E-08	0.000197
2	120372.52	-1.9988E-08	0.000308	-2.2171E-04	1.000000	-1.5238E-05	0.069261
3	162970.10	9.4879E-06	0.146350	-9.8134E-07	0.004426	3.4382E-05	0.156274
4	164493.10	1.5072E-06	0.232480	7.3266E-06	0.033047	-2.2001E-04	1.000000
5	391530.45	-6.3384E-06	0.977690	-8.7374E-08	0.000394	-2.8728E-07	0.001306
6	1208580.00	1.3954E-07	0.002152	9.0970E-08	0.000410	-1.8579E-08	0.000084
7	1310412.38	2.7564E-08	0.000425	-3.4525E-06	0.015572	-3.1098E-06	0.014135
8	1610211.37	5.5281E-09	0.000085	-2.5788E-07	0.001163	8.3555E-06	0.037978
9	1696417.45	4.2753E-07	0.006595	1.0185E-07	0.000459	3.2656E-07	0.001484
10	1853628.28	4.5237E-08	0.000698	2.3618E-08	0.000107	-1.8531E-06	0.008423

3-3 previously show that the spring is very compliant in the Z-direction with a stiffness of 7.94 pN/m. This additional compliance will lower the overall spring constant for the mode and result in a lower resonant frequency that when only the rotational motion is considered. The evidence

of motion in additional degrees of freedom at resonance does not however invalidate the assumption that the mirror will rotate about the X-axis for excitations that occur below the resonant frequency. Furthermore, the electrostatic force that is applied to the micromirror is always an attractive force, drawing the moving electrode down toward the fixed electrode. Thus, if resonance is avoided, smooth rotational motion in one degree-of-freedom is still accomplished. This does, however, show the limitations of the 1DOF model assumption, which limits the analysis to only low frequency responses where resonant behavior may be avoided. Table 5-1 also includes the resonant frequencies and their participation factors for modes 2 through 10. It is noticed that several of the modes have motion that acts in more than one direction.

5.1.2 Dynamic Characterization

In addition to the lumped parameter estimation and the modal analysis results to determine the natural frequencies of the micromirrors, some experimental data was obtained using a Laser Doppler Vibrometer (LDV), courtesy of the Integrated Microsystems Group at the University of Florida. This device measures the velocity of a point on a device as it is excited over a range of frequencies. The excitation signal can be a swept sine wave, or chirp signal, or it can also be white noise, which will excite the device at all frequencies in the given range. Due to limited signal generation capabilities and time constraints, the excitation signal chosen for this experiment was an acoustic impulse, generated by firing a small cap-gun, which produces a loud noise. This effectively generates a white noise signal that can excite the microdevice, and the resulting velocity of the device is recorded by the LDV. Generating the pulse in this manner is simple and does not require signal generation; however the acoustic impulse is not guaranteed to be the same signal each time it is produced. This experiment was performed five times on each of the three micromirror arrays. Figure 5-3 shows an example of the time response of the micromirrors to the acoustic impulse taken for device 2, trial 1.

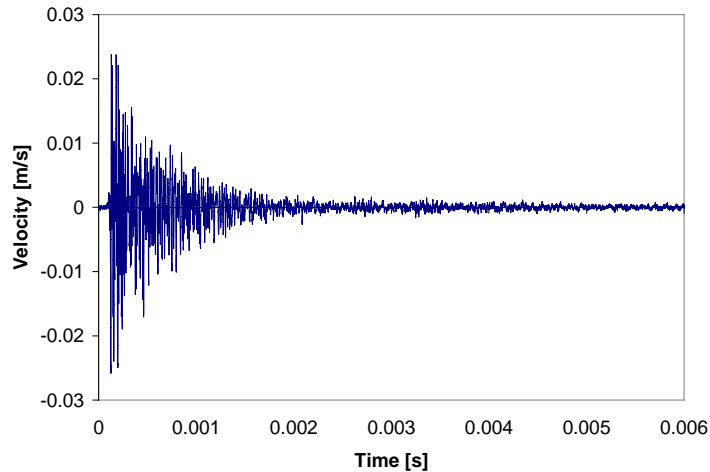
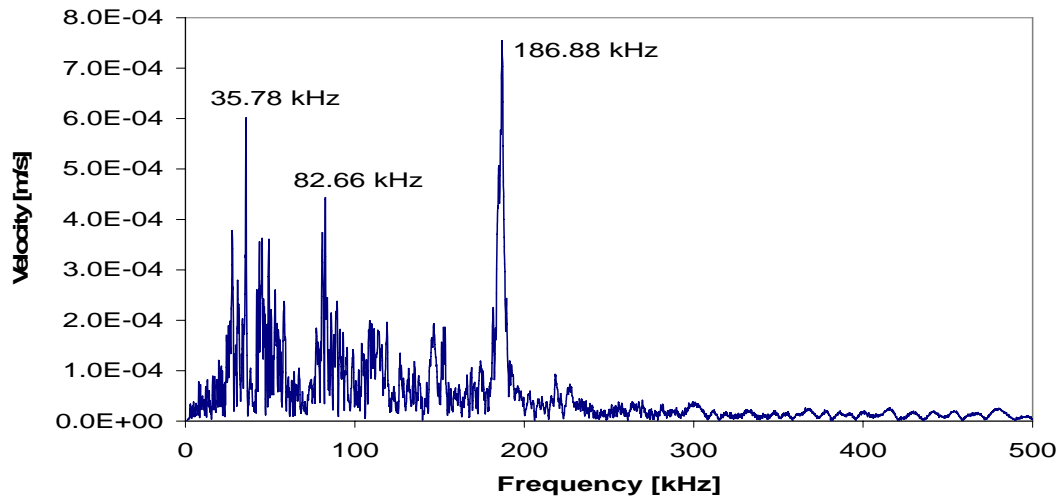
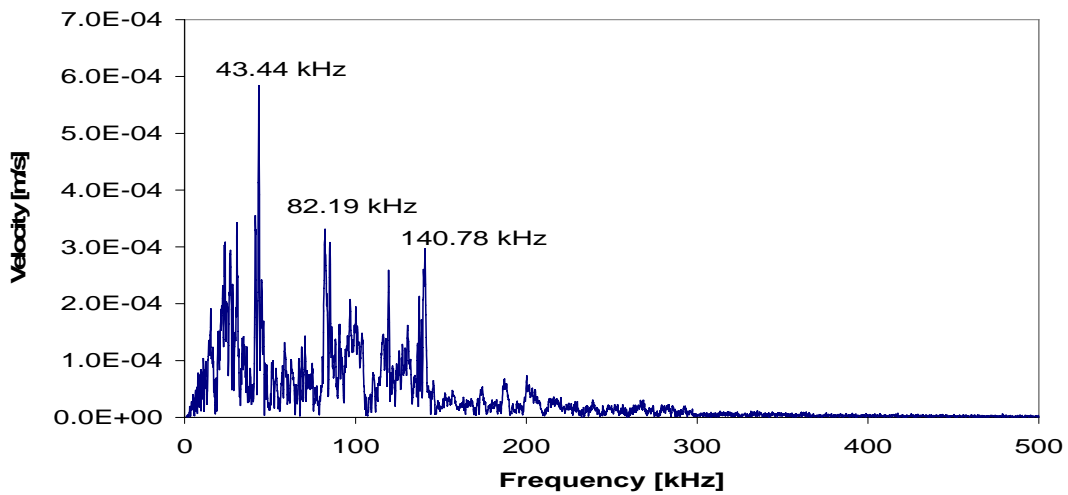


Figure 5-3. Time series data of the micromirror response to an acoustic impulse taken with a laser doppler vibrometer. This is the response of device 2, trial 1.

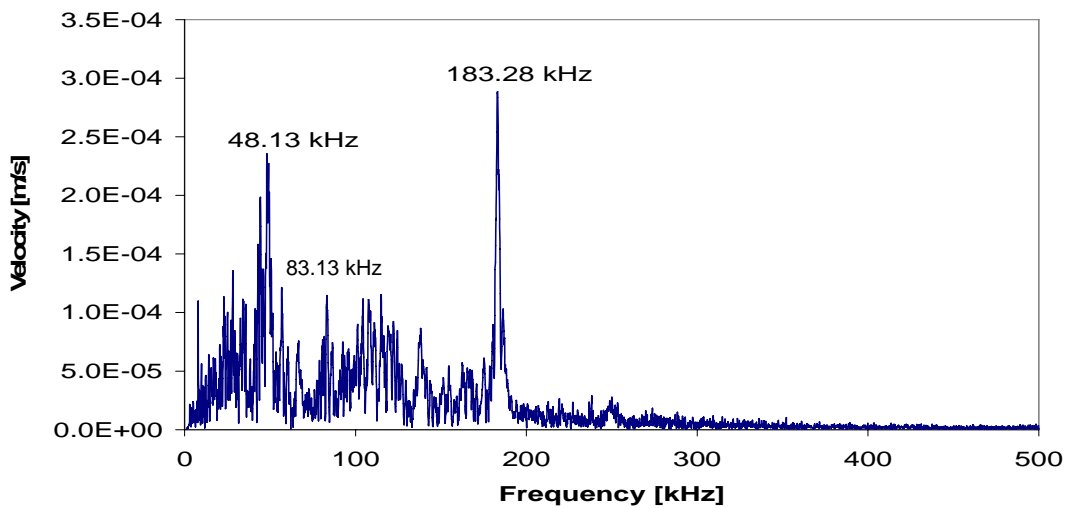
The time series data can be examined in the frequency domain by a Fast Fourier Transform (FFT) of the velocity of the micromirror surface. Dominant spikes in the FFT indicate a resonant frequency for the device. Figure 5-4 shows examples of the FFT results for several of the tests. It is clear from these results that there is considerable noise occurring in the measurements, the source of which has not been identified. As such, it can make it more difficult to identify which peaks are in fact resonant frequencies. The complete FFT results for each LDV measurement are given in Appendix C. In each of the measurements, there appear consistently to be three results that stand out. All of the measurements had a large resonant peak that occurred in the range of 40 kHz. A spike occurs in this frequency range for LDV measurements in which no impulse signal was given, and is therefore considered to be result of noise in the environment. This noise could be caused by another piece of laboratory equipment or system in the area, and unfortunately the cause was never identified. It is assumed that this frequency is not in fact a resonant behavior. The results are summarized for here in Table 5-2 for the two dominant resonant frequencies of each test, excluding the lower frequency 40 kHz range results. The next appearance of resonance that occurs throughout the LDV measurements occurs in the range



A



B



C

Figure 5-4. Results from the LDV experiment showing resonant peaks. A) Device 1, trial 4. B) Device 2, trial 1. C) Device 3, trial 4.

of 80 kHz and it is assumed that this is the first resonant mode. In this case, this validates the results obtained from the FEA modal analysis in which the first natural frequency was found to occur at 84 kHz. Higher frequency resonances occur in each of the measurements, showing that for devices 1 and 3, large responses occurring in the range of 180 kHz, and for device 2, near 140 kHz. These higher order responses are also consistent with the modal analysis results.

Table 5-2. The first three natural frequencies determined from the LDV experiment. Results from the linear model, using Equation 5-1, and the modal FEA are included for comparison.

Device	Trial	Frequency (kHz)	
		1st	2nd
1	1	81.41	186.88
	2	81.41	187.81
	3	81.71	187.03
	4	82.66	186.88
	5	81.56	187.19
2	1	82.19	140.78
	2	85.63	139.53
	3	85.31	136.56
	4	92.02	137.03
	5	85.31	136.10
3	1	80.91	182.34
	2	90.31	183.91
	3	81.41	180.63
	4	83.13	183.28
	5	83.28	183.28
Model Eq. 5-1		188.12	--
Modal Analysis		84.74	120.37

5.2 Open-Loop Step Response

The open-loop response of the system is determined by the actuation voltage signal that is given to the micromirrors. For open-loop operation, it is necessary to determine a calibration relationship between the desired angular position and the actuation voltage needed to achieve such position. This relationship is often determined experimentally. If variations in the devices due to fabrication tolerances or other system disturbances are present, then the calibration must

be performed for each separate micromirror device to ensure the correct calibration is obtained. This approach of individually calibrating each micromirror device is not practical or efficient. The effects of parametric uncertainty on the device performance using a given calibration are examined for the step response. The effects of pull-in and hysteresis are also examined.

5.2.1 Effects of Parametric Uncertainty on Step Response

To illustrate the effects of parametric uncertainty on the system, the open-loop response of the plant model is considered using different values of stiffness, k_m . Figure 5-5 shows the response to a step input command of 7 degrees (0.12 radians) for the nominal stiffness value, and for variations of $\pm 10\%$. To further illustrate this concept, all of the parameters in the system described in Equation 5-3 are subject to parametric variation, including the mass moment of inertia, J , the damping, b , the spring stiffness, k_m , and the electrostatic torque, T_e . If each of these parameters is allowed to vary by $\pm 10\%$ from the nominal value, there are a very large number of possible plants to consider. It is assumed that calibration is performed on the device for the nominal parameter values. Figure 5-6 shows the open-loop plant responses of the nonlinear plant model to a step input of 7 degrees of the system model for 50 randomly generated sets of parameters J , b , k_m , and T_e that are allowed to vary by $\pm 10\%$ of their nominal values. It is clear that with the presence of uncertainties, a step input to the open-loop plant will result in steady-state error in the response. In order to correct for this in open-loop operation, the system must be carefully recalibrated for each device to ensure the proper response is achieved.

5.2.2 Effects of Pull-in and Hysteresis on Open-Loop Response

Electrostatic instability and hysteresis can also greatly affect the system response in open-loop operation. Recall from the discussion in Section 3.3, that pull-in occurs when the electrostatic force generated by the actuator exceeds the mechanical restoring force of the structure, causing the mirror to be pulled down to the substrate at its maximum displacement.

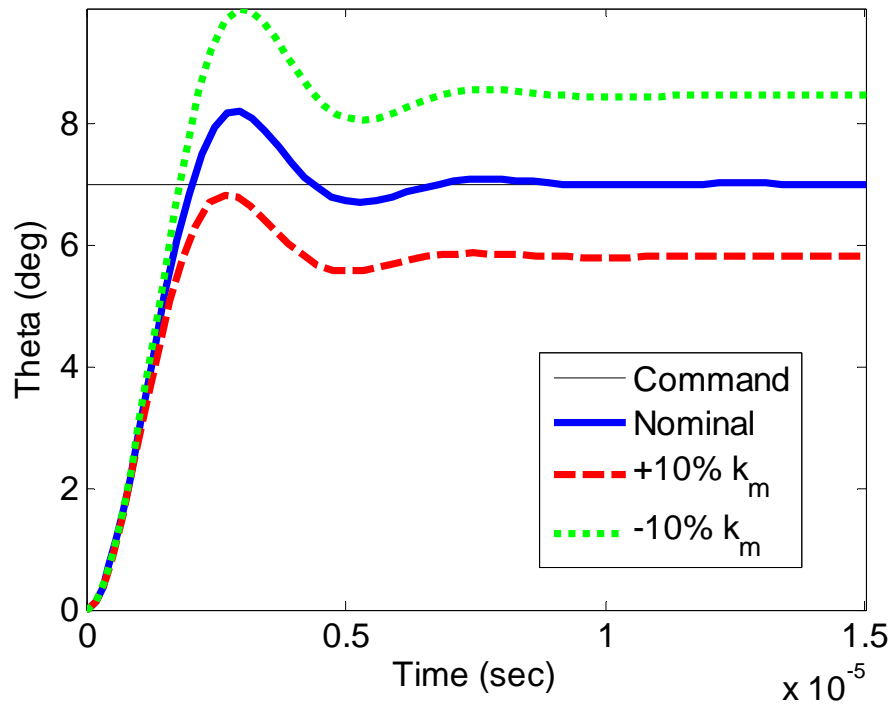


Figure 5-5. Open-loop response to a step input of 7 degrees for the nonlinear plant dynamics and variations in spring stiffness, k_m .

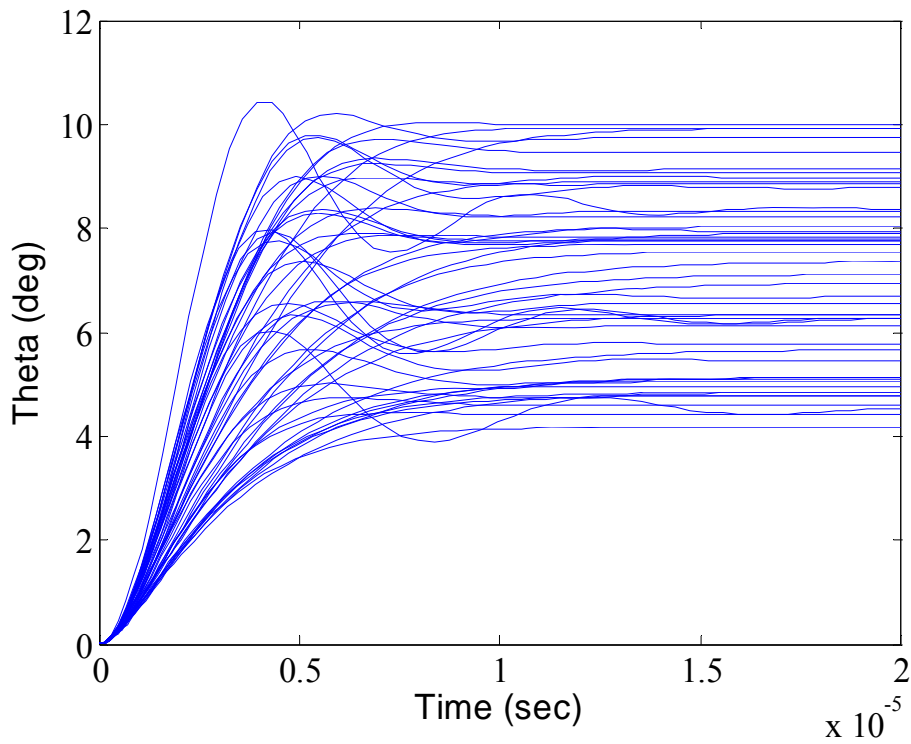


Figure 5-6. Open-loop nonlinear plant response to a step input of 7 degrees for 50 random parameter variations.

The mirror will remain in this position until the actuating voltage has been reduced below the holding-voltage, causing hysteresis. The effects of pull-in and hysteresis for the static response are investigated in Chapters 3 and 4, but there are dynamic effects that can affect pull-in as well. It is known that pull-in is affected by resonance, and it is therefore assumed that the micromirrors operate at frequencies below resonance [40]. If the system is driven dynamically by a voltage that is greater than the holding voltage and less than the pull-in voltage, it is still possible for the inertial effects to cause the mirror to experience pull-in and remain pulled in until the applied voltage is reduced below the holding voltage. In order to incorporate this effect into the dynamic model, the system response is subjected to a set of discontinuous, piecewise defined behaviors. When the angle, θ , becomes greater than or equal to the pull-in angle, θ_{PI} , the system response sets θ equal to the final pull-in position, θ_F . After pull-in has occurred, the system response remains pulled-in until the voltage drops below the holding voltage, V_H . The system then returns to the released position, θ_R . This response is shown in Figure 5-7 for sinusoidal commands of amplitudes of 14.9° , 16.6° , and 17.2° . The corresponding voltage command is also shown in the figure. Again, for commands beyond the pull-in angle of 16.5° , the response shows pull-in and remains in this state until the actuation voltage is reduced below the holding voltage of 68 V.

In the case of a step command, overshoot in the system response becomes very critical when driving the device to a position that is near the pull-in point. In the case of large overshoot in the response, the device will pull-in and will not be released as the voltage command for a step input is constant. Figure 5-8 shows the open-loop step response of the system for commands of 12° , 14° , and 17° . It is expected that the command input of 17° will result in pull-in as it is greater than the pull-in angle. However in this case, overshoot in the response for a step

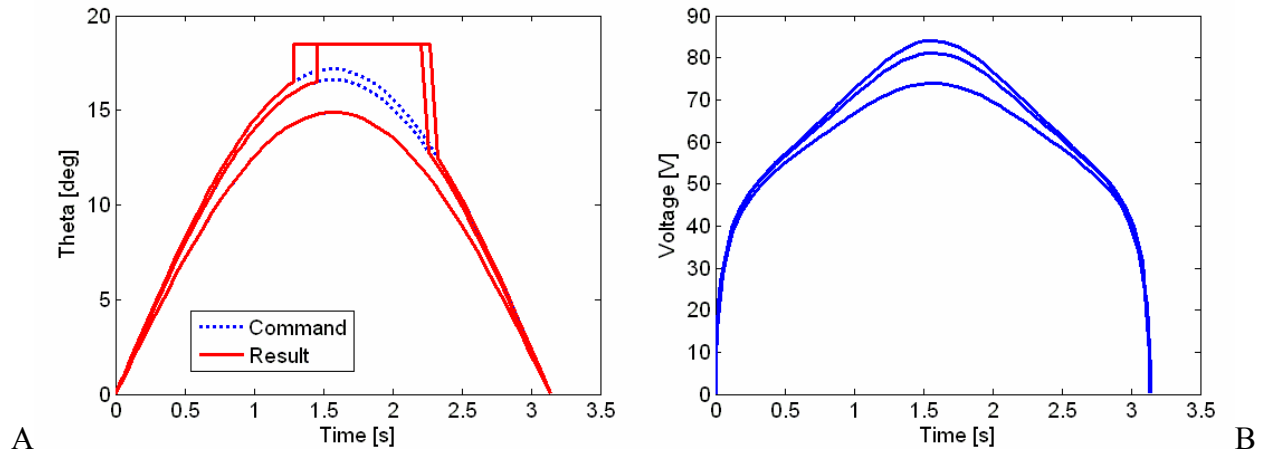


Figure 5-7. Open-loop responses to a sinusoidal input showing hysteresis. A) Results of angle of rotation over time. B) Voltage signals that correspond to the command inputs.

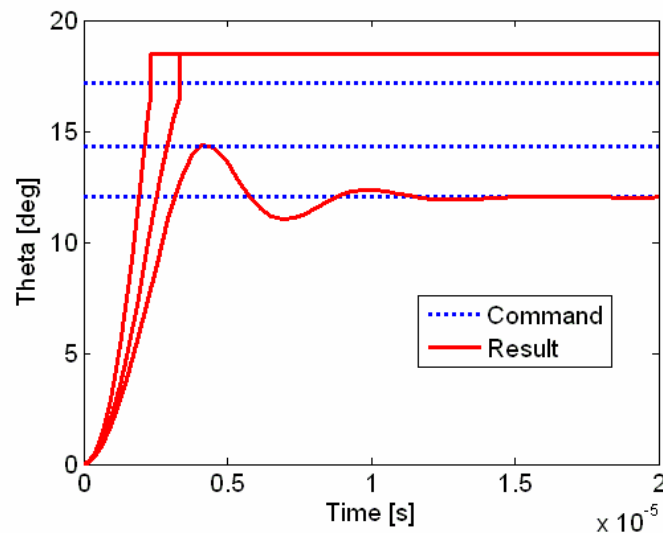


Figure 5-8. Open-loop responses to a step command showing overshoot that result in pull-in. command of 14° also results in pull-in of the response as the overshoot causes the device to move beyond the pull-in point, and the actuation voltage applied is not less than the holding voltage required to release it. This is another example of the effects of hysteresis on the response of the system where the inertial effects plays a role, referred to as dynamic pull-in [111]. Dynamic pull-in can result in cases where the velocity of the actuator is high as it approaches the pull-in point. This can be caused in the case of applying instantaneous actuation voltages, and it

can cause the actuator to pull-in at a lower voltage than the static pull-in voltage. This dynamic effect is difficult to model, and is affected by the damping of the system. For zero damping in a parallel plate system, the dynamic pull-in can occur at an 8% lower voltage than the static pull-in voltage; however the presence of damping in the system decreases this effect.

5.2.3 Continuous Characterization of Micromirror Arrays

The optical profiler measurement system described in Section 4.2.1 used to collect static performance data was also used to apply continuous voltage as a partial sine wave. The voltage was increased and decreased without resetting to zero in between measurements, which allows the effect of hysteresis to be studied. This is done by applying a voltage signal such as that shown in Figure 5-9 with amplitudes ranging from 44 volts to 85 volts following a partial sine wave, with measurements taken at every ten degrees of phase. The results for a set of four mirrors from array 3 are shown as a function of phase in Figure 5-9, and as a function of voltage in Figure 5-10. In this instance, only two of the micromirrors, 1 and 3, experienced pull-in and hysteresis, while the other two, 2 and 4, did not.

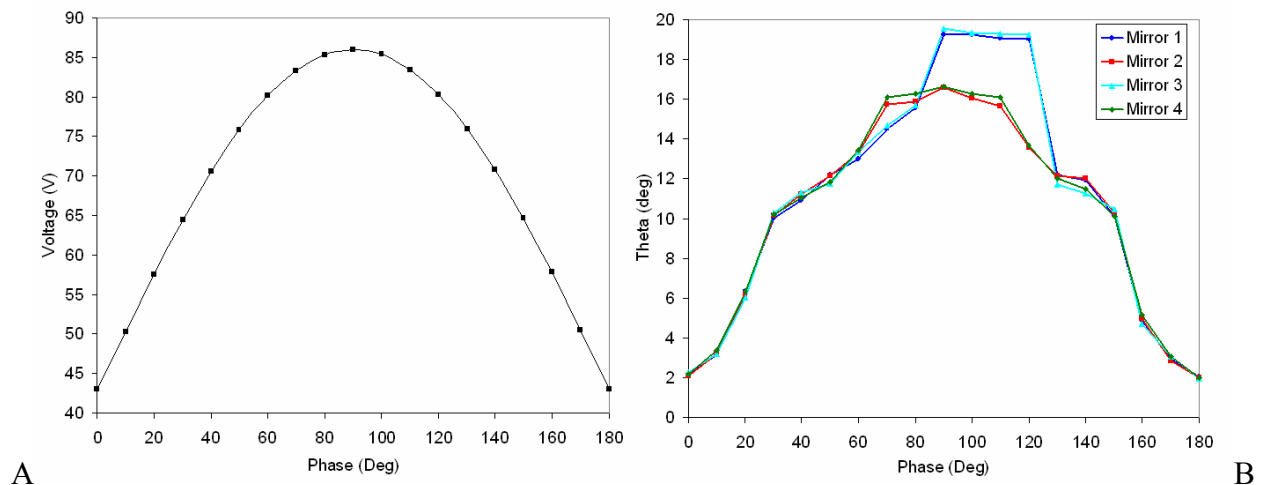


Figure 5-9. Results from dynamic study showing pull-in and hysteresis. A) Actuation signal applied for dynamic study. B) Results from applying the actuation signal.

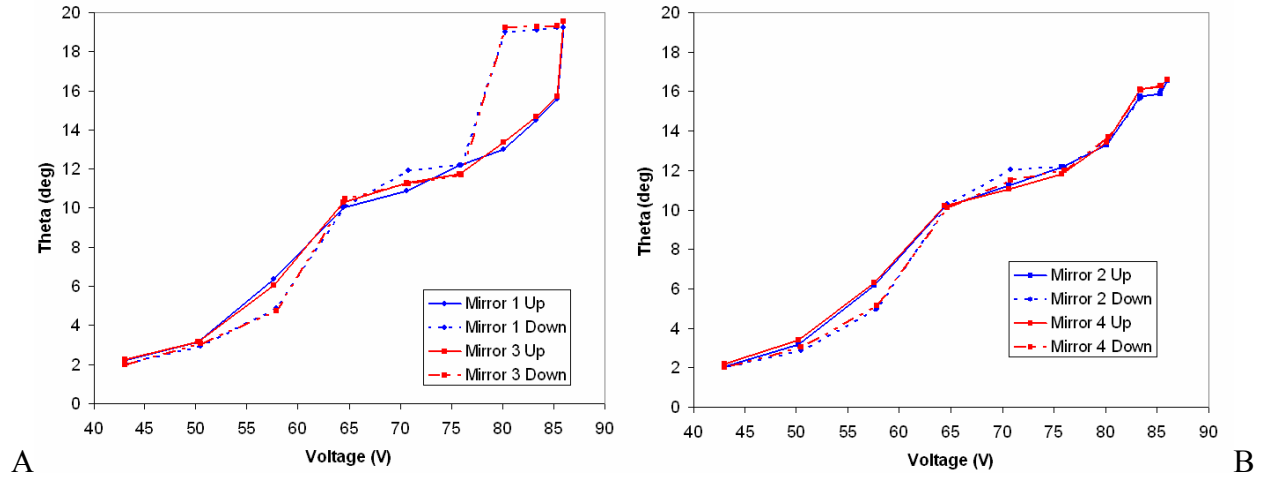


Figure 5-10. Results showing the hysteretic behavior of the micromirrors. A) Mirrors 1 and 3 show pull-in and hysteresis. B) Mirrors 2 and 4 do not have pull-in.

5.3 Hysteresis Case Study: Progressive-Linkage

As discussed in the literature review Section 2.3, there are ways that researchers have used nonlinear flexure designs to mitigate electrostatic pull-in and hysteresis. One such nonlinear flexure design is presented here, called a progressive-linkage [57], [58]. The design and function of the linkage is presented and it is analyzed to show how it affects the electrostatic instability and hysteresis in open-loop operation. The results presented are only theoretical and have not been fully realized in fabrication.

5.3.1 Progressive-Linkage Design

Electrostatic instability occurs when the electrostatic force becomes too great for the mechanical spring to handle. If the characteristics of the mechanical restoring force can be altered such that this pull-in never occurs, then the micromirror device could operate continuously over its full range of motion, from 0 to 19 degrees for the micromirror designs of studied in this dissertation. This done at the cost of increased actuation voltages. The following analysis proposes a new design for the spring that has a nonlinear restoring force such that the stiffness characteristics increase significantly as the spring is rotated.

The analysis for this design is based on an equivalent four-bar model as depicted in Figure 5-11. The geometric relationships between the links are also shown in Figure 5-11. The kinematics of the mechanism can be denoted by the following vector sum where the vectors denote the position and orientation of each side of the mechanism shown in Figure 5-11.

$$\bar{r}_2 = \bar{r}_0 + \bar{r}_1 - \bar{r}_3. \quad (5-12)$$

Since the four-bar mechanism is a one-degree-of-freedom device, the angles θ_2 and θ_3 can be described as a function of θ_1 . That is, the length and orientation of each side can be used to determine the relationships of the angles θ_2 and θ_3 . By using the y and z components of the vector \bar{r}_2 , an expression for θ_2 is given as

$$\theta_2 = \tan^{-1} \left(\frac{r_{2z}}{r_{2y}} \right). \quad (5-13)$$

In order to determine the angle θ_3 , begin with the relationship

$$r_2^2 = r_d^2 + r_3^2 - 2r_3r_d \cos \gamma_3. \quad (5-14)$$

This yields an expression for γ_3 .

$$\gamma_3 = \cos^{-1} \left(\frac{r_d^2 + r_3^2 - r_2^2}{2r_d r_3} \right) \quad (5-15)$$

An expression for θ_d is found from

$$\theta_d = \tan^{-1} \left(\frac{r_{0z} + r_{1z}}{r_{0y} + r_{1y}} \right) \quad (5-16)$$

The angle θ_3 is given as

$$\theta_3 = \theta_d + \gamma_3. \quad (5-17)$$

To realize this design scheme in a surface micromachined device, the design will be subject to the limits and constraints of the micromachining process. One of the challenges

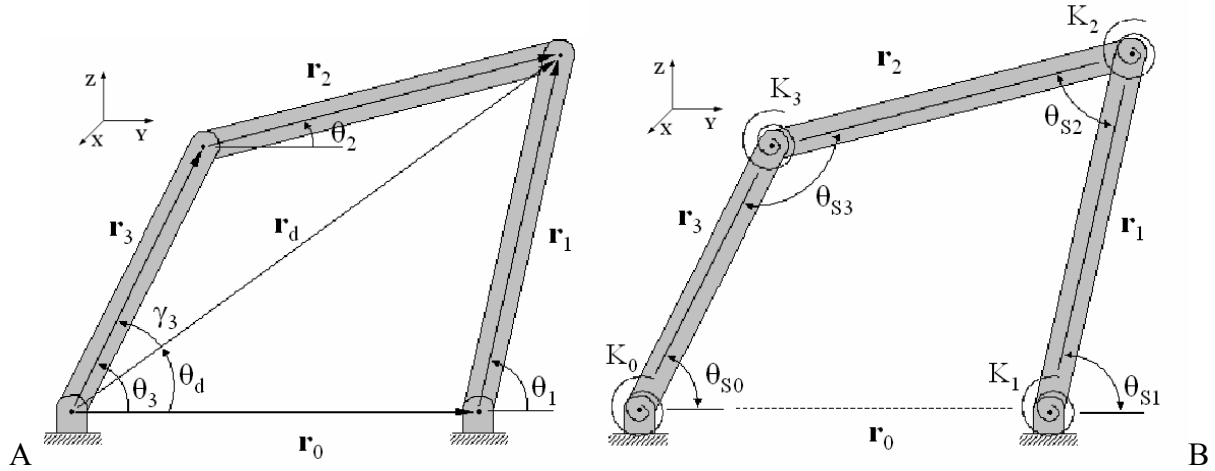


Figure 5-11. Diagram of four-bar mechanism for progressive linkage analysis. A) The vectors and geometry for kinematic analysis. B) The springs and angles for force and moment analysis.

to realizing this mechanism in a surface micromachining process is to find suitable joint configurations that will allow for the creation of a four-bar mechanism. For the sake of this discussion it is assumed that this 2-D representation of the four-bar linkage is created using a series of thin beams, kinematically spaced by r_i ($i = 0, 1, 2, 3$), each joint may be considered as a beam in torsion that provides a restoring force to the system. Seen in Figure 5-12, a beam of length L with a rectangular cross-section of dimensions $w \times t$ is used to model the stiffness at the joints. The restoring torque on the member can be calculated by

$$T_{s,i} = \frac{K_i(\theta_{s,i} - \theta_{s,i0})G}{L} \quad (5-18)$$

for each joint $i = 0, 1, 2, 3$, where $G = \frac{E}{2(1+\nu)}$ is the shear modulus, $(\theta_{s,i} - \theta_{s,i0})$ is the change

in the rotation at the joint from its unloaded position (the free length configuration of the torsional spring), and K_i is given as

$$K_i = \frac{tw^3}{16} \left[\frac{16}{3} - 3.36 \frac{w}{t} \left(1 - \frac{w^4}{12t^4} \right) \right] \quad (5-19)$$

when $t > w$. For the case of $t < w$, the expression is

$$K_i = \frac{wt^3}{16} \left[\frac{16}{3} - 3.36 \frac{t}{w} \left(1 - \frac{t^4}{12w^4} \right) \right] \quad (5-20)$$

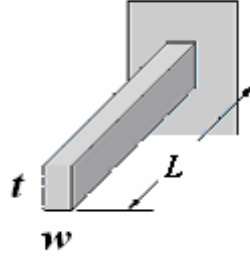


Figure 5-12. Cantilever beam with cross-section $w \times t$, and length L .

The resulting static force and moment equations can be determined from the free body diagrams in Figure 5-13.

$$\sum \bar{F}_{bar1} = \bar{F}_1 + \bar{F}_2 = 0 \quad (5-21)$$

$$\sum \bar{F}_{bar2} = -\bar{F}_2 + \bar{F}_3 = 0 \quad (5-22)$$

$$\sum \bar{F}_{bar3} = -\bar{F}_3 + \bar{F}_0 = 0 \quad (5-23)$$

$$\sum \bar{M}_{joint1} = \bar{T}_{S1} - \bar{T}_e + \bar{T}_{S2} + \bar{r}_1 \times \bar{F}_2 = \bar{0} \quad (5-24)$$

$$\sum \bar{M}_{joint2} = -\bar{T}_{S2} + \bar{T}_{S3} - \bar{r}_2 \times \bar{F}_3 = \bar{0} \quad (5-25)$$

$$\sum \bar{M}_{joint3} = \bar{T}_{S0} - \bar{T}_{S3} - \bar{r}_3 \times \bar{F}_0 = \bar{0} \quad (5-26)$$

The relationships above combine to determine the torque output for a progressive linkage design. The dimension of the mechanism that is the easiest to change in the design is the horizontal distance separating the anchor points of the device, referred to above as \bar{r}_0 . Figure 5-14 shows the output of the progressive linkage for different values of r_0 . For a value of r_0 less than 10 μm , the structure will become very stiff before the mirror reaches its maximum angle and

it will not be able to fully rotate. This is seen for values of r_0 equal to 4, 6, and 8 μm . As the value of r_0 is increased, the structure becomes more compliant. Figure 5-15 shows plots of the

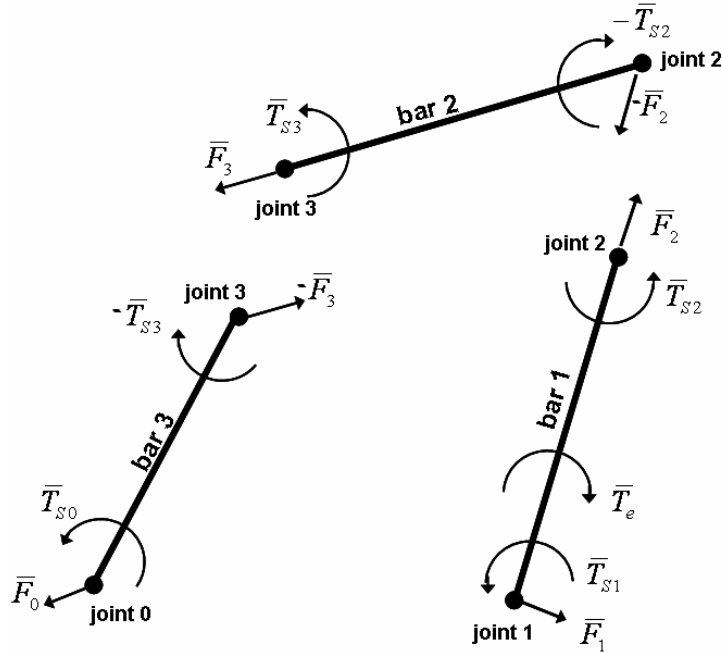


Figure 5-13. Free body diagrams for each member of the linkage.

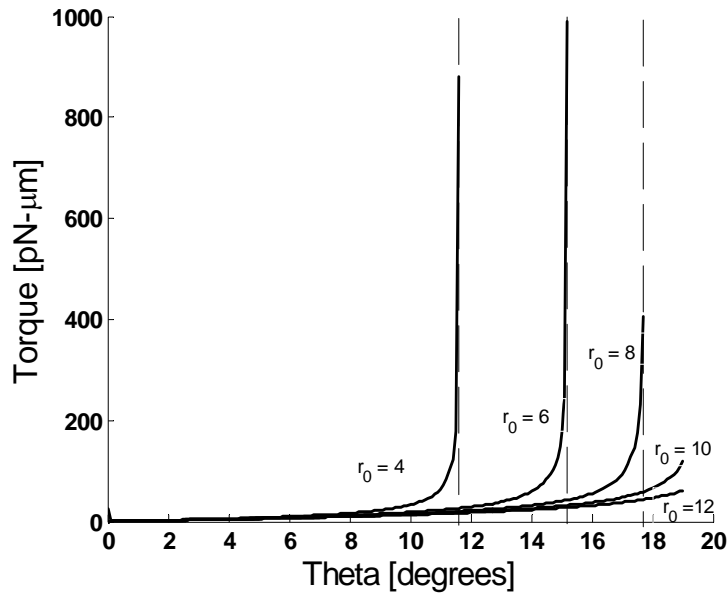


Figure 5-14. Progressive-linkage behavior for different values of r_0 in μm .

behavior of the progressive linkage for r_0 equal to $9 \mu\text{m}$ overlaying the electrostatic torque curves from Figure 3-21. Tables 5-3 and 5-4 give the link length and joint dimensions used for this progressive-linkage design. The Young's Modulus is assumed to be 164.3 GPa and the Poisson's ratio is 0.22. The linear restoring force from Figure 3-21 is also included for comparison. The requirements for pull-in to occur are that the electrostatic and mechanical torques be equal in magnitude and slope. The progressive linkage creates a stiffness profile that eliminates the occurrence of the second condition such that the stiffness curve does not at any point run tangent to the electrostatic torque curves and therefore does not exhibit pull-in behavior. The static θ -V profile for a device using a progressive linkage is shown in Figure 5-16. The cost of this extended actuation range is that larger voltages are required.

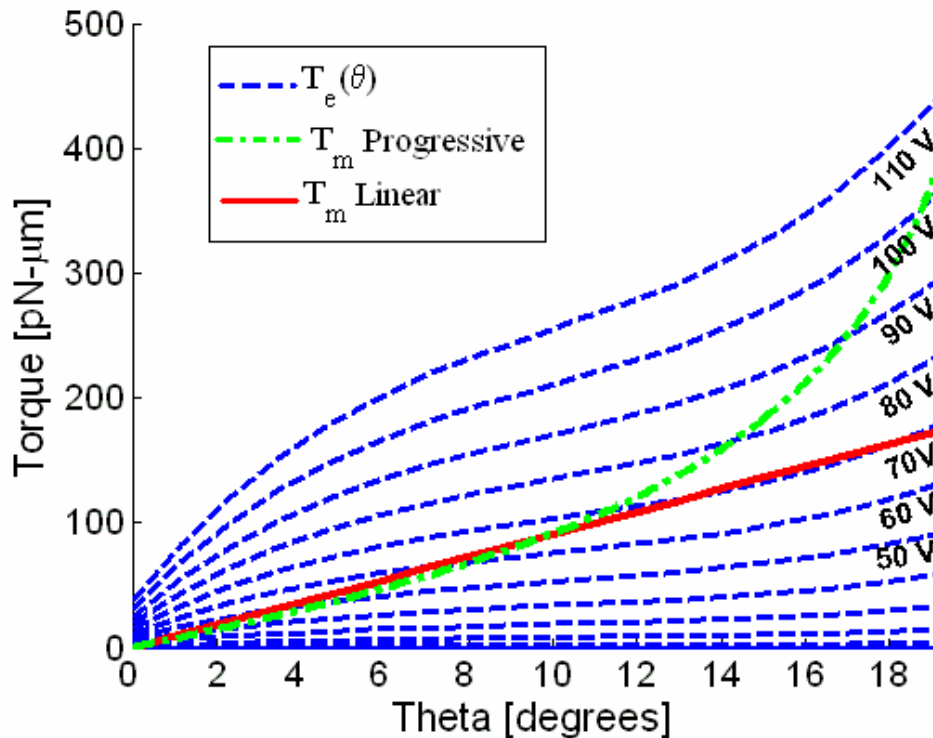


Figure 5-15. Progressive linkage output for r_0 equal to $9 \mu\text{m}$ along with the electrostatic torque curves and the linear restoring torque.

Table 5-3. Link length dimensions used for progressive-linkage design.

Link	Length (μm)
r_0	9.000
r_1	8.625
r_2	9.953
r_3	4.375

Table 5-4. Joint dimensions used for progressive-linkage design.

Joint	Dimension (μm)		
	T	w	L
0	2.50	1.00	66
1	2.50	1.00	66
2	2.25	3.00	111
3	2.25	3.50	111

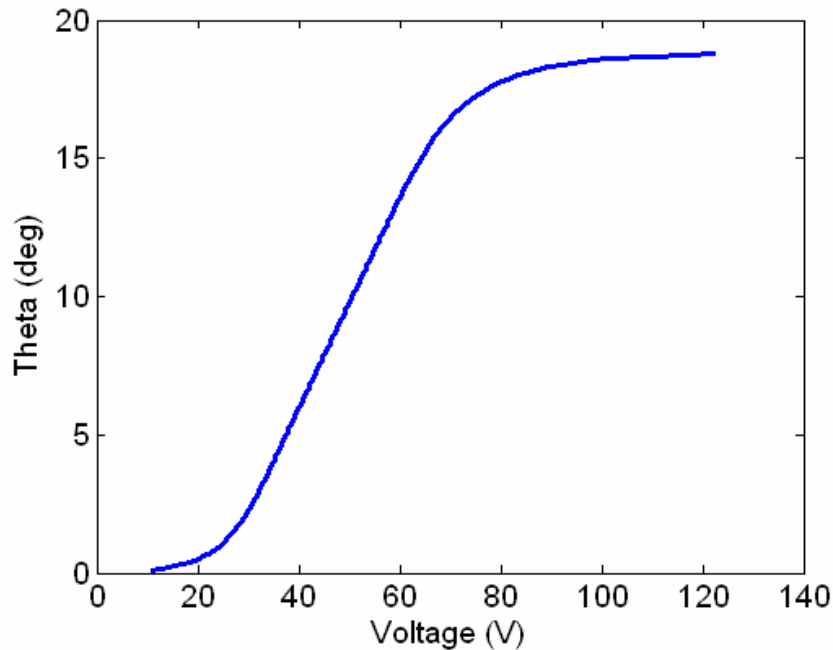


Figure 5-16. Static θ - V relationship for micromirror with a progressive-linkage.

Recall from Section 3.4.5 that a bifurcation analysis may be used to examine the electrostatic pull-in behavior for a system with a nonlinear spring constant. The equations for the analysis now include the progressive spring constant that is a function of the rotation angle, expressed as $k_m(\theta)$. The expression for the fixed point solutions is now

$$\lambda_j = \frac{1}{2} \frac{b}{J} \pm \frac{1}{2} \sqrt{\left(\frac{b}{J}\right)^2 + 4 \left(\frac{1}{J} \frac{\partial T_e(\theta_{ei})}{\partial x_1} - \frac{k_m(\theta_{ei})}{J}\right)}$$

$j = 1, 2$
 $i = 1, 2, 3$

(5-27)

Applying this analysis to the device using the progressive linkage yields the bifurcation diagram shown in Figure 5-17. It is clear from this analysis that the device is able to reach angles up to 18 degrees using higher voltages of up to 130 V. Figure 5-18 shows how the bifurcation plot will change as the progressive stiffness profile increases or decreases by a factor of 2.

5.3.2 Open-Loop Response Using a Progressive-Linkage

Because this device does not experience pull-in, it is assumed that there is no hysteresis in the response. Therefore the system will be able to respond to actuation signals such as a sine wave or step command without having pull-in. The system open-loop response to sinusoidal inputs is shown in Figure 5-19. Figure 5-20 shows the step response to inputs of 12°, 14.3°, 17.1°, and 18°. Unlike the system with a linear spring force, this device is able to achieve positions beyond the pull-in angle. As stated before, the actuation voltages for this device with a progressive linkage will be higher than for the results using a linear spring in Figures 5-7 and 5-8.

5.3.3 Parametric Sensitivity of the Progressive-Linkage

It was shown in Chapter 4 how the mechanical spring that consisted of only one set of beams was sensitive to fabrication tolerances. It thus seems logical to assume that by adding complexity to the spring design in terms of the progressive-linkage will add to the effects of this sensitivity. The following discussion will examine the effects of fabrication tolerances on the progressive-linkage design. The methods of analysis will follow that of Section 4.1, in which first the effects of changing only one parameter at a time are examined. Then, Monte Carlo

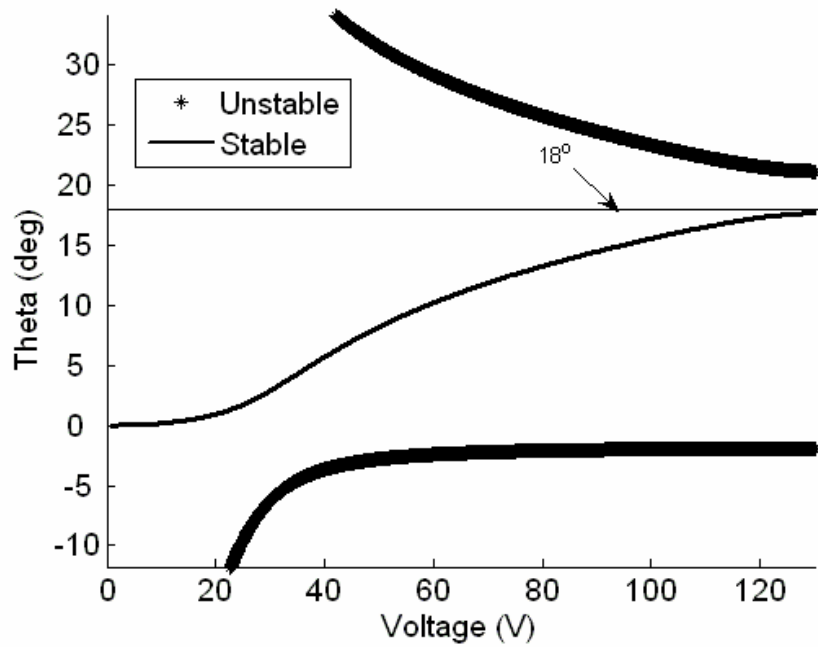


Figure 5-17. Bifurcation diagram for micromirror using a progressive-linkage to avoid pull-in behavior.

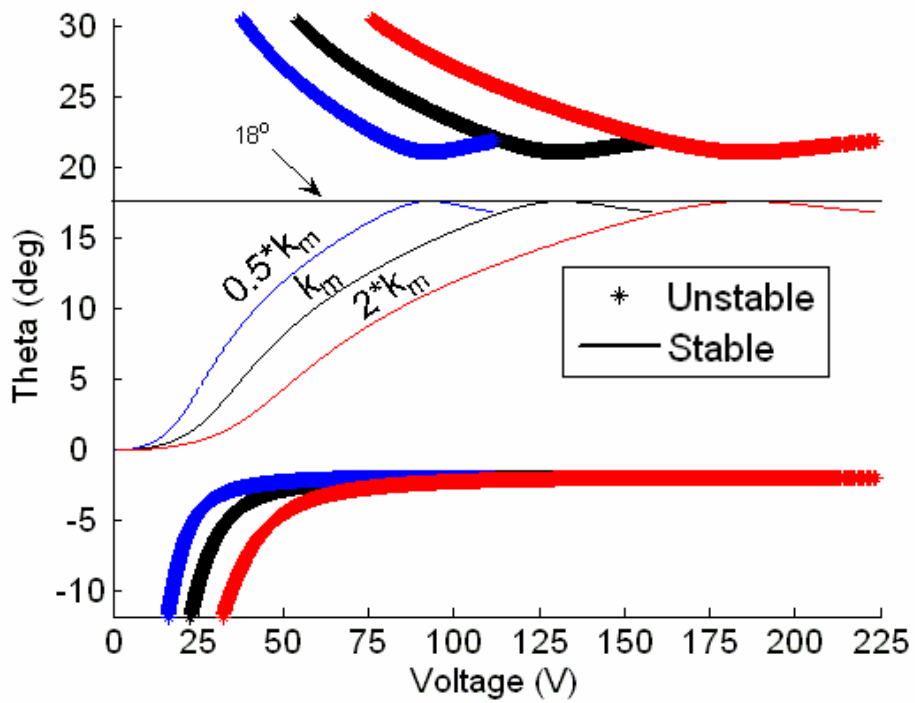


Figure 5-18. Bifurcation diagram for the micromirrors using a progressive-linkage to avoid pull-in behavior for different values of mechanical stiffness.

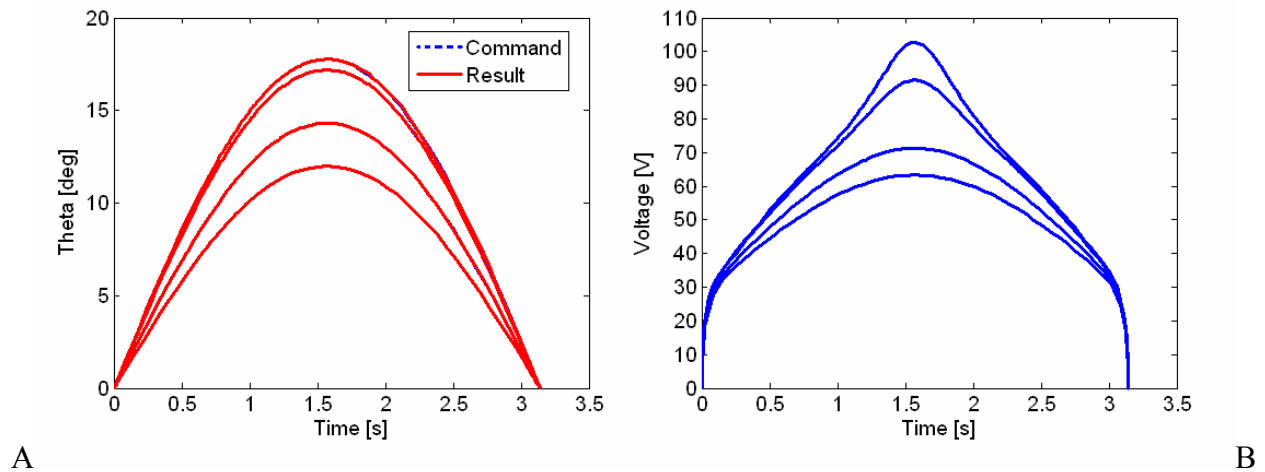


Figure 5-19. Open-loop responses to a sinusoidal input for the device using a progressive-linkage. A) Results of angle of rotation over time. B) Voltage signals that correspond to the command inputs.

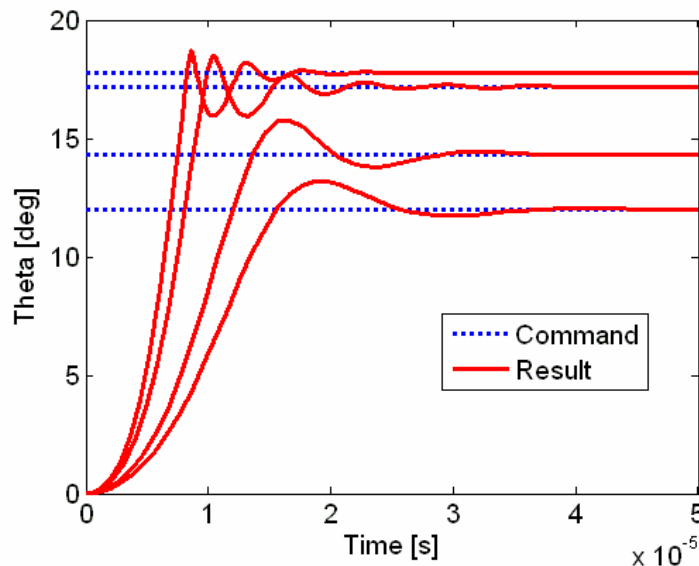


Figure 5-20. Open-loop response to a step input for device using a progressive-linkage. simulations are done to look at the effects of randomly varying all of the uncertain parameters. The uncertain parameters are assumed to vary in a Gaussian distribution, identified by a mean and standard deviation given from known fabrication tolerances.

Table 5-3 and 5-4 gave numbers for the progressive-linkage design variables that are used to evaluate the four bar linkage model. The torsional spring constants, calculated by Equation 5-

11, depend on the values of w and t from Table 5-4, as well as the Young's modulus, E . The dimensions of the joints are subject to the fabrication tolerances of the surface micromachining process. Assume for this given design, that the joints 0, 1, 2, and 3 are fabricated as beams in the layers MMPoly1, MMPoly1, MMPoly4, and MMPoly3, respectively. This means that each joint will be subject to the errors in layer thickness and linewidth that are defined from the fabrication tolerances given for the manufacturing process. Table 5-5 lists this information, including the nominal joint dimensions, t and w , the respective fabrication layer used to make each joint, and the associated fabrication errors given in terms of mean and standard deviation. For example, joints 0 and 1 are to be fabricated in layer MMPoly1, making their dimensions prone to variation in the thickness of MMPoly1. All of the layers are subject to variation in Young's Modulus, previously stated to be 164.3 ± 3.2 GPa. Other errors in the fabrication can occur that will affect the design of the four-bar type linkage in terms of the link lengths, however these are neglected here, and only the errors associated with the joint stiffness are being considered in this analysis.

Table 5-5. Uncertainties in the joint dimensions for a proposed progressive-linkage design.

Joint	Dimension (μm)		Fabrication Layer	Uncertainty of Dimension Mean \pm St. Dev.(μm)	
	T	w		t (thickness)	w (linewidth)
0	2.50	1.00	MMPoly1	1.02 ± 0.0023	--
1	2.50	1.00	MMPoly1	1.02 ± 0.0023	--
2	2.25	3.00	MMPoly4	2.29 ± 0.0063	-0.07 ± 0.05
3	2.25	3.50	MMPoly3	2.36 ± 0.0099	-0.24 ± 0.05

The sensitivity of the progressive-linkage design is examined when only one variable is altered at a time. Figure 5-21 shows the results from this analysis in terms of the mechanical torque as a function of rotation angle as each variable is changed by one standard deviation from the mean. The two variables that have the greatest effect on the stiffness profile of the nonlinear spring are the thickness of layer MMPoly3, and the linewidth of MMPoly3. In order to examine the effects of changing multiple variables at the same time, Monte Carlo simulation is done in

the same fashion as in Section 4.1.2. Each variable is randomly varied according to a Gaussian distribution defined by the mean and standard deviation of that variable. For this progressive-linkage design, 50 simulations are performed, and the results in terms of the torque-theta profile are shown in Figure 5-22. It is striking to see the very large effects of these very small parametric perturbations, and from a qualitative point-of-view, it becomes evident that the current proposed design will be very sensitive to the fabrication. In a case such as this, design optimization is recommended to find a design for the linkage that is less sensitive to these errors. This is suggested for future work to explore alternative joint designs and variations of the progressive linkage that will make it less prone to parametric uncertainties.

5.3.4 Progressive-Linkage Prototype

Despite the limitations of the design that are revealed through the parametric analysis in Section 5.3.3, a prototype of the micromirror with the progressive-linkage has been developed. This design, illustrated in Figure 5-23, was developed and fabricated in the SUMMiT V micromachining process with joint configurations consisting of a series of thin beams as modeled in Section 5.3.1. Figure 5-24 shows a micrograph image of the progressive-linkage and the micromirror device. Because of the planar fabrication requirements of surface micromachining, the diagonal top member of the four-bar device, \bar{r}_2 , can be acquired via a kinematically equivalent L-shaped beam, shown in Figure 5-24. It should be noted that for an array of micromirrors that required close spacing, this is perhaps not an ideal design implementation as the linkage itself occupies a significant amount of space behind the micromirror. A more compact implementation that could be located underneath the mirror or to the side would be preferred. Due to time-constraints with the available fabrication run, in-depth analysis of the device performance was not conducted before the final design was submitted for

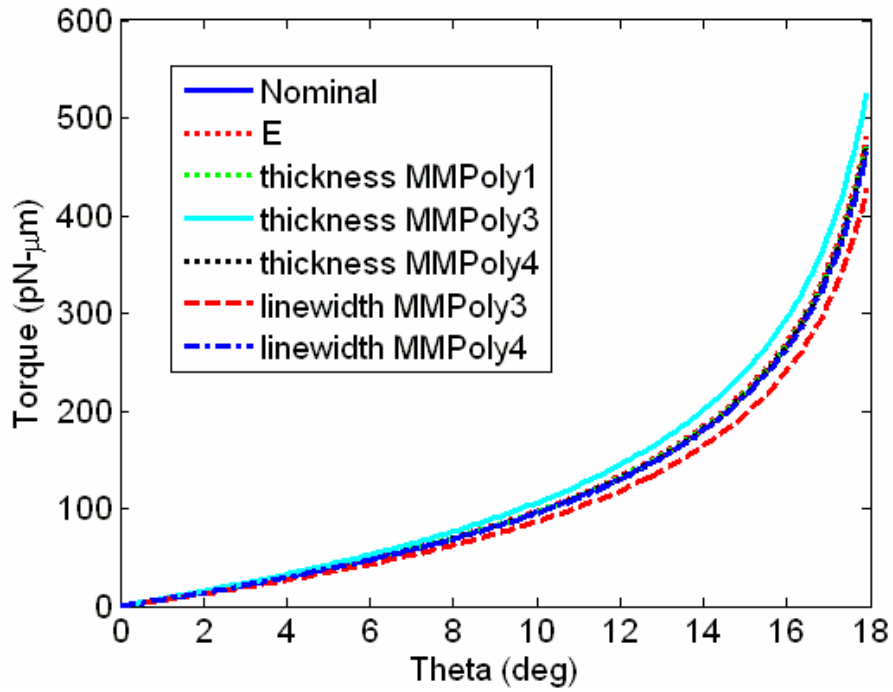


Figure 5-21. Results of parametric analysis for individual errors in joint fabrication of the progressive-linkage.

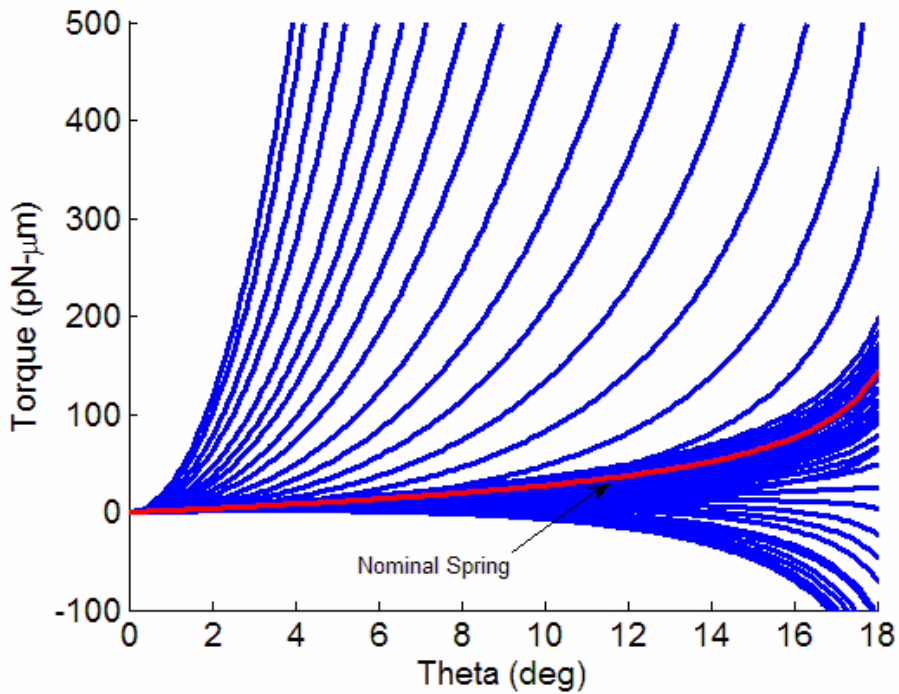


Figure 5-22. Fifty Monte Carlo simulation results for varying the joint fabrication parameters for the progressive-linkage design. The nominal spring value is shown for comparison.

fabrication. This is an unfortunate but sometimes common occurrence encountered by MEMS-designers who may be restricted by the time-tables of foundry services and available project funding. It also gives a good example of the consequences of incomplete a priori analysis.

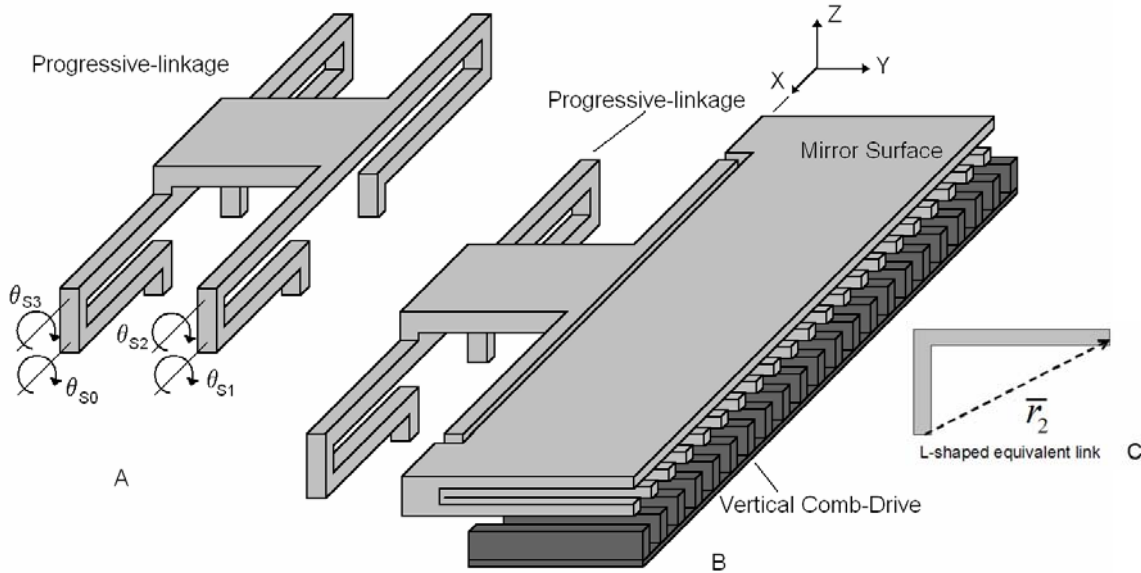


Figure 5-23. Schematic drawing of the prototype progressive linkage spring. A) Progressive linkage spring. B) Spring attached to the micromirror. C) Drawing of L-shaped equivalent beam.

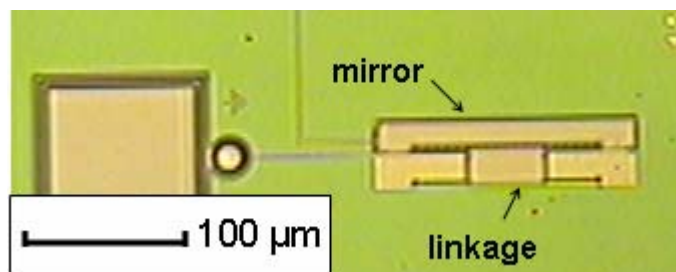


Figure 5-24. Micrograph of the prototype micromirror with a progressive linkage spring.

As previously stated, the proposed linkage design prototype was fabricated, and subsequently tested using the WYKO NT1100 optical profiler located at Sandia National Laboratories in Albuquerque, NM. This is the same optical profiler discussed in Section 4.2.2. The results of this static experimentation are shown in Figure 5-25 as the rotation angle, θ_l , that was measured for an applied actuation voltage. It is clear that the voltages required to actuate the

micromirror with the progressive-linkage are higher than for the micromirror without the progressive linkage. It is not clear however if the progressive device was able to accomplish the nonlinear spring behavior desired. After the device was rotated to approximately 14 degrees, all subsequent measurements failed to record proper data files. This issue was first discussed in Section 4.2, where for high angles of rotation, the measurement machine routinely had difficulty taking measurements. Thus, it is inconclusive to state whether the pull-in point of the micromirrors was in fact delayed by the spring design or not. It is suspected however that the linkage did not perform its intended function, and the data beyond 14 degrees of rotation did not record because the mirror had in fact pulled in.

In order to investigate the device performance to try to identify if the proposed progressive-linkage design implemented is working properly, the structure of the progressive-linkage has been examined using FEA. Just as with the previous mechanical spring analysis of Section 3.4, the progressive-linkage is modeled in ANSYS using beam189 elements [99]. As the structure is displaced about the X-axis, it soon becomes clear from looking at the resulting displacement of the linkage, that the design is not operating as the intended four-bar model, but is instead deflecting in the positive Z-direction, out-of-plane. This Z-direction deflection prevents the joints, which are fabricated as thin beams, from rotating as they are intended. Figure 5-26 shows the results of the FEA analysis of the prototype design for both linear deflection analysis, and nonlinear, large-deflection analysis. The nonlinear analysis begins to deviate from the linear results for very large deflections, but does not produce the desired nonlinear stiffness profile for the range of motion of the micromirror. It becomes evident from this deflection, that the progressive-linkage in this current design implementation is not providing the appropriate motion that is capable of providing the nonlinear stiffness profile to

affect the pull-in behavior of the device. This becomes a very good example of the importance of performing careful analysis of a MEMS design prior to fabrication. The above theoretical model presented for the progressive linkage is still valid. The challenge remains however to find the appropriate design implementation that will carry out the four-bar linkage design principles. This remains as future work.

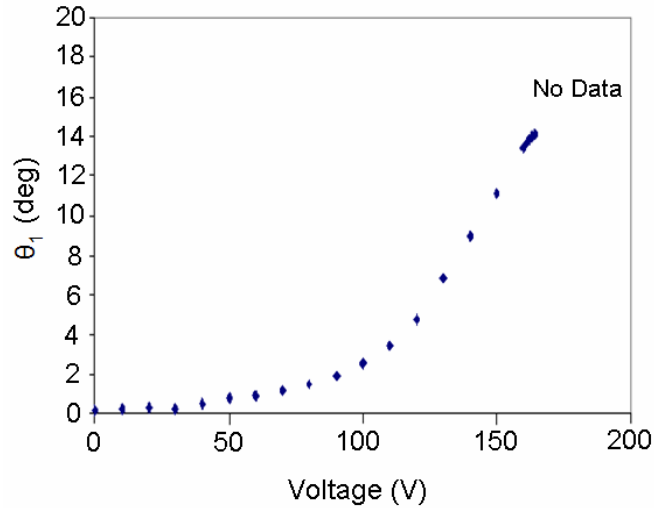


Figure 5-25. Experimental data collected for the prototype of the micromirror with the progressive-linkage

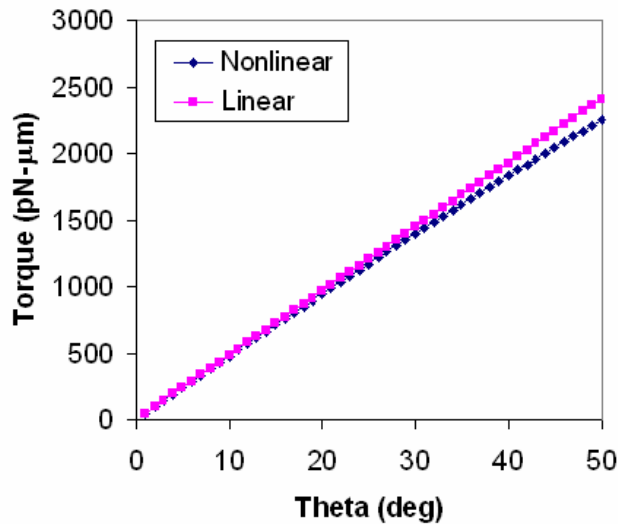


Figure 5-26. Results from FEA of the prototype progressive-linkage design for linear and nonlinear deflection analysis shows the prototype progressive-linkage fails to produce the desired stiffness profile.

5.5 Chapter Summary

The work presented in this chapter expanded upon the static modeling methods developed in Chapters 3 and 4 to examine the dynamic characteristics of the system. In keeping with previous modeling assumption, the lumped parameter model for the micromirrors is presented as a one degree-of-freedom mass-spring-damper system. The damping characteristics are assumed to have a low damping ratio based on the results from similar devices in the literature. The natural frequency of the device is determined from the mass, which is estimated from the volume of the moving micromirror, and the spring constant that was calculated and characterized in Chapter 3. This determined the natural frequency of the micromirrors to be 188 kHz.

Modal analysis performed using FEA on the structure determined the first natural frequency to be lower, at 84 kHz, and it was found that this frequency responded in more than one degree-of-freedom. An examination of the participation factors for the response of the first mode in each direction reveals that the primary direction of the response is in the rotational X-direction (ROTX), which corresponds to the one-degree-of-freedom model assumption. However, it is clear that motion in other directions, namely the Z-direction affects the compliance of the system and the response, resulting in a lower than predicted first natural frequency. This additional degree of freedom acting in the Z-axis direction significantly lowered the effective spring constant for this mode, thus lowering the natural frequency. The modal analysis results are verified by experimental measurements taken with a LDV to determine resonant behavior for the devices. While the results from these experiments were affected by noise, it is clear that resonant peaks do occur near the values predicted by the modal analysis results.

It is clear that the first mode does respond primarily in the ROTX direction, and the evidence of motion in additional degrees of freedom at resonance does not invalidate the

assumption that the mirror will rotate about the X-axis for excitations that occur below the resonant frequency. The electrostatic force that is applied to the micromirror is always an attractive force, drawing the moving electrode down toward the fixed electrode. Thus, if resonance is avoided, smooth rotational motion in one degree-of-freedom is still accomplished. This does, however, show the limitations of the 1DOF model assumption, which limits the analysis to only low frequency responses where resonant behavior may be avoided.

Additionally, the hysteresis behavior for the micromirrors is examined, and it is found that the theoretical model is able to predict not only the pull-in, as demonstrated previously, but also the point at which the mirrors will release from pull-in as the actuation voltage is reduced. Experimental results from the optical profiler validate these findings. Hysteresis causes a deadband in the actuation capabilities that can be detrimental to the performance of the micromirrors, and thus actuation within the hysteresis loop should be avoided. The effects of pull-in and hysteresis also have the ability to negatively affect the dynamic response for actuation signals that occur below the pull-in voltage. To alleviate the problems associated with electrostatic instability, a novel solution is presented, called a progressive linkage.

The progressive linkage creates a nonlinear mechanical restoring force that increases as the electrostatic force increases. It is shown through theoretical predictions that this method can be effective at eliminating pull-in, with the cost of requiring increased actuation voltages. Sensitivity analysis reveals however that this design is very sensitive to the fabrication tolerances, and therefore should be optimized to ensure better performance. A prototype of the progressive linkage design is presented along with some experimental data that unfortunately is inconclusive. Further design development and analysis of the progressive linkage device is considered as future work.

CHAPTER 6 CONTROL DESIGN AND SIMULATION

Now that a dynamic model has been developed for the micromirrors, controllers may be designed for the system with the goal of ensuring steady-state performance regardless of changes to the plant dynamics. As seen in recent literature and the work presented in Chapter 5, active and passive control approaches have been successful at both extending travel range of electrostatic actuators and for improving tracking, disturbance rejection, transient response, system bandwidth and stability, and in reducing steady-state errors. For active control design considerations, in this dissertation the linearized model of the system was used for determining the controller gains before implementing them on the nonlinear plant models. The general form of a feedback control system is shown in Figure 6-1 for unity feedback. In this chapter, PID and LQR controllers are developed and implemented to further quantify the significance of model uncertainties, pull-in and hysteresis. The PID and LQR control designs in Sections 6.1 and 6.2 only consider the performance of single micromirrors. The model and performance of the micromirrors as an array is discussed in Section 6.3. Here, the unique issue of how to control an array of micromirrors that are not individually controllable is explored. This section will demonstrate a model of multiple mirrors as a single-input/multiple-output (SIMO) system and will discuss the feedback signals available by considering two different kinds of optical sensors: position detecting sensors (PSD) and charge-coupled devices (CCD). The performance of these sensors is considered as well as the impact they will have on implementation of closed-loop control system on the array of micromirrors.

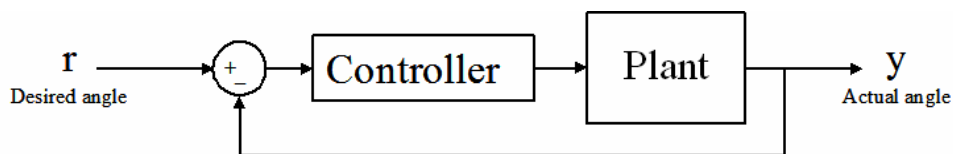


Figure 6-1. Basic block diagram with unity feedback.

6.1 PID Control

Proportional-Integral-Derivative (PID) control is perhaps the most widely used kind of control scheme [102]. The appeal of PID control is that it applies to almost any system, even those for which a system model is not known. There are many techniques that may be used to define the control gains and to tune them for the best performance. It is popular because it is easy to design and fairly intuitive to determine the control parameters for systems modeled with second-order dynamics.

6.1.1 PID Control Theory

The general form of the transfer function for a PID controller is

$$G_C(s) = K_P + K_I \frac{1}{s} + K_D s = K_P \left(1 + \frac{1}{T_i s} + T_d s \right) \quad (6-1)$$

where

$$T_i = \frac{K_P}{K_I} \quad (6-2)$$

and

$$T_d = \frac{K_D}{K_P} \quad (6-3)$$

The block diagram of this system is shown in Figure 6-2. The closed-loop transfer function for this block diagram, with the plant modeled as a linear second order system is

$$\frac{C(s)}{R(s)} = \frac{G_C(s)G_P(s)}{1 + G_C(s)G_P(s)H(s)} \quad (6-4)$$

Assuming unity feedback, that is $H(s) = 1$, and substituting Equation 6-1 into 6-4 gives an expression for the closed-loop transfer function.

$$\frac{C(s)}{R(s)} = \frac{(s^2 K_D + s K_P + K_I)}{s^3 + (2\zeta\omega_n + K_D)s^2 + (K_P + \omega_n^2)s + K_I} \quad (6-5)$$

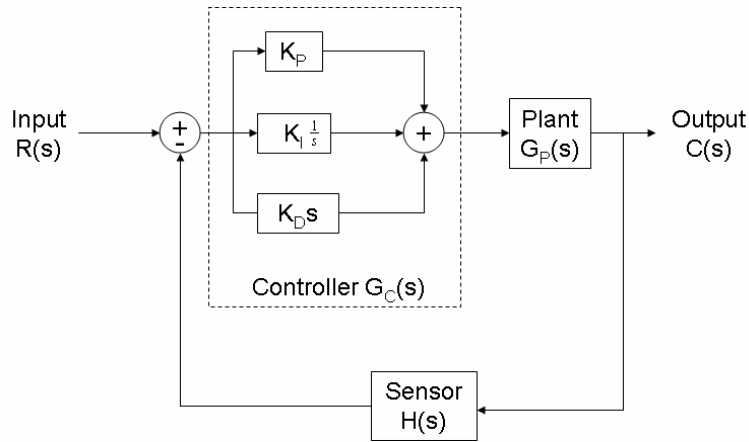


Figure 6-2. Block diagram with PID controller.

The proportional term is a gain that attenuates the magnitude of the system response. The integral term seeks to eliminate steady-state error in the system. The derivative term, as seen in the denominator of Equation 6-5, is associated with the damping term, and as K_D increases, the system damping will also increase affecting the rise time and settling time of the response. The gain K_D is also in the numerator, and can act as a high pass filter that will amplify high frequency noise. Design methods, such as root locus, can be employed to help derive the proper control gains for a particular desired performance [102].

This details in general, how a PID controller affects a linear second-order system. For the micromirror array models presented in the previous chapters, a linearized version has been developed using a linear first order approximation of the capacitance function in Section 3.4.4. A set of PID control gains are chosen using trial and error to yield a linearized closed-loop response characteristic of a an overdamped system with zero overshoot, and to drive the steady-state error to zero. This controller is implemented on both a linear and nonlinear plant.

6.1.2 PID Results

A PI controller is implemented on the system in an effort to ensure zero steady-state error despite the presence of model uncertainty. Using only a simple proportional controller (P-

controller) on the system is not sufficient to ensure zero steady-state error for different plant variations, therefore an integral term is included. The controller gains are chosen as the proportional gain, $K_P = 100$, and the integral gain, $K_I = 100,000$. It was found that the derivative controller term, K_D is not needed. To compare the effects of the nonlinear terms in the electrostatic model, the step response of the linearized plant model is compared to that of the nonlinear plant model in Figure 6-3. Step responses are shown for both models for different step values ranging from 2 degrees to 16 degrees, and the effects of the nonlinear terms begin to appear as the transient response of the nonlinear plant is affected by the magnitude of the step input. The closed-loop system has no overshoot, which is important in electrostatic systems that experience pull-in. For a system application with strict transient performance requirements, this set of gains however may not be sufficient at very low command angles.

As has been shown in the experimental characterization data for these micromirrors in Chapters 4 and 5, an important control objective is to drive the response to have zero tracking errors in the presence of plant uncertainties. Figure 6-4 shows the effects of model uncertainty for the nonlinear plant response, including model variations of $\pm 10\%$ variation in the spring stiffness, k_m . Open-loop analysis in Chapter 5 presented the open-loop plant responses of the system for 50 randomly generated sets of parameters m , b , k_m , and T_e that are allowed to vary by $\pm 10\%$ of their nominal values. The closed loop response of those same 50 plants is shown in Figure 6-5 for parametric variations ranging from $\pm 10\%$ to a very high value of $\pm 90\%$. It is clear that even this simple PI controller drives all of the plants to zero steady-state error, achieving the goal of position tracking.

6.1.3 PID Controller Response to Hysteresis

While it is preferable to avoid driving the micromirrors in the unstable range of motion, it is possible that this could occur, especially as the pull-in point is known to vary for different

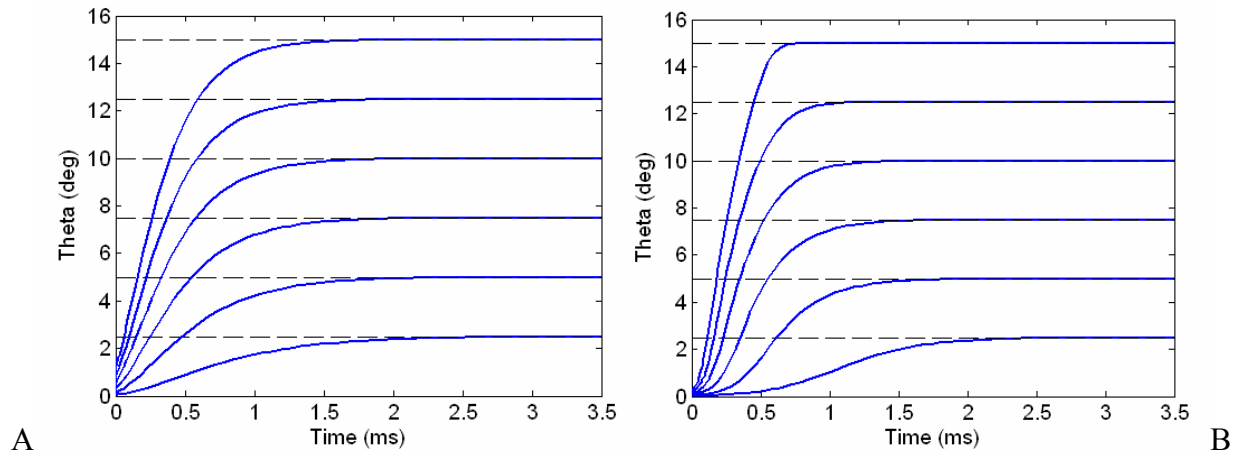


Figure 6-3. Step responses for PID controller. A) Linear plant model. B) Nonlinear plant model.

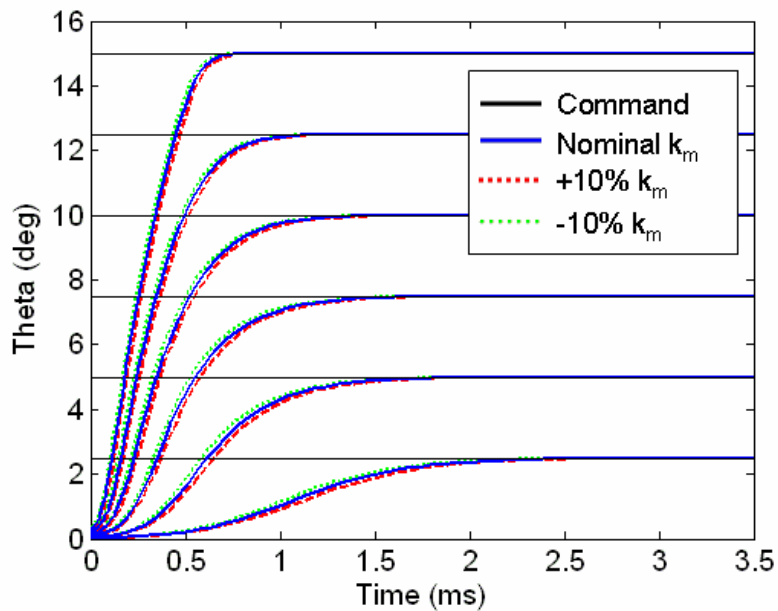


Figure 6-4. Closed-loop PID response to different step inputs when the spring constant is varied by $\pm 10\%$.

micromirrors and for dynamic operating conditions. The discussion in Section 5.2.2 demonstrated the open-loop hysteretic behavior of the micro devices when subject to electrostatic pull-in. Here, this same scenario is considered for the case of the closed-loop system with a PID controller in place. The result is that if the mirror is commanded to an unstable position, and subsequently pulls-in, the controller will see this position error and

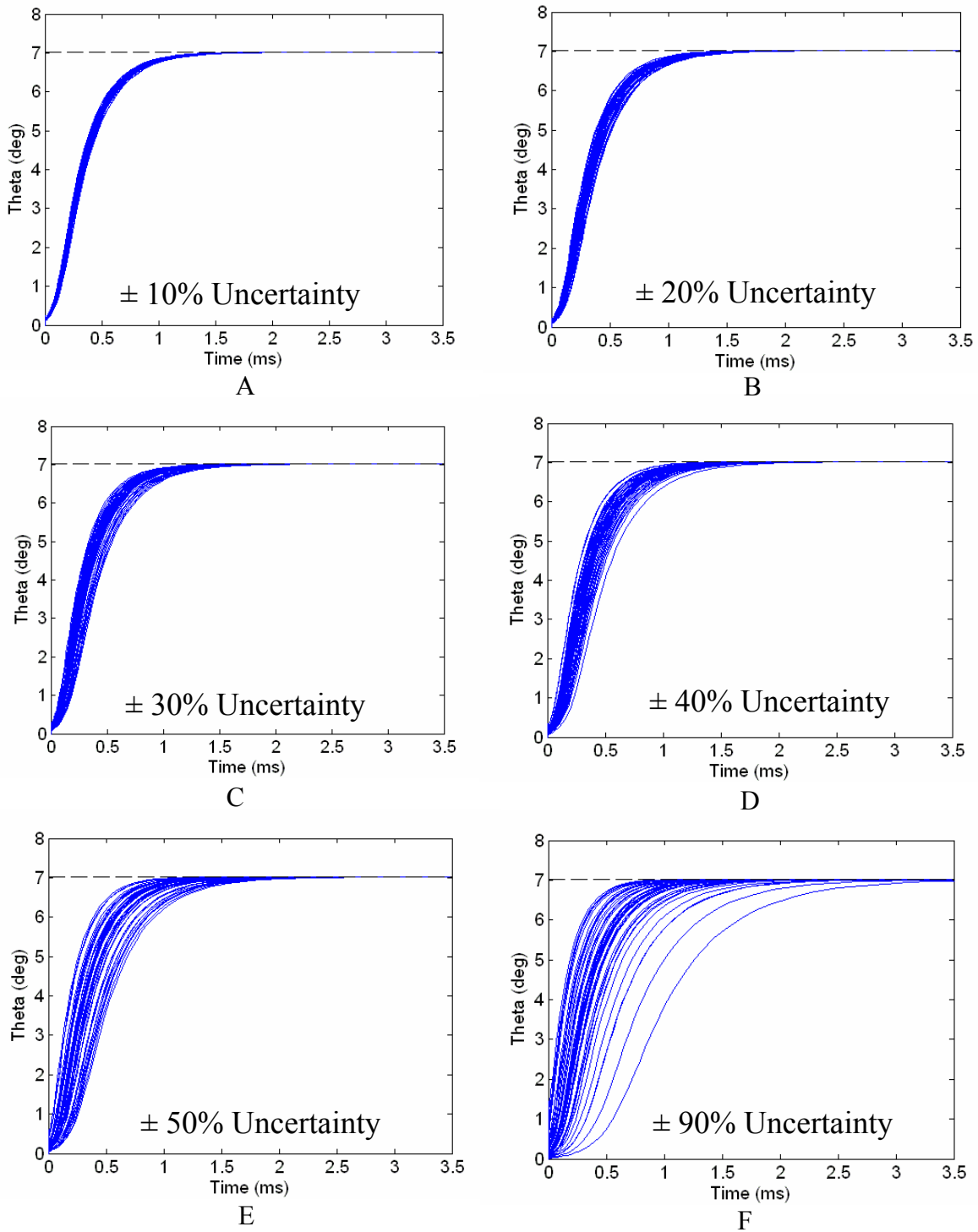


Figure 6-5. Closed-loop PID response to a step input of 7 degrees for 50 random sets of parametric variations. Parameters are allowed to vary by A) 10%, B) 20%, C) 30%, D) 40%, E) 50%, and F) 90%.

seek to correct it. The controller will command the actuator with lower voltages until the holding voltage is reached, and the mirror will release from pull-in. The position of the released mirror will still not be the correct commanded position, which is an unstable position that cannot be reached. So this cycle will repeat itself, as shown in Figure 6-6, resulting in a fast switching behavior until the commanded position of the mirror returns to the stable range of motion. In Figure 6-6, it is clear that this switching behavior would be undesirable for the system, and could even result in damage to the micromirrors; however one benefit of the controller response is that the effect of the hysteresis is mitigated by the controller, and the mirror position returns from pull-in at an earlier time than the response without the controller. This control behavior demonstrates potentially undesirable behavior that could result, and it is not suggested that this PID control implemented for motion in the unstable range is ideal. The control algorithm can easily be augmented to detect electrostatic pull-in conditions to keep the switching response from occurring, and thus avoid potentially damaging the device, but still keep the added benefit of reducing the effect of hysteresis. This discussion is also useful to show once again, the need for eliminating this electrostatic instability in the response, which may be done with the progressive linkage design proposed previously.

Section 5.3 presented the design of a progressive-linkage that can be utilized to eliminate the effects of pull-in and hysteresis. It was demonstrated theoretically that this device can provide actuation over an extended range of the mirror's motion at higher actuation voltages. Using this progressive linkage to eliminate pull-in however does not guarantee that the effects of fabrication tolerances will not play a role in device performance. With the added complexity in the design, parametric uncertainty in the dimensions of the linkage could contribute even more to variations in the system performance; hence closed-loop control is still necessary. Figure 6-7

shows the closed-loop PID step responses for the micromirrors with the progressive linkage, and they are in fact able to achieve stable rotation above the pull-in limit of 16.5 degrees. Also shown are the PID step responses for the 50 random plant variations with $\pm 10\%$ variation of model parameters.

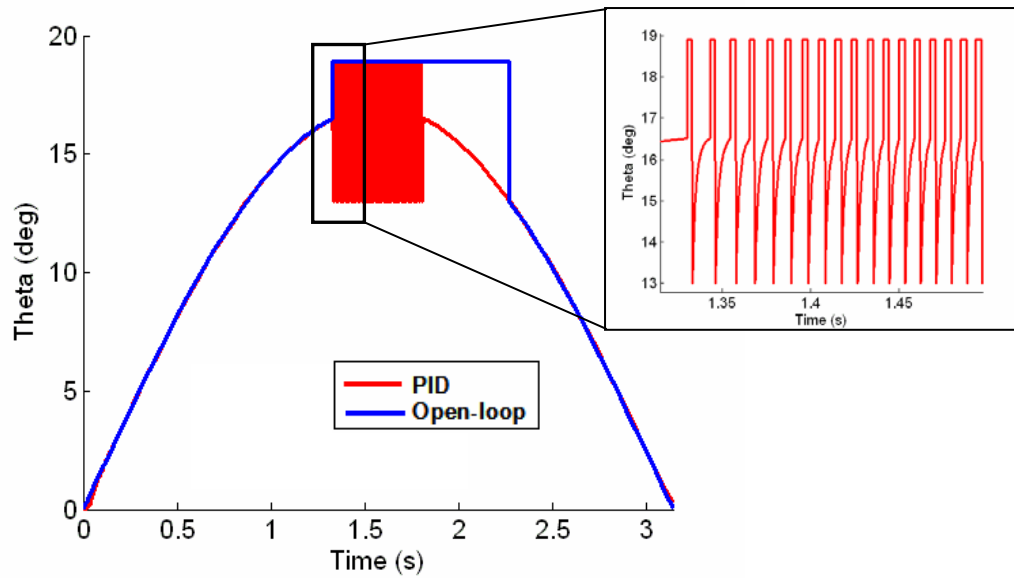


Figure 6-6. Closed-loop PID response to a commanded position in the unstable region.

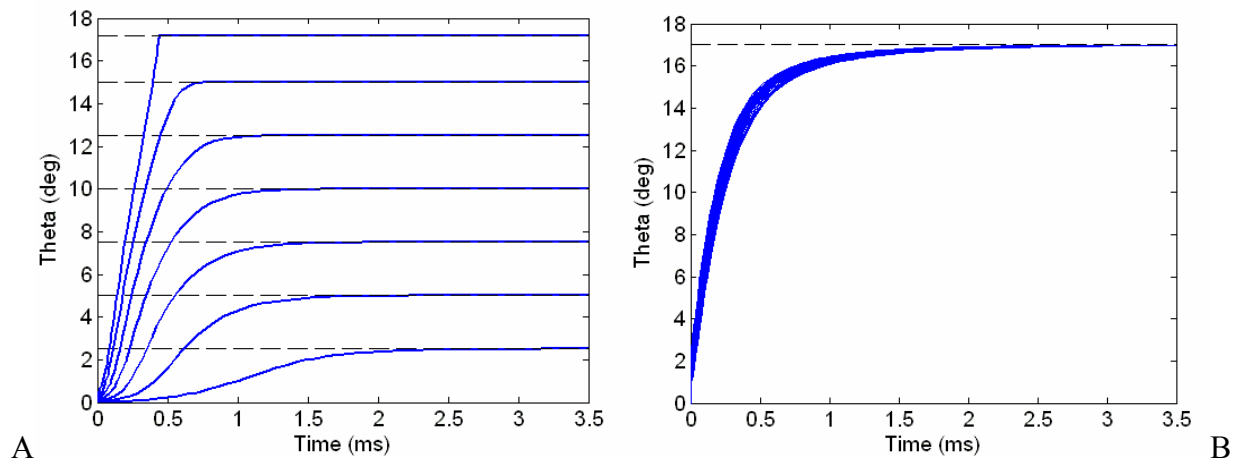


Figure 6-7. Closed-loop step responses for PID controller for a system using a progressive-linkage. A) Step responses of different magnitudes. B) Step responses of 50 plants with model uncertainties.

6.2 LQR Control

Linear quadratic regulator (LQR) control is an optimal control method that uses a linear state-space model of the plant to design a stable controller that seeks to minimize the response of the system states and the control actuation. LQR control design is concerned with minimizing a cost function that balances the control effort with the system states according to defined weights. This type of control requires full-state feedback and that the system is completely controllable. In order to apply LQR control to the system of micromirrors in which only position information is available, a state estimator must be employed for the velocity state.

6.2.1 LQR Control Theory

First, the LQR control problem will be considered for the regulator problem in which the controller will seek to reject noise and disturbances, and drive all the states of the system to zero. LQR control can also be used to track an input trajectory, and this case will be considered second. The LQR regulator problem, shown in the block diagram in Figure 6-8, assumes full-state feedback. Cases without full-state feedback will require the use of an estimator and will be discussed in section 6.2.1.

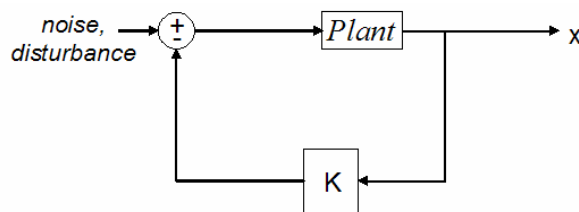


Figure 6-8. General block diagram for LQR controller problem

The plant is modeled as a continuous time, linear system described by a set of state-space equations

$$\begin{aligned}\dot{x} &= Ax + Bu \\ y &= Cx + Du\end{aligned}\tag{6-6}$$

It is desired to find a controller that minimizes a cost function, J ,

$$\min_K J = \int_0^{\infty} (x^* Q x + u^* R u) dt \quad (6-7)$$

where Q is a matrix that relates to tracking performance and R is a matrix related to control actuation [102]. The values of Q and R are chosen to apply penalties to the states and actuator commands. The Q and R matrices are either a positive-definite Hermitian or a real symmetric matrix. A Hermitian matrix is a square matrix that is equal to its own conjugate transpose. The superscript * next to a variable denotes its complex conjugate. The optimal controller, K , that minimizes this cost function is

$$u = -Kx(t) \quad (6-8)$$

Substituting Equation 6-8 into Equation 6-6 gives

$$\dot{x} = Ax - BKx = (A - BK)x \quad (6-9)$$

Thus, Equation 6-7 becomes

$$J = \int_0^{\infty} (x^* Q x + x^* K^* R K x) dt = \int_0^{\infty} x^* (Q + K^* R K) x dt \quad (6-10)$$

The following relationship sets a condition that restricts K to be finite.

$$x^* (Q + K^* R K) x = -\frac{d}{dt} (x^* P x) \quad (6-11)$$

where P is a positive-definite Hermitian or real symmetric matrix. Evaluating the right hand side of Equation 6-11 and substituting in Equation 6-9 yields

$$-\dot{x}^* P x - x^* P \dot{x} = -x^* \left[(A - BK)^* P + P (A - BK) \right] x \quad (6-12)$$

Equation 6-12 must hold true for any x , therefore

$$(A - BK)^* P + P (A - BK) = -(Q + K^* R K) \quad (6-13)$$

If $A - BK$ is a stable matrix, there exists a positive-definite matrix P that satisfies Equation 6-13. In order to determine this matrix P , evaluate the cost function J .

$$J = \int_0^{\infty} x^* (Q + K^* RK) x dt = -x^* P x \Big|_0^{\infty} \quad (6-14)$$

Since $A-BK$ is stable, all of the eigenvalues are assumed to have negative real components and $x(\infty) \rightarrow 0$. Equation 6-14 becomes

$$J = x^*(0) P x(0) \quad (6-15)$$

Because R is defined as a positive-definite Hermitian matrix, it can be written in terms of a nonsingular matrix, T .

$$R = T^* T \quad (6-16)$$

Substitute Equation 6-16 into 6-13 to get

$$\begin{aligned} (A^* - K^* B^*) P + P(A - BK) + Q + K^* T^* T K = \\ A^* P + PA + [TK - (T^*)^{-1} B^* P]^* [TK - (T^*)^{-1} B^* P] - P B R^{-1} B^* P + Q = 0 \end{aligned} \quad (6-17)$$

The minimization of the cost function J with respect to K requires the minimization of

$$x^* [TK - (T^*)^{-1} B^* P]^* [TK - (T^*)^{-1} B^* P] x \quad (6-18)$$

with respect to K . This expression is nonnegative and the minimum occurs when it is zero, or when

$$TK = (T^*)^{-1} B^* P \quad (6-19)$$

Hence, the optimal matrix K is found by

$$K = T^{-1} (T^*)^{-1} B^* P = R^{-1} B^* P \quad (6-20)$$

The matrix P in Equation 6-20 must satisfy the reduced-matrix Riccati equation

$$A^* P + PA - P B R^{-1} B^* P + Q = 0 \quad (6-21)$$

Equation 6-21 must be solved for the matrix P , whose existence guarantees that the system is stable. Once P is found, it is substituted back into Equation 6-20 to find the optimal gain matrix K that is used in the control law of Equation 6-8.

The above development for the LQR controller considered the development of an optimal controller for the case of driving all of the states in the system to zero. LQR can also be designed for tracking a desired input trajectory, r . Consider the trajectory, described by

$$\begin{aligned} r &= Fz \\ z &= Hx \end{aligned} \quad (6-22)$$

for some observable matrices F , and H . In this case, z represents the actual trajectory of the system as a function of the states, and this can include any noise in the sensor as well. An error signal, e , is defined as the difference between the reference (desired) input, r , and the actual trajectory.

$$e = r - z \quad (6-23)$$

For this problem, the cost function J can be defined in terms of the error signal.

$$J = \int_0^{\infty} (e^* Q_e e + u^* R_e u) dt \quad (6-24)$$

Equation 6-24 can be rewritten as follows

$$J = \int_0^{\infty} (x^* Q x + u^* R u + 2x^* N u) dt \quad (6-25)$$

with

$$Q = (HA - FH)^* Q_e (HA - FH) \quad (6-26)$$

$$R = B^* H^* Q_e H B + R_e \quad (6-27)$$

$$N = (HA - FH)^* Q_e H B \quad (6-28)$$

$$Q_e = I, \quad R_e = \rho I \quad (6-29)$$

where ρ is a constant value describing the weighting function on the control effort.

The goal is to find the optimal controller that minimizes the cost function of Equation 6-25, and this is determined from solving the following algebraic Riccati equation with an additional term describing the error signal.

$$A^*P + PA - (PB + N)R^{-1}(B^*P + N^*)Q = 0 \quad (6-30)$$

The solution of Equation 6-30 results in the matrix P such that the controller is described as

$$K = [R^{-1}B^*P \quad R^{-1}N^*] = [K_{fb} \quad K_{ff}] \quad (6-31)$$

where K_{fb} and K_{ff} are the feedback and feedforward controller gains, respectively. The control law is thus written as

$$u = -(K_{fb}x + K_{ff}e) \quad (6-32)$$

The use of this LQR control law for tracking a reference command with zero steady-state error requires that the system include an internal model of the reference command. In the case of a step command, the system must include an integrator and be what is called a type-one system [108]. If the system model does not already include an internal model, then it must be included in the controller. LQR optimal control for a tracking control of a step input for a plant that does not include an integrator has the block diagram shown in Figure 6-9. There is a feed-forward gain, K_{ff} , and a feed-back gain, K_{fb} , as in Equation 6-32. In this case, the error signal is the

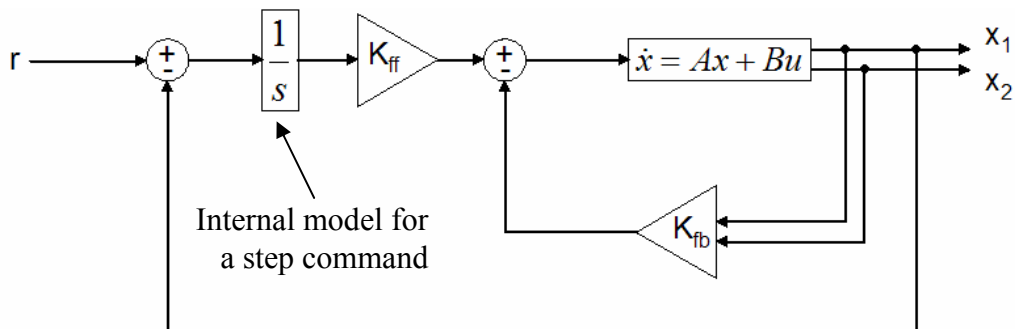


Figure 6-9. Block diagram of LQR control with an internal model for tracking a step command.

difference between the desired reference command, r , and the position state, x_1 . It is assumed that full-state feedback is available for this system for the feedback loop. In cases where full-state feedback is not available, state-estimation is required. This situation is discussed in Section 6.2.2.

6.2.2 State Estimation

The derivation of the control law for LQR control assumes that full-state feedback is available for the controller. In many cases, full-state information is not available, and state-estimation must be used. A block diagram representation for the control system using a state estimator is given in Figure 6-10. L is the estimator gain matrix. State estimation estimates the state variables of the system based on the measurements of the output and the control variables.

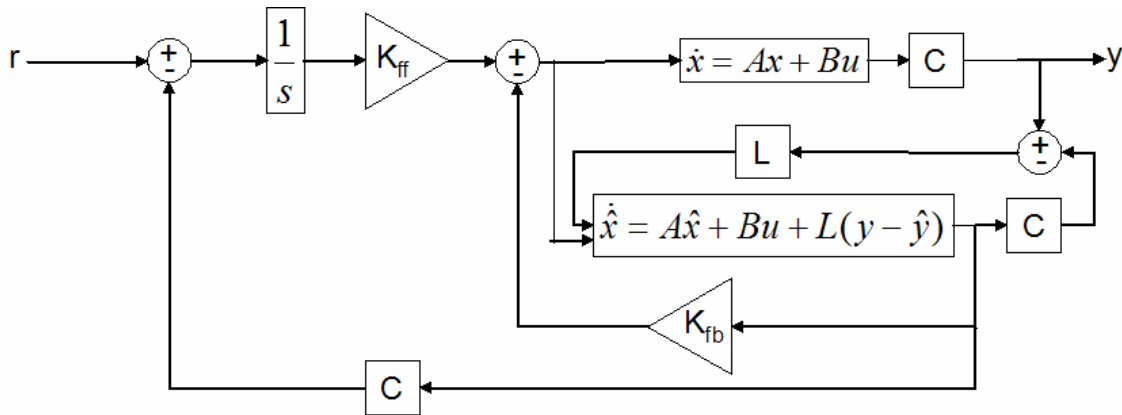


Figure 6-10. Block diagram of LQR controller using a state-estimator for a plant without an integrator.

In the case shown in the block diagram, assume that there are two states, x_1 and x_2 , but only x_1 is available, hence $C = [1 \ 0]$, and the output y is

$$y = Cx = [1 \ 0] \begin{Bmatrix} x_1 \\ x_2 \end{Bmatrix} \quad (6-33)$$

Let \hat{x} represent the vector of the estimated states. The control law of Equation 6-32 becomes

$$u = -(K_{fb}\hat{x} + K_{ff}e) \quad (6-34)$$

The mathematical model for the estimator is similar to the plant model of Equation 6-6 with additional terms included to estimate the error to compensate for inaccuracies in matrices A and B. The estimation error is the difference between the measured output and the estimated outputs. The mathematical model for the estimator is

$$\dot{\hat{x}} = A\hat{x} + Bu + L(y - \hat{y}) \quad (6-35)$$

where the A, B, C, D are the matrices of the plant model from Equation 6-6, and $\hat{y} = C\hat{x}$.

One method to design the estimator matrix gain, L , is to use Ackermann's formula for pole placement for single-input systems. In this method, the gain L is calculated such that the state feedback signal places the closed-loop poles of the estimator at desired closed-loop pole locations, λ . Ackermann's formula is

$$L = [0 \quad 0 \cdots 0 \quad 1] [B \quad AB \quad \cdots \quad A^{n-1}B]^{-1} \phi(A) \quad (6-36)$$

for an arbitrary integer n . The term $\phi(A)$ is the characteristic polynomial of matrix A.

$$\phi(A) = A^n + \alpha_1 A^{n-1} + \alpha_2 A^{n-2} + \cdots + \alpha_{n-1} A + \alpha_n I \quad (6-37)$$

The coefficients α have a relationship with the roots of the polynomial, λ , which are also the closed-loop pole locations.

$$(s - \lambda_1)(s - \lambda_2) \cdots (s - \lambda_n) = s^n + \alpha_1 s^{n-1} + \alpha_2 s^{n-2} + \cdots + \alpha_{n-1} s + \alpha_n \quad (6-38)$$

This approach of designing the state estimator depends on the proper placement of the desired pole locations. The most frequently used approach is to choose pole locations from the root locus such that they are far to the left of the dominant poles of the plant.

6.2.3 LQR Results

An LQR controller is designed along with a state-estimator for the micromirror system using the linear plant model. The control design is done in Matlab using the 'lqr' command, and

the estimator is designed using the ‘acker’ command. The results are simulated on the linear plant model and the nonlinear model.

The weights Q and R are chosen to be

$$Q = \begin{bmatrix} 0 & 0 & 0 \\ 0 & 0 & 0 \\ 0 & 0 & 100000 \end{bmatrix} \quad (6-39)$$

$$R = 0.0001$$

The gain matrix from the LQR design produces a feedforward gain, $K_{ff} = [-100000.00]$, and a feedback gain vector, $K_{fb} = [0.0585388701 \quad 0.0000000952]$. The open-loop poles of the linear plant model of the micromirrors are $p = -307489.41 \pm 977754.00i$. Therefore, the desired closed-loop pole locations for the state-estimator are chosen to be $\lambda = [-3 \times 10^8, -3 \times 10^8]$. These closed-loop poles for the estimator are chosen as they lie far to the left of the open-loop poles on the real axis of the S-plane. Here, they are chosen to be repeated poles because the real part of the open-loop poles are repeated, but it is not required that they be the same value.

The response of the linear plant model and the nonlinear plant are for step inputs of different magnitudes are seen in Figure 6-11. The closed-loop system response for the LQR

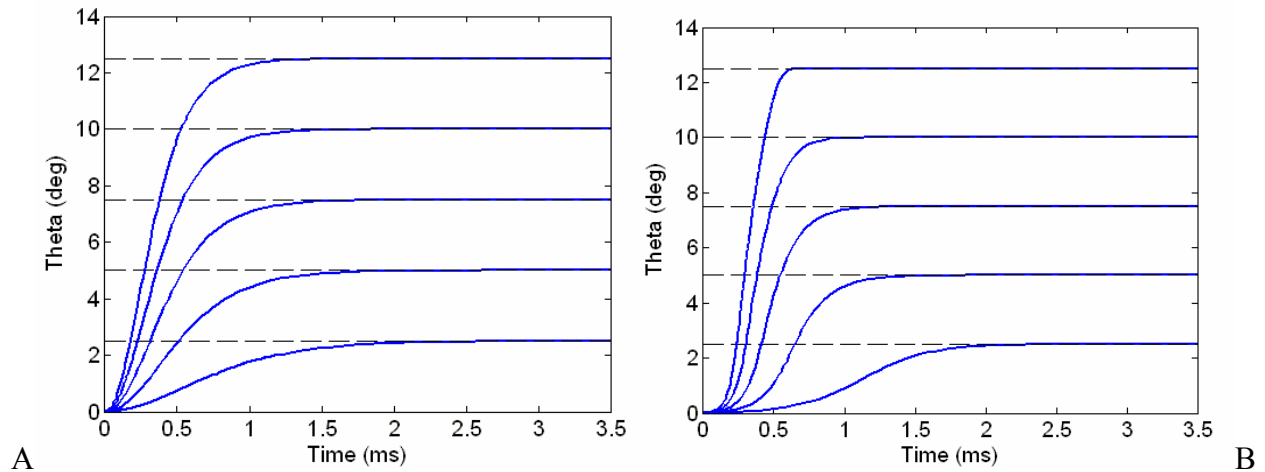


Figure 6-11. Step responses for LQR controller. A) Linear plant model. B) Nonlinear plant model.

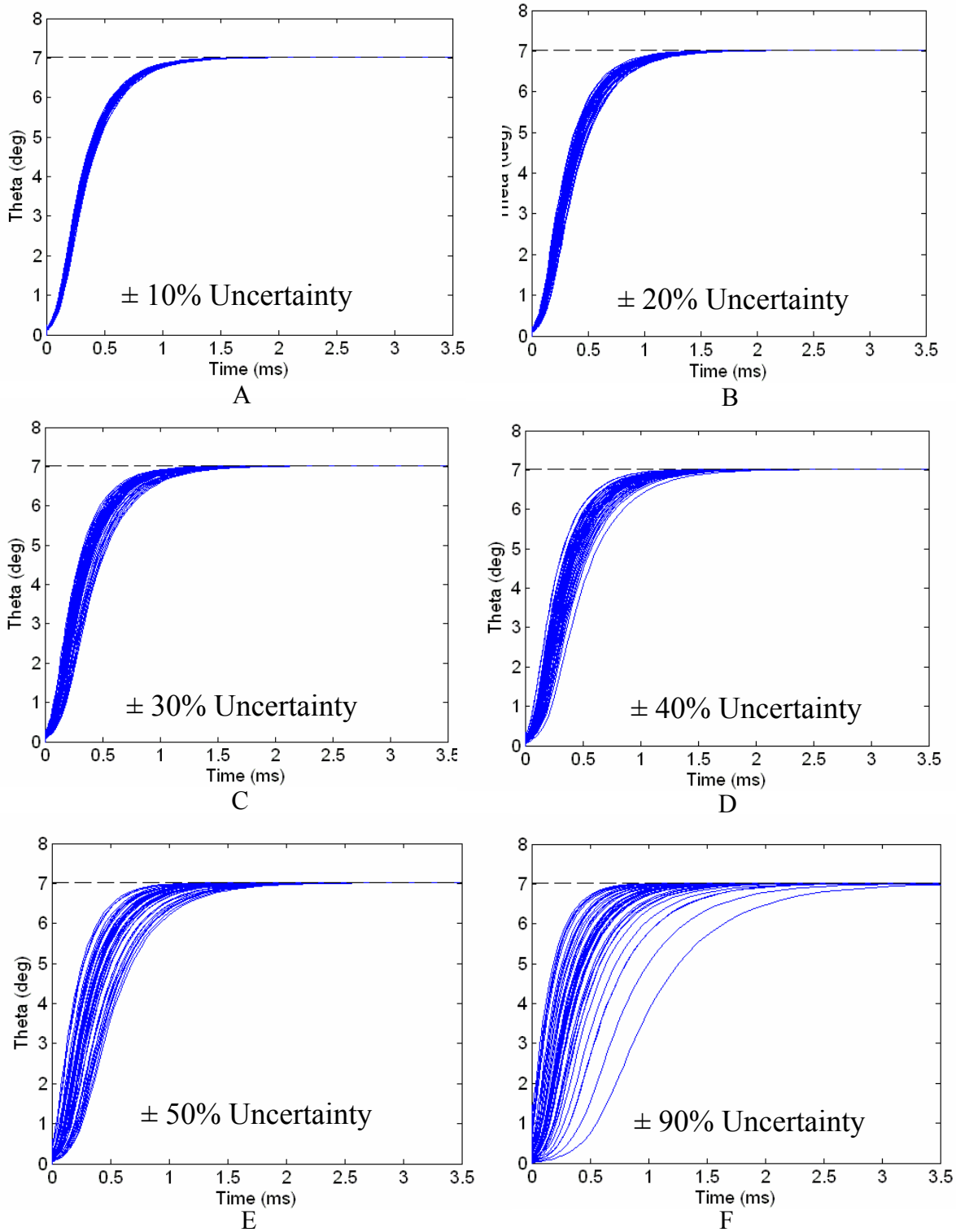


Figure 6-12. Closed-loop LQR response to a step input of 7 degrees for 50 random parameter variations.

controller is shown to be similar to that from the PID. The speed of the system response is dictated by the choices of Q and R in the control design. The effects of parametric model uncertainty are examined by testing the controller for the 50 plant models with variations from $\pm 10\%$ on the model parameters up to $\pm 90\%$ and the response to a step input is shown in Figure 6-12. The results for the LQR appear to be consistent with the results for the PID controller.

6.2.4 LQR Controller Response to Hysteresis

For the PID controller, discussion is presented in Section 6.1.3 concerning the response of the closed-loop system when the micromirror is commanded to an unstable position, and thus experiences electrostatic pull-in and hysteresis. In that demonstration, the behavior of the controller was found to result in an undesirable switching behavior that nevertheless did improve the hysteretic response. For the same conditions operating with an LQR controller using state-estimation, the controller would not be able to function in this unstable range of motion. Recall from LQR control theory presented in Section 6.2.1 and 6.2.2 that the state-estimation requires full controllability of the system, and this is not the case in the unstable range of motion. As a result, for implementing an LQR controller on this system it is particularly beneficial to avoid the electrostatic instability through the use of a progressive-linkage.

Based on the similarity between the responses from the PID and LQR controllers, it is safe to assume that the closed-loop LQR performance for the system with a progressive-linkage will be very similar to that of Figure 6-7. Figure 6-13 shows the closed-loop LQR step responses for the micromirrors with the progressive linkage, and they are able to achieve stable rotation above the pull-in limit of 16.5 degrees. Also shown are the LQR step responses for the 50 random plant variations with $\pm 10\%$ variation of model parameters.

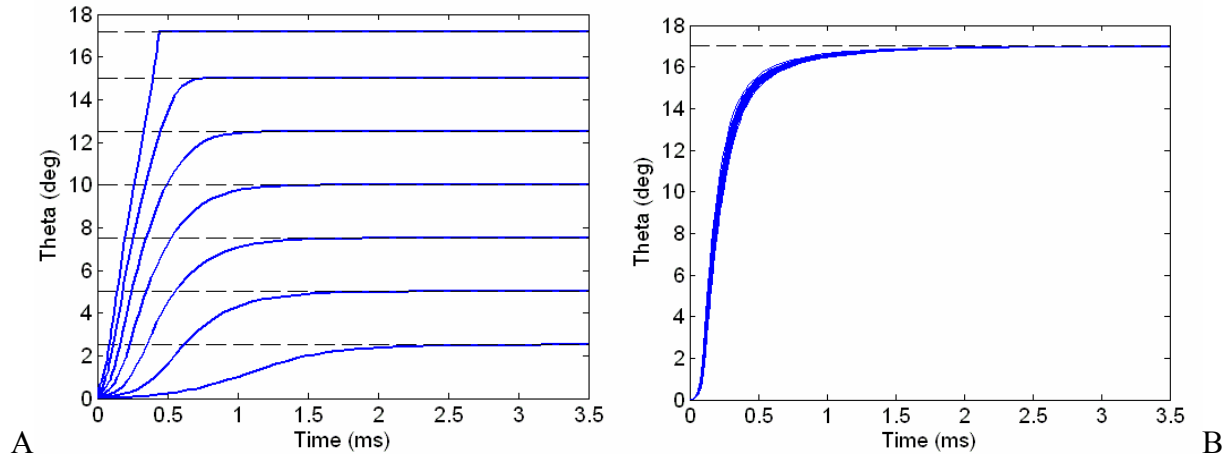


Figure 6-13. Closed-loop step responses for LQR controller for a system using a progressive-linkage. A) Step responses of different magnitudes. B) Step responses of 50 plants with model uncertainties.

6.3 Modeling the Micromirror Array

The work thus far has focused on modeling and control of just a single micromirror from an array of mirrors, assuming a single-input/single-output (SISO) system. In reality, these micromirrors are part of an array that is single-input/multiple-output (SIMO) since there is only one actuation voltage applied, but each individual mirror is capable of having a unique response. This section will demonstrate a model of multiple mirrors as a SIMO system and will discuss the feedback signals available by considering two different kinds of optical sensor: position detecting sensors (PSD) and charge-coupled devices (CCD). PSDs measure the locations and intensity of the incident light and output the position of the center of gravity (CG) of the total light distribution. These devices are inexpensive and easy to use; however the positions of the individual micromirrors are obscured. By contrast, a CCD sensor is able to output the locations of the individual light sources; however they are much more expensive devices and require considerably more computation and processing methods to utilize the sensor information.

The controllers developed in Section 6.1 and 6.2 are implemented on the array model to determine their effectiveness at reducing the steady-state error of the system as a whole when

model uncertainties are present. Considering the system of micromirrors as they function in an array is a critical step in expanding the application of feedback control from just one device, to being able to control very large arrays that are required for many adaptive optics applications.

6.3.1 Modeling the Array of Mirrors

The preceding chapters have developed analytical models for individual micromirror components that have a SISO structure. Extending this to a SIMO model that includes multiple micromirror arrays is accomplished by simply adding multiple mirror models in parallel as the plant of the system. Figure 6-14 shows this system architecture in which a single input is given to the array of mirrors, and multiple outputs from that system are produced. These outputs are the position states for each individual micromirror. Figure 6-15 shows schematically what this system architecture looks like for a system that assumes 5 micromirrors in the array. This image is not drawn to scale so that the individual mirrors and rays of light can be seen. While in reality the array is much larger, using only 5 mirrors allows for a more tractable demonstration of array performance in the simulation environment. It can be difficult to compare the results for a larger number of mirrors.

Just as it was shown for the open-loop dynamic model in Chapter 5, if the model parameters vary, the response of each mirror will vary for a given input signal. If all the mirrors

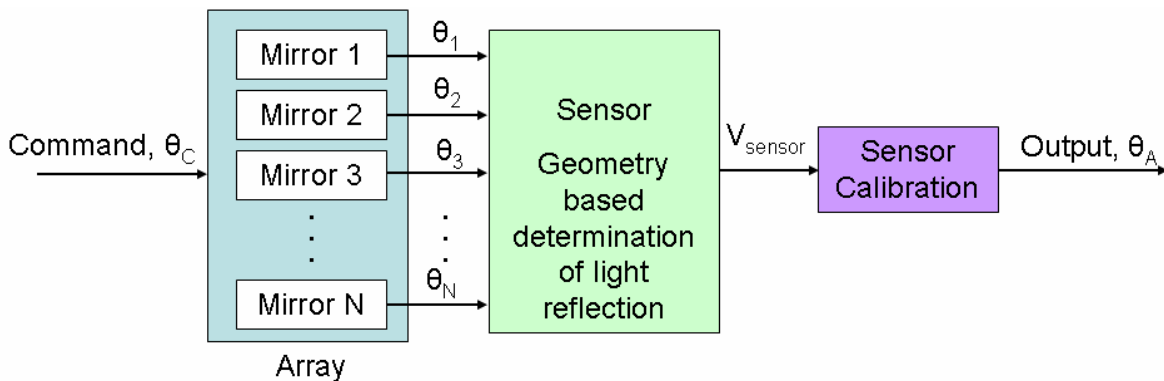


Figure 6-14. Schematic of modeling an array of mirrors as a SIMO system.

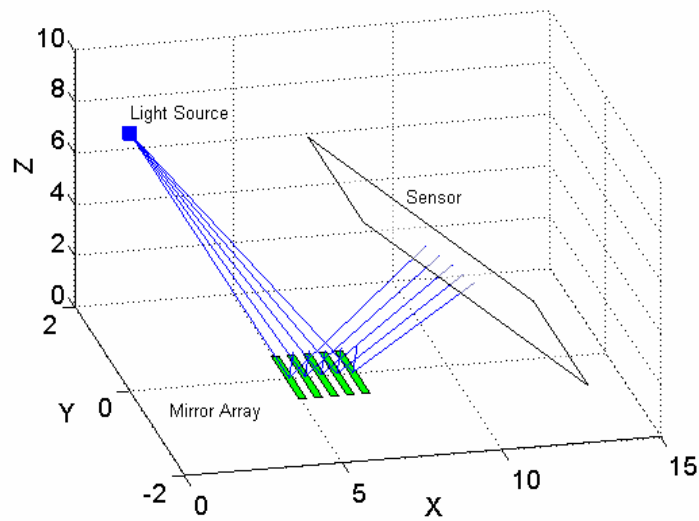


Figure 6-15. Schematic drawing of an array of 5 mirrors.

in the array have the same plant model, then they will all have the same response. However, if the model parameters of each mirror in the array are allowed to independently take on values subject to uncertainty in mass, stiffness, damping ratio, and capacitance, then the results are not so well behaved. The challenge comes from determining one overall error metric that can be used for the feedback controller such that the errors in the system can be decreased. Thus, the goal becomes trying to decrease the total amount of error in the system, which means it is possible for the individual errors in the mirror responses to still exist. While model uncertainty can be controlled effectively for one mirror at a time, trying to implement control for this SIMO array system is a more difficult problem.

One problem with controlling this array system comes from choosing the appropriate measurement to use as a feedback signal. In the case that each mirror could be controlled independently, then one approach is to treat it as multiple SISO systems in parallel and provide one control signal for each micromirror and measure its individual performance. In that case, the problem quickly becomes one of scale for determining the best way to accomplish this for a very

large array. The case for SIMO system does not have to deal with the issue of scaling multiple control algorithms, but rather how to apply a single controller to a group of mirrors. While each mirror can behave independently, there is still only one available control input to the system. The type of sensor chosen to provide the measurement is critical in determining the overall performance metric for the system, and the type of error signal used for the feedback control system. To better understand this, several available sensor types are considered for determining the impact each would have on detecting and interpreting the system performance. The sensors considered here are position sensing detectors (PSD), and charge-coupled devices (CCD).

6.3.2 Sensor Types

When a light source is incident on the surface of a PSD, the sensor will output a current or voltage signal that corresponds to the location of the center of the total distribution of the light intensity on the sensor surface. This location can be considered as the center of gravity (CG) of the total light on the sensor surface. PSDs can be one dimensional, which means that they are able to detect the CG of the light in only one direction, or two dimensional, detecting the CG of the light in two directions. Consider in Figure 6-16, the case of light from one array of mirrors reflecting onto a 1-D PSD in which there are errors in the actual positions compared to the desired positions. Errors in spacing between the spots of light can result in CG measurement that is different from that desired. The control system seeing this error will try to correct such that the CG error goes to zero, when in fact this can cause the actual deflections of the micromirrors in the array to be different values from what is desired. Figure 6-16 also shows the 1-D PSD with errors in linearity that could be caused by off axis rotations of the mirrors. For small rotations, the same problem of error in the CG occurs. Since the 1-D array is only able to measure the CG in terms of one direction (y-axis shown), the off-axis deflection cannot be

directly measured. There is also the case that for a very large error in spacing or linearity, some of the light could be deflected off of the 1-D PSD entirely, also affecting the location of the CG.

For a single micromirror array being measured by a 2-D PSD, similar problems in calculating the CG occur, except in this case it is possible to locate the CG in both the x and y-axes. As seen in Figure 6-17, errors in spacing can shift the CG in the y-direction, but linearity

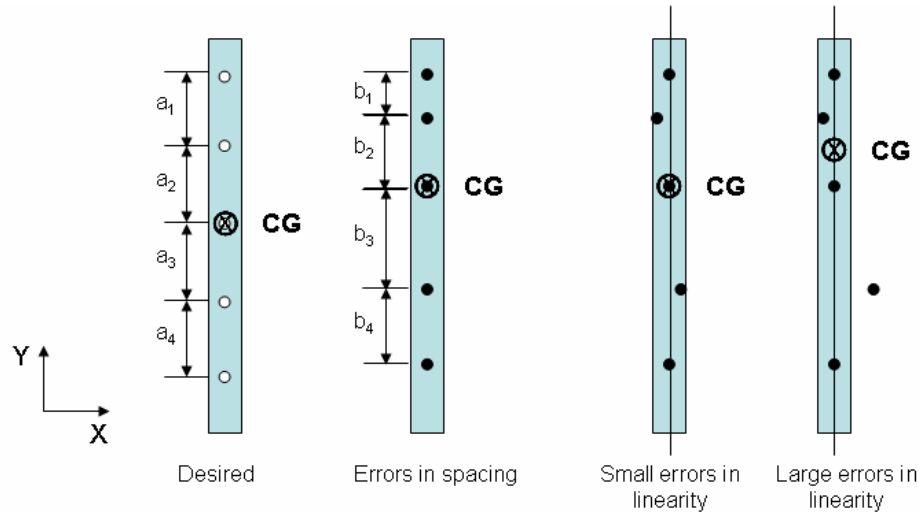


Figure 6-16. Illustration of the measured center of gravity (CG) on a 1-D PSD when there are errors in the spacing and linearity of the micromirrors.

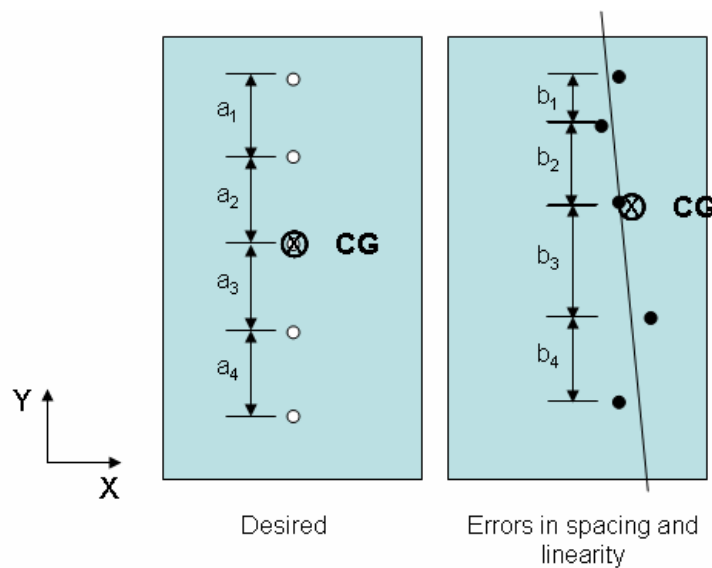


Figure 6-17. Illustration of the measured center of gravity (CG) on a 2-D PSD when there are errors in the spacing and linearity of the micromirrors.

errors can also shift the CG in the x-direction. Despite the limitations of PSDs, they offer the advantages of giving an analog signal with a very fast response. In addition, PSDs are typically more affordable than CCDs.

To avoid the problems such as those described for using a PSD and to allow for the simultaneous measurement of light from multiple micromirrors in an array, one may use a CCD. The CCDs are an array of metal-oxide-semiconductor (MOS) diodes that are able to provide digital information of the light intensity of each pixel in the CCD array. This information can be interpreted using an image processing algorithm to determine the location of each separate spot of light from the micromirror arrays. Then it is possible to obtain x and y-direction displacement measurements for each spot and compare that with the desired positions. This is illustrated in Figure 6-18 for light from two arrays in which the dark spot indicates the actual position of the

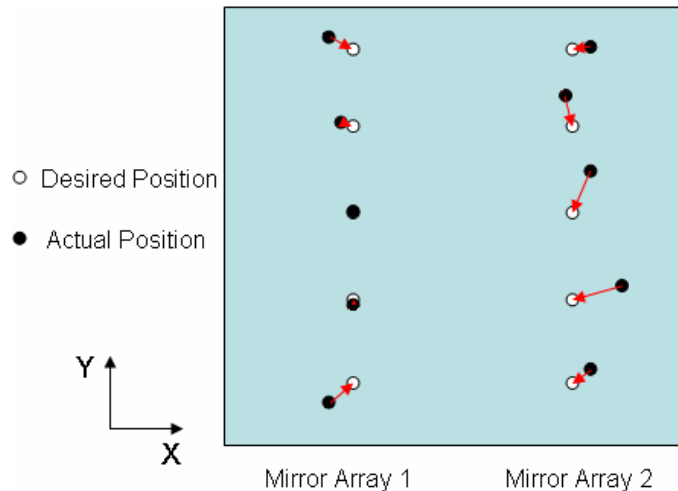


Figure 6-18. Illustration of the measured errors of the reflected light from two micromirror arrays onto a CCD.

reflected light, and the white spots indicate the desired positions. The error is drawn as a vector from the actual to the desired positions. If each row of mirrors were given a separate actuation voltage signal, it would be possible to control the position of each spot to reduce the individual error signals. Because the mirror arrays discussed here have only one actuation signal available

for the entire array, it will only be possible to reduce the overall error signal by perhaps using a sum of the squares of the displacement error vectors. An additional error metric could be to consider statistical yields, such as trying to achieve desired performance goals for a certain percentage of mirrors. The ability to reduce the error is further limited in that the mirrors have only one axis of rotation; thus the x and y errors are not independent.

6.4 Modeling the Sensor Response

Including the sensor model into the simulation of the micromirror arrays involves taking the geometry of the problem into account. Assuming that the locations of the light source, the micromirrors, and the sensor are known, this becomes a calculation of the system geometry to determine the location of the reflected light. Figure 6-19 shows a schematic of beam steering with only one micromirror. The light source, each micromirror, and the sensor, are given a coordinate frame such that they can be located and oriented in space with respect to a global reference frame, E. Light that travels to the micromirror is defined by the vector $\bar{r}_{A0 \rightarrow B0}$. Following the laws of reflection, light reflecting off of a flat mirror will have an angle of reflection that is equal to the angle of incidence, such as that shown in Figure 6-20. In general, the angle, Ψ , between two vectors, \bar{a} and \bar{b} as shown in Figure 6-20, can be calculated using the dot product relationship.

$$\bar{a} \bullet \bar{b} = |\bar{a}| |\bar{b}| \cos \Psi \quad (6-40)$$

In this case, the two vectors are the vector $\bar{r}_{A0 \rightarrow B0}$ and the unit normal vector of the mirror surface, \hat{b}_k . Therefore, the angle of incidence, ϕ , is given as,

$$\phi = \cos^{-1} \left(\frac{-\bar{r}_{A0 \rightarrow B0} \bullet \hat{b}_k}{|\bar{r}_{A0 \rightarrow B0}| |\hat{b}_k|} \right) \quad (6-41)$$

Knowing the angle of incidence, ϕ , now allows for the vector of the reflected light to be calculated. It is possible to determine the distance between the unit normal vector of the mirror and the light source as shown in Figure 6-21 by calculating two vectors $\bar{\delta}_1$ and $\bar{\delta}_2$ that are perpendicular to each other at point N, and form a right triangle with the vector $\bar{r}_{A0 \rightarrow B0}$ as the hypotenuse. The vector $\bar{\delta}_2$ is along the \hat{b}_k unit vector. The magnitudes of these two vectors are

$$|\bar{\delta}_1| = |\bar{r}_{A0 \rightarrow B0}| \sin \phi \quad (6-42)$$

$$|\bar{\delta}_2| = |\bar{r}_{A0 \rightarrow B0}| \cos \phi \quad (6-43)$$

A location for the reflected light, point R, can be found by reflecting vector $\bar{\delta}_1$ about the unit normal vector \hat{b}_k at point N, resulting in a new vector, $r\bar{\delta}_1$, that reveals a location through which the reflected ray passes. Now there is a known relationship for the reflected ray of light, represented by the vector, $\bar{r}_{B0 \rightarrow R}$.

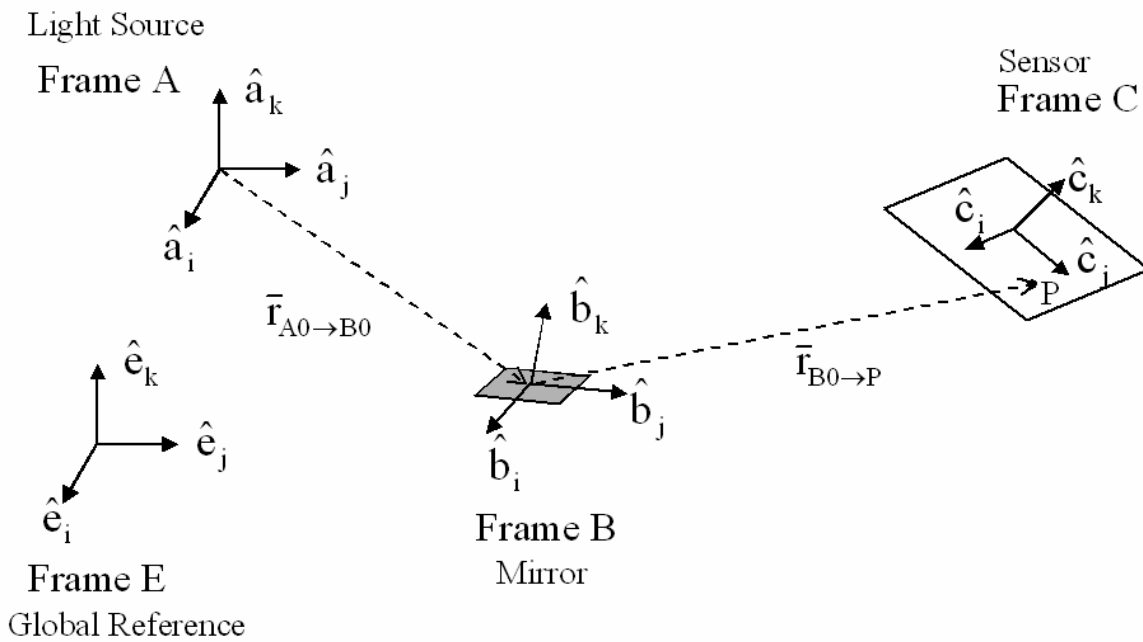


Figure 6-19. Schematic of the beam steering experiment with only one micromirror.

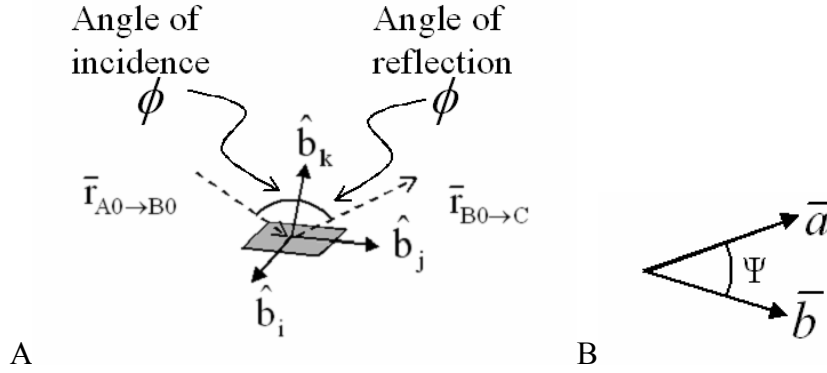


Figure 6-20. Geometry used to determine the angle of incidence and reflection. A) The angle of incidence is equal to the angle of reflection. B) For two vectors \mathbf{a} and \mathbf{b} , the angle between them, Ψ , can be determined from the dot product.

Next, the intersection of this ray of light with the plane of the sensor can be calculated. Referring to Figure 6-22, let the sensor plane in Frame C be defined by three points, C_1 , C_2 , and C_3 which have global coordinates (C_{ix}, C_{iy}, C_{iz}) , where the subscript i may equal 1, 2, or 3. The vector of the reflected ray of light, $\vec{r}_{B0 \rightarrow R}$, is given by two points, the origin of the B frame, $B0$, and the point R, which are known to have global coordinates $(B0_x, B0_y, B0_z)$ and (R_x, R_y, R_z) , respectively. The orientation of the B frame will represent the angle of rotation of the micromirrors as they are actuated, and will rotate about the \hat{b}_i unit vector. The intersection of the vector with the plane, at point P, is found by simultaneously solving the following four equations for the variables x , y , z , and t .

$$\begin{vmatrix} x & y & z & 1 \\ C_{1x} & C_{1y} & C_{1z} & 1 \\ C_{2x} & C_{2y} & C_{2z} & 1 \\ C_{3x} & C_{3y} & C_{3z} & 1 \end{vmatrix} = 0 \quad (6-44)$$

$$B0_x + (R_x - B0_x)t = x \quad (6-45)$$

$$B0_y + (R_y - B0_y)t = y \quad (6-46)$$

$$B0_z + (R_z - B0_z)t = z \quad (6-47)$$

Solving for t yields,

$$\frac{\begin{vmatrix} 1 & 1 & 1 & 1 \\ C_{1x} & C_{2x} & C_{3x} & B0_x \\ C_{1y} & C_{2y} & C_{3y} & B0_y \\ C_{1z} & C_{2z} & C_{3z} & B0_z \end{vmatrix}}{\begin{vmatrix} 1 & 1 & 1 & 0 \\ C_{1x} & C_{2x} & C_{3x} & -B0_x \\ C_{1y} & C_{2y} & C_{3y} & -B0_y \\ C_{1z} & C_{2z} & C_{3z} & -B0_z \end{vmatrix}} = t \quad (6-48)$$

This value for t calculated from Equation 6-36 may be substituted back into Equations 6-45, 6-46 and 6-47 to solve for the (x, y, z) global coordinates of the intersection point P. This process can be repeated for multiple mirrors to determine the coordinates of their reflected light on the sensor. Now that the reflected light can be located, it is possible to calculate the sensor measurement for the system depending upon the type of sensor used.

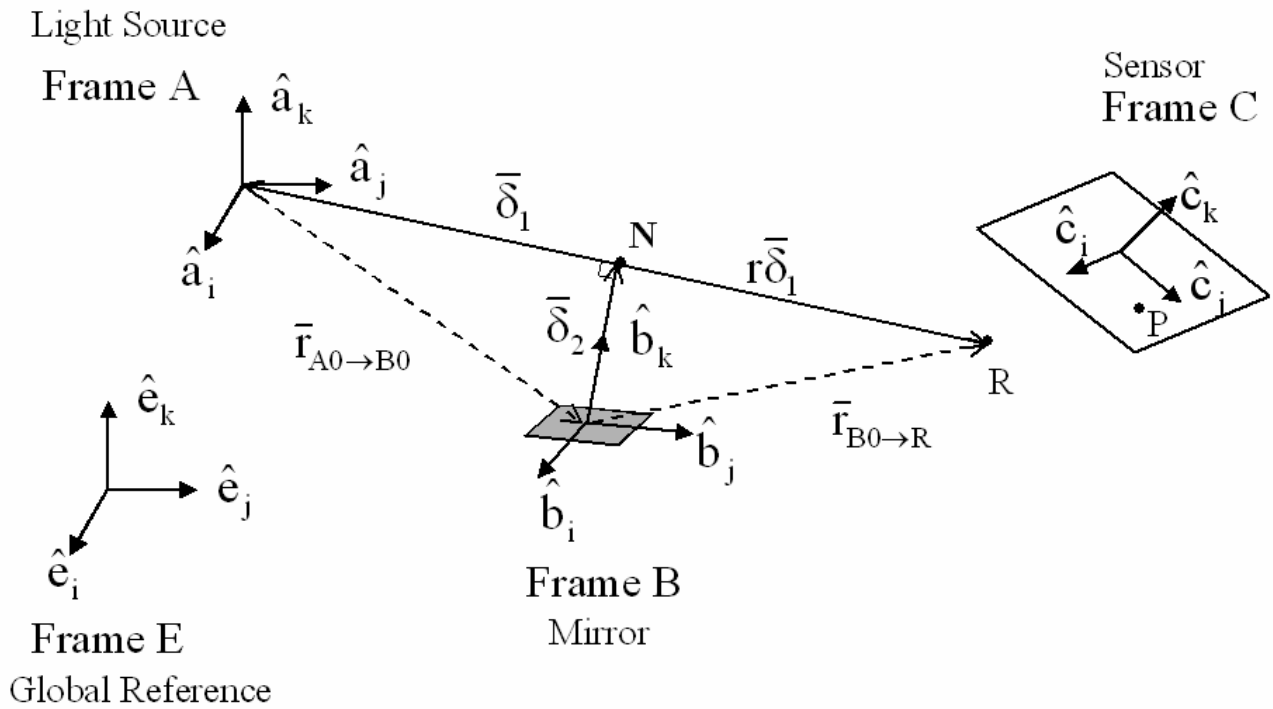


Figure 6-21. Calculating the reflected ray of light.

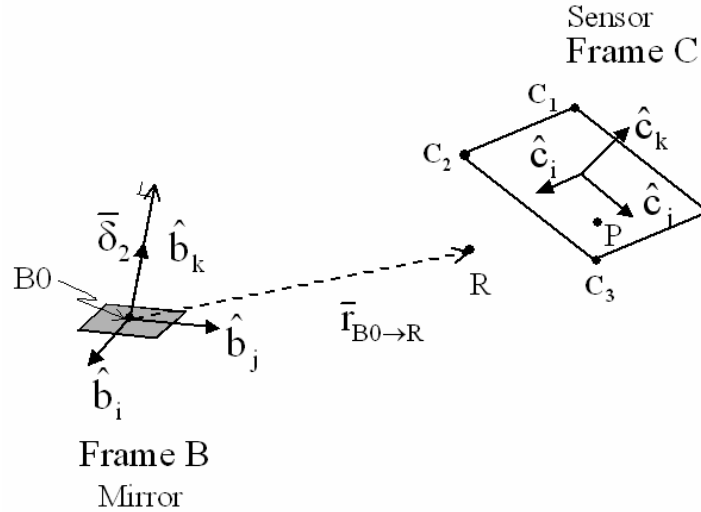


Figure 6-22. The intersection of the line from B0 to R and the plane C occurs at point P.

6.4.1 PSD Response

A 1-D PSD is incorporated into the model for the system of arrays by calculating the locations of the reflected light and determining the center of gravity of the light. Laser light is known to have a Gaussian distribution of light intensity, with the light being more intense in the center of the beam, and reducing toward the outside of the beam [105]. Therefore, for the model of sensor performance, the light from the mirrors is weighted accordingly such that the light in the center has a higher intensity, following a Gaussian distribution. Center of gravity may be calculated as

$$CG = \frac{1}{W} \sum_{i=1}^n w_i \bar{r}_i \quad (6-49)$$

where W represents the total weighting of the light intensity, w_i represents the weight of the light intensity for one ray of light, and r_i represents the position of the ray of light on the sensor for n total rays of light.

Figure 6-23 shows a representation of a system of 5 micromirrors in which the light is reflected onto a sensor. This figure is not drawn to scale so that the individual light rays are

more easily seen. The CG of the light is calculated for this ideal case as equal to the position of the center mirror. A 2-D representation of the reflection on the sensor is also shown. The CG is output as a voltage between ± 10 V, where a value of 0 V indicates the CG is at the center, +10 V indicates the CG is at the top, and -10 V indicates that the CG is at the bottom of the sensor array. In order to relate this sensor value of the CG back to a meaningful measurement in terms of the angle of rotation of the mirrors, θ , the sensor output is determined first for an ideal set of mirrors. This calibration then allows the sensed CG to be converted to an angle corresponding to the angle of the micromirrors, θ . The calibration result for the case of 5 micromirrors is given in

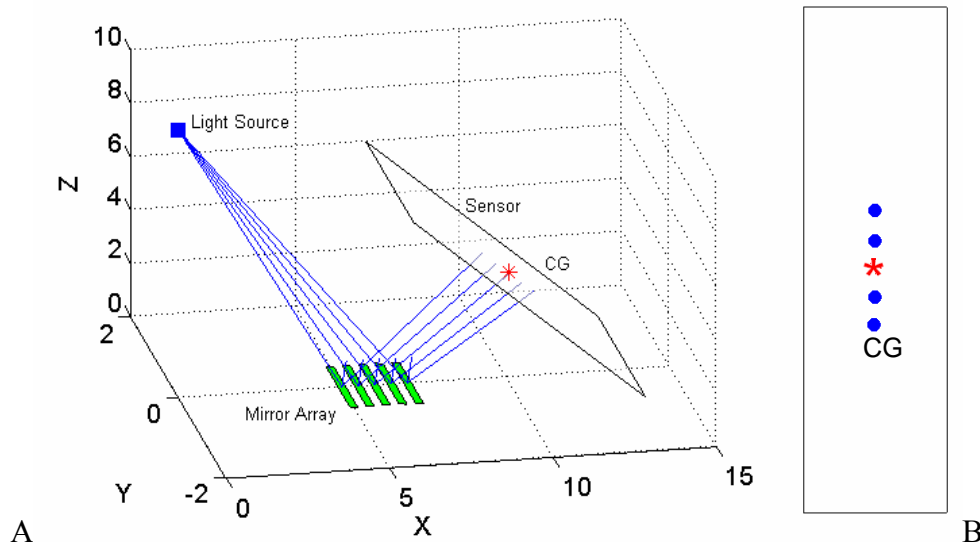


Figure 6-23. Schematic of 5 micromirrors in an array reflecting light onto a PSD sensor. A) The CG of the measurement is calculated in the sensor plane. B) A 2-D view of the reflected light on the sensor plane with the CG marked in the red star.

Figure 6-24. If any of the reflected light is directed off of the sensor, then this light is not recorded and its contribution is neglected in calculating the CG. This can cause a shift in the measured value of the CG.

In order to evaluate the effectiveness of this sensor at providing feedback signals to the system, the sensor response is determined for the case of 5 micromirrors with randomly varied

models. Figure 6-25 shows the resulting open-loop step response for each mirror and the overall CG measurement. Also shown are the position errors for each mirror and the overall error. The sensor outputs the location of the CG of all 5 mirror responses showing that on average, the 5 mirrors of the array have a steady-state error. In the case of a broken device or a mirror in the

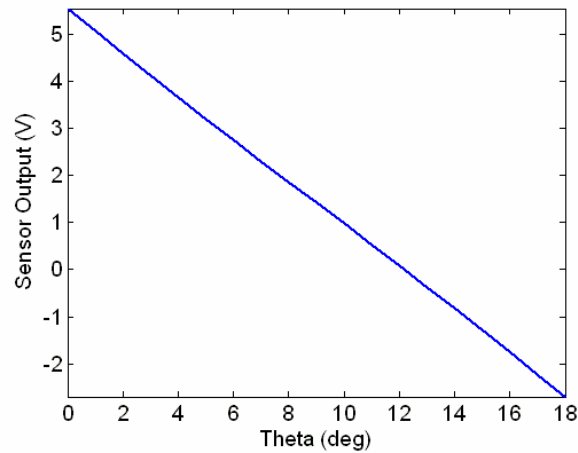


Figure 6-24. Calibration of the PSD for ideal case of five micromirrors.

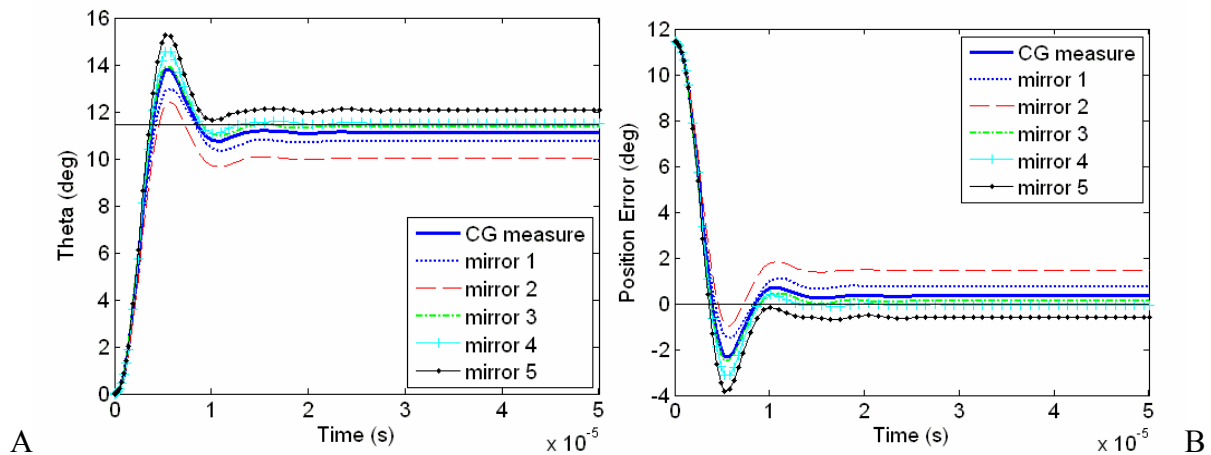


Figure 6-25. Open-loop results to a step response for an array of 5 micromirrors with model uncertainty. A) Step response. B) Position error.

array with very deviant behavior, the CG calculation can be greatly affected. If one mirror is broken and remains stationary, the CG calculation for the overall array will be affected. This is shown in Figure 6-26 in which one mirror is broken and does not actuate while the other mirrors

are considered to have the ideal model with no uncertainty. It is clear that the inclusion of model uncertainty in the other mirrors would only add to the calculated error of the CG. This could also be the case that occurs when some mirrors in the array experience pull-in at different times. This illustrates a limitation of using a PSD for the sensing mechanism.

The model of the array of mirrors and the sensor can be incorporated into a control system like that in Figure 6-27. To illustrate the effects of using a PSD as the sensor for this

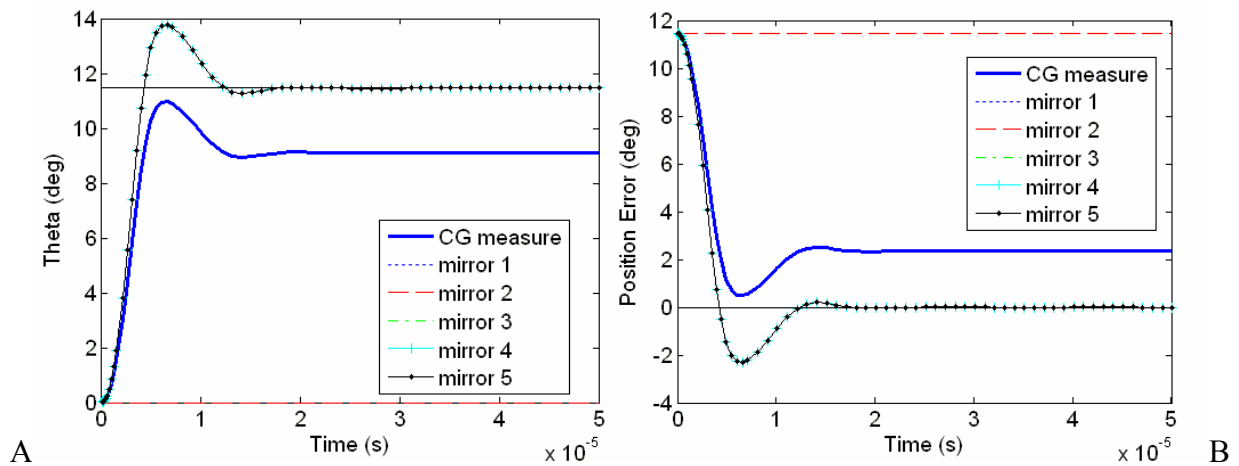


Figure 6-26. Open-loop response for system with one broken mirror and 4 ideal mirrors, measured by a PSD. A) Step response. B) Position error.

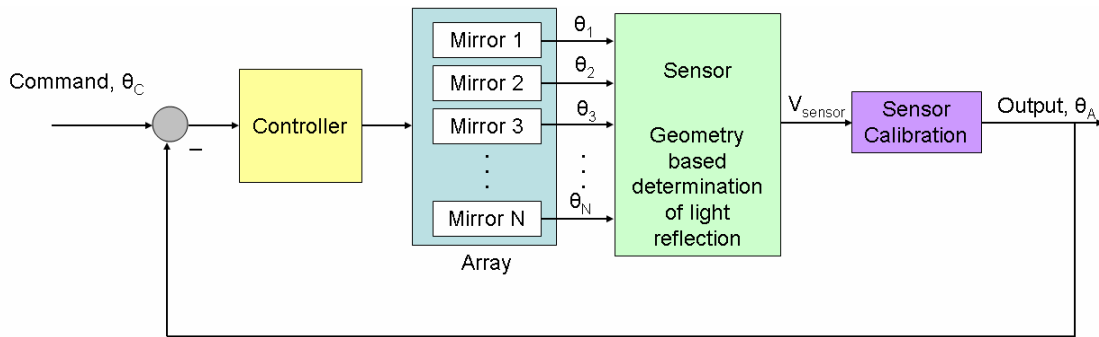


Figure 6-27. Incorporating feedback control into array model.

micromirror array system, the closed loop response is determined. Figure 6-28 shows the response for a PID controller, and likewise, Figure 6-29 shows the response using the LQR controller. In both cases, the CG measurement is used as the feedback signal, and the controllers

thereby only see this average error measurement. The controllers are both able to reduce the average error of the system, but this is really only accomplished by shifting the responses of the 5 mirrors. In this case, the two mirrors, 3 and 4, that had the least amount of error in the open-

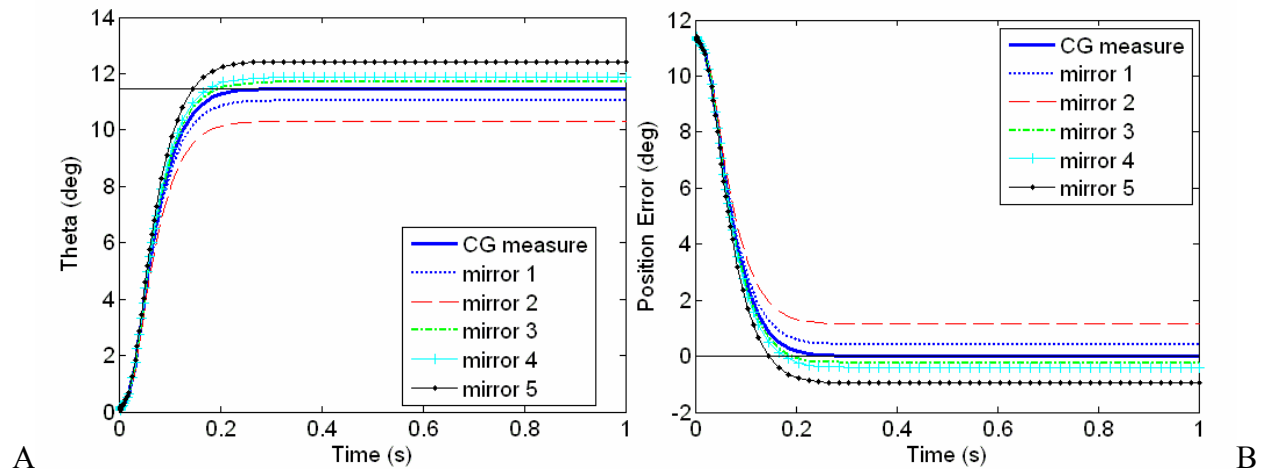


Figure 6-28. Controlled PID step response using PSD sensor. A) Step response. B) Position error.

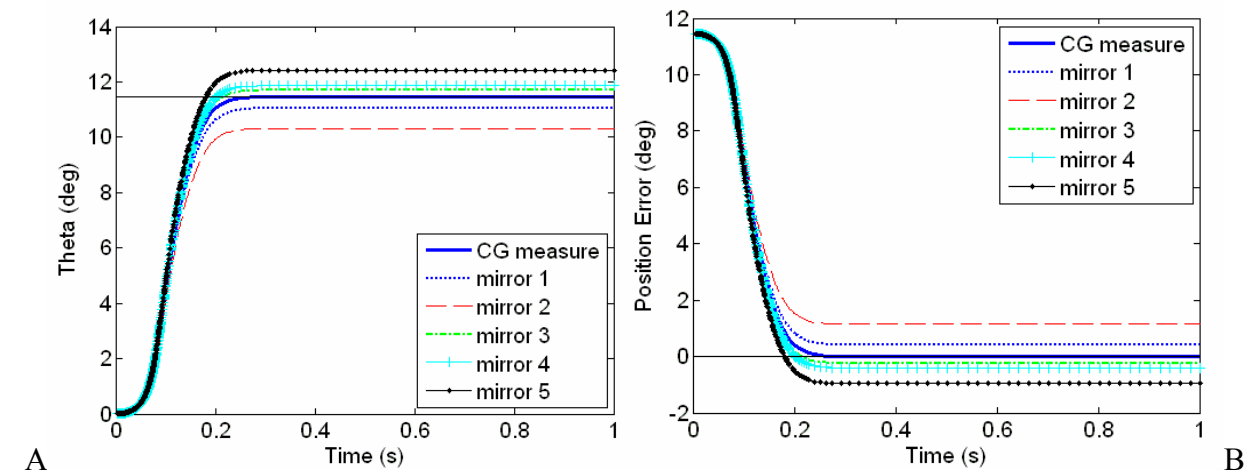


Figure 6-29. Controlled LQR step response using PSD sensor. A) Step response. B) Position error.

loop response are actually shifted so that in the controlled system, they have more error. Another weakness is illustrated in closed-loop control in the case of a device in which one mirror in the array is not functioning. Shown in Figure 6-30 is the closed-loop PID response of the system

with one mirror broken, and it is clear that in order to compensate for the malfunctioning mirror, the system instead drives the other four mirrors to an incorrect position.

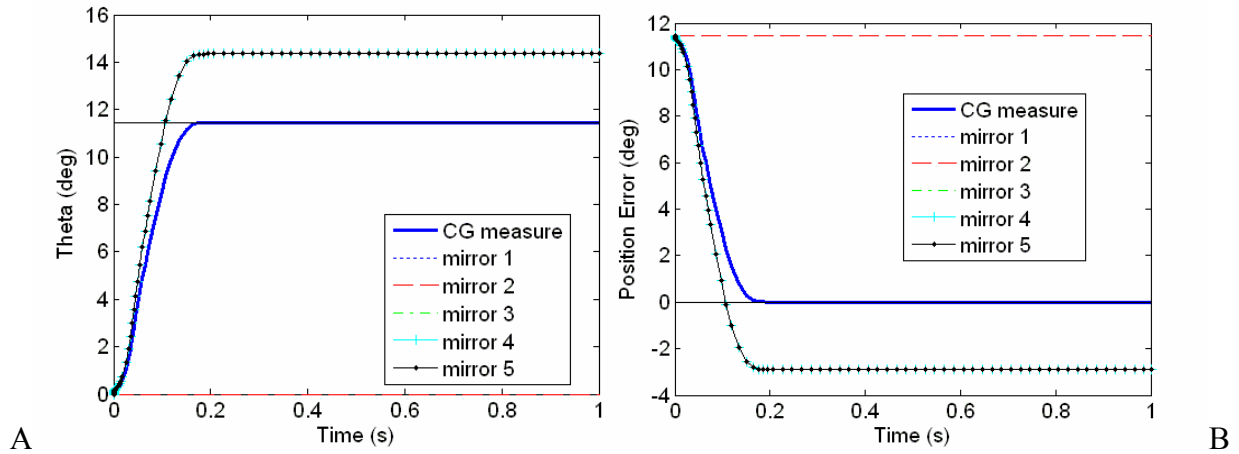


Figure 6-30. Closed-loop response for system with one broken mirror and 4 ideal mirrors, for a PID controller and a PSD sensor. A) Step response. B) Position error.

6.4.2 CCD Response

CCD sensors have an advantage over the PSDs in that they can measure and interpret the response of each mirror in the array separately, such as in the Figure 6-31. The limitation of the SIMO system still imposes a requirement that these sensor measurements be compiled into only one metric. Using a CCD for this SIMO system has many of the same limitations of the PSD. The error metric used to compare the actual micromirror position to the desired micromirror position may be limited to represent some average of the errors of all of the mirrors. In this case, the results for using a CCD are not an improvement over using a PSD. However, the ability of the CCD to identify individual positions of the micromirrors does allow for some advantages. For instance, in the case of a damaged or broken micromirror, the actuation for that one mirror may remain at zero, or have a drastically deviant behavior compared to a mirror that is working properly. Using a PSD sensor, the measurement from the damaged mirror will remain part of the CG calculation, thus skewing the overall results. With the appropriate processing algorithm, the

data from the CCD can be used to identify any mirrors that are broken or have highly unusual behavior and eliminate those mirrors from the control consideration. This is demonstrated simplistically in Figure 6-32 in which the PID closed-loop system is able to identify the broken micromirror that remains at zero degrees actuation, and thus eliminates that measurement from the error metric. Additional error metrics may also be defined, such as identifying a yield for the

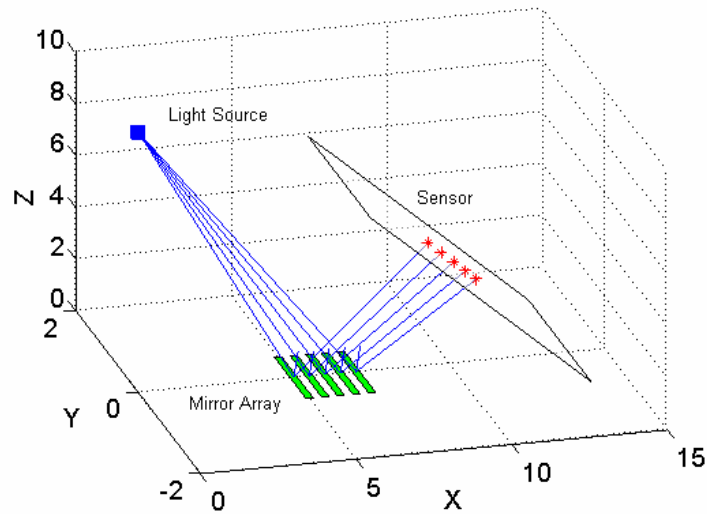


Figure 6-31. Schematic of 5 micromirrors in an array reflecting light onto a CCD sensor where each separate location of the light can be measured.

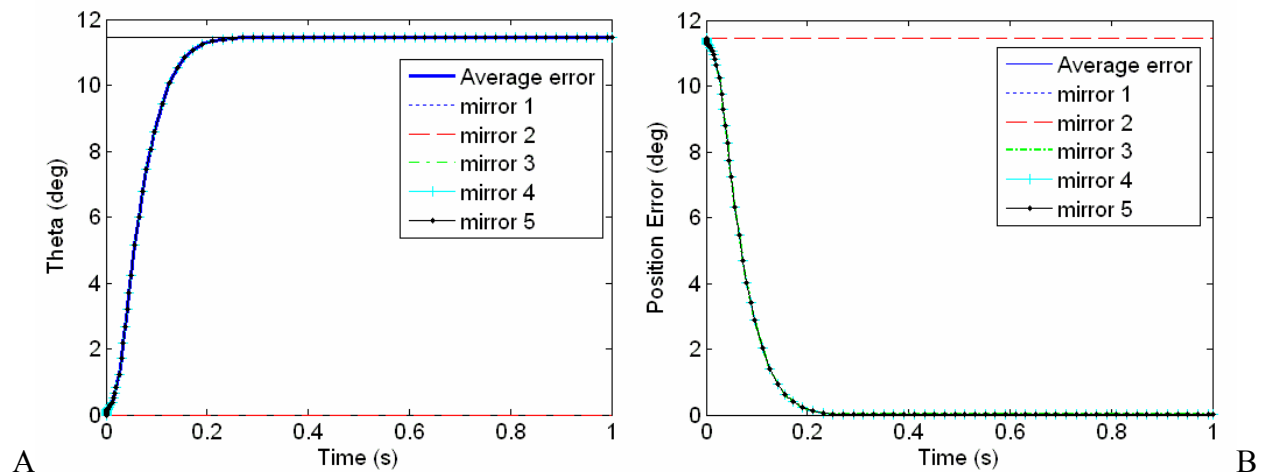


Figure 6-32. Closed-loop response for system with one broken mirror and 4 ideal mirrors, for a PID controller and a CCD sensor. A) Step response. B) Position error.

array such that a certain percentage of the mirrors are guaranteed to have minimal error, even if it means that other mirrors will have larger errors. Weights can be assigned to the measurements to determine those mirrors that have a higher priority in the error measurement.

6.4.3 Summary of Sensor Analysis

It is clear that the limitations in the controllability of the individual micromirrors inhibit the ability of the controller to affect only some aggregate response for the system. The PSD sensor, while fast, inexpensive, and easy to use, is not able to differentiate the responses of the single mirrors, and is therefore most affected by deviations in the single mirrors responses. The CCD sensor is a more expensive option, both in purchase cost and computational efficiency, however it does allow for more flexible parsing of the error signal that can be used to concentrate the control effort on a subset of selected micromirror responses. In the case of trying to control more than one array of mirrors, or for a system of mirrors with SISO controllability, then the CCD array would be the obvious choice of sensor because it can detect multiple locations of light. The issue of sensor noise was not taken into account in this study, but this too will affect the outcome of the control system. The level of noise will vary depending on the sensor chosen, as well any noise from the environment such as vibrations. While noise levels for a given PSD or CCD product vary by the make and model of the sensor, CCDs typically have lower noise.

6.5 Chapter Summary

The control algorithms explored in this chapter, including PID and LQR, are designed based on the 1DOF model developed in previous chapters, and the closed-loop system is analyzed in simulation to explore the effectiveness of these control schemes and examine unique issues that may be encountered, such as the electrostatic instability phenomena. Other implementation issues are addressed, including choosing the appropriate sensing elements with which to detect the micromirror position for feedback. The different sensor types discussed are

all optical, that is they can measure the position of light reflected from the micromirrors, and depending on the type of sensor chosen, they can operate in one or two degrees of freedom. PSDs are only able to report the aggregated results for all light incident on the sensor surface, while CCDs are able to report individual signals from different sources. Due to the actuation limitations for the micromirror arrays in this study, it is concluded that a PSD sensor is adequate for the system, but there are still advantages that can be obtained from the use of a CCD. The next step in this work, which is included in the list of future work, is to develop an optical testbed to implement the control algorithms presented here, and to determine their ability to influence the precision and accuracy of the micromirror arrays. The optical testbed must also consider the implementation issues of noise in the feedback loop from the sensor and from the environment. Additional studies concerning control design include examining the PID and LQR controllers for response at higher frequencies and exploring further nonlinear dynamic behaviors that result from the electrostatic instability.

CHAPTER 7 CONCLUSIONS AND FUTURE WORK

The work presented here is an effort to model and analyze the behavior of MEMS micromirror arrays that have inconsistent behaviors caused by parametric uncertainties and nonlinear effects from electrostatic actuation. The micromirror arrays are evaluated first by extensive analytical modeling and experimental validation to determine their performance and understand the effects of fabrication variations. Using tolerance information from the fabrication process, it was shown that it is possible to model the effects of fabrication variations on the performance of the mirrors and to determine the sensitivity of that performance with respect to a particular parameter. These modeled results are compared to open-loop characterization data obtained using an optical profiler. It is apparent that there exists varying behaviors for the mirrors of the arrays in terms of the static voltage-displacement relationships and the electrostatic pull-in and hysteresis that can affect the dynamic system response as well. Electrostatic instability is addressed here through the introduction of a progressive-linkage that provides a continuous, nonlinear restoring force to the device that allows it to theoretically achieve stable actuation over the entire range of motion of the micromirror. Bifurcation theory was used to further characterize the electrostatic behaviors and the effectiveness of the progressive linkage to mitigate these behaviors.

To validate the dynamic modeling, modal analysis was performed using FEA on the structure and validated experimentally using measurements obtained using a Laser Doppler Vibrometer. An examination of the participation factors for the response of the first mode in each direction reveals that the primary direction of the response is in the rotational X-direction (ROTX), which corresponds to the one-degree-of-freedom model assumption. However, it is clear that motion in other directions, namely the Z-direction (vertical) affects the compliance of

the system and the response, resulting in a lower than predicted first natural frequency. Because the electrostatic force that is applied to the micromirror is always an attractive force, drawing the moving electrode down toward the fixed substrate and if resonance is avoided, smooth rotational motion in one degree-of-freedom is still accomplished. The presence of extra degrees of freedom does, however, show the limitations of the 1DOF model assumption, which limits the analysis to only low frequency responses where resonant behavior may be avoided.

To further evaluate the effects of uncertain system behavior, simple feedback controllers are developed using a linear system model and then applied to the nonlinear model. This work demonstrates the use of PID and LQR control, and tests these controllers on nonlinear plant models with varying parameters. The results from both controller designs show that they are able to provide stable actuations with no overshoot for a range of plant models. The cost of applying these control methods comes in terms of the speed of the response. The open-loop dynamics, while exhibiting some overshoot behavior in the transient response, operates on a very fast time-scale, on the order of μs . Closing the loop on the system slows the response time by several orders of magnitude to ms; however, this is still a sufficiently fast response time for many applications, and the added benefits of the controllers at eliminating overshoot and correcting system response in the presence of model uncertainty are clearly worthwhile.

After modeling and developing controllers considering only one micromirror at a time, the system is evaluated as an entire array of devices. The SIMO structure of the system puts limitations on the ability to control each micromirror individually, and it is important to consider the type of feedback information available and how it is utilized. Both PSD and CCD optical sensors are considered and it is found that with both sensors, it is possible to correct for the average errors of the system, while not guaranteeing that each micromirror in the array will in

itself attain perfect position tracking. Use of a CCD sensor does have advantages however that can allow for more advanced sensor processing allowing for selective control of the sensor data, such as identifying outliers and ensuring their measurements are not retained in the feedback signal. An optical testbed is developed in order to study the effectiveness of control implementation on the actual micromirror arrays. Laser beam steering and a PSD sensor are used for position feedback, and preliminary results illustrate the ability to implement feedback control of these systems.

This research presented in this dissertation provides a validated theoretical model basis that allows for the development of micromirrors for adaptive optics applications that are robust to parametric uncertainties that commonly arise through microfabrication processes as well as to disturbance rejection and plant nonlinearities. Future work includes exploration of dynamic response of the system at higher frequencies, and development of optimally designed devices that are less sensitive to the effects of variations in the fabrication process. In addition, the passive (progressive linkage) and active controller development presented in this dissertation, additional work is needed to be expanded to refine the designs with inclusion of design optimization and expansion of the modeling techniques used. While many researchers develop models of the system performance, very few use these analytical techniques to optimize the device performance. The application of optimal design methods and closed-loop control techniques will enable both cost reduction as the devices will no longer require extensive calibration for open-loop performance, as well as improved performance and reliability. The impact of this work is not limited to the application of micromirror or micro-optics design. The design and optimization methods used in the creation of these new actuator designs will create a general design framework that can be used in the development of many new MEMS devices.

This will aid researchers in all future design efforts and improve the design and development process.

The PID and LQR controllers presented in Chapter 6 can be adapted and refined to meet specific performance metrics defined by the application requirements. The gains proposed for the controllers are quite high, and limitations in hardware capabilities may require these gains to be lowered, and the stability of the system must always be maintained. Additional study is required to determine the effects of noise and disturbances on the feedback loop, as well as how this affects the stability of the system. The results of the modal analysis in Chapter 4 show that the one-degree-of-freedom motion of the system is not valid during resonant behavior, therefore it is recommended to avoid driving the system to resonance. However, it would be very interesting to study the nonlinear dynamics of the system at higher frequencies to identify the effects relating to resonance and to electrostatic pull-in.

In order to design a robust microsystem that can be deployed in a wide variety of scenarios, the device should have on-chip sensing capabilities built in so that the actuation, sensing, and control can be packaged into a complete system. The development of such sensing and control strategies will contribute to the advancement of precision optical applications. The incorporation of on-chip sensing mechanisms into the device will allow for compact realization of complete microsystems. The method proposed in [91] for using piezoresistive methods within SUMMiT VTM fabrication is novel and its success will open up new areas of device applications. Several feedback mechanisms should be investigated, including piezoresistive, capacitive, and optical sensing methods. There is also a need to integrate sensing mechanisms at the device level to allow for the realization of complete, compact microsystems. Piezoresistive and

capacitive methods seem very promising in this area, however noise in the sensor output will need to be carefully examined and minimized.

The development of an experimental test bed was also initiated at the University of Florida as part of the research where further development is still needed before implementation and validation of the presented closed-loop controllers can be realized. In doing so, this work will provide a greater impact on the development of micromirrors for adaptive optics applications that are robust to parametric uncertainties that commonly arise through microfabrication processes as well as to disturbance rejection and plant nonlinearities.

APPENDIX A MODEL GEOMETRY

The dimensions used for creating the electrostatic model for one unit cell of the device geometry are shown in Figure A-1 by layer. All dimensions in μm are shown for layer MMPoly 0, and the subsequent layer dimensions are shown in relation to the MMPoly 0 ground plane. The model is created by drawing these areas in the X-Y plane, and extruding the thickness in the positive Z-axis.

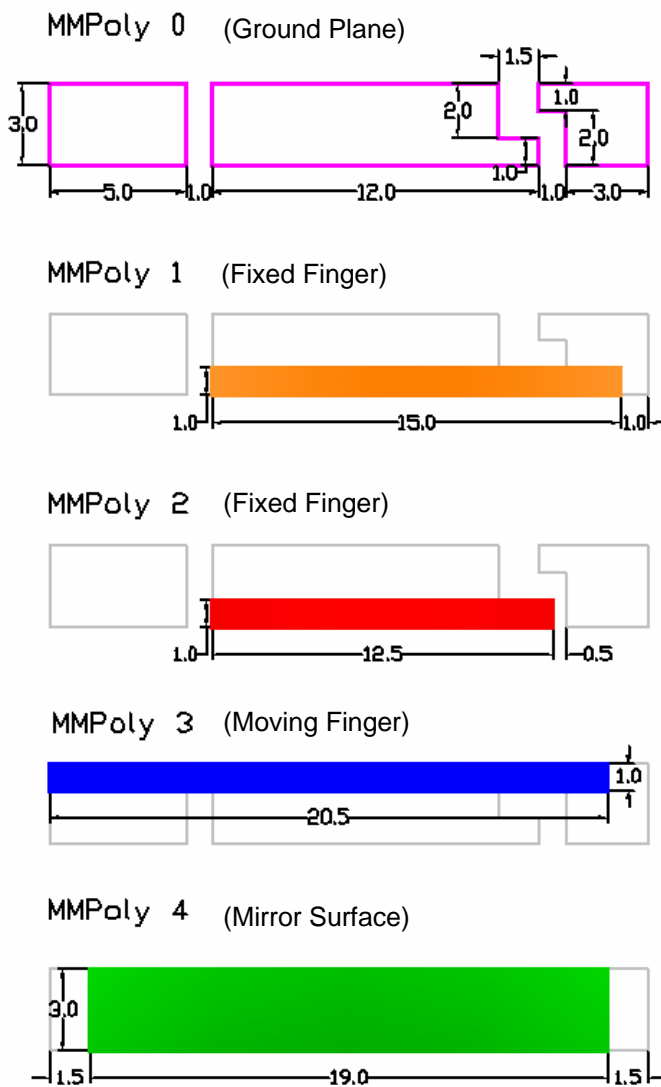


Figure A-1. Geometry dimensions in μm for creating electrostatic model.

APPENDIX B
MONTE CARLO SIMULATION INPUTS

This appendix shows the values used to perform the Monte Carlo simulations in Chapter 4. The values were determined from a random number generator in order to have a normal distribution about a mean and standard deviation. Five-hundred sets of random values were generated, and are shown as histograms here. Also shown is the histogram of the calculated mass values.

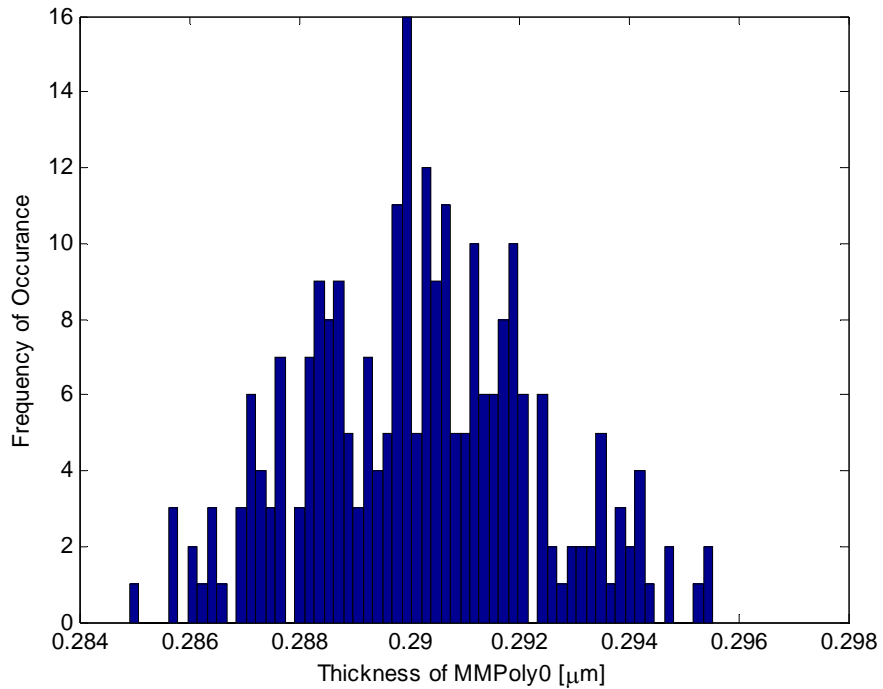


Figure B-1. Histogram of values for the thickness of layer MMPoly0.

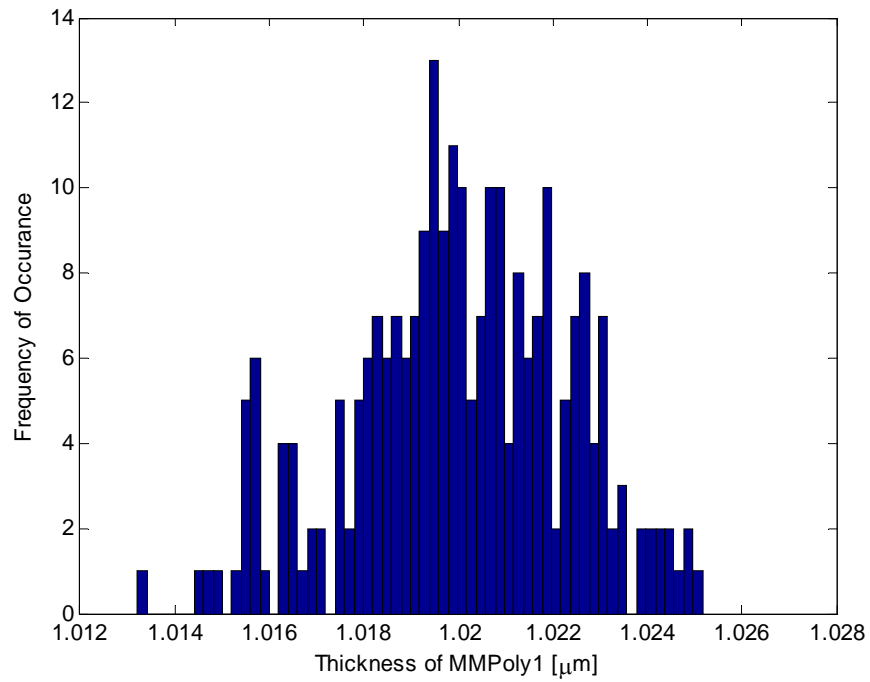


Figure B-2. Histogram of values for the thickness of layer MMPoly1.

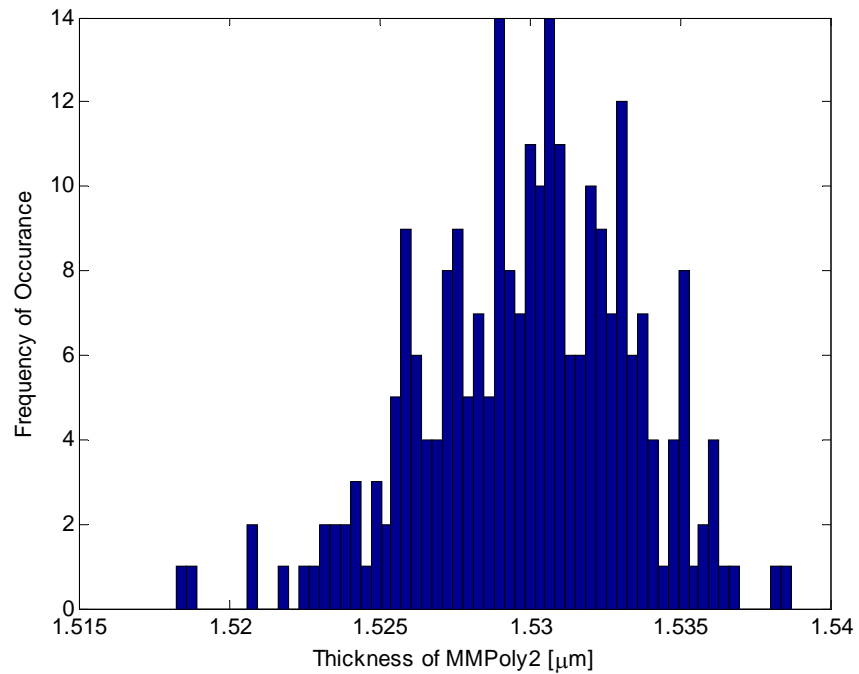


Figure B-3. Histogram of values for the thickness of layer MMPoly2.

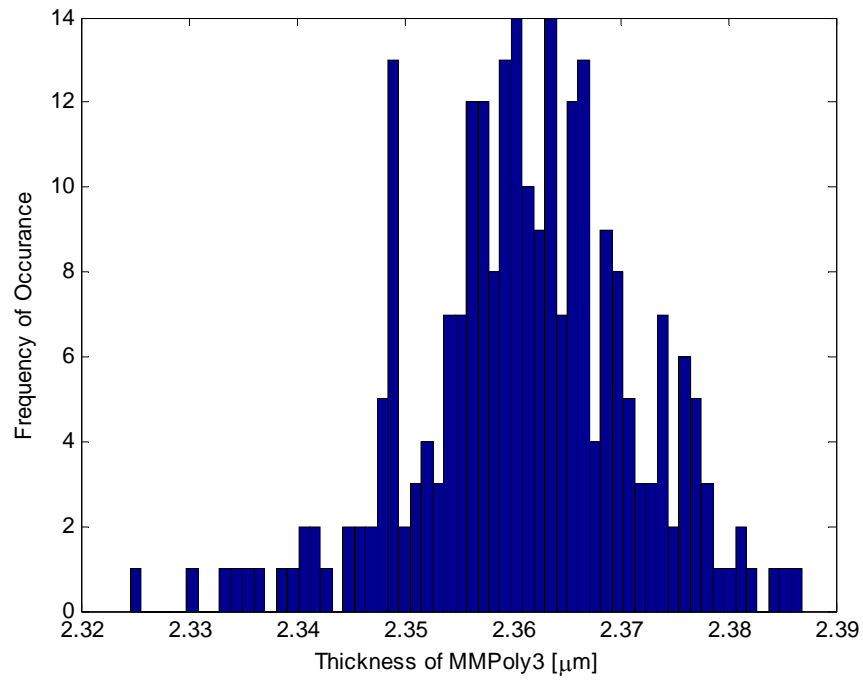


Figure B-4. Histogram of values for the thickness of layer MMPoly3.

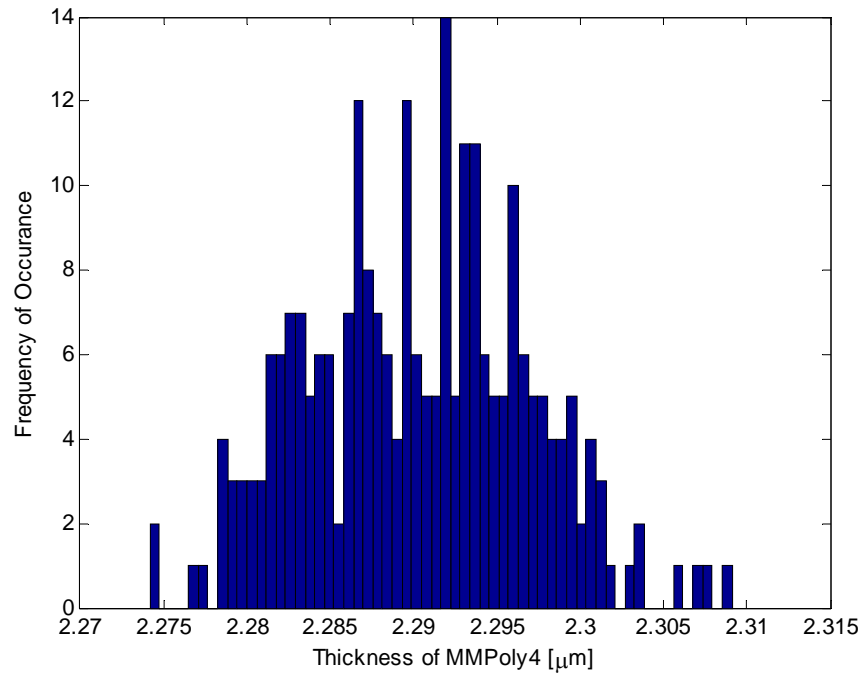


Figure B-5. Histogram of values for the thickness of layer MMPoly4.

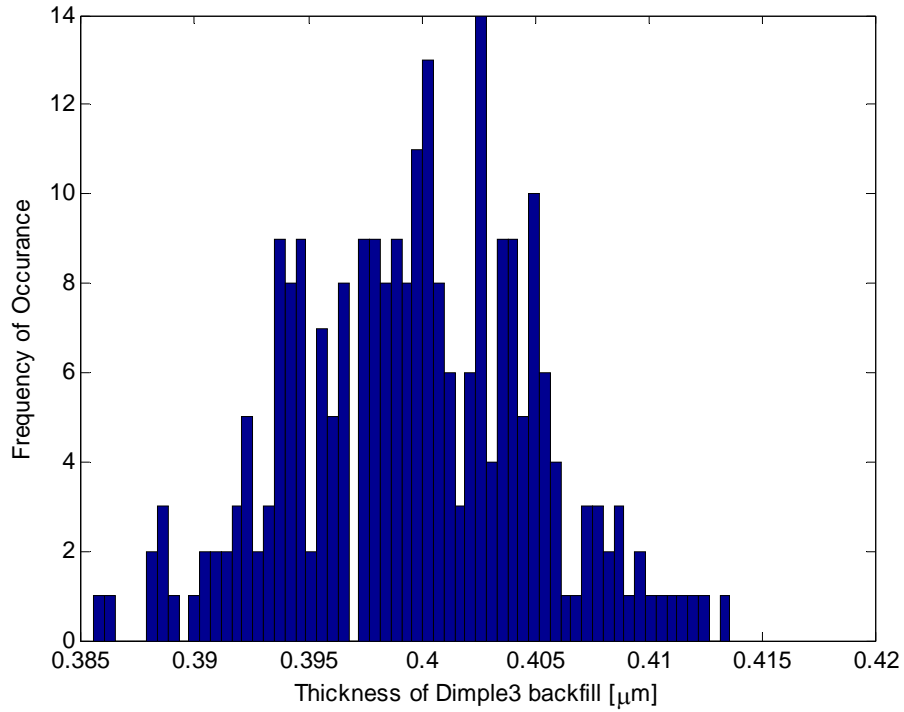


Figure B-6. Histogram of values for the thickness of Dimple3 backfill.

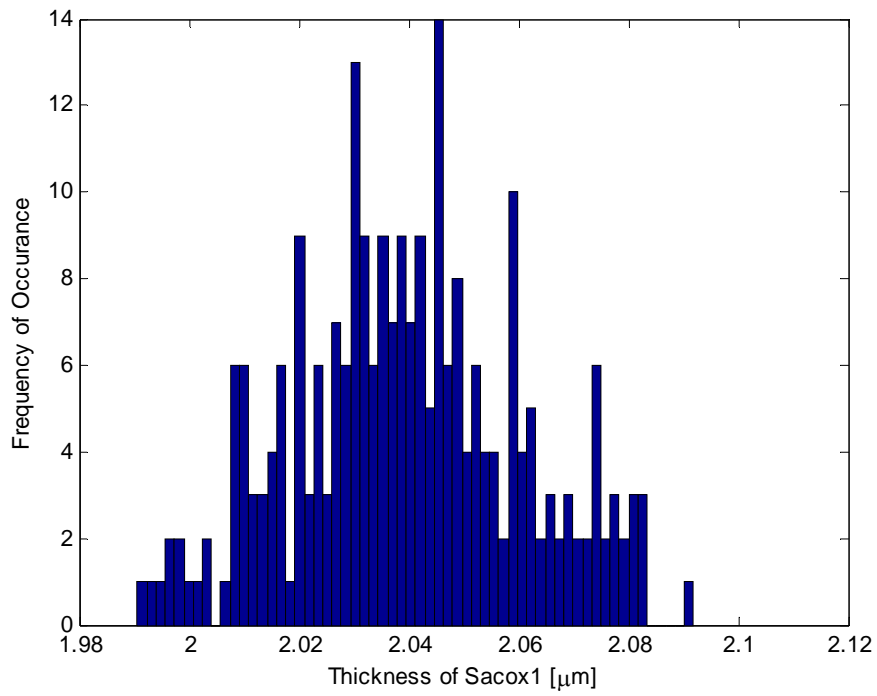


Figure B-7. Histogram of values for the thickness of layer Sacox1.

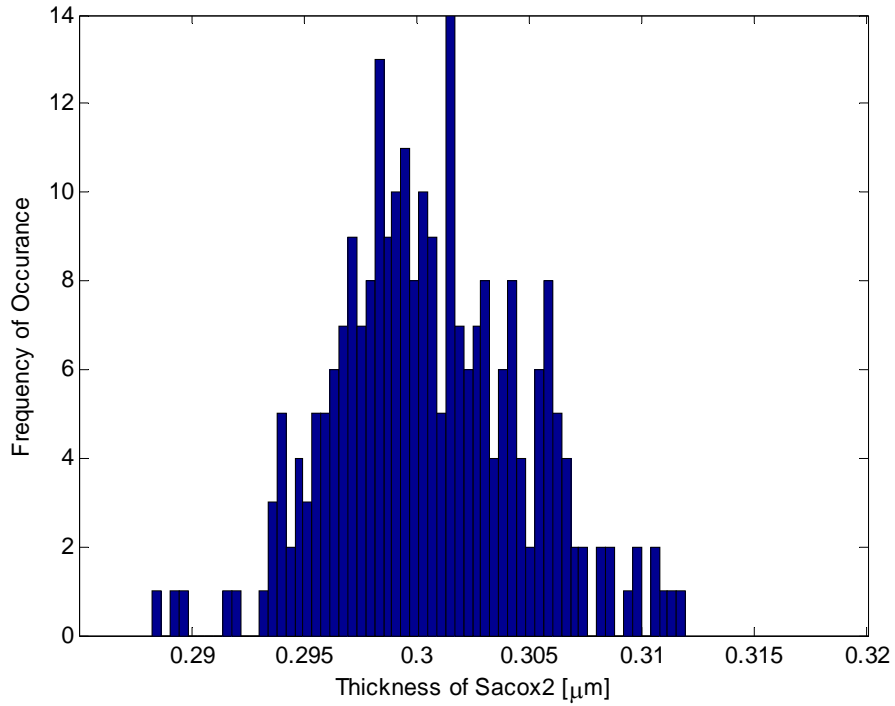


Figure B-8. Histogram of values for the thickness of layer Sacox2.

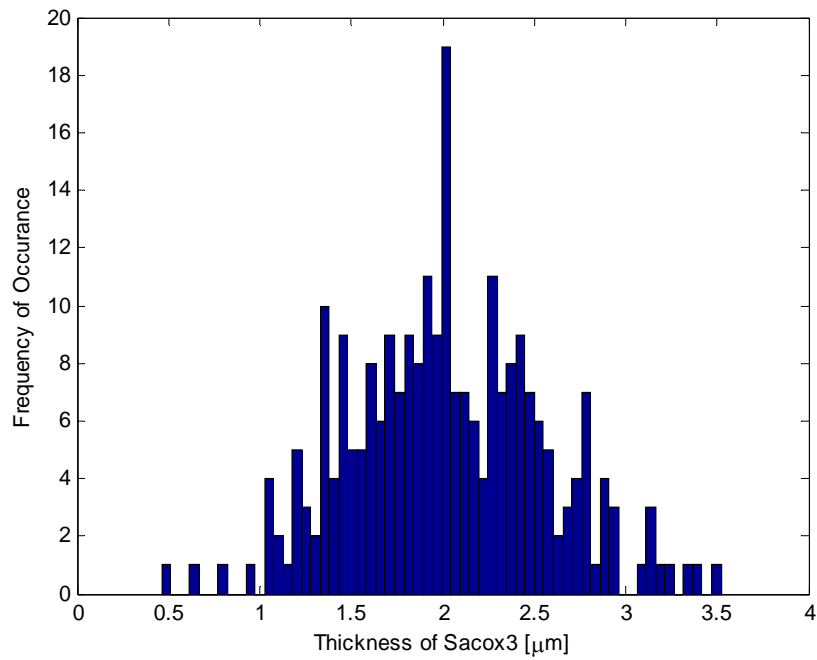


Figure B-9. Histogram of values for the thickness of layer Sacox3.

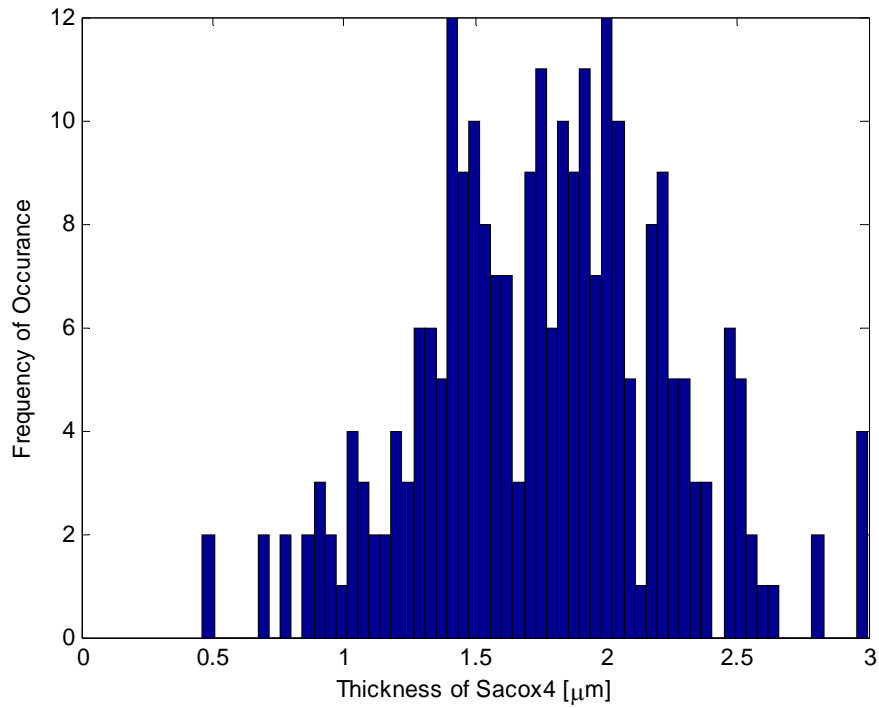


Figure B-10. Histogram of values for the thickness of layer Sacox4.

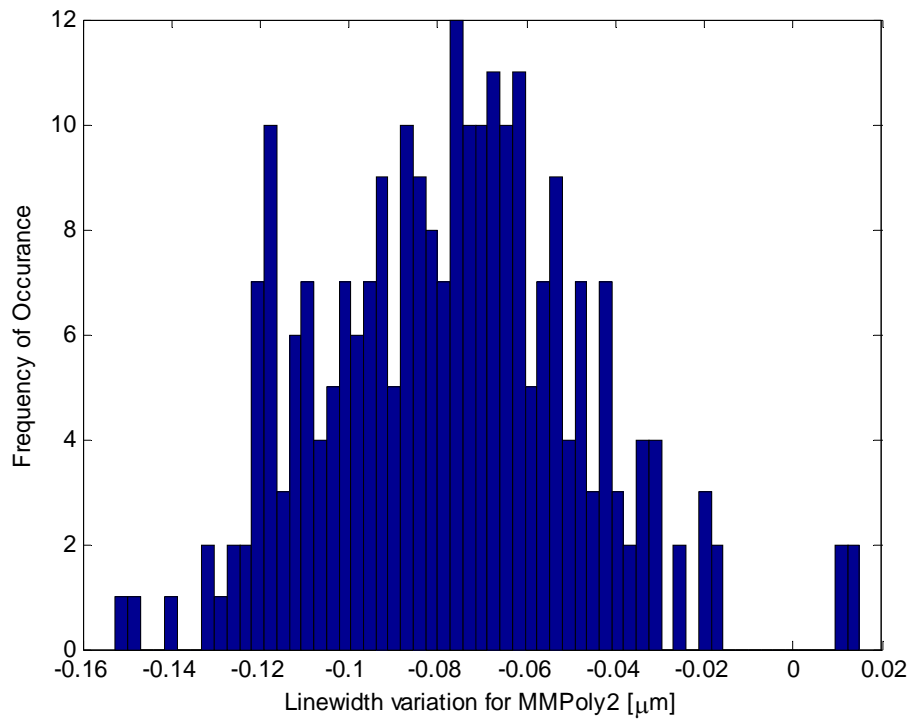


Figure B-11. Histogram of values for the linewidth variation of layer MMPoly2.

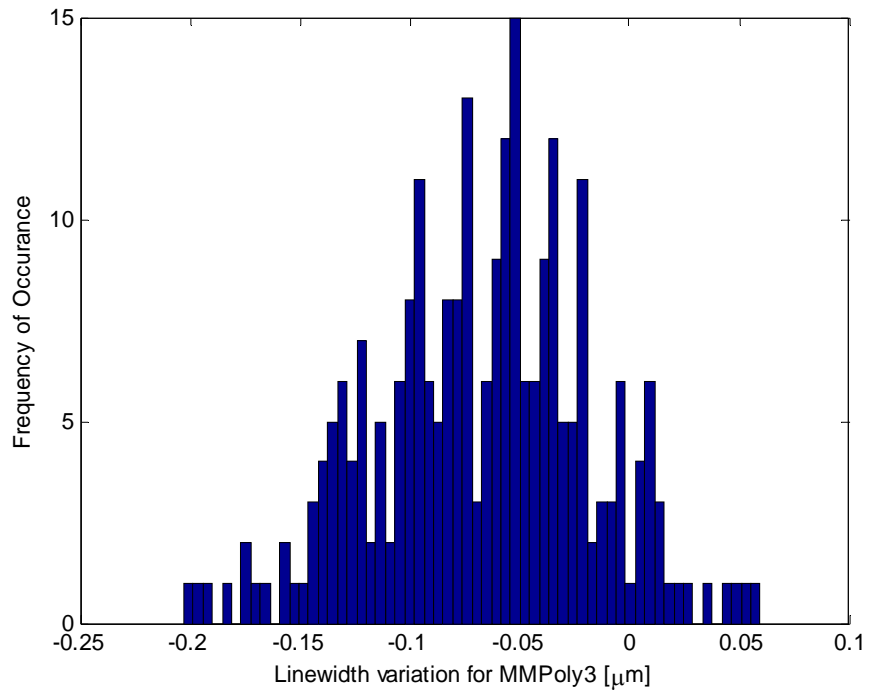


Figure B-12. Histogram of values for the linewidth variation of layer MMPoly3.

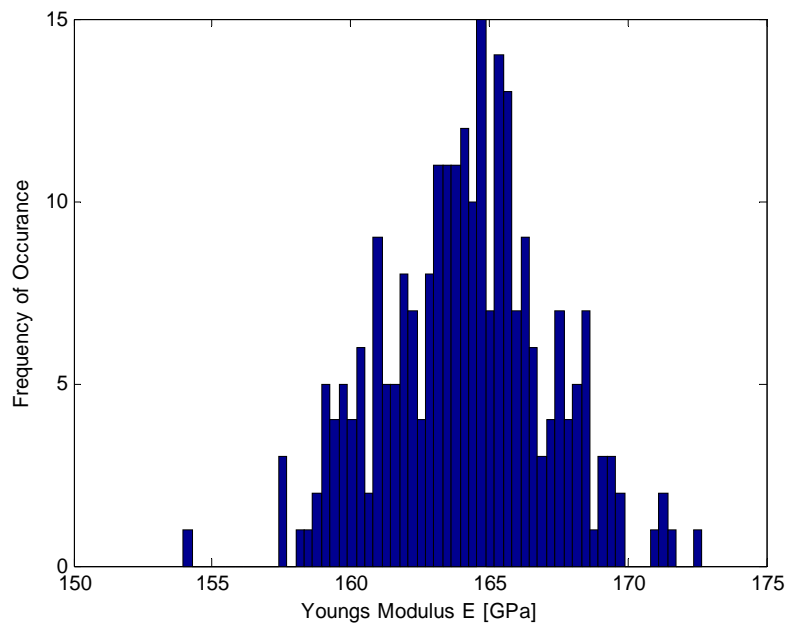


Figure B-13. Histogram of values for the linewidth variation of layer MMPoly4.

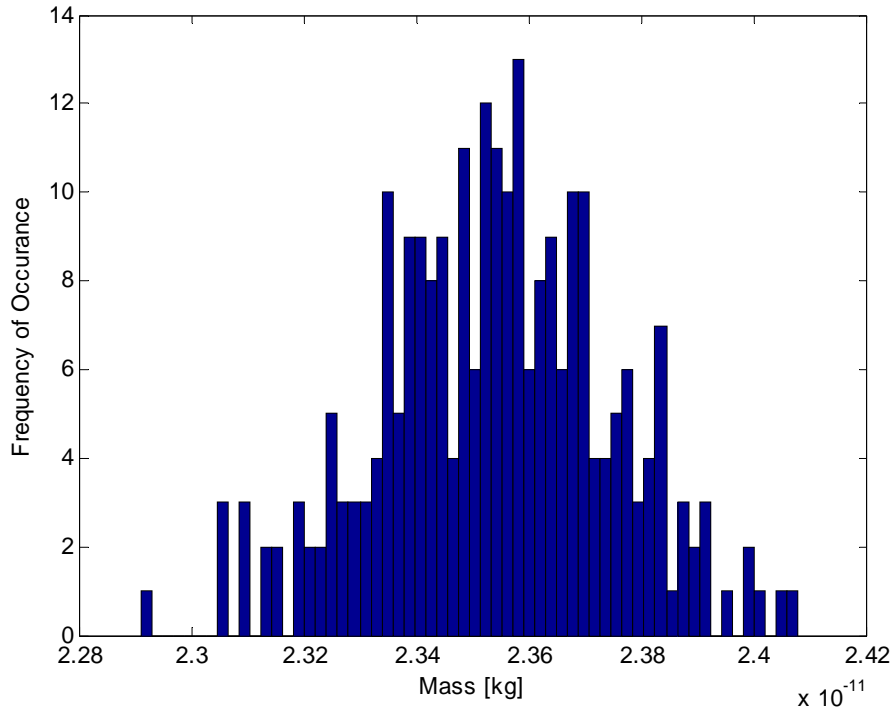


Figure B-14. Histogram of the mass values calculated from the parametric variation data.

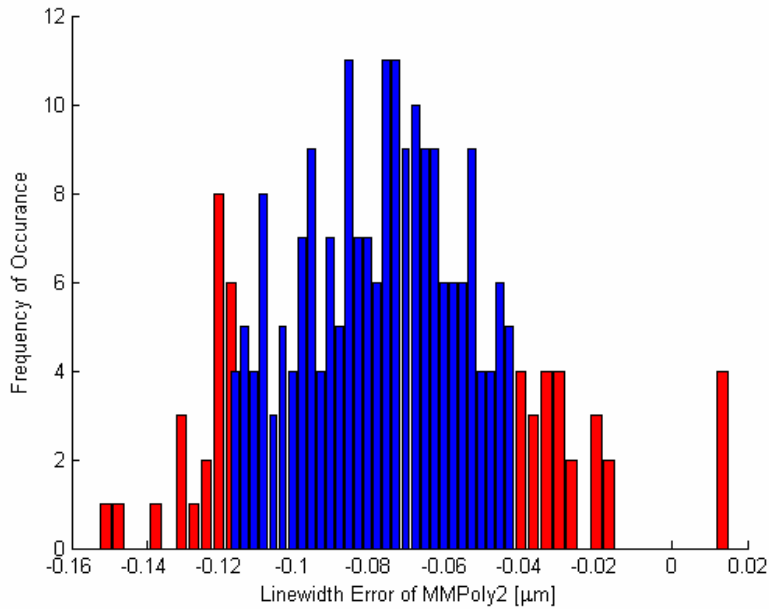


Figure B-15. Histogram of values from the Monte Carlo simulations for the linewidth error of MMPoly2. Values in blue lie within the 95% confidence interval, and values in red lie without.

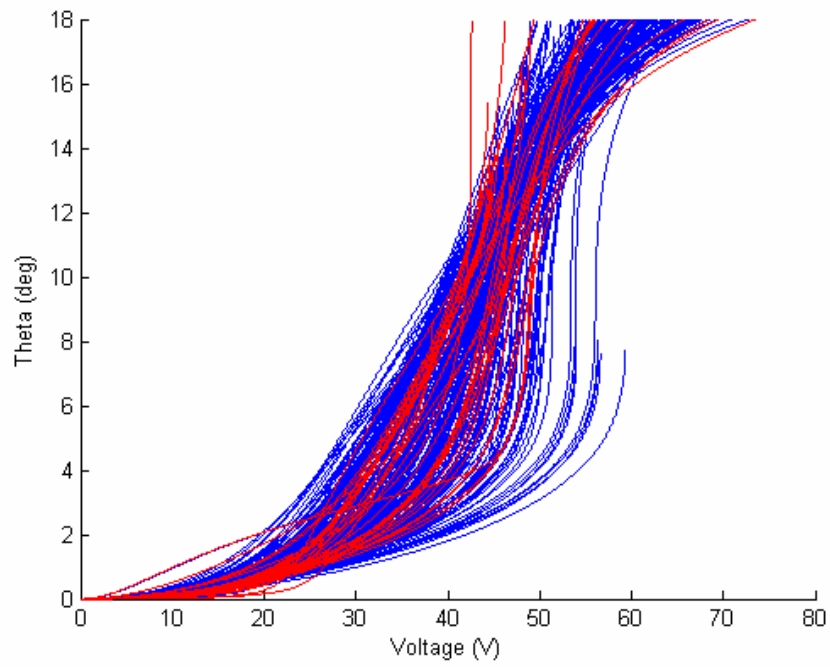


Figure B-16. Static displacement curves from the Monte Carlo simulations that indicate the effect of large variations in the linewidth error of MMPoly2.

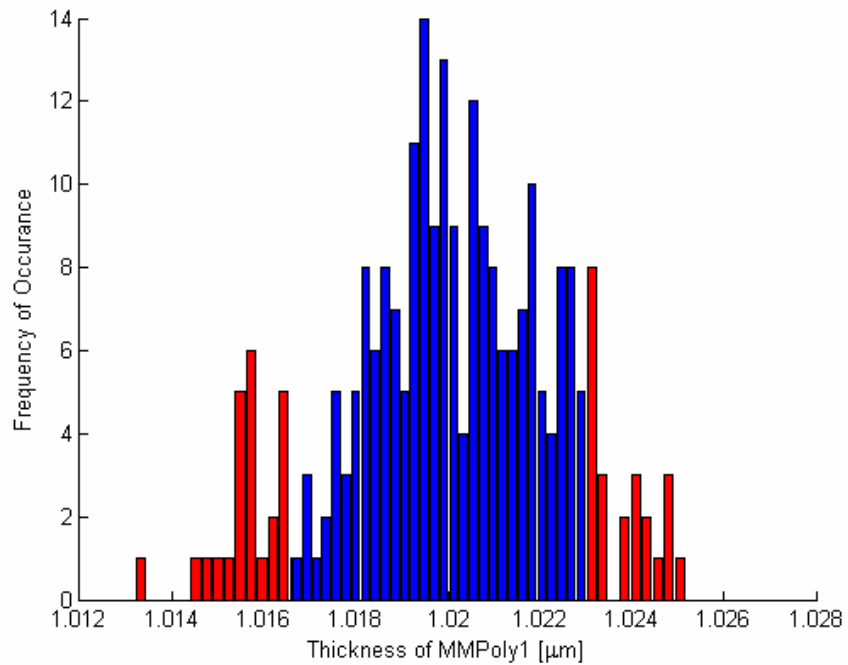


Figure B-17. Histogram of values from the Monte Carlo simulations for the layer thickness of MMPoly1.

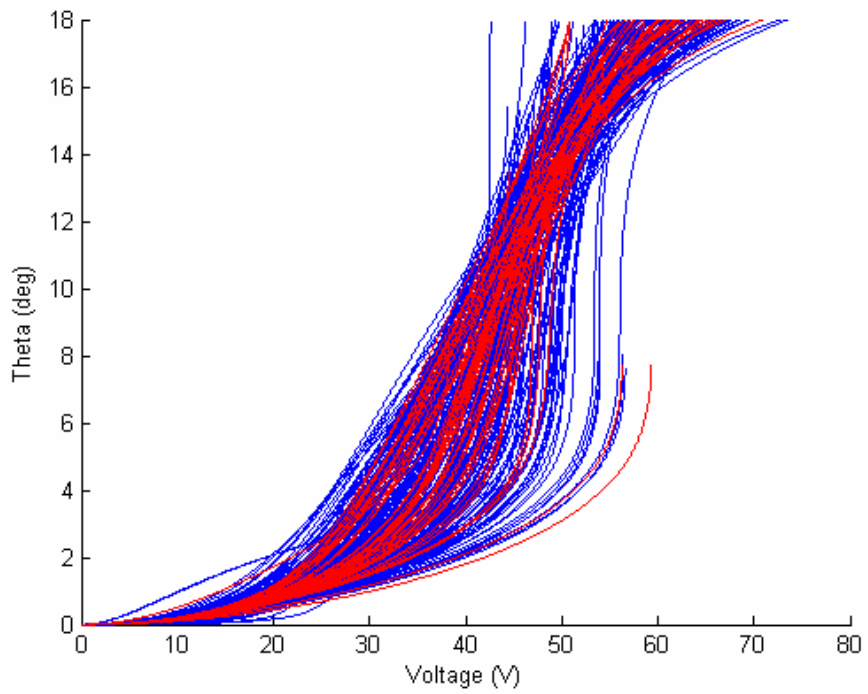


Figure B-18. Static displacement curves from the Monte Carlo simulations that indicate the effect of large variations in the thickness of MMPoly1.

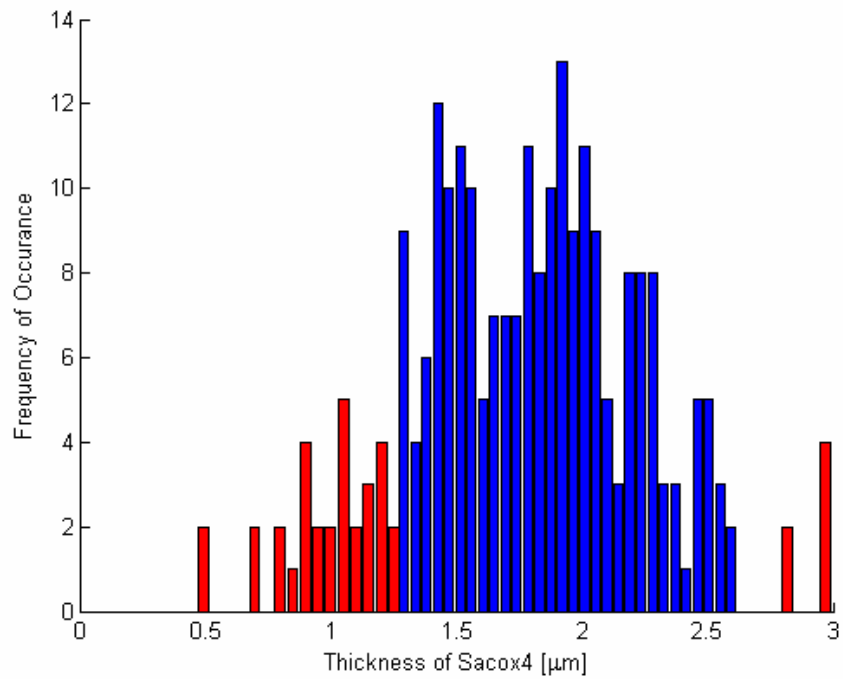


Figure B-19. Histogram of values from the Monte Carlo simulations for the layer thickness of Sacox4.

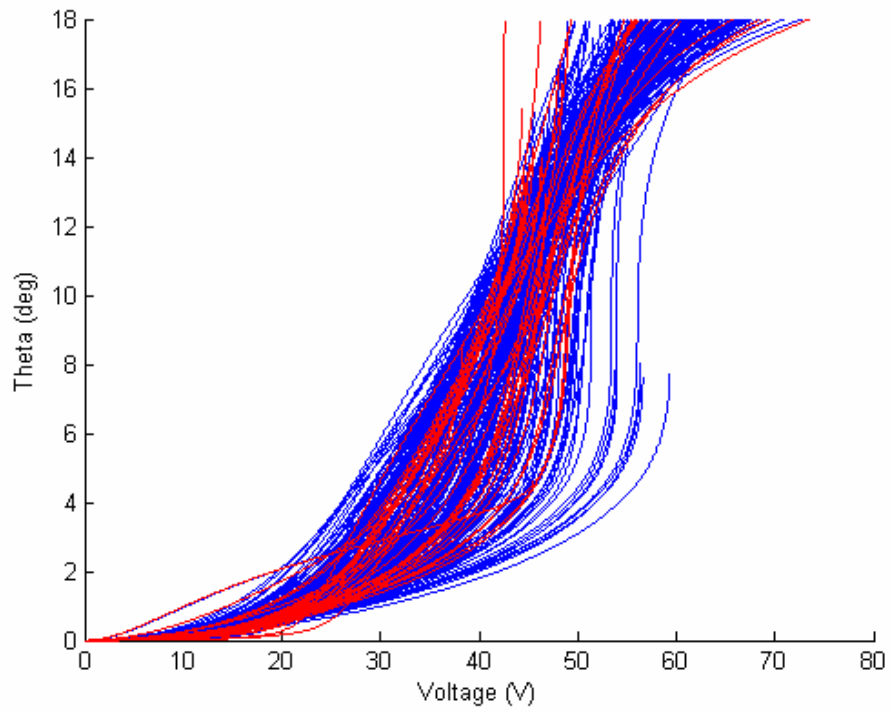


Figure B-20. Static displacement curves from the Monte Carlo simulations that indicate the effect of large variations in the thickness of Sacox4.

APPENDIX C
LASER DOPPLER VIBROMETER RESULTS

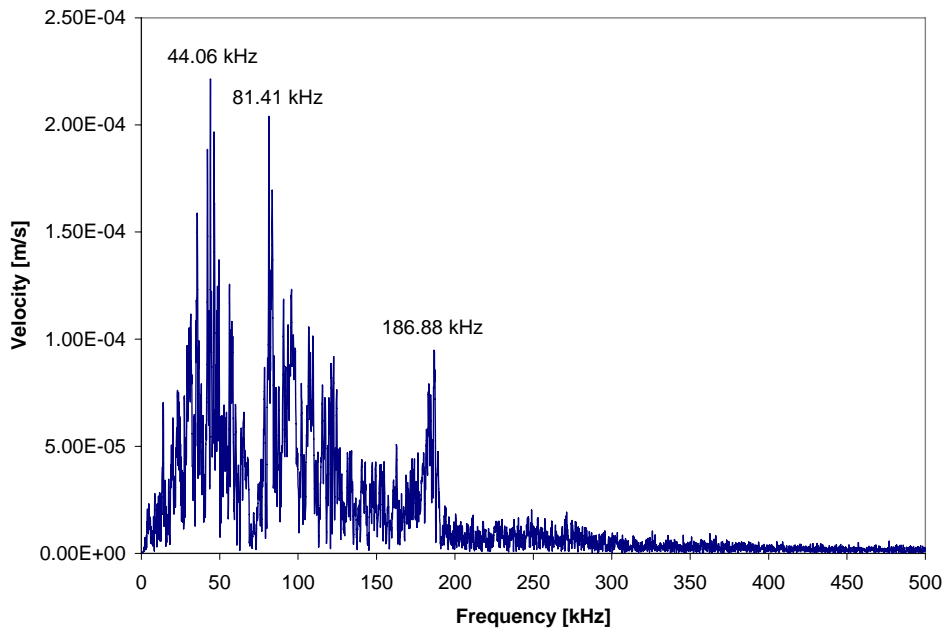


Figure C-1. Magnitude of FFT results for device 1, trial 1.

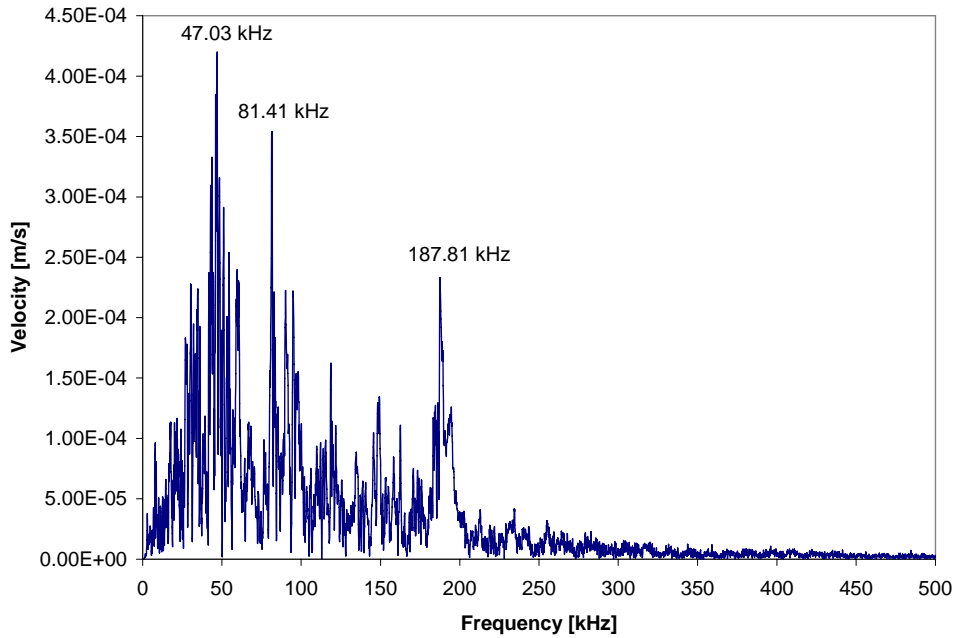


Figure C-2. Magnitude of FFT results for device 1, trial 2.

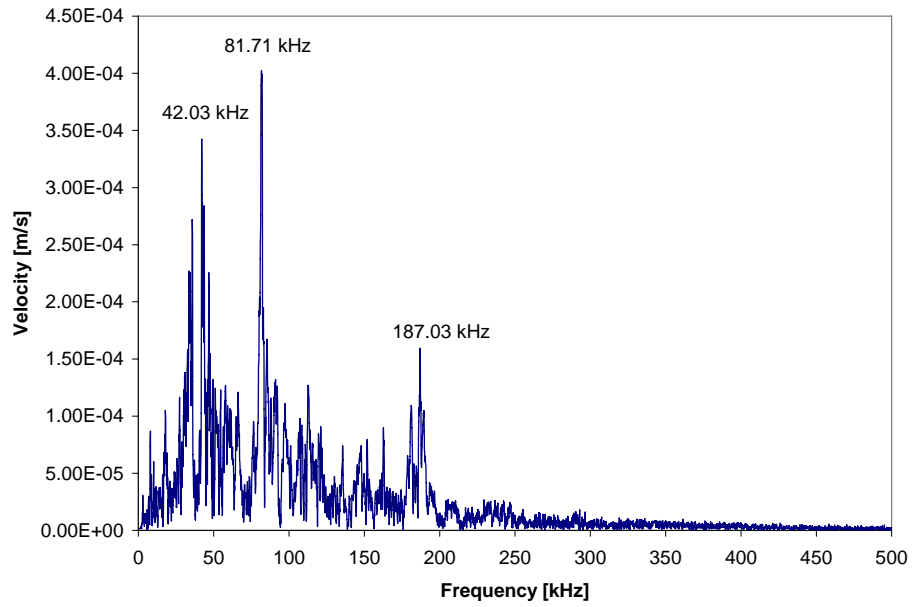


Figure C-3. Magnitude of FFT results for device 1, trial 3.

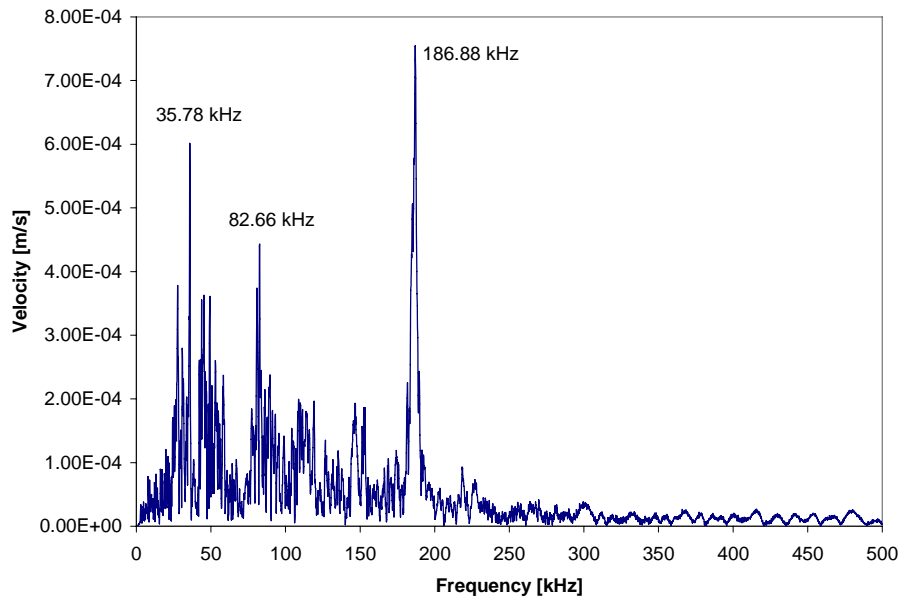


Figure C-4. Magnitude of FFT results for device 1, trial 4.

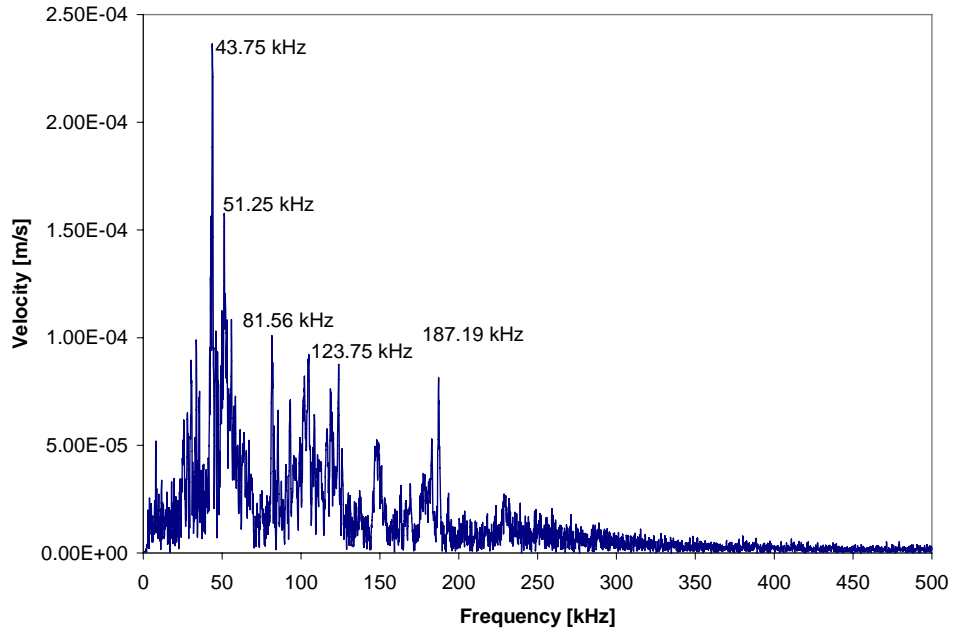


Figure C-5. Magnitude of FFT results for device 1, trial 5.

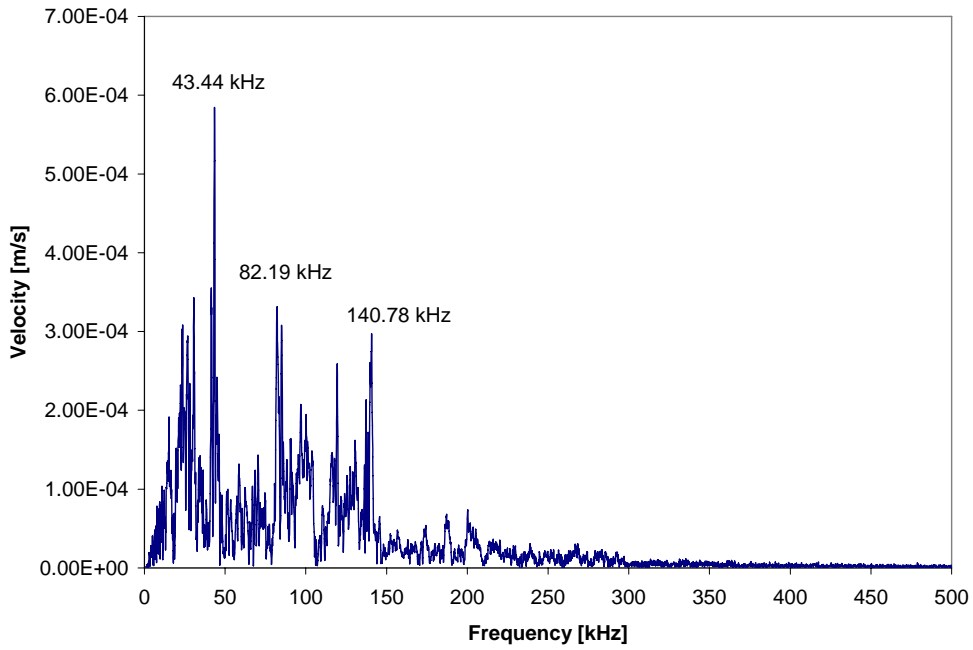


Figure C-6. Magnitude of FFT results for device 2, trial 1.

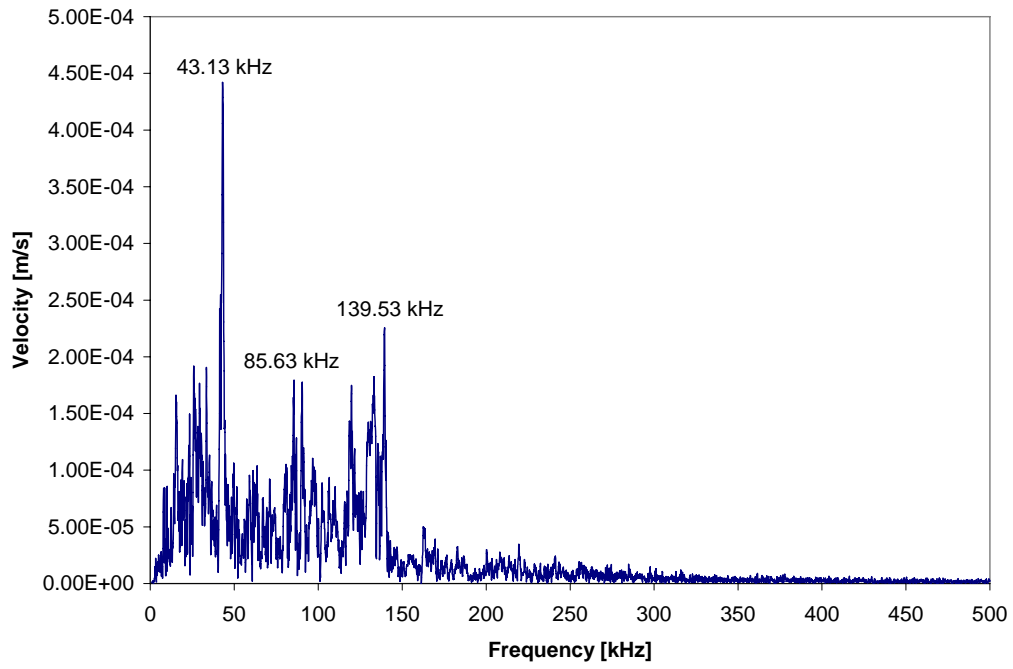


Figure C-7. Magnitude of FFT results for device 2, trial 2.

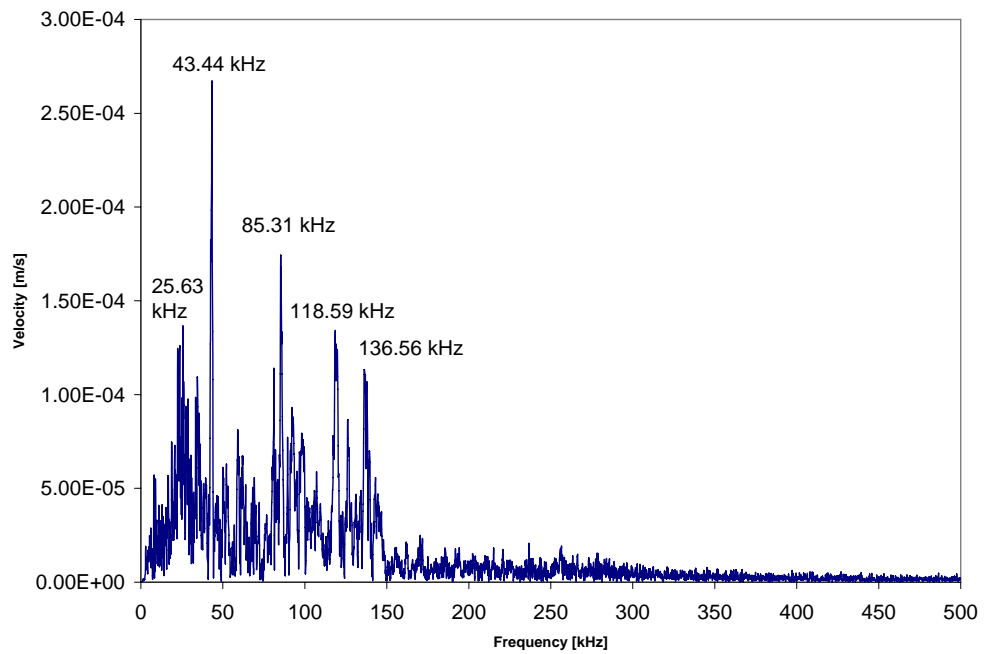


Figure C-8. Magnitude of FFT results for device 2, trial 3.

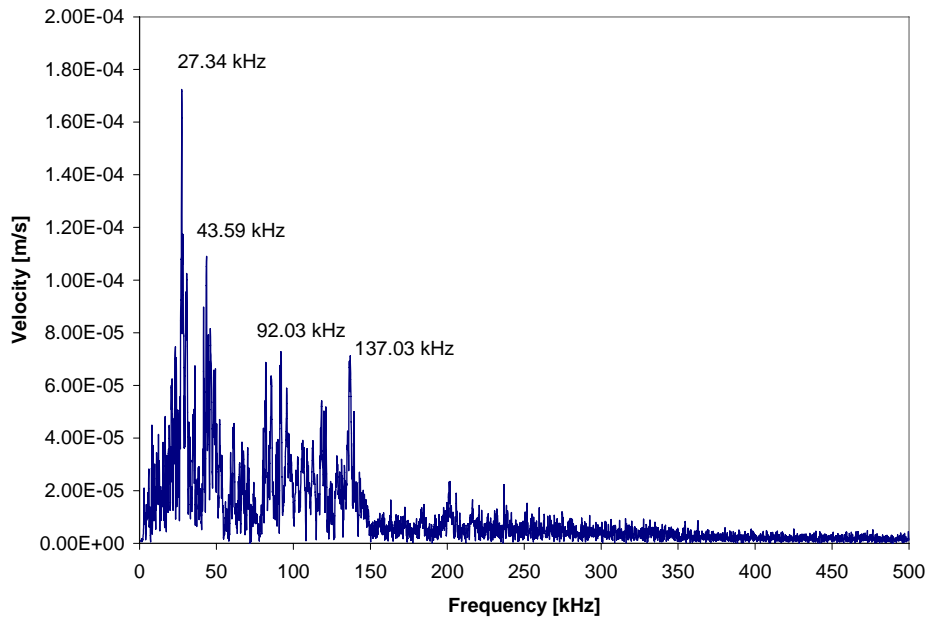


Figure C-9. Magnitude of FFT results for device 2, trial 4.

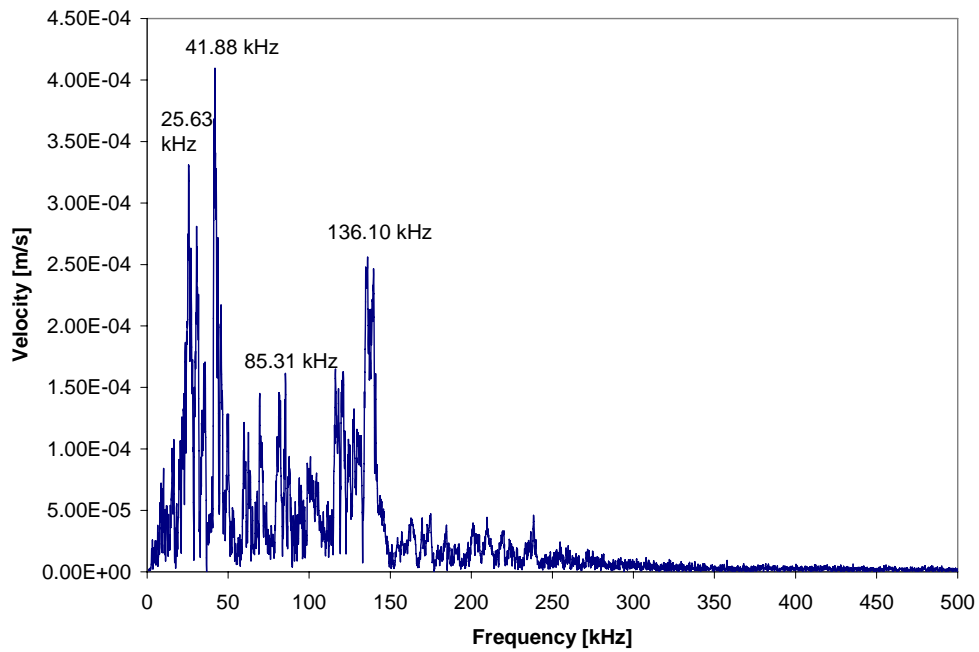


Figure C-10. Magnitude of FFT results for device 2, trial 5.

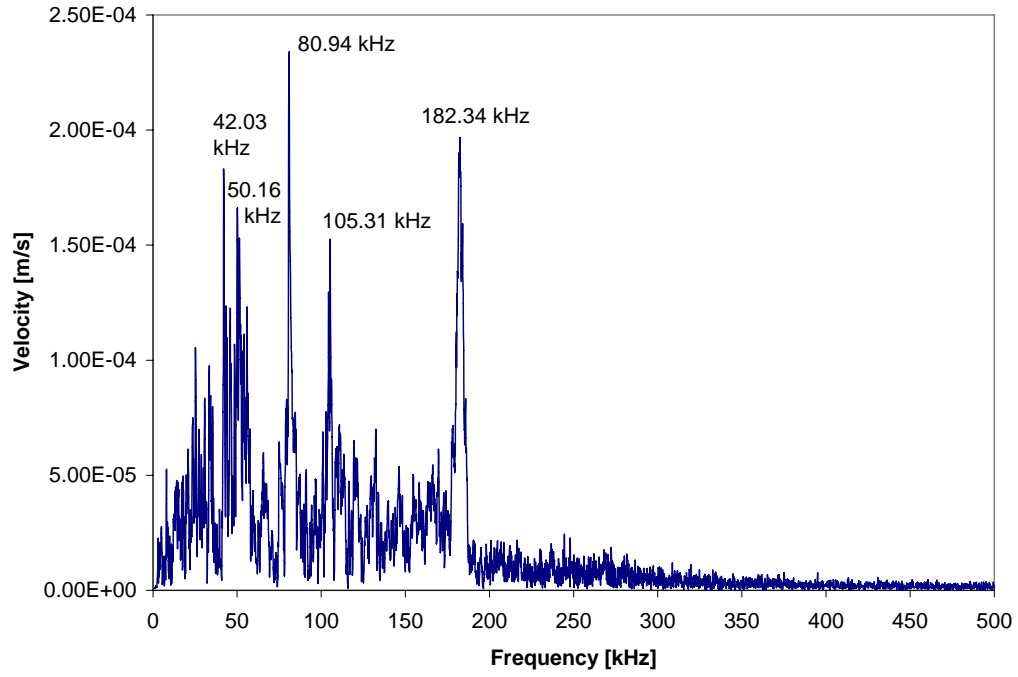


Figure C-11. Magnitude of FFT results for device 3, trial 1.

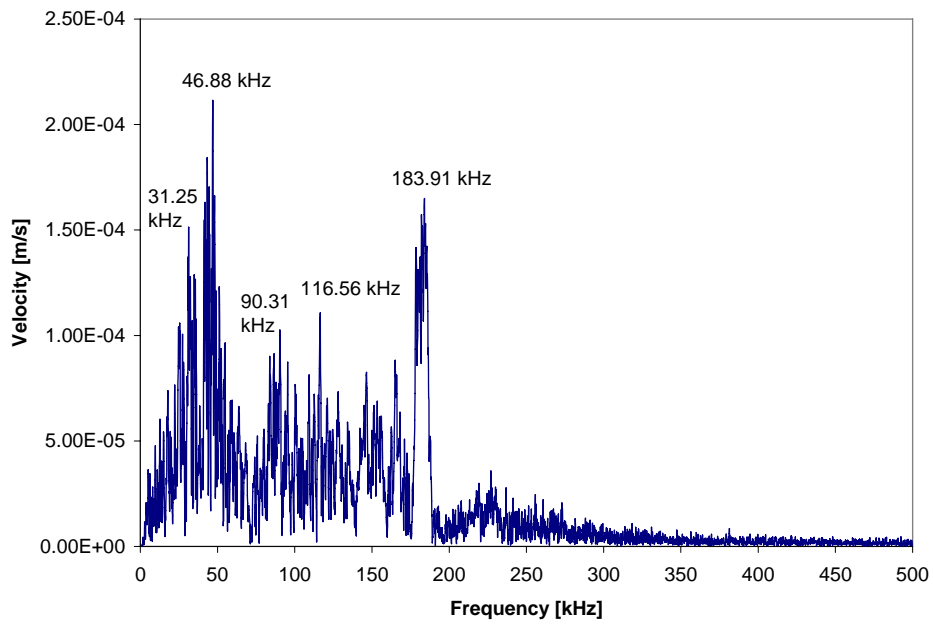


Figure C-12. Magnitude of FFT results for device 3, trial 2.

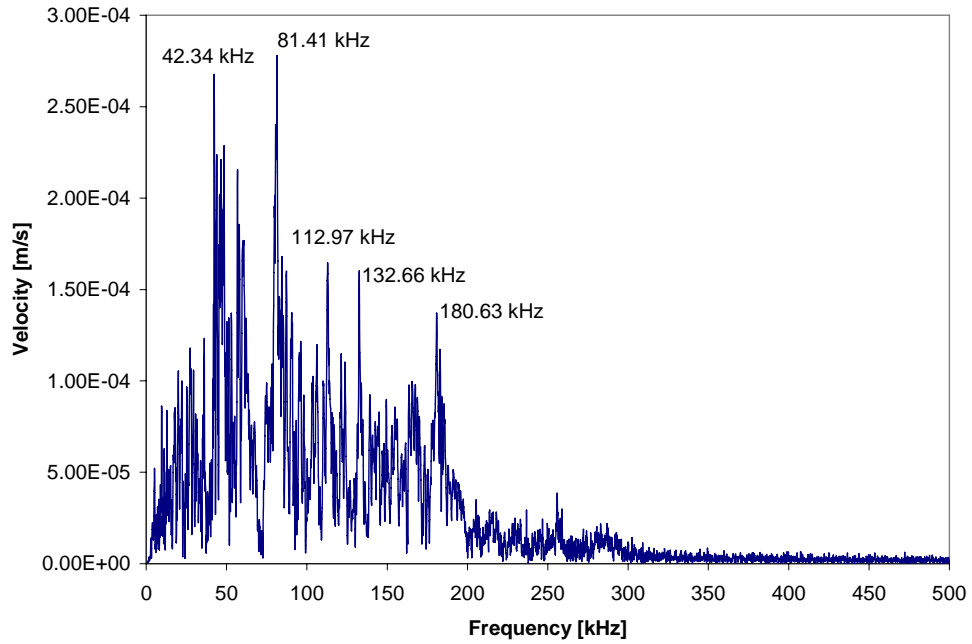


Figure C-13. Magnitude of FFT results for device 3, trial 3.

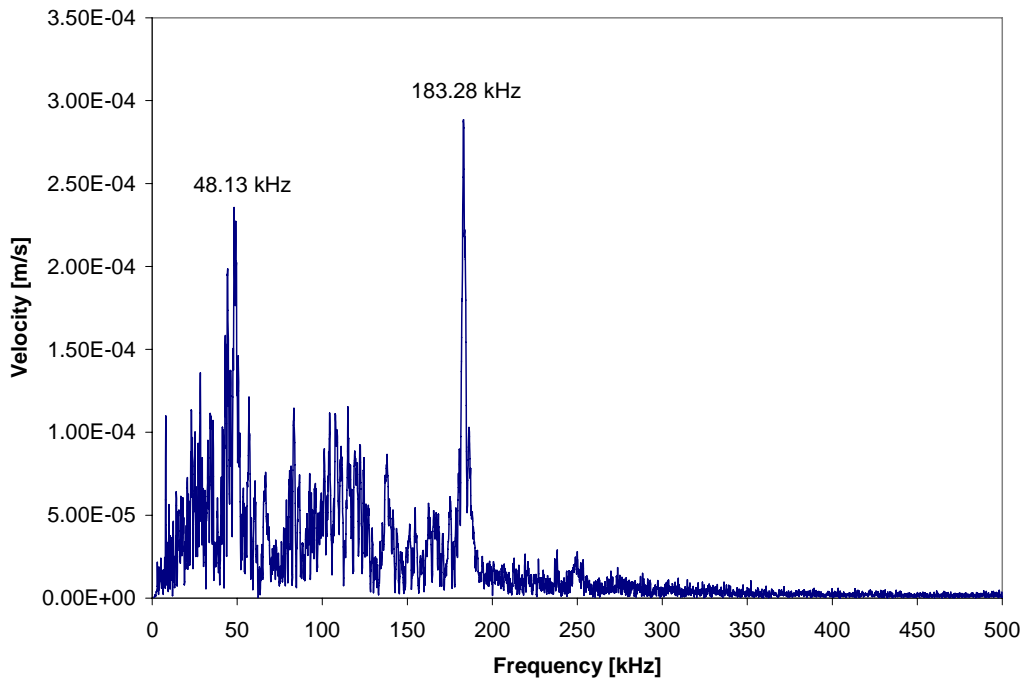


Figure C-14. Magnitude of FFT results for device 3, trial 4.

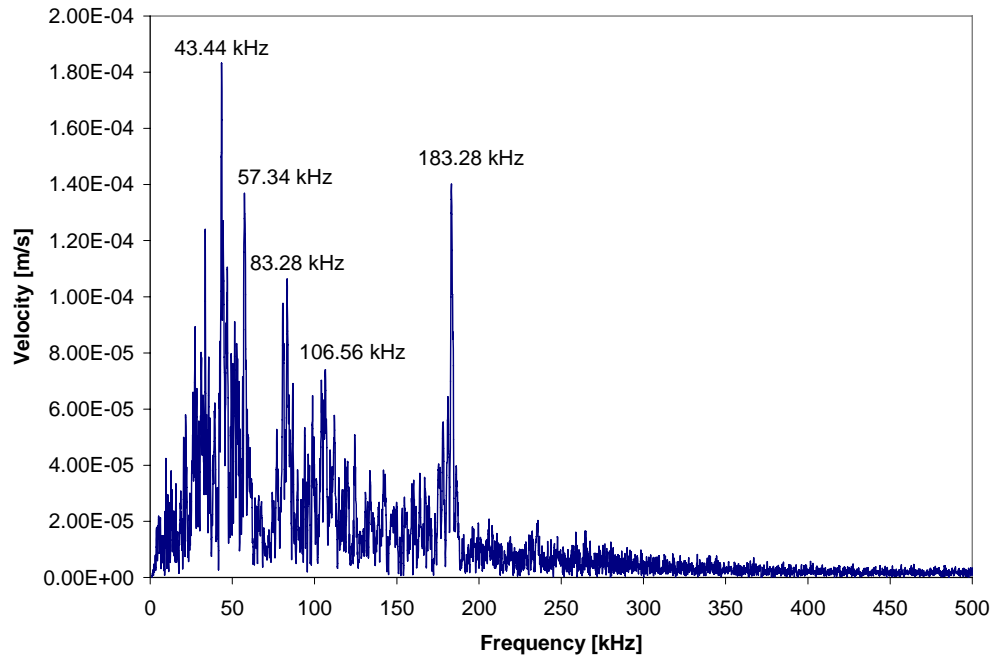


Figure C-15. Magnitude of FFT results for device 3, trial 5.

LIST OF REFERENCES

- [1] O. Solgaard, F.S.A. Sandejas, and D.M. Bloom, "Deformable grating optical modulator," *Optics Letters*, vol. 17, no. 9, pp. 688-690, 1992.
- [2] D. Dudley, W. Duncan, and J. Slaughter, "Emerging digital micromirror device (DMD) applications," *Proc. SPIE*, vol. 4985, 2003.
- [3] S.D. Senturia, *Microsystem Design*, Boston, MA: Kluwer Academic Publishers, 2001.
- [4] G.T. Kovacs, N.I. Maluf, and K.E. Petersen, "Bulk micromachining of silicon," *Proc. IEEE*, vol. 86, no. 8, pp. 1536-1551, 1998.
- [5] J.M. Bustillo, R.T. Howe, and R.S. Muller, "Surface micromachining for microelectromechanical systems," *Proc. IEEE*, vol. 86, no. 8, pp. 1552-1574, 1998.
- [6] Sandia National Laboratories. (2005, Sept. 9). SUMMiT V Design Manual. Last Access: Sept. 9, 2007. Available e-mail: memsinfo@sandia.gov Message: SUMMiT Design Manual
- [7] J.W. Wittwer, T. Gomm, and L.L. Howell, "Surface micromachined force gauges: uncertainty and reliability," *J. Micromech. Microeng.*, vol. 12, pp.13-20, 2002.
- [8] J. Wittwer, "Predicting the effects of dimensional and material property variations in micro compliant mechanisms," M.S. Thesis, Dept. Mech. Eng., Brigham Young Univ., 2001.
- [9] J.W. Wittwer, M.S. Baker, and L.L. Howell, "Robust design and model validation of nonlinear compliant micromechanisms," *J. Microelectromech. Syst.*, vol. 15, no. 1, 2006.
- [10] S. Park, and R. Horowitz, "Adaptive control for z-axis MEMS gyroscopes," in *Proc. Amer. Controls Conf.*, Arlington, VA, 2001, pp. 1233-1228.
- [11] S. Park, and R. Horowitz, "Adaptive control for the conventional mode of operation of MEMS gyroscopes," *J. Microelectromech. Syst.*, vol. 12, no. 1, pp. 101-108, 2003.
- [12] W. N. Sharpe, Jr., B. Yuan, and R. Vaidyanathan, "Measurements of Young's modulus, Poisson's ratio, and tensile strength of polysilicon," in *Proc. IEEE 10th Ann. Int. Workshop Microelectromech. Syst.*, Nagoya, Japan, 1997, pp. 424-429.
- [13] A. Tauntranont, V.M. Bright, J. Zhang, W. Zhang, J. Neff, and Y.C. Lee, "MEMS-controllable microlens array for beam steering and precision alignment in optical interconnect systems," in *Proc. Solid-State Sensor and Actuator Workshop*, Hilton Head Island, SC, 2000, pp. 101-104.
- [14] D. Hah, S.T. Huang, J.C. Tsai, H. Toshiyoshi, and M.C. Wu, "Low-voltage, large-scan angle MEMS analog micromirror arrays with hidden vertical comb-drive actuators2," *J. Microelectromech. Syst.*, vol. 13, no. 2, pp. 279-289, 2004.

- [15] P.B. Chu, I. Brener, C. Pu, S.S. Lee, J.I. Dadap, S. Park, K. Bergman, N.H. Bonadeo, T. Chau, M. Chou, R.A. Doran, R. Gibson, R. Harel, J.J. Johnson, C.D. Lee, D.R. Peale, B. Tang, D.T.K. Tong, M.J. Tsai, Q. Wu, W. Zhong, E.L. Goldstein, L.Y. Lin, J.A. Walker, "Design and nonlinear servo control of MEMS mirrors and their performance in a large port-count optical switch," *J. Microelectromech. Syst.*, vol 14, no. 2, pp. 261-273, 2005.
- [16] S. Huang, J-C. Tsai, D. Hah, H. Toshiohi, and M.C. Wu, "Open-loop operation of MEMS WDM routers with analog micromirror array," in *Proc. IEEE/LEOS Int. Conf. on Optical MEMS*, Lugano, Switzerland, 2002, pp. 179-180.
- [17] L. Zhou, M. Last, V. Milanovic, J.M. Kahn, and K.S.J. Pister, "Two-axis scanning mirror for free-space optical communication between UAVs," in *IEEE/LEOS Optical MEMS 2003*, Hawaii, USA, 2003.
- [18] Lucent Technologies. (Last Access: 2007, June 18), LambdaRouter Mirror. [Online]. Available: http://www.alcatel-lucent.com/wps/PA_1_A_1OB/images/Photos/Other_Photos/Lambda_mirror_LR.jpg
- [19] B. Mi, D.A. Smith, H. Kahn, F.L. Merat, A.H. Heuer, and S.M. Phillips, "Static and Electrically Actuated Shaped MEMS Mirrors," *J. Microelectromech. Syst.*, vol. 14, no. 1, pp. 29-36, 2005.
- [20] L. J. Hornbeck. (2006, June 13). Digital Light Processing™: A new MEMS-based display technology. *Texas Instruments*. [Online]. Last Access: Sept. 11, 2007. Available: http://www.dlp.com/downloads/default.aspx?&ref=/downloads/white_papers/117_Digital_Light_Processing_MEMS_display_technology.pdf
- [21] M.A. Butler, E.R. Deutsch, S.D. Senturia, M.B. Sinclair, W.C. Sweatt, D.W. Younger, and G.B. Hocker, "A MEMS-based programmable diffraction grating for optical holography in the spectral domain," in *IEDM Tech. Digest Int. Electron Devices Meeting*, Washington, D.C., 2-5, 2001, pp. 41.1.1-41.1.4.
- [22] E.R. Deutsch, J.P. Bardhan, S.D. Senturia, G.B. Hocker, D.W. Youngner, M.B. Sinclair, and M.A. Butler, "A large-travel vertical planar actuator with improved stability," in *12th Int. Conf. on Solid State Sensors, Actuators and Microsystems*, Boston, MA, 2003, pp. 352-355.
- [23] G.B. Hocker, D. Younger, E. Deutch, A. Volipicelli, S. Senturia, M. Butler, M. Sinclair, T. Plowman, and A.J. Ricco, "The polychrometer: a MEMS diffraction grating for synthetic spectra," in *Proc. Solid-State Sensor and Actuator Workshop*, Hilton Head Island, SC, 2000, pp. 89-91.
- [24] E.S. Hung, and S.D. Senturia, "Extending the travel range of analog-tuned electrostatic actuators," *Journal Microelectromechanical Systems*, vol. 8, no. 4, pp. 497-505, 1999.

- [25] S.D. Senturia, "Diffractive MEMS: the polychrometer and related devices," in *IEEE Conf. Optical MEMS*, Lugano, Switzerland, 2002.
- [26] N.O.P. Arancibia, S. Gibson, and T.-C. Tsao, "Adaptive control of MEMS mirrors for beam steering," in *Proc. ASME Int. Mechanical Eng. Congress and Expo.*, Anaheim, CA, 2004.
- [27] B.-S. Kim, S. Gibson, and T.-C. Tsao, "Adaptive control of a tilt-mirror for laser beam steering," *Proc. American Control Conference*, Boston, MA, 2004, pp. 3417-3421.
- [28] N. G. Dagalakis, T. LeBrun, and J. Lippiatt, "Micro-mirror array control of optical tweezer trapping beams," in *Proc. 2nd IEEE Conf. Nanotechnology*, Washington D.C., 2002. pp. 177-180.
- [29] T.G. Bifano, J. Perreault, R.K. Mali, and M.N. Horenstein, "Micromechanical deformable mirrors," *IEEE J. of Sel. Topics Quantum Electron.*, vol. 5, no. 1, pp.83-89, 1999.
- [30] M.N. Horenstein, S. Pappas, A. Fishov, and T.G. Bifano, "Electrostatic micromirrors for subaperturing in an adaptive optics system," *J. Electrostatics*, vol.54, pp. 321-332, 2002.
- [31] T. Weyrauch, M.A. Vorontsov, T.G. Bifano, J.A. Hammer, M. Cohen, and G. Cauwenberghs, "Microscale adaptive optics: wave-front control with a μ -mirror array and a VLSI stochastic gradient descent controller," *Applied Optics*, vol. 40, no. 24, pp. 4243-4253, 2001.
- [32] J.B. Stewart, T.G. Bifano, P. Bierden, S. Cornelissen, T. Cook, and B.M. Levine, "Design and development of a 329-segment tip-tilt piston mirrorarray for space-based adaptive optics," in *Proc. SPIE*, vol. 6113, 2006, pp. 181-189.
- [33] J.J. Gorman, and N.G. Dagalakis, "Modeling and disturbance rejection control of a nanopositioner with application of beam steering," in *Proc. ASME Int. Mech. Eng. Cong.*, Washington, D.C., 2003.
- [34] J.J. Gorman, N.G. Dagalakis, and B.G. Boone, "Multi-loop control of a nanopositioning mechanism for ultra-precision beam steering," in *Proc. SPIE*, vol. 5160, 2005, pp. 170-181.
- [35] Sandia National Laboratories. (1999, Nov. 11). Sandia micromirrors may be part of next generation space telescope. [Online]. Last Access: Sept. 11, 2007. Available: <http://www.sandia.gov/media/NewsRel/NR1999/space.htm>
- [36] J.R.P. Angel, "Ground-based imaging of extrasolar planets using adaptive optics," *Nature*, vol. 368, pp. 203-207, 1994.
- [37] A. Roorda, and D.R. Williams, "The arrangement of the three cone classes in the living human eye," *Nature*, vol. 397, pp. 520-522, 1999.

- [38] R.D. Ferguson, D.X. Hammer, C.E. Bigelow, N.V. Iftimia, T.E. Ustun, S.A. Burns, A.E. Elsner, and D.R. Williams, "Tracking adaptive optics scanning laser ophthalmoscope," in *Proc. SPIE*, vol. 6138, 2006, pp. 232-240.
- [39] R.K. Gupta, and S.D. Senturia, "Pull-in time dynamics as a measure of absolute pressure," in *Proc. IEEE 10th Annual Int. Workshop on MEMS*, 1997, pp. 290-294.
- [40] J.I. Seeger, and B.E. Boser, "Parallel-plate driven oscillations and resonant pull-in," in *Tech. Dig. Solid-State Sensor, Actuator, and Microsyst. Workshop*, 2002, pp. 313-316.
- [41] D. Bernstein, R. Guidotti, and J.A. Pelesko, "Analytical and numerical analysis of electrostatically actuated MEMS devices," in *Proc. Modeling Simulation Microsyst.*, 2000, pp. 489-492.
- [42] O. Degani, E. Socher, A. Lipson, T. Leitner, D.J. Setter, S. Kaldor, and Y. Nemirovsky, "Pull-in study of an electrostatic torsion microactuator," *J. Microelectromech. Syst.*, vol. 7, no. 4, pp. 373-379, 1998.
- [43] G. Flores, G.A. Mercado, and J.A. Pelesko, "Dynamics and touchdown in electrostatic MEMS," in *Proc. of IDETC/CIE 19th ASME Biennial Conf. Mech. Vibration and Noise*, Chicago, IL, 2003.
- [44] O. Francais, and I. Dufour, "Dynamic simulation of an electrostatic micropump with pull-in hysteresis phenomena," *Sensors and Actuators A*, vol. 70, pp. 56-60, 1998.
- [45] M.-A. Gretillat, Y.-J. Yang, E.S. Hung, V. Rabinovich, G.K. Ananthasuresh, N.F. de Rooij, and S.D. Senturia, "Nonlinear electromechanical behavior of an electrostatic microrelay," in *Transducers '97 IEEE Int. Conf. Solid-State Sensors and Actuators*, Chicago, IL, 1997, pp. 1141-1144.
- [46] D. Hah, H. Toshiyoshi, and M.C. Wu, "Design of electrostatic actuators for MOEMS applications," in *Design, Test, Integration, and Packaging of MEMS/MOEMS 2002 Proc. SPIE*, vol. 4755.
- [47] D. Hah, P.R. Patterson, H.D. Nguyen, H. Toshiyoshi, and M.C. Wu, "Theory and experiments of angular vertical comb-drive actuators for scanning micromirrors," *IEEE J. Sel. Topics Quantum Electron.*, vol. 10, no. 3, pp. 505-513, 2004.
- [48] R. Legtenberg, J. Gilbert, S.D. Senturia, and M. Elwenspoek, "Electrostatic curved electrode actuators," *J. Microelectromech. Syst.*, vol. 6, no. 3, pp. 257-265, 1997.
- [49] Y. Nemirovsky, and O. Bochobza-Degani, "A methodology and model for the pull-in parameters of electrostatic actuators," *J. Microelectromech. Syst.*, vol. 10, no. 4, pp. 601-615, 2001.

- [50] Z. Xiao, XT Wu, W. Peng, and K.R. Farmer, "An angle-based approach for rectangular electrostatic torsion actuators," *J. Microelectromech. Syst.*, vol. 10, no. 4, pp. 561-568, 2001.
- [51] Z. Xiao, W. Peng, and K.R. Farmer, "Analytical behavior of rectangular electrostatic torsion actuators with nonlinear spring bending," *J. Microelectromech. Syst.*, vol. 12, no. 6, pp. 929-936, 2003.
- [52] X.M. Zhang, F.S. Chau, C. Quan, Y.L. Lam, and A.Q. Liua, "A study of the static characteristics of a torsional micromirror," *Sensors and Actuators A*, vol. 90, pp. 73-81, 2001.
- [53] J. Zhang, Y.C. Lee, V.M. Bright, and J. Neff, "Digitally positioned micromirror for open-loop controlled applications," in *Proc. IEEE MEMS*, 2002, pp. 536-539.
- [54] Z. Xiao, and K.R. Farmer, "Instability in micromachined electrostatic torsion actuators with full travel range," in *Transducers 2003 12th Int. Conf. Solid State Sensors, Actuators and Microsystems*, Boston, MA, 2003, pp. 1431-1434.
- [55] X. Wu, R.A. Brown, S. Mathews, and K.R. Farmer, "Extending the travel range of electrostatic micro-mirrors using insulator coated electrodes," in *2000 IEEE/LEOS Int. Conf. Optical MEMS*, 2000, pp. 151-152.
- [56] D.M. Burns, and V.M. Bright, "Nonlinear flexures for stable deflection of an electrostatically actuated micromirror," in *Proc. SPIE*, vol. 3226, 1997, pp. 125-136.
- [57] J.R. Bronson, G.J. Wiens, and J.J. Allen, "Modeling and alleviating instability in a MEMS vertical comb drive using a progressive linkage," in *Proc. IDETC/CIE 2005 ASME Int. Design Eng. Tech. Conf.*, Long Beach, CA, 2005.
- [58] J.J. Allen, J.R. Bronson, and G.J. Wiens, "Extended-range tiltable micromirror," US Patent SD7962S106240 (pending). Technical Advance filed March 1, 2005. Application filed July 28, 2006.
- [59] J.I. Seeger, and S.B. Crary, "Stabilization of electrostatically actuated mechanical devices," in *Transducers '97 IEEE Int. Conf. on Solid-State Sensors and Actuators*, Chicago, IL, 1997, pp. 1133-1136.
- [60] J.I. Seeger, and B.E. Boser, "Dynamics and control of parallel plate actuators beyond the electrostatic instability," in *Transducers '99 10th Int. Conf. on Solid-State Sensors and Actuators*, Sendai, Japan, 1999, pp. 474-477.
- [61] E.K. Chan, and R. W. Dutton, "Electrostatic micromechanical actuator with extended range of travel," *J. Microelectromech. Syst.*, vol. 9, no. 3, pp. 321-328, 2000.

- [62] J.A. Pelesko, and A.A. Triolo, "Nonlocal problems in MEMS device control," *J. Eng. Math.*, vol. 41: pp. 345-366, 2001.
- [63] E.K. Chan, and R. W. Dutton, "Effects of capacitors, resistors and residual charge on the static and dynamic performance of electrostatically actuated devices," in *Proc. SPIE*, vol. 3680, 1999, pp. 120-30.
- [64] J.I. Seeger, and B.E. Boser, "Charge control of parallel-plate, electrostatic actuators and the tip-in instability," *J. Microelectromech. Syst.*, vol. 12, no. 5, pp. 656-671, 2003.
- [65] R.N. Guardia, R. Aigner, W. Nessler, M. Handtmann, L.M Castaner, "Control positioning of torsional electrostatic actuators by current driving," in *Third Int. Euro. Conf. Advanced Semiconductor Devices and Microsyst.*, Sinolenice Castle, Slovakia, 2000, pp. 91-94.
- [66] R. Nadal-Guardia, A. Dehe, R. Aigner, and L.M. Castaner, "Current drive methods to extend the range of travel of electrostatic microactuators beyond the voltage pull-in point," *J. Microelectromech. Syst.*, vol. 11, pp. 255-263, 2002.
- [67] J.M. Kyynaraninen, A.S. Oja, and H. Seppa, "Increasing the dynamic range of a micromechanical moving plate capacitor," *Anal. Intergr. Circuits Signal Processing*, vol. 29, no. 1-2, pp. 61-70, 2001.
- [68] P.B. Chu, and K.S.J. Pister, "Analysis of closed-loop control of parallel-plate electrostatic microgrippers," in *Proc. Int. Conf. Robotics and Automation*, San Diego, CA, 1994, pp. 820-825.
- [69] J. Chen, W. Weingartner, A. Azarov, and R.C. Giles, "Tilt-angle stabilization of electrostatically actuated micromechanical mirrors beyond the pull-in point," *J. Microelectromech. Syst.*, vol. 13, no. 6, pp. 988-997, 2004.
- [70] M.S. Lu, and G. Fedder, "Closed-loop control of a parallel-plate microactuator beyond the pull-in limit," in *Solid-State Sensor Actuator and Microsyst. Workshop*, Hilton Head, SC, 2002, pp. 255-258.
- [71] M.S.-C. Lu, and G.K. Fedder, "Position control of parallel-plate microactuators for probe-based data storage," *J. Microelectromech. Syst.*, vol. 13, no. 5, pp. 759-769, 2004.
- [72] D. Piyabongkarn, Y. Sun, R. Rajamani, A. Sezen, and B.J. Nelson, "Travel range extension of a MEMS electrostatic microactuator," *IEEE Trans. Control Syst. Tech.*, vol. 13, no. 1, pp. 138-145, 2005.
- [73] H.S. Sane, "Energy-based control for MEMS with one-sided actuation," in *Proc. Amer. Controls Conf.*, Minneapolis, MN, 2006, pp. 1209-1214.

- [74] D.H.S. Maithripala, J.M. Berg, and W.P. Dayawansa, "Nonlinear dynamic output feedback stabilization of electrostatically actuated MEMS," in *Proc. 42nd IEEE Conf. Decision and Control*, Maui, HI, 2003, pp. 61-66.
- [75] P. Cheung, R. Horowitz, and R. Howe, "Design, fabrication, position sensing and control of an electrostatically-driven polysilicon microactuator," *IEEE Trans. Magnetics*, vol. 32, pp. 122-128, 1996.
- [76] K.M. Liao, Y.C. Wang, C.H. Yeh, and R. Chen, "Closed-loop adaptive control for electrostatically driven torsional micromirrors," *J. Microlith., Microfab., Microsyst.*, vol. 4, no. 4, 2005.
- [77] D.A. Horsley, N. Wongkomet, N. Horowitz, and A.P. Pisano, "Precision positioning using a microfabricated electrostatic actuator," *IEEE Trans. Magnetics*, vol. 35, no. 2, pp. 993-999, 1999.
- [78] S. Pannu, C. Chang, R.S. Muller, and A.P. Pisano, "Closed-loop feedback-control system for improved tracking in magnetically actuated micromirrors," in *IEEE/LEOS Opt. MEMS 2000*, pp. 107-108.
- [79] R.K. Messenger, T.W. McLain, L.L. Howell, "Feedback control of a thermomechanical inplane microactuator using piezoresistive displacement sensing," in *ASME Int. Mechanical Eng. Congress Expo*, Anaheim, CA, 2004.
- [80] R.K. Messenger, T.W. McLain, L.L. Howell, "Piezoresistive feedback for improving transient response of MEMS thermal actuators," in *Proc. SPIE*, vol. 6174, 2006.
- [81] N. Yazdi, H. Sane, T.D. Kudrle, and C.H. Mastrangelo, "Robust sliding-mode control of electrostatic torsional micromirrors beyond the pull-in limit," *Transducers 2003 IEEE Int. Conf. Solid-State Sensors and Actuators*, 2003, pp. 1450-1453.
- [82] D. Hernandez, S.-S. Park, R. Horowitz, A.K. Packard, "Dual-stage track-following servo design for hard disk drives," in *Proc. Amer. Control Conf.*, 1999.
- [83] H.C. Liaw, D. Oetomo, B. Shirinzadeh, and G. Alici, "Robust motion tracking control of piezoelectric actuation systems," in *Proc. IEEE Int. Conf. Robotics and Automation*, Orlando, FL, 2006, pp. 1414-1419.
- [84] S.E. Lyshevski, "Nonlinear microelectromechanical systems (MEMS) analysis and design via the lyapunov stability theory," in *Proc. IEEE Conf. Decision and Control*, vol. 5, 2001, pp. 4681-4686.
- [85] G. Zhu, J. Penet, and L. Saydy, "Robust control of an electrostatically actuated MEMS in the presence of parasitics and parametric uncertainties," in *Proc. American Controls Conf.*, Minneapolis, MN, 2006, pp. 1233-1238.

- [86] S.H. Lee, S.E. Bak, and Y.H. Kin, "Design of a dual-stage actuator control system with discrete-time sliding mode for hard disk drives," in *Proc. IEEE Conf. Decision and Control*, vol. 4, 2000, pp. 3120-3125.
- [87] J.C. Chiou, Y.C. Lin, and S.D. Wu, "Closed-loop fuzzy control for torsional micromirror with multiple electrostatic electrodes," in *IEEE/LEOS Opt. MEMS*, 2002, pp. 85-86.
- [88] D.V. Dao, T. Toriyama, J. Wells, and S. Sugiyama, "Silicon piezoresistive six-degree of freedom force-moment micro sensor," *Sensors and Materials*, vol. 15, no. 3, pp. 113-135, 2002.
- [89] D.V. Dao, T. Toriyama, J. Wells, and S. Sugiyama, "Six-degree of freedom micro force-moment sensor for applications in geophysics," in *15th Annual IEEE Conf. on MEMS*, Las Vegas, NV, pp. 312-315.
- [90] Y. Li, M. Papila, T. Nishida, L. Cattafesta, and M. Sheplak, "Modeling and optimization of a side-implanted piezoresistive shear stress sensor," in *Proc. SPIE 13th Annual Int. Symp. Smart Structures and Materials*, San Diego, CA, 2006.
- [91] G. Roman, J. Bronson, G. Wiens, J. Jones, and J. Allen, "Design of a piezoresistive surface micromachined three-axis force transducer for microassembly," in *Proc. Int. Mech. Eng. Conf.*, Orlando, FL, 2005.
- [92] R. Schellin, and G. Hess, "Silicon subminiature microphone based on piezoresistive polysilicon strain gauges," *Sensors and Actuators A*, vol. 32, no. 1-3, pp. 555-559, 1992.
- [93] D.P. Arnold, T. Nishida, L.N. Cattafesta, and M. Sheplak, "A directional acoustic array using silicon micromachined piezoresistive microphones," *J. Acoust. Soc. Amer.*, vol. 113, no. 1, pp. 289-298, 2003.
- [94] H.L. Stalford, C. Apblett, S.S. Mani, W.K. Schubert, and M. Jenkins, "Sensitivity of piezoresistive readout device for microfabricated acoustic spectrum analyzer," in *Proc. SPIE*, vol. 5344, pp.36-43.
- [95] R. Dieme, G. Bosman, M. Sheplak, and T. Nishida, "Source of excess noise in silicon piezoresistive microphones," *J. Acoust. Soc. Amer.*, vol. 119, pp. 2710-2720, 2006.
- [96] H. Xie, and G.K. Fedder, "Vertical comb-finger capacitive actuation and sensing for CMOS-MEMS," *Sensors & Actuators A*, vol. 95, pp. 212-221, 2002.
- [97] B.D. Jensen, M.P de Boer, N.D. Masters, F. Bitsie, and D.A. LaVan, "Interferometry of actuated microcantilevers to determine material properties and test structure nonidealities in MEMS," *J. Microelectromech. Syst.*, vol. 10, no. 3, 2001.

- [98] S. Limary, H. Sterart, L. Irwin, J. McBrayer, J. Sniegowski, S. Montague, J. Smith, M. de Boer, and J. Jakubczak, "Reproducibility data on SUMMiT," in *Proc. SPIE*, vol. 3874, 1999, pp. 102-112.
- [99] ANSYS, Inc. (2007, June 19). ANSYS Product Information and Documentation. [Online]. Last Access: Sept. 11, 2007. Available: <http://www.ansys.com>
- [100] F. Pan, J. Kubby, E. Peeters, A.T. Tran, and S. Mukherjee, "Squeeze-film damping effect on the dynamic response of a MEMS torsion mirror," in *Tech. Proc. Int. Conf. Modeling and Simulation of Microsystems*, 1998, pp. 474-479.
- [101] M. Zecchino, and E. Novak. (2001, June 19). MEMS in motion: a new method for dynamic MEMS metrology. *Veeco, Inc. website*. [Online]. Last Access: Sept. 11, 2007. Available: <http://www.veeco.com/pdfs.php/69>
- [102] K. Ogata, *Modern Control Engineering, Fourth Ed.*, Upper Saddle River, NJ: Prentice Hall, 2002.
- [103] K. Zhou, and J.C. Doyle, *Essentials of Robust Control*, Upper Saddle River, NJ: Prentice Hall, 1998.
- [104] G.E. Dullerud, and F. Paganini, *A Course in Robust Control Theory: A Convex Approach*, New York, NY: Springer, 1999.
- [105] A. Ashkin, "History of optical trapping and manipulation of small-neutral particle, atoms, and molecules," *IEEE J. Sel. Topics Quantum Electronics*, vol. 6, no. 6, pp. 841-856, 2000.
- [106] J.A. Pelesko, and D.H. Bernstein, *Modeling MEMS and NEMS*, Boca Raton, FL: Chapman and Hall/CRC, 2003.
- [107] A.H. Nayfeh, and B. Balachandran, *Applied Nonlinear Dynamics: Analytical, Computational, and Experimental Methods*, New York, NY: John Wiley and Sons, 1995.
- [108] R.C. Dorf, and R.H. Bishop, *Modern Control Systems 9th ed.*, Upper Saddle River, NJ: Prentice Hall, 2001.
- [109] J.R. Taylor, *An Introduction to Error Analysis: The Study of Uncertainties in Physical Measurements 2nd ed.*, Sausalito, CA: University Science Books, 1982.
- [110] L. Guilbeau, "The history of the solution of the cubic equation," *Mathematics News Letters*, vol. 5, no. 4, 1930.
- [111] D. Elata, and H. Bamberger, "On the dynamic pull-in of electrostatic actuators with multiple degrees of freedom and multiple voltage sources," *J. Microelectromech. Syst.*, vol. 15, no. 1, 2006.

- [112] L. Mattsson, "Experiences and challenges in multi material micro metrology," in *Proc. 2nd Annual Int. Conf. Micromanufacturing*, Clemson, SC, 2007, pp. 318-322.
- [113] W.A. Moussa, H. Ahmed, W. Badawy, and M. Moussa, "Investigating the reliability of the electrostatic comb-drive actuators utilized in microfluidic and space systems using finite element analysis," *Canadian J. Electrical Computer Syst.*, vol. 27, no. 4, pp. 195-200, 2002.

BIOGRAPHICAL SKETCH

Jessica Bronson graduated with honors from the University of Missouri at Columbia with a B.S. in mechanical engineering in December 2002. Ms. Bronson began her graduate studies in January 2003 under Professor Gloria Wiens in the Space Automation and Manufacturing Mechanisms Laboratory at the University of Florida in Gainesville. Shortly after beginning graduate school, Ms. Bronson was awarded an internship at Sandia National Laboratories in Albuquerque, New Mexico as a fellow through the Microsystems, Engineering, and Science Applications (MESA) Institute at Sandia. In 2004, she was granted the Sandia National Laboratories Campus Executive Fellowship that allowed her to continue to develop her research program at the university, in addition to returning to New Mexico for internships at Sandia each summer for the next three years. The focus of her Ph.D. research is to develop and implement closed-loop control systems for Microelectromechanical Systems (MEMS) micromirrors. The impact of this research is that it will increase accuracy, performance and repeatability leading to advances in imaging and communications technology. Upon completion of her Ph.D., Ms. Bronson hopes to continue her work in MEMS and control systems by obtaining a position at a leading research laboratory.